

UNIVERSITY OF OXFORD

DEPARTMENT OF ENGINEERING SCIENCE

Flexoelectricity in Nematic Liquid Crystals

submitted by

Claudius Kischka

Wolfson College

A thesis submitted for the degree of

Doctor of Philosophy

Trinity Term 2011

Acknowledgement

I would like to acknowledge the guidance and encouragement that my supervisors - Professor Peter Raynes and Professor Steve Elston - provided during my time as a D.Phil. student. I would also like to thank the EPSRC for their financial support for this work. Merck UK and ZBD have been particularly generous by providing the liquid crystal materials and devices without which this project would not have been possible in its present form. I also wish to thank both past and present members of the liquid crystals group at Oxford University for their encouragement and support during my time as a member, especially Dr Lesley Parry-Jones and Paul Brimicombe for interesting and enlightening discussions.

Finally I wish to thank my parents and family for their support and love during my four year residence in Oxford and my work on this project.

Abstract

Flexoelectricity in liquid crystals is thought to be due to a coupling between dielectric properties and shape anisotropy of the molecules and described by the flexoelectric coefficients e_1 and e_3. Two experiments are needed to measure e_1 and e_3 and it is usual to measure the difference $(e_1 - e_3)$ and the sum $(e_1 + e_3)$ and then calculate e_1 and e_3.

The first experiment to measure the difference $(e_1 - e_3)$ uses a TN structure with an in-plane applied electric field. Due to the dielectric coupling, the director aligns with the electric field and due to the flexoelectric effect, the director tilts out of plane. This tilt is measured optically using two laser beams at oblique incidence, e.g. 45°. Using a theoretical model the experimental data is fitted and the difference $(e_1 - e_3)$ extracted.

The second experiment to measure the sum $(e_1 + e_3)$ uses a Pi cell. Applying an ac voltage the transmission through the device is a repeating oscillating signal which contains 1st and 2nd harmonics. The 1st harmonic corresponds to the flexoelectric effect and the 2nd harmonic to the dielectric effect. Using a lock-in amplifier, the harmonics were measured and the sum $(e_1 + e_3)$ extracted using a theoretical model to fit the experimental data. Unfortunately, the data proved the experiment to be unreliable and another method was developed, which uses a HAN cell.

The third experiment uses simple pulses in a HAN cell and also measures the sum $(e_1 + e_3)$. The big disadvantage of the HAN cell is an internal voltage, which is created by the homeotropic alignment layer and the flexoelectric polarisation. The internal voltage has the same effect on the director profile as the flexoelectric effect, which is a big problem in measuring flexoelectricity. Using a material, which is non ionic and has no flexoelectricity, the internal bias could be measured and taken into account. Applying short dc pulses of opposite sign, the flexoelectric effect can be

observed by the optical response and can be measured.

Using these experiments, a number of investigation are being carried out such as the correlation between flexoelectricity and the molecular structure, ions, elastic properties, molecular orientation, dielectric anisotropy $\Delta\epsilon$, and order parameter S. The results showed that flexoelectricity only depends on ions and dielectric properties which was very interesting and surprising at the same time.

List of publications

Papers:

- R.A. Ewings, C. Kischka, L.A. Parry-Jones and S.J. Elston, **Measurement of the difference in flexoelectric coefficients of nematic liquid crystals using a twisted nematic geometry**, *Phys. Rev. E*, **73**, 011713, (2006)
- C. Kischka, L.A. Parry-Jones, S.J. Elston and E.P. Raynes, **Measurement of the Flexoelectric Coefficients e_1 and e_3 in Nematic Liquid Crystals**, *34. Arbeitstagung Fluessigkristalle*, Freiburg (Germany) (2006)
- P.D. Brimicombe, C. Kischka, S.J. Elston and E.P. Raynes, **Measurement of the Twist Elastic Constant of Nematic Liquid Crystals Using Pi-Cell Devices**, *J. Appl. Phys.*, **101**, 043108, (2007)
- C. Kischka, L.A. Parry-Jones, S.J. Elston and E.P. Raynes, **Measurement of the Flexoelectric Coefficients e_1 and e_3 in Nematic Liquid Crystals**, *Mol. Cryst. Liq. Cryst.*, **480**, pp. 103, (2008)
- C. Kischka, S.J. Elston and E.P. Raynes, **Measurement of the Sum (e_1+e_3) of the Flexoelectric Coefficients e_1 and e_3 in nematic liquid crystals using a HAN cell**, *Mol. Cryst. Liq. Cryst.*, **494**, pp. 93, (2008)
- P.S. Salter, C. Kischka, S.J. Elston and E.P. Raynes, **The influence of chirality on the difference in flexoelectric coefficients investigated in Uniform Lying Helix, Grandjean and twisted nematic structures**, *Liq. Cryst.* **36**, pp. 1355, (2009)
- C. Kischka, L.A. Parry-Jones, S.J. Elston and E.P. Raynes, **Investigation of the influence of dielectric anisotropy $\Delta\epsilon$ on the difference $(e_1 - e_3)$ of the flexoelectric coefficients of nematic liquid crystals**, to be submitted
- C. Kischka, S.J. Elston and E.P. Raynes, **Investigating the influence of the molecular structure on the difference $(e_1 - e_3)$ of the flexoelectric coefficients in nematic liquid crystals**, to be submitted
- C. Kischka, S.J. Elston and E.P. Raynes, **Measurement of the rotational viscosity γ_1 in nematic liquid crystals using a TN-Cell with an in-plane applied electric field**, to be submitted

Details of attendance at conferences

- British Liquid Crystal Conference (BLCS) April 2005 in Exeter, UK
  Poster contribution
- 34. Arbeitstagung Fluessigkristalle March 2006 in Freiburg, Germany
  Poster contribution
- British Liquid Crystal Conference (BLCS) April 2006 in York, UK
  Oral contribution
  Poster contribution
- International Liquid Crystal Conference (ILLC) July 2006 in Colorado, USA
  Oral contribution
  Poster contribution
- Flexoelectric Conference September 2006 in Oxford, UK
  Oral contribution
  Poster contribution
- British Liquid Crystal Conference (BLCS) conference March 2007 in Sheffield, UK
  Oral contribution
  Poster contribution
- European Conference of Liquid Crystal (ECLC) July 2007 in Lisbon, Portugal
  Poster contribution
- British Liquid Crystal Conference (BLCS) conference March 2008 in Norwich, UK
  Oral contribution

Contents

1 Introduction **1**

1.1 Liquid Crystals 1

1.1.1 History 1

1.1.2 The liquid crystal phase 4

1.1.3 The director and order parameter 5

1.1.4 Chirality 7

1.2 Physical Properties 7

1.2.1 Elastic constants 8

1.2.2 Dielectric anisotropy 10

1.2.3 Optical anisotropy: Birefringence 13

1.2.4 Magnetic anisotropy 13

1.2.5 Viscosity 14

1.2.6 Flexoelectricity 15

1.3 Liquid Crystal Devices 16

1.3.1 Construction 16

1.3.2 Alignment 17

1.3.3 Cell Structures 18

1.3.4 Polariser 20

2 Flexoelectricity **22**

2.1 Introduction 22

2.2 Experimental Ideas 25

2.2.1 Measurement of sum $(e_1 + e_3)$ 27

2.2.2 Measurement of difference $(e_1 - e_3)$ 30

2.3 Applications . . . 32
2.3.1 Bistability (ZBD) . . . 32
2.3.2 Chiral Flexoelectro-optic Effect . . . 33

3 Theory **35**
3.1 Introduction . . . 35
3.2 Definition . . . 37
3.2.1 Coordinate System . . . 37
3.3 Molecular field . . . 38
3.4 Dissipation function . . . 40
3.4.1 Dissipation function with flow . . . 41
3.4.2 Dissipation function without flow . . . 42
3.5 Bulk Energy . . . 44
3.5.1 Elastic Energy . . . 44
3.5.2 Electrostatic Energy . . . 44
3.5.3 Flexoelectric Energy . . . 48
3.5.4 Total Bulk Energy . . . 49
3.6 Surface Energy . . . 50
3.7 Computation . . . 51
3.8 Example: Freedericksz geometry . . . 54
3.9 Optics . . . 61

4 Overview of Material Properties **64**
4.1 Measurement of elastic, dielectric and refractive properties . . . 64
4.1.1 Measurement of $K_{11}, K_{33}, \epsilon_{\parallel}, \epsilon_{\perp}$ . . . 64
4.1.2 Measurement of K_{22} . . . 68
4.1.3 Measurement of $n_{\parallel}, n_{\perp}$ . . . 74
4.1.4 Measurement of nematic-isotropic transition temperature T_{NI} 75
4.1.5 Error investigation . . . 76
4.2 Overview of materials . . . 76
4.2.1 Molecular structure . . . 77
4.2.2 Non-Ionic materials . . . 78
4.2.3 Elastic Properties . . . 78

4.2.4 Molecular orientation 79
4.2.5 Dielectric anisotropy $\Delta\epsilon$ 79
4.2.6 Order Parameter S 80
4.2.7 Overview of material's properties 80

5 TN cell to measure difference $(e_1 - e_3)$ 82
5.1 Introduction 82
5.2 Theory 83
5.3 Experiment 88
5.3.1 Electric field 88
5.3.2 Experimental set-up 89
5.3.3 Data 92
5.3.4 Automation of experiment 95
5.3.5 Pretilt 96
5.3.6 Thickness degeneracity 96
5.3.7 Sign 98
5.3.8 Ions 99
5.3.9 Automation of fitting 101
5.3.10 Error investigation 102
5.3.11 Surface Energy 104
5.3.12 Frequency dependence 105
5.3.13 Limitations of the method 105
5.4 Results 106
5.4.1 Materials E7 and E70A 106
5.4.2 Non-ionic materials 108
5.4.3 Molecular structure materials 110
5.4.4 Elastic properties materials 111
5.4.5 Molecular orientation materials 112
5.4.6 Dielectric anisotropy $\Delta\epsilon$ materials 113
5.4.7 Overview 114
5.5 Conclusion 115
5.5.1 Experiment 115

5.5.2 Non-Ionic materials . . . 116
5.5.3 Molecular structure . . . 117
5.5.4 Elastic Properties . . . 117
5.5.5 Molecular orientation . . . 118
5.5.6 Dielectric anisotropy $\Delta\epsilon$ . . . 118
5.5.7 Future . . . 120

6 Pi cell to measure sum ($e_1 + e_3$) 122
6.1 Introduction . . . 122
6.2 Theory . . . 124
6.2.1 Finding E_z . . . 129
6.2.2 Surface Energy . . . 131
6.2.3 Dissipation function . . . 132
6.2.4 Optics . . . 135
6.2.5 Preinvestigation of cell structure . . . 137
6.3 Experiment . . . 139
6.3.1 Production of cell with high pretilt . . . 139
6.3.2 Experimental Set-up . . . 140
6.3.3 Data . . . 141
6.3.4 Frequency dependence . . . 144
6.3.5 Automation . . . 144
6.3.6 Fitting . . . 145
6.4 Results . . . 146
6.4.1 Material E7 . . . 146
6.4.2 Material CB . . . 149
6.4.3 Dielectric properties materials . . . 150
6.4.4 Non-ionic materials . . . 151
6.5 Conclusion . . . 153
6.5.1 Future . . . 155

7 Simple pulses to measure sum ($e_1 + e_3$) 156

7.1 Introduction . . . 156
7.2 Theory . . . 158
7.3 Experiment . . . 162
7.4 Results . . . 166
7.5 Conclusion . . . 168
7.5.1 Future . . . 169

8 Summary and Conclusion 170

8.1 Experiments . . . 170
8.1.1 TN cell to measure difference ($e_1 - e_3$) . . . 170
8.1.2 Pi cell to measure sum ($e_1 + e_3$) . . . 171
8.1.3 Simple pulses to measure sum ($e_1 + e_3$) . . . 172
8.2 Calculation of e_1 and e_3 . . . 172
8.3 Results . . . 175
8.3.1 Non-Ionic materials . . . 175
8.3.2 Molecular structure . . . 176
8.3.3 Elastic Properties . . . 177
8.3.4 Molecular orientation . . . 177
8.3.5 Dielectric anisotropy $\Delta\epsilon$ . . . 178
8.4 Future . . . 178
8.4.1 Experiments . . . 178
8.4.2 Materials . . . 180
8.4.3 New theory . . . 180

A Measurement of the viscosity γ_1 197

A.1 Introduction . . . 198
A.2 Experiment . . . 199
A.3 Results . . . 202
A.4 Conclusion . . . 204

Chapter 1

Introduction

1.1 Liquid Crystals

1.1.1 History

In 1888, Friedrich Reinitzer, an Austrian botanist at the German University of Prague, observed that cholesteryl benzoate, an extract of carrot, had two distinct melting points [1]. At a temperature of 145°C it melted, becoming cloudy white and viscous and at a temperature of 179°C, it became clear. Intrigued by his observations, Reinitzer contacted Otto Lehmann, who had developed a polarizing microscope which contained a heating stage. Lehmann confirmed Reinitzer's observation and he also discovered that this new phase, between temperatures of 145°C and 179°C, shared the physical properties of a crystal and a liquid at the same time [2]; he named it "Fliessende Kristalle" (in English: "liquid crystal (LC)") and the name was born. However, many opponents argued that the materials were not pure and that the impurities were the reason for the observations. This was disproved by Schenk, who used a pure material and who also observed the liquid crystal phase [3].

In 1904, Merck in Darmstadt, Germany, sold the first commercial available liquid crystal materials for analytical purposes. Scientists discovered that the liquid crystal phase occurred mostly in materials with rod shaped molecules [4] and they were classed as *calmatic* (rod-like) [5]. *Calmatics* and other classes of liquid crystal materials, where a change in temperature induces the phase change, are grouped as *thermotropic*. Subsequently a new group was found, the *lyotropic*, where the phase change is induced by varying the concentration of water, and they have been found to play a major role in biological systems. *Lyotropic* liquid crystals also play a major role in detergents like soap, washing powder, washing liquid, etc. and they are the largest single commercial market of liquid crystals.

However, there were no commercial applications and therefore liquid crystals were unknown to the ordinary man on the street and only investigated by scientists because of their interesting new phase and properties. This situation suddenly changed in the 1970s, when liquid crystals were used in simple displays for calculators and watches. This was possible because of two discoveries, the "Twisted Nematic Liquid Crystal Display (TN LCD)" in 1971 [6] and the "Stable Room Temperature Liquid Crystal Material" in 1972 [7, 8]. But the applications were limited to displays which contained only a few segments or lines (of the order of 10-20).

With the discoveries of "Amorphous Silicon Thin Film Transistors (TFT)" [9] in the early 1980s (used in TN LCD's) and "Super Twisted Nematic Liquid Crystal Display (STN LCD)" in 1982 [10, 11], the door was opened to address up to 100 lines with STN and up to 1000 lines with TN-TFT. These new technologies were used in displays such as PC monitors and laptops. However, they were not yet suitable for TVs because of the slow response speed (>20ms), low contrast ratio (<500:1), poor viewing angle together with contrast (grayscale) inversion, and high production costs.

In the late 1990s, the "old" modes "Vertically Aligned Nematic (VAN)" [12] and "In-Plane Switching (IPS)" [13, 14] were revisited and combined with the TFT technology. This enabled LCs to be used in TVs to overcome the problems of response speed, contrast ratio and viewing angle. These two technologies (VAN-TFT and IPS-TFT) dominate the LCD TV market today.

However for simple displays used in calculators and watches, the TN technology is still used because of its low cost. For more complex displays like advanced calculators, ATM machines etc., where response speed and viewing angle are not very important, the STN technology is used because it is cheaper than TN-TFT displays. The more complex TN-TFT technology is mainly used in PC monitors, laptops and mobile phones.

The general public refers to TN-TFT, VAN-TFT and IPS-TFT displays in general as TFT displays. But there is a big difference. TN-TFT technology is cheaper than VAN-TFT and IPS-TFT but is compromised on viewing angle and response speed, which is not a big problem for the PC, laptop and mobile phone market. The VAN-TFT and IPS-TFT are very different compared to each other from the technological point of view but are very similar in their performance. The VAN-TFT has a fast response speed but the IPS-TFT has a better viewing angle. Never the less, the ordinary man on the street who is interested in buying a TV or PC doesn't know the difference and he is only interested in performance like response time, viewing angle, contrast and brightness. One way to improve the performance is to optimise the liquid crystal material. Therefore, it is necessary to know and understand the chemical and physical properties of the liquid crystal material; these are discussed in this chapter.

1.1.2 The liquid crystal phase

Most displays produced today contain *thermotropic calmatic* liquid crystals which have two main phases, the *nematic* and *smectic* phases. These two phases were first identified and named by Friedel in 1922 [5]. In the isotropic liquid phase, the material does not posses any positional or orientational order (Fig. 1.1 a). Decreasing

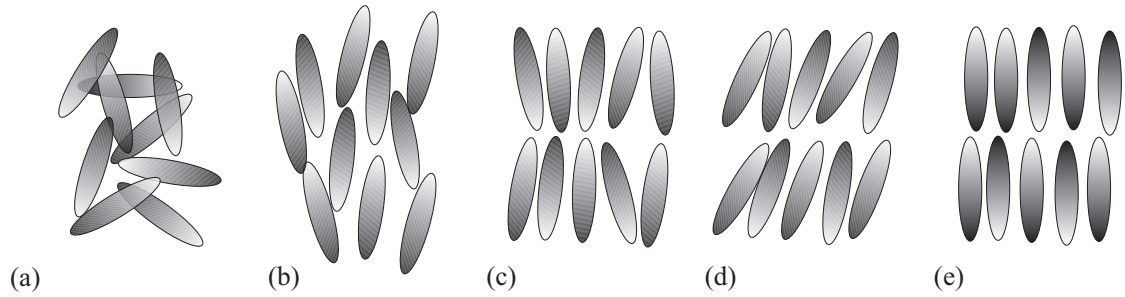


Figure 1.1: a) Isotropic liquid phase, b) Nematic phase, c) Smectic A phase, d) Smectic C phase, e) Solid state

the temperature into the liquid crystal phase, some amount of orientational order is gained and the phase is known as the *nematic* liquid crystal phase (Fig. 1.1 b). Further cooling increases the positional and orientational order and a new phase can be observed, which is called the *smectic* liquid crystal phase (Fig. 1.1 c and d). Not all *calmatic* LC materials contain a *smectic* phase. Decreasing the temperature further leads to the solid state of the material (Fig. 1.1 e). The majority of commercial devices use and rely on the *nematic* phase for the function of the display. Due to the importance of the *nematic* phase, it is investigated and used in this project. The temperature range in which the *nematic* phase exists is increased by mixing different single LC materials together. Modern liquid crystal materials are a mixture of 4 to 20 single components with a wide temperature range of -30°C to +100°C.

1.1.3 The director and order parameter

In the nematic phase the molecules have an amount of orientational order but no positional order. This ordering is thought to be due to the attraction and packing constraints of the molecules. The orientational order allows us to define an average direction of the molecules called the *director*, which is denoted by the unit vector $\vec{n}$ (or $\mathbf{n}$), as shown in Figure 1.2 a). The *director* represents the symmetry axis of the

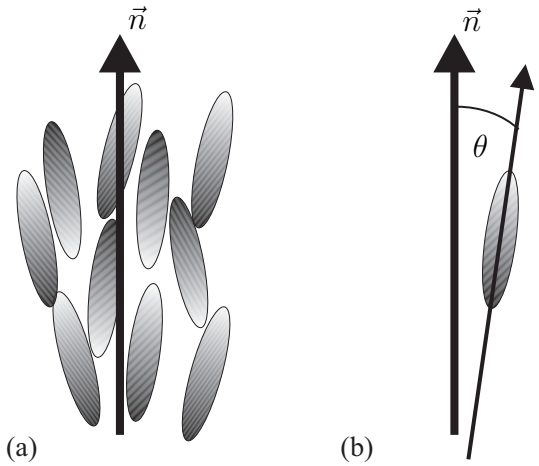


Figure 1.2: a) Nematic phase with director $\vec{n}$, b) Angle θ between director and individual molecule

orientational distribution and the direction of the director cannot be defined, which leads to $\vec{n} \equiv -\vec{n}$. The *director* can either be the average direction of an individual molecule over time or the spatial average of many molecules in a snapshot in time. Due to the symmetric structure of the molecules, the polarity of the director is undefined.

To quantify just how much order is present in a material, an *order parameter* S is defined. Traditionally, the *order parameter* is given as follows:

$$S = \langle P_2(\cos\theta) \rangle = \left\langle \frac{3}{2}\cos^2\theta - \frac{1}{2} \right\rangle$$

where θ is the angle between the *director* and the long axis of each molecule (Fig. 1.2 b). The brackets denote an average overall of the molecules in the sample. In an isotropic liquid, the average of the cosine terms is zero, and therefore the *order parameter* is equal to zero [15]. For a perfect crystal, the *order parameter* evaluates to one. Typical values for the *order parameter* of a liquid crystal material range between 0.4 and 0.7, depending on the temperature. Figure 1.3 shows the

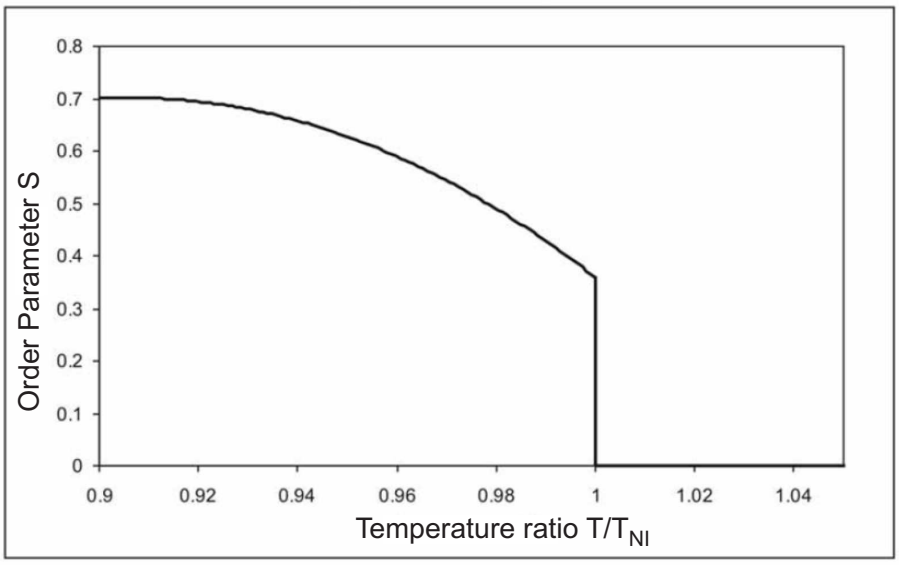


Figure 1.3: Order parameter S versus temperature

order parameter S versus the temperature ratio, which is defined as the ratio between the temperature T and the nematic-isotropic transition temperature T_{NI}. The nematic-isotropic transition temperature T_{NI} is defined as the temperature where the material goes from the liquid crystal phase into the isotropic phase. Figure 1.3 shows clearly that by heating up the material and increasing the temperature, the order parameter S decreases until the temperature reaches the nematic-isotropic transition temperature T_{NI}, where the order parameter S suddenly changes to zero.

1.1.4 Chirality

Liquid crystal materials can have chiral properties and the chiral nematic phase is also known as the *cholesteric* phase. The molecular chirality produces a bulk helicity, whereby the distance over which the director rotates by 360° is defined as the pitch P. Chirality occurs naturally in some liquid crystal materials but can be produced in achiral materials by adding a chiral dopant.

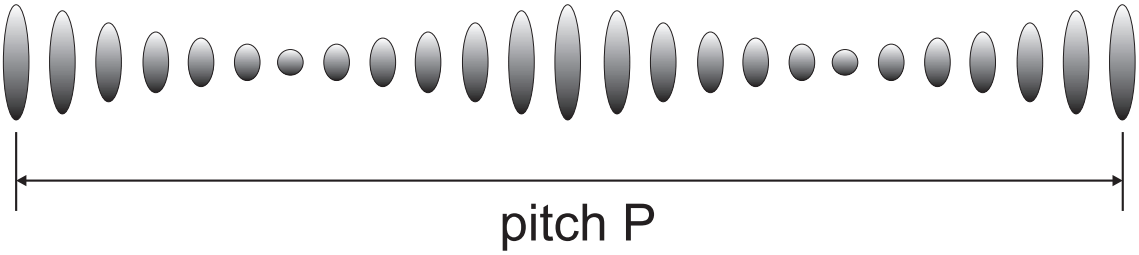


Figure 1.4: Chiral nematic phase with pitch P

1.2 Physical Properties

The physical properties of the liquid crystal material are caused by the chemical structure of the molecule, which leads to a certain ordering of the molecules to each other. *Calmatic* liquid crystals are long rod shaped molecules and the chemical structure of 4-pentyl-4'-cyanobiphenyl (5CB), a typical molecule, is shown in Figure 1.5 a). In general, the molecule is composed of aromatic and aliphatic rings to which a C_nH_{2n+1} chain is attached on one side and a CN (Carbon Nitrogen) group on the other side (Fig. 1.5 b)). The CN group attracts electrons from the rest of the molecule, which leads to a strong concentrated negative charge density at the CN group and a weak positive charge density across the rest of the molecule and, therefore, to a permanent dipole. It is common to replace the CN group with a F (Fluorine) group, which also creates a stronger permanent dipole, whereby the F

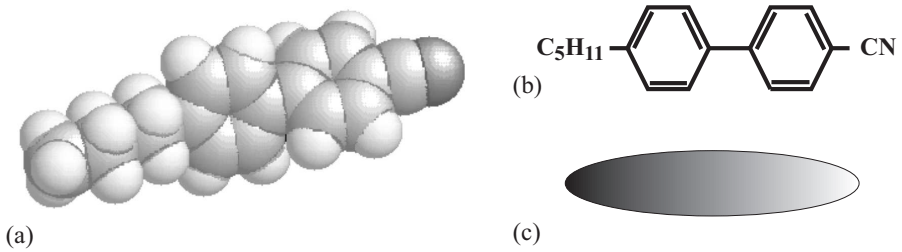


Figure 1.5: 4-pentyl-4'-cyanobiphenyl (5CB): a) Space-filling model of 5CB, b) Chemical structure of 5CB, c) Symbol of a liquid crystal used in this thesis

group is also negatively charged and the rest of the molecule positive.

The interesting physical properties of liquid crystals are caused by the long rod shape and the ordering. There are different optical, electrical and magnetical properties along the long axis compared to the short axis. Also, the molecules tend to align parallel to each other which results in elastic forces. The optical, electric, and elastic properties make liquid crystals useful for displays, which are also known as electro-optic displays.

Additionally it is important to point out that all physical properties of liquid crystals vary with temperature. This will be discussed briefly in this thesis because all experiments were carried out at room temperature and the temperature dependence was not investigated in detail.

1.2.1 Elastic constants

The molecules tend to align parallel to each other due to complex van de Waals forces between the molecules and due to the packing order. This uniform parallel alignment of the local molecules represents the equilibrium state which corresponds to the state of minimum free energy and results in elastic forces between the liquid crystal molecules. If an external force, like a boundary force, an electric or magnetic field or material flow, is applied, the external force distorts the parallel alignment of

the molecules and pulls them away from each other but the elastic forces between the molecules try to pull back and align the molecules parallel to each other. Any distortion can be expressed by the three deformations *splay*, *twist*, or *bend*, as shown in Figure 1.6.

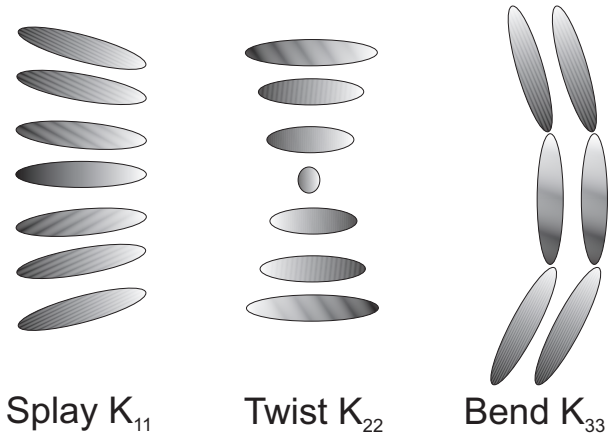


Figure 1.6: The three types of deformation: *splay*, *twist* and *bend*

Splay describes the deformation when the molecules are being pulled off on one side and pushed together on the other side and can be mathematically expressed by $\vec{S} = \vec{n}(\nabla \cdot \vec{n})$. *Twist* occurs when the molecules are being rotated and can be mathematically expressed by $\vec{T} = \vec{n} \cdot (\nabla \times \vec{n})$. *Bend* occurs when the molecules are in parallel but curve to one side and can be mathematically expressed by $\vec{B} = \vec{n} \times (\nabla \times \vec{n})$. The unit of the three deformations is $\frac{1}{m}$ and the deformations can be measured and expressed as the elastic constants: K_{11} for *splay*, K_{22} for *twist*, and K_{33} for *bend*. The energy density (energy per volume) can be expressed by the Frank elastic energy density w_d [16], which is given by

$$\begin{aligned} w_d = & \frac{1}{2}K_{11}\vec{S}^2 + \frac{1}{2}K_{22}\vec{T}^2 + \frac{1}{2}K_{33}\vec{B}^2, \\ = & \frac{1}{2}K_{11}\left(\nabla \cdot \vec{n}\right)^2 + \frac{1}{2}K_{22}\left(\vec{n} \cdot (\nabla \times \vec{n}) - q\right)^2 \\ & + \frac{1}{2}K_{33}\left(\vec{n} \times (\nabla \times \vec{n})\right)^2, \end{aligned} \tag{1.1}$$

where the parameter q represents the pitch P of the liquid crystal and the relationship between q and P is $q = \frac{2\pi}{P}$. The unit of the elastic energy density w_d is $\frac{J}{m^3} = \frac{Nm}{m^3} = \frac{N}{m^2}$, of the elastic constant K_{ii} is N (typical values are around 10pN [17]), of *splay* $\vec{S}$ is $\frac{1}{m}$, of *twist* $\vec{T}$ is $\frac{1}{m}$, of *bend* $\vec{B}$ is $\frac{1}{m}$, of $\vec{S}^2$ is $\frac{1}{m^2}$, of $\vec{T}^2$ is $\frac{1}{m^2}$, and of $\vec{B}^2$ is $\frac{1}{m^2}$. Multiplying K_{ii} with e.g. $\vec{S}^2$ leads to the unit of the energy density.

The deformation of nematic liquid crystals by boundaries plays an important role to orient thin samples. In this case, the molecules are uniformly aligned at the substrate by boundary interaction and this fixed orientation can be transferred to the bulk by elastic forces. There are three basic kinds of uniform orientation. The homeotropic alignment is characterized by an orientation of the director perpendicular to the bounding walls. In the planar aligned samples, the director orientation is uniformly parallel to the substrate. The intermediate case of orientation is the uniform tilt of the director with respect to the substrate planes.

1.2.2 Dielectric anisotropy

Molecules have a strong permanent electric dipole, caused by the configuration of the aromatic rings and the negative charged CN group, as shown in Figure 1.5. Further, an applied electric field rearranges the free charges inside the aromatic rings, which causes an induced electric dipole. The permanent dipole and the induced dipole cause a dielectric anisotropy with a permittivity $\epsilon_{\parallel}$ along the long axis and a permittivity $\epsilon_{\perp}$ perpendicular to the long axis, as shown in Figure 1.7. Permittivity is a property of a material which describes the electric flux density $\vec{D}$, also known as displacement field $\vec{D}$, produced by an applied electric field. The electrical anisotropy is quantified by the dielectric anisotropy $\Delta\epsilon$, which is defined as $\Delta\epsilon = \epsilon_{\parallel} - \epsilon_{\perp}$ and its value is in the range of -10 to 50 but typical materials used in commercial displays use dielectric anisotropies in the range of -4 to 11 [18]. For a positive dielectric anisotropy

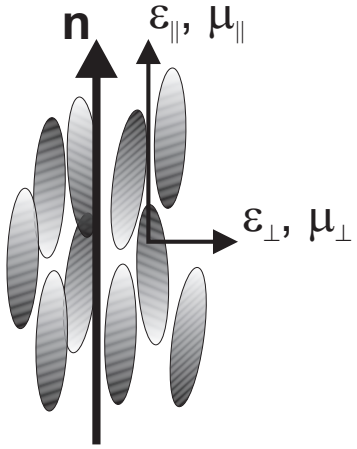


Figure 1.7: Electric and magnetic properties: $\epsilon_{\parallel}$ and $\epsilon_{\perp}$, $\mu_{\parallel}$ and $\mu_{\perp}$

$\Delta\epsilon$, the director tends to align along an applied electric field and the director tends to align perpendicular to an applied electric field for a negative dielectric anisotropy. Using a material with a positive dielectric anisotropy and applying an electric field on a dipole, the negative part of the dipole feels a force towards the positive charges of the electric field and the positive part of the dipole feels a force toward the negative charges of the electric field, as shown in Figure 1.8. These forces lead to a moment, which rotates the dipole until the momentum is zero and the dipole is in a stable position, which is also the lowest energy state. If the dipole is in the unstable position, which is also the highest energy state, a small interruption is necessary to force the dipole out of its position and the leading momentum forces it into the lowest energy state. Applying an electric field on many dipoles, they will all feel a momentum and will rearrange into the lowest energy state, as shown in Figure 1.8.

The electrostatic energy density w_e is defined by

$$w_e = -\frac{1}{2}\vec{D} \cdot \vec{E}, \tag{1.2}$$

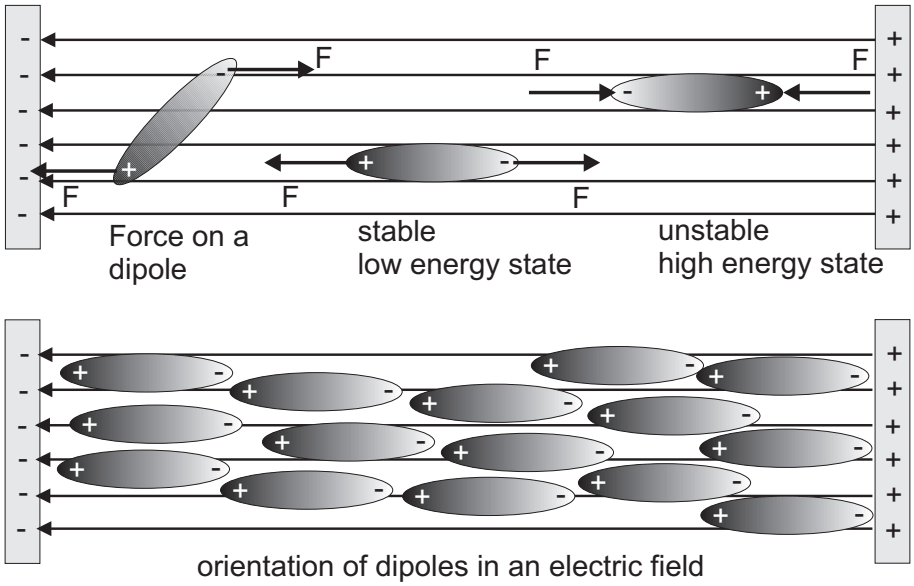


Figure 1.8: Electric field rearranges electric dipoles

where $\vec{E}$ is the electric field and $\vec{D}$ is the displacement field, where $\vec{D}$ is defined as

$$\vec{D} = \epsilon_0 \overleftrightarrow{\epsilon}\ \vec{E}, \tag{1.3}$$

and where ϵ_0 is the permittivity of free space and $\overleftrightarrow{\epsilon}$ is the permittivity tensor. The unit of the electric energy density w_e is $\frac{J}{m^3} = \frac{Nm}{m^3} = \frac{N}{m^2}$, of the electric field $\vec{E}$ is $\frac{V}{m} = \frac{N}{C}$ and of the displacement field $\vec{D}$ is $\frac{C}{m^2}$. ϵ_0 is the permittivity of free space and it is defined as $\epsilon_0 = 8.85 \times 10^{-12}\frac{F}{m} = 8.85^{-12}\frac{C^2}{Nm^2}$.

Using an applied dc voltage, the dipoles will be rearranged once only until the lowest energy state is reached. However, using an ac voltage, which changes the applied electric field frequently, the dipoles are in a permanent rearrangement. If the frequency is increasing, it will be harder for the dipoles to follow the electric field and at a threshold frequency, the dipoles are not able to follow the electric field.

1.2.3 Optical anisotropy: Birefringence

Light is an electro-magnetic wave with a very high frequency. This means that the dipoles have too much inertia to follow the changing electro-magnetic wave of light. In general, the refractive index n can be calculated using $n = \sqrt{\epsilon\mu}$ [19], where ϵ is the relative permittivity, and μ the magnetic permeability. Because liquid crystal materials are non-magnetic, this equation simplifies to $n \approx \sqrt{\epsilon}$. However, this equation does not apply to liquid crystals because of the high frequency of light. The permanent dipoles cannot follow the frequency of light but the free charges inside the rings of the dipoles can follow the electro-magnetic wave and they are affected by the wave. Due to the shape of the molecule, the free charges are affected differently by the light and a refractive index $n_{\parallel}$ for the long axis and $n_{\perp}$ for the short axis can be defined. These cause an optical anisotropy $\Delta n = n_{\parallel} - n_{\perp}$, also known as birefringence. Typical values are in the range of 0.05 to 0.3.

1.2.4 Magnetic anisotropy

Liquid crystals are usually diamagnetic. Applying a magnetic field induces an electric current in the aromatic rings due to the free charges. This current creates a magnetic moment opposite the applied magnetic field so that the director aligns with the magnetic field if the magnetic anisotropy $\Delta\chi$ is positive [20]. If the magnetic anisotropy $\Delta\chi$ is negative, the magnetic field aligns the director perpendicular to the applied field. Similar to the dielectric anisotropy, a magnetic anisotropy can be defined as $\Delta\chi = \chi_{\parallel} - \chi_{\perp}$ (Fig. 1.7). However, the magnetic anisotropy is only interesting from a scientific point of view because it is very difficult, almost impossible, to drive a commercial display with magnetic fields.

1.2.5 Viscosity

Liquid crystals have anisotropic flow properties, which play a very important role in the switching speed and behaviour of commercial devices [18]. The viscosity obtained from a measurement depends on the measurement geometry and three different configurations are shown in Figure 1.9. The viscosity η describes the shearing

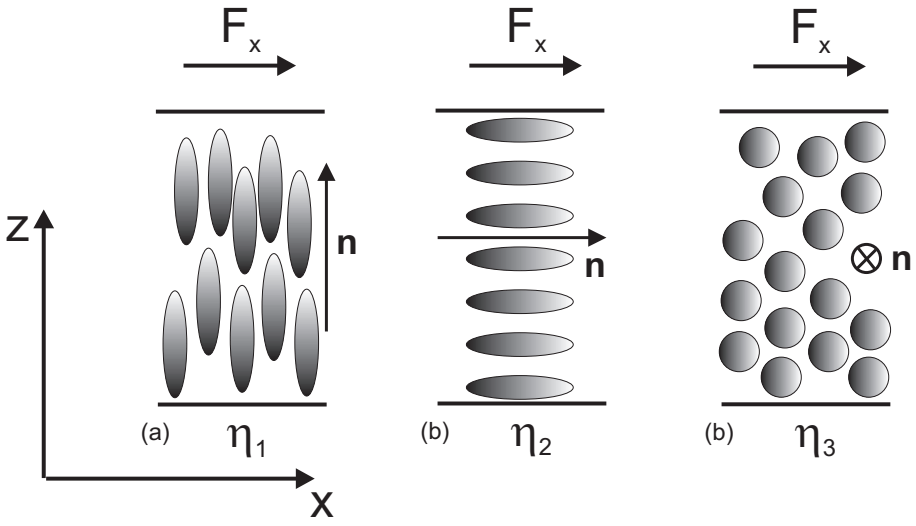


Figure 1.9: Possible configurations for viscosity measurements

stress of a force $\vec{F}$ per unit velocity gradient. For a force in the x-direction the viscosity η is therefore:

$$\eta = \frac{\frac{F_x}{A}}{\frac{dv_x}{dz}}, \tag{1.4}$$

where A is the surface area at which the force is applied and v the velocity of the liquid crystal close to the upper plate. Depending on the director, three different viscosities can be defined. If the director is perpendicular to the flow velocity and parallel to the flow velocity gradient, the viscosity is called η_1; if the director is parallel to the flow, the viscosity is called η_2 and if the director is perpendicular to the flow as well as perpendicular to the flow velocity gradient it is called η_3. But

there are five viscosity parameters in total [21], as shown in Figure 1.10, and they are called the Miesowicz coefficients $(\eta_1, \eta_2, \eta_3, \eta_4, \gamma_1)$ [22]. It is more common to use

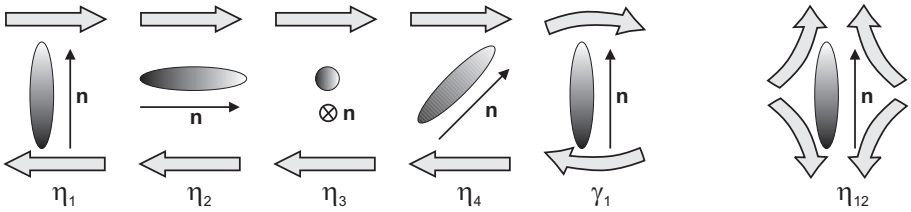


Figure 1.10: Miesowicz Viscosities: $\eta_1, \eta_2, \eta_3, \eta_4$, and γ_1. The Helfrich Coefficient $\eta_{12} = 4\eta_4 - 2(\eta_1 + \eta_2$ is often substituted for η_4.

the Helfrich Coefficient η_{12} [23, 24] instead of η_4. The cross-term η_{12} is defined as

$$\eta_{12} = 4\eta_4 - 2(\eta_1 + \eta_2). \tag{1.5}$$

Typical values are 150 mPas for η_1 and 50 mPas for η_2 and η_3 [15]. However, the dominant viscosity when switching liquid crystal devices is γ_1 and typical values are between 70 mPas and 200 mPas [18]. All viscosity coefficients decrease in magnitude with increasing temperature.

Another common notation to describe the viscosities are the Leslie coefficients $(\alpha_1, \alpha_2, \alpha_3, \alpha_4, \alpha_5)$ [25]. The Leslie viscosities arose from theoretical discussions compared to the Miesowicz viscosities, which are based on physical considerations.

1.2.6 Flexoelectricity

Flexoelectricity is the physical property which was investigated in this project. Therefore, the physical properties, history, and existing measurement will be discussed in detail in the next chapter before our new methods, experiments and results are presented in this thesis.

1.3 Liquid Crystal Devices

1.3.1 Construction

In general, a liquid crystal device is made from two glass plates coated with indium tin oxide (ITO), which is a transparent conductor. The gap ($2\mu m$-$10\mu m$) between the glass plates is filled with liquid crystal material, as shown in Figure 1.11. On

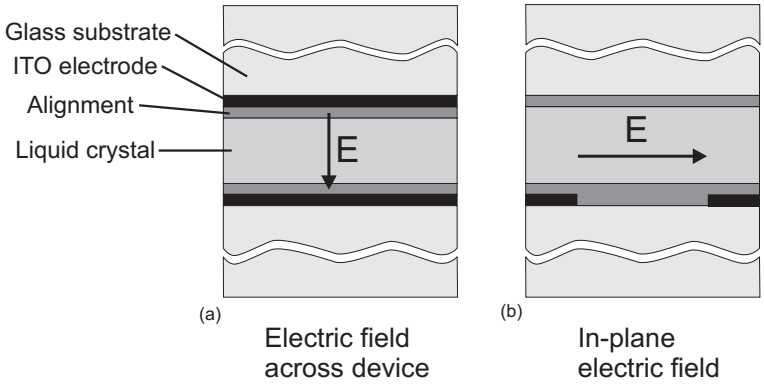


Figure 1.11: Construction of a liquid crystal device: a) Electric field across device, b) In-plane electric field

top of the ITO layer is an alignment material, which defines the orientation of the director. The glass plates are assembled with the ITO layers inside the cell. The plates are kept at a constant distance by spacers, which are in the range of 2μm to 10μm. The conductive ITO layer allows the application of a voltage to be applied between the plates, which creates an electric field in the liquid crystal layer. This electric field can reorientate the director and switch the device. It is possible to apply electric fields across the device (Fig. 1.11 a) and in-plane (Fig. 1.11 b), depending on the design of the ITO layer.

The devices for this research project were made manually in our clean room. The ITO coated glass was bought in large sized plates and cut by ourselves. After structuring the ITO layer, the alignment layer was applied. A mixture of UV-glue

and e.g. 10μm spacer was applied on one glass plate to glue the device together. A UV-light source hardened the glue and liquid crystal material was put on one open side of the device and sucked into the two plates by capillary forces. The quality of the device is highly dependent on the alignment and on a uniform distance between the glass plates.

1.3.2 Alignment

The alignment layer defines the orientation of the director at the surface in the absence of an applied field. The orientation of the director can be either planar (also called homogeneous), tilted or homeotropic (normal) to the surface, as shown in Figure 1.12. A planar alignment can be realised by evaporating SiOx at an angle

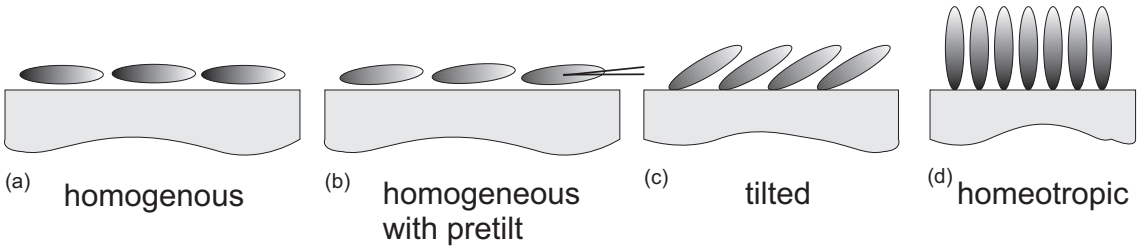


Figure 1.12: Alignment: a) planar alignment, b) planar with small pretilt, c) tilted, d) homeotropic

of 30° onto the glass plate (Fig. 1.12 a) [26]. In practice, it is easier to realise the planar alignment by spinning a polymer like PVA or polyimide (PI) on the glass plate and rubbing it in the preferred direction. This alignment is in fact not perfectly planar and has a pretilt (Fig. 1.12 b) between 0.1° and 2.0° [27, 28]. Evaporating SiOx at an angle of 5° [29, 26] onto the glass plates leads to a tilted alignment (Fig. 1.12 c). The pretilt is about 30° [30] and depends also on the liquid crystal material [27]. The homeotropic alignment is realised by depositing a surfactant such as Lecithin onto the glass plates or a special PI material (Fig. 1.12 d).

1.3.3 Cell Structures

Freedericksz constructed the first experimental liquid crystal device in the 1920s [31, 32]. But it wasn't until the 1970s that the first commercial device was made. This was possible due to the fact that the TN technology and the dynamic scattering mode were invented, the nematic phase existed in a bigger temperature range, the physical properties were improved, and ITO was available as a conductive layer. In honour of Freedericksz, a cell with planar alignments, where the rubbing direction is opposite on both glass plates as shown in Figure 1.13 a), is known as the *Freedericksz cell*.

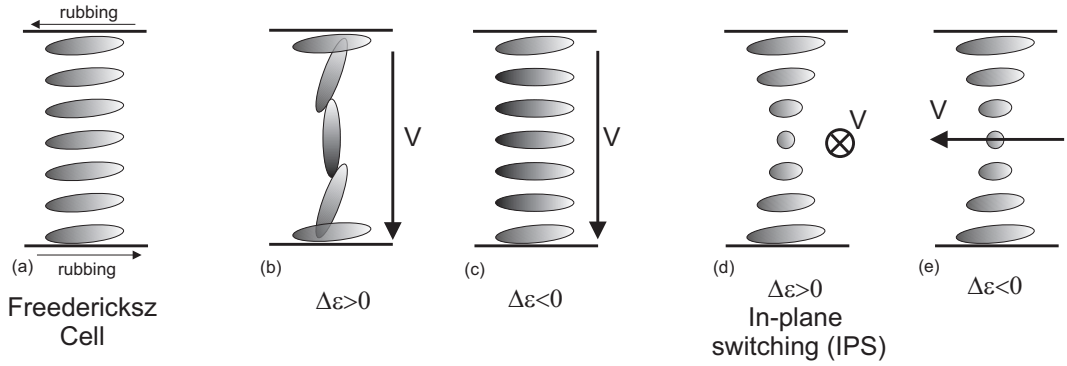


Figure 1.13: Freedericksz Cell

Applying an electric field across the device aligns the director with the field for positive $\Delta\epsilon$ (Fig. 1.13 b). Using a material with negative $\Delta\epsilon$ (Fig. 1.13 c) distorts the director only minimally.

Applying an in-plane field with positive $\Delta\epsilon$ (Fig. 1.13 d) twists the director in the same plane as the field is applied. This is known as in-plane switching (IPS) and is used in many commercial TV displays. Using a negative $\Delta\epsilon$ (Fig. 1.13 e) material can give the same result as the positive $\Delta\epsilon$ case if the electric field is applied parallel to the director. But this case is not used in commercial displays because $\Delta\epsilon$ for a negative material is much smaller than for a positive material and larger fields

would be necessary to create the same distortion as for a positive $\Delta\epsilon$ material.

The *Freedericksz cell* is one of many different cell structures. The most important structures are the *splayed cell*, *twisted nematic* (TN), *hybrid aligned nematic* (HAN) and *homeotropic cell*, as shown in Figure 1.14.

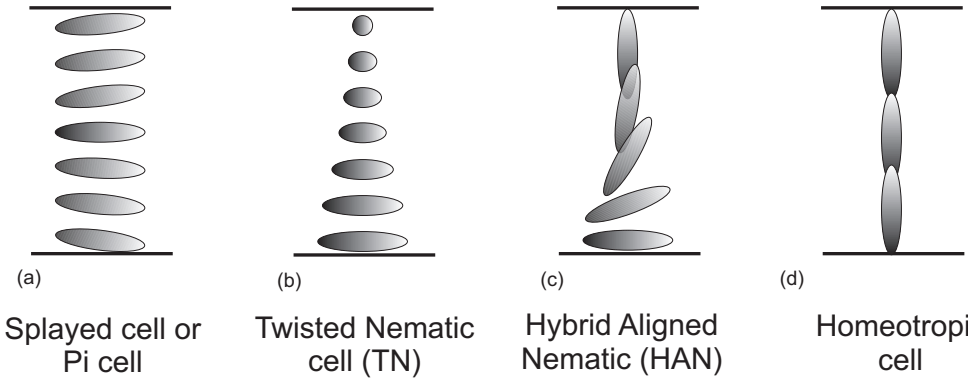


Figure 1.14: The most important cell structures beside the Freedericksz cell are (a) Splayed cell or Pi cell, (b) Twisted Nematic cell (TN), (c) Hybrid Aligned Nematic (HAN), and (d) Homeotropic cell

The rubbing direction of the *splayed cell* is equal on both glass plates which leads also to a parallel alignment (Fig. 1.14 a). This structure is also called a *Pi cell* and looks very similar to a *Freedericksz cell* but it shows different transitions when a voltage is applied and increased.

The *twisted nematic cell* (TN) has planar alignment but both surfaces are rotated by 90° to each other (Fig. 1.14 b). Such a device was first built by Schadt and Helfrich in 1971 [6] and it is still used in simple and cheap display for e.g. watches and calculators or for PC monitors and laptops, with the TFT technology. The direction of the rotation is not defined for an achiral material. But it is possible to add a small amount of chiral dopant material into the liquid crystal material, which supports and defines the direction of the rotation. This leads to two possible TN structures. The first one is a uniform TN structure, which looks like a combination of a TN structure with the tilt characterization of a *Freedericksz cell*. The second

possible structure is a splayed TN structure which looks like a combination of an TN structure with the tilt characterization of a *splayed cell*. Which structure will be formed depends on the rubbing direction and the rotational direction caused by the chiral dopant material. If the pitch P is smaller than the device thickness d ($P < d$), a rotation of 180, 270, etc. can be created [10, 11]. This structure is know as *Super Twisted Nematic* (STN) and is still used today in complex displays for e.g. calculators and ATM machines.

The *hybrid aligned nematic cell* (HAN) has a homeotropic alignment on one side and and a planar alignment on the other surface (Fig. 1.14 c). The director profile (which is defined as director orientation across the cell thickness) is, therefore, asymmetrical and has a strong splay and bend deformation. The HAN structure is mostly used for scientific measurements but rarely used in display applications.

Using homeotropic alignment on both glass substrates (Fig. 1.14 d) and applying an electric field across the device doesn't distort the director profile for a positive $\Delta\epsilon$ material. However, using a negative $\Delta\epsilon$ material and applying an electric field across the device distorts the director profile. A *homeotropic cell* with a negative $\Delta\epsilon$ material is also known as *vertical aligned nematic* (VAN) and used in many TV displays.

1.3.4 Polariser

A polariser is a film that changes a beam of electromagnetic waves (light) of undefined or mixed polarisation into a beam with well-defined polarisation. Liquid crystal devices work on the basis that an applied electric field changes the orientation of the molecules. This therefore changes the polarization of the light that travels through them due to the different refractive properties parallel and perpendicular to the molecule. The experiments, which were developed here, were conducted by

mounting a polariser and an analyser, which are rotated 90° to each other. Light travels first through the polariser before entering the liquid crystal device. The incoming light of the device has therefore the same polarisation as the polariser. With an applied electric (or magnetic) field, the orientation of the molecules can be controlled and therefore the polarisation of the outgoing light that leaves the device. If the polarisation of the outgoing light has not been changed compared to the incoming light, the analyser, which is mounted 90° to the polariser, cuts off all the light and a dark state is shown. If the polarisation of the outgoing light has been rotated partly or completely to 90°, the analyser allows light to travel through and a grey or bright state is shown. This is the basic working principal of a liquid crystal device, which is also called an electro-opto device. In commercial displays the polariser and analyser are glued to the glass plates. In the field of research this is not the case: the polariser and analyser are mounted on a separate stage to change the angle of the polarisation independent of the position of the liquid crystal cell.

This chapter is an introduction to the field of liquid crystals, with the exception of flexoelectricity, which was investigated in this project. The physical properties, history, and some existing measurement of flexoelectricity are discussed in details in the next chapter before our new methods, experiments and results are presented in this thesis.

Chapter 2

Flexoelectricity

2.1 Introduction

The flexoelectric effect was first described by Meyer [33] in 1969 and originally he called it the *piezoelectric effect*. In 1974, de Gennes [34] introduced the term *flexoelectricity*, which is still used today. Classically, the *flexoelectric effect* in nematic liquid crystals is associated with molecular shape anisotropy and molecular polarisation at the microscopic level [35, 36, 37]. It is often assumed that nematic liquid crystal molecules are simple, straight, rod shaped structures. However, due to the large number of angled bonds in each molecule, they have complex shape anisotropy, and even in a simple picture they should be considered as tapered (sometimes referred to as pear shaped (Fig. 2.1 a) and/or bent (sometimes referred to as banana shaped (Fig. 2.1 b). Assuming the molecules are tapered with only longitudinal dipoles, applying an electric field aligns the molecules along the electric field and due to the shape anisotropy, a splay distortion is created (Fig. 2.1 c). The resulting polarisation P_f is expressed by the flexoelectric coefficient e_1 multiplied by a splay vector $\vec{S} = \vec{n}\,(\nabla \cdot \vec{n})$. Similarly, bent shaped molecules with a transverse dipole

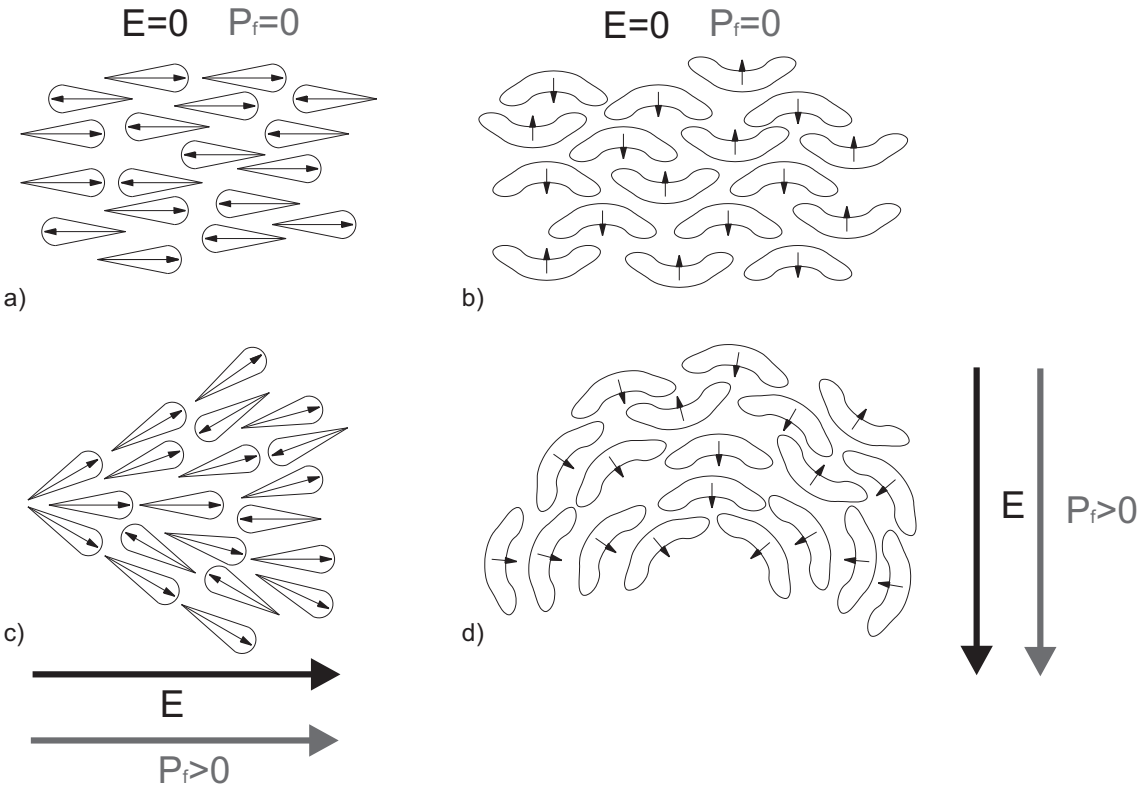


Figure 2.1: Splay and bend deformation

result in a bend distortion under field application (Fig. 2.1 d), the polarisation P_f from which is expressed by the flexoelectric coefficient e_3 multiplied by a bend vector $\vec{B} = (\nabla \times \vec{n}) \times \vec{n}$. But in reality, the distortion created by flexoelectricity is not only splay or bend, it is a combination of both: splay and bend. Therefore, the flexoelectric polarisation $\vec{P_f}$ [33, 38, 39] is the sum of both types of distortions and it is defined as

$$\begin{aligned} \vec{P_f} &= e_1 \vec{S} + e_3 \vec{B} \\ &= e_1 \vec{n} \, (\nabla \cdot \vec{n}) + e_3 \, (\nabla \times \vec{n}) \times \vec{n}. \end{aligned} \tag{2.1}$$

It is assumed that in nematic liquid crystal materials, the splay coefficient e_1 is much bigger than the bend coefficient e_3 due to the long rod shaped structure. Further, it is assumed that the dielectric anisotropy $\Delta\epsilon$ exhibits a linear or quadratic

correlation to the flexoelectric coefficients due to the understanding that the electric field rearranges the molecular dipoles and the shape anisotropy is creates an additional distortion. If the dielectric anisotropy $\Delta\epsilon$ is very small, the number of rearranged dipoles is also small and therefore the distortion created by the shape anisotropy. If the dielectric anisotropy $\Delta\epsilon$ is big, a larger number of dipoles will be rearranged, which create a bigger distortion. Therefore, it is assumed that the dielectric anisotropy $\Delta\epsilon$ exhibits a direct correlation to flexoelectricity.

To determine e_1 and e_3, it is more common and easier to measure the sum $(e_1 + e_3)$ and the difference $(e_1 - e_3)$ of the two coefficients rather than the single parameters e_1 and e_3 themselves. The sum $(e_1 + e_3)$ and the difference $(e_1 - e_3)$ also occur naturally in different experiments, and once they are measured, e_1 and e_3 can be calculated. One way to illustrate this is the bulk flexoelectric torque $\vec{T_f}$ [38, 39, 40], which is defined as

$$\vec{T_f} = (e_1 + e_3)\,\vec{n} \cdot \nabla\vec{E} + (e_1 - e_3)\left[(\nabla \cdot \vec{n})\,\vec{E} - \nabla\left(\vec{n} \cdot \vec{E}\right)\right]. \tag{2.2}$$

The torque equation shows that the sum $(e_1 + e_3)$ can be measured in structures where a gradient in the electric field is present [41, 42], which can be realised by applying an electric field across the cell. This is not the case for the difference $(e_1 - e_3)$, where either a uniform electric field with a gradient in the director profile is necessary or a gradient in the product between director profile and electric field. **The following information about the sign of the flexoelectric coefficients should be noted:** Working in the field of flexoelectricity, it is important to notice that there is great confusion over the sign issue. In 1969, Meyer [33] defined the signs of e_1 and e_3, as shown in Equation 2.1. However, in 1987, Patel and Meyer [43] defined, in their publication about the chiral flexoelectro-optic effect, which is described in more detail later, new splay e_s and bend e_b flexoelectric coefficients,

whereby $e_s = e_1$ and $e_b = -e_3$. This small change led to great confusion about the sign and makes it more difficult to compare results, because the measurement of the sum $(e_1 + e_3)$ in the 1969 Meyer notation is the difference $(e_s - e_b)$ in the 1987 Meyer notation and the other way around for the measurement of the difference. To clarify the situation, in our work we use the sign convention and notation originally defined in 1969 as e_1 and e_3 .

2.2 Experimental Ideas

In the last 40 years, research groups all over the world have developed and worked on different experiments and ideas to measure the sum $(e_1 + e_3)$ and difference $(e_1 - e_3)$ of the flexoelectric coefficients. In the beginning, flexoelectricity was very interesting from a scientific point of view but did not have any commercial application. Therefore, there was not much research until the 1990s, when suddenly the chiral flexoelectro-optic effect and bistable devices, which rely on flexoelectricity, showed promising commercial applications. This increased efforts to measure flexoelectricity but there were no standard experiments developed to determine e_1 and e_3. Depending on the experiment used for the same material, the magnitude of the sum $(e_1 + e_3)$ and difference $(e_1 - e_3)$ measured, can vary strongly, as shown for the material MBBA, which was the first liquid crystal material studied at room temperature. Table 2.1 shows some $(e_1 + e_3)$ results and Table 2.2 some $(e_1 - e_3)$ results.

There is a big problem in measuring and understanding flexoelectricity so that the commercial applications and the materials used in them can be optimised. The deficit in experimental methods and understanding of flexoelectricity was the driving force for this thesis. For example, in 1971, Helfrich [35, 50] tried to calculate e_1 and e_3 using the shape of the molecules. He described the shape with angles and lengths

Material	$(e_1 + e_3)$ [pC/m]	T [°C]	Ref
MBBA	-2.3	36	[44]
MBBA	-25	20	[45]
MBBA	-15±2	20	[46]
MBBA	-29±20%	20	[36, 47]
MBBA	-54±10	30	[48]

Table 2.1: Results for the sum $(e_1 + e_3)$ for the material MBBA

Material	$(e_1 - e_3)$ [pC/m]	T [°C]	Ref
MBBA	+3.3±0.7	20	[49]
MBBA	+14±1	30	[48]

Table 2.2: Results for the difference $(e_1 - e_3)$ for the material MBBA

but depending on how these dimensions are chosen, the values for e_1 and e_3 vary quite a lot. Also, Derzhans [51, 52] tried to calculate e_1 and e_3 by investigating the relationship between the dielectric terms and the flexoelectric properties. It is also thought that the flexoelectric effect might be partly or completely be influenced by ions [53]. Another idea was that flexoelectricity is caused by a quadrapolar effect [36, 37, 54, 55], whereby the molecule has a quadrapole charge distribution and when quadrapoles are forced to a splay structure, the charge distribution becomes uneven and a polarisation occurs. These few examples show how difficult this whole topic is and that it is not clear what causes flexoelectricity. Therefore, it is crucial to develop experiments to measure flexoelectricity and then investigate different sets of materials systematically to understand flexoelectricity. This is the goal given in this thesis - to look at existing methods and improve them or develop new ideas. Before presenting our experiments in the coming chapters, a brief overview of the existing methods of measuring the sum $(e_1 + e_3)$ and difference $(e_1 - e_3)$ are given in this chapter.

Before presenting the existing methods, some notes and thoughts about the diffi-

culty of measuring flexoelectricity are discussed. The determination of e_1 and e_3 is difficult, because flexoelectricity has only a small influence on the director distortion. Once the applied electric field orientates the molecular dipoles, it then takes time for the shape anisotropy to create the distortion. Therefore, in commercial displays and most applications where an ac voltage with a high frequency is applied, flexoelectricity can be neglected because it will lead to a small re-normalisation of the elastic constants [56, 57], although in practice this effect may be screened out by ions which are present in the material [58]. However, there are ways and ideas to measure flexoelectricity. The easiest way would be to apply a dc voltage, which gives the shape anisotropy enough time to create the distortion. However, the dc field has the big disadvantage that ions, which are present in the liquid crystal materials, drift to the electrode and weaken the electric field until it is cancelled out completely. The dc voltage would also induce additional ions at the electrodes, therefore, dc voltages should be avoided. On the other hand, ac voltages with a frequency of 1kHz or more do not create problems with ions but they also show a very small flexoelectric effect which can be neglected. One way to find a good compromise is to use an ac voltage whereby the frequency is so low that the flexoelectric effect can be observed but the problems with ions are minimised.

2.2.1 Measurement of sum $(e_1 + e_3)$

Prost and Pershan [36, 41, 59] were the first to measure the sum of the flexoelectric coefficients $(e_1 + e_3)$ (in MBBA), and their technique was a very elegant one. It involved observing the diffracted orders from homeotropically aligned interdigitated electrode cells, as shown in Figure 2.2. Applying an electric field with a high frequency determines the dielectric part and applying a low frequency field determines the flexoelectric part.

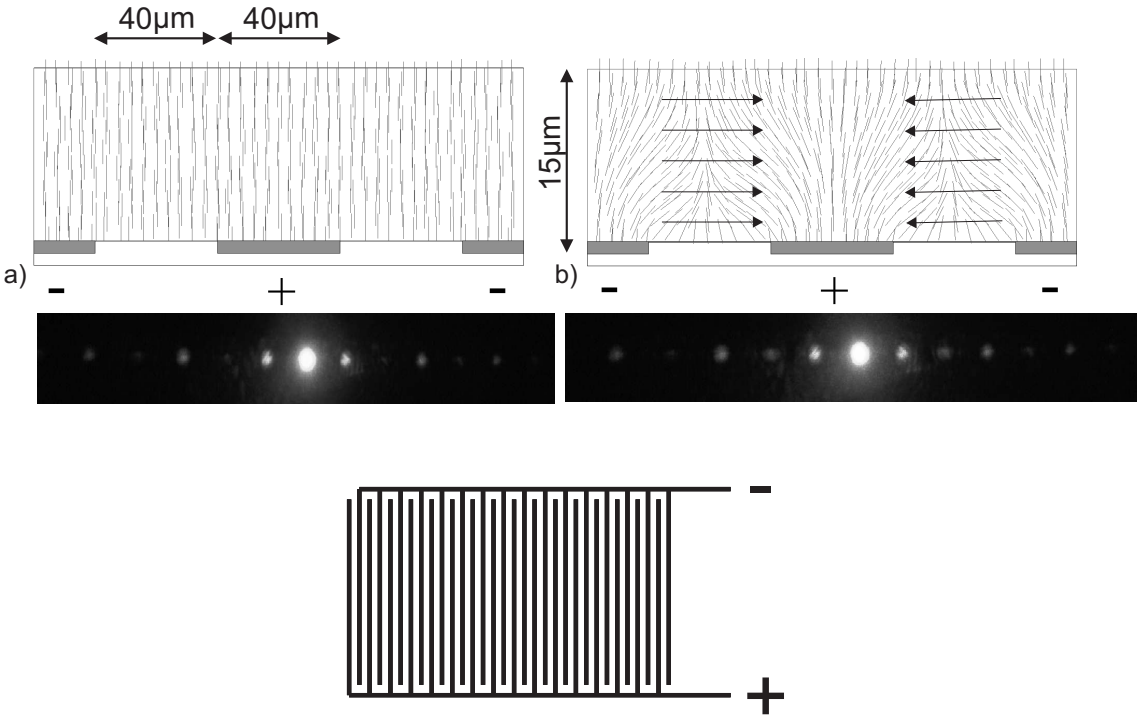


Figure 2.2: Interdigital electrode with in-plane electric field a) no electric field b) applied electric field

Since that time, measurements of (e_1+e_3) have been focused on the use of the hybrid-aligned nematic (HAN) cell. This is because of the large bulk flexoelectric coupling as a result of the non-uniform electric field present in the cell even at very low fields, i.e. a thresholdless effect. Madhusudana and Durand [45] used such a cell to measure $(e_1 + e_3)$ in MBBA, simply making use of the fact that the director distortion is different for positive and negative applied voltages, as shown in Figure 2.3. However, ionic screening can lead to problems with this method, and in fact when it is taken into account, leads to a completely different result for both the sign and magnitude of $(e_1 + e_3)$, as pointed out by Ponti et al. [56]. Warrier and Madhusudana [60] improved their approach by applying an alternating field to the device at a frequency above that at which there is significant ionic response. By using a lock-in amplifier to analyse the component of the time dependent optical response that is at the

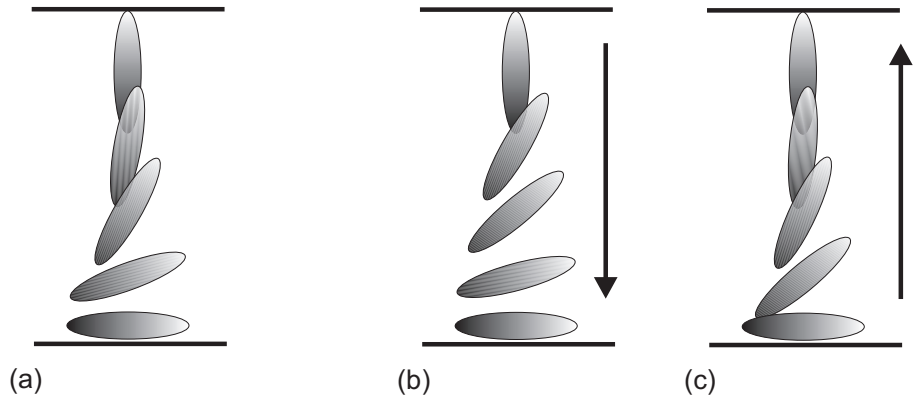


Figure 2.3: a) HAN structure with electric field across the cell for b) positive voltage and c) negative voltage

same frequency as the applied signal (as opposed to twice that frequency, which would indicate a dielectric effect), the flexoelectric response can be measured and interpreted. A clever approach was taken by Takahashi et al. [48, 61], who used an AC field followed by a short measurement period of DC field of the same amplitude, in order to minimise the amount of time for which the DC field was applied, hence minimising the ionic drift. However, DC measurements on HAN cells continue to be carried out, including the use of a sophisticated guided wave approach to analyse the director structures present [62, 63]. This led to further debate over the effect of ionic screening on flexoelectric measurements [64, 65]. The detailed information derived from these experiments, however, revealed the important result that in order to correctly model the HAN cell, an offset voltage must be included, implying that surface polarisation must exist due to the asymmetric anchoring conditions. Even a measurement method that uses an AC applied voltage (such as that employed by Warrier and Madhusudana) would be influenced by this net offset voltage.

2.2.2 Measurement of difference $(e_1 - e_3)$

Measuring the difference of the coefficients $(e_1 - e_3)$ is in principle simpler than measuring the sum $(e_1 + e_3)$, because there is no requirement for a non-uniform electric field. However, as described above, in order to couple to $(e_1 - e_3)$ the

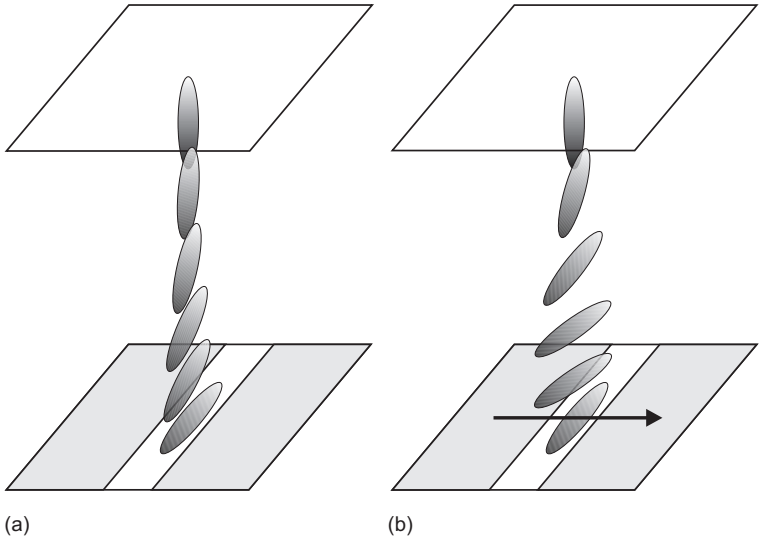


Figure 2.4: HAN cell with in-plane electric field

director cannot be coplanar with the electric field. Dozov et al. [49, 48, 66] proposed a method which again used DC measurements in HAN cells, but this time with an in-plane electric field perpendicular to the initial molecular plane, as shown in Figure 2.4. This technique has the advantage of being applicable to achiral materials, although the issues mentioned above relating to surface polarisation may impact on the measurements.

The alternative measurement method is to use a uniform lying helix (ULH) structure, as shown in Figure 2.5, which was first described by Patel and Meyer [43] in 1987. Creating the ULH structure parallel to the glass plates and applying a DC voltage between the substrates causes the optical axis to rotate in-plane by an angle ϕ and the direction of the rotation depends on the sign of the DC voltage. This effect is known as the flexoelectro-optic effect [43, 67, 68] and is linear for small electric

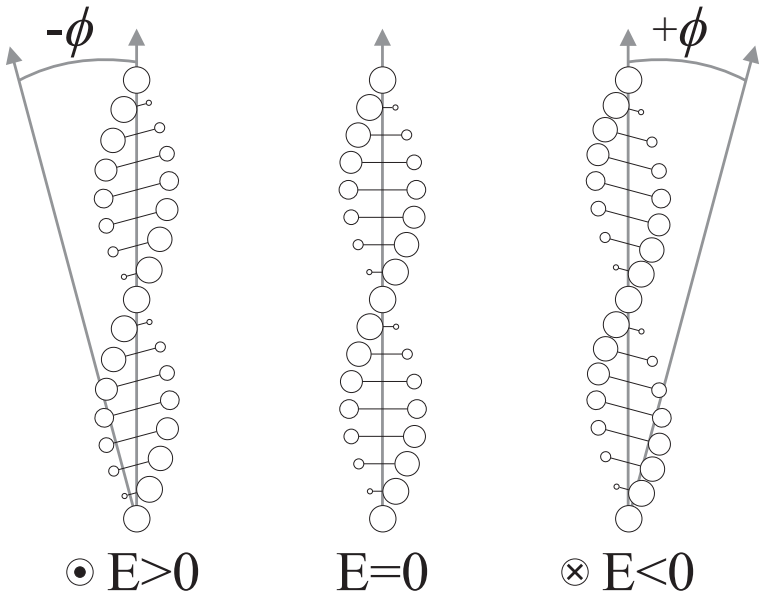


Figure 2.5: ULH structure with electric field into the plane and rotated optical axis by angle ϕ depending on the direction of the applied field

fields. The response time is very fast and in the range of about 100 microseconds [67]. By using a liquid crystal material with a low dielectric anisotropy, it is possible to get a rotation angle ϕ up to 22.5° [69, 70]. The flexoelectro-optic effect has the advantage of being a very simple technique with no data fitting required to extract $(e_1 - e_3)$ from the experimental measurements. However, the uniform lying-helix (ULH) texture required to make the measurement is both difficult to achieve and very unstable, making the method somewhat unreliable. Moreover, it is strictly only applicable to highly chiral materials with pitches smaller than visible wavelengths. Also, as it requires the application of a quasi-DC voltage (usually a slow square wave), it can be susceptible to confusion due to ionic screening effects. This method has been employed to characterise bimesogenic materials which exhibit extremely high flexoelectric coefficients [71, 72, 73, 74, 75, 76]

2.3 Applications

The potential for display devices based on flexoelectricity has been the cause of much of the driving mechanism for the recent increase in research into flexoelectricity. As noted above, flexoelectric polarisation is often screened out by ionic polarisation, and so it can only really be of use when the driving pulses are of extremely short duration. Therefore, the potential uses fall into two categories: bistable displays, where a short driving pulse is applied in which the flexoelectric polarisation brings about some kind of surface reorientation, and very fast-response displays, where the driving voltage is rapidly changed with time.

2.3.1 Bistability (ZBD)

There has been active interest in bistable switching in liquid crystal systems for many years and there have been a number of ideas relating to bistability in nematic systems [77, 78, 79]. The most promising system has been the zenithally bistable device (ZBD) [80, 81, 82, 83, 84, 85, 86], subsequently exploited by ZBD Displays Ltd in the UK [87]. This device uses a surface relief diffraction grating to stabilise two states, as shown in Figure 2.6, which uses flexoelectric switching with positive and negative voltage pulses. Related to this is the post-aligned bistable nematic (PABN) developed by Hewlett-Packard [88]. This uses a three-dimensional surface structure to stabilise two states, which again uses flexoelectric switching with positive and negative voltage pulses. The aim is to develop a high information density reflective paper-like electronic display.

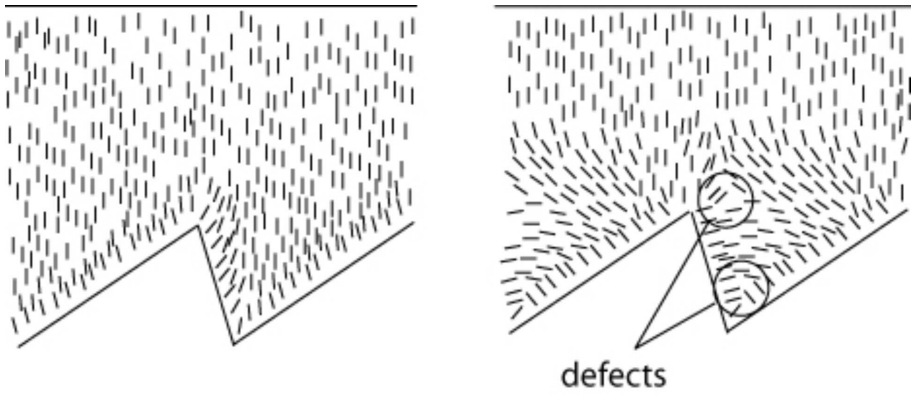


Figure 2.6: Diffraction grating with electric field across the cell

2.3.2 Chiral Flexoelectro-optic Effect

As described in Section 2.2.2, the chiral flexoelectro-optic effect is used as a measurement technique for the difference of the flexoelectric coefficients ($e_1 - e_3$), but it also has huge potential as a display technology. Not only does the effect exhibit rapid (sub-millisecond) in-plane switching without the use of in-plane electrodes, but it can achieve full electro-optic modulation and has high temperature independence. After the initial discovery and work of Patel, Meyer and Lee [43, 67, 68], the idea was taken up and developed by the Chalmers Group [89]. They showed that the amplitude of the high-speed modulation could be optimised if the coupling to the dielectric anisotropy is minimised [69]. This allowed a field induced tilt of up to 22.5° to be obtained, maximising the electro-optic contrast. More careful theoretical analysis was also undertaken to link key parameters with the behaviour and to predict how the optical properties of the distorted structure change [70]. As mentioned above, the major drawback of using the chiral flexoelectro-optic effect in the ULH geometry is the lack of stability of this structure in transforming to the Grandjean or planar texture, in which the helix is perpendicular to the substrates. One way of overcoming this problem is to polymer stabilise the ULH texture once formed [90, 91]. However, when the polymer is present in sufficient concentrations

to stabilise the ULH texture, it reduces significantly the achievable switching angle at a given electric field. One possible solution is to use periodic surface alignment - which was primarily pursued by Komitov - either via surface gratings similar to those used in the ZBD [92], or by using a polymer network that is present only at the surface [93].

In the past few years, there has also been interest in using the chiral flexoelectro-optic effect in the Grandjean texture by applying an in-plane electric field, analogous to the method of Ewings et al. [94] for measuring $(e_1 - e_3)$. The primary reason for doing this is that by coupling to the flexoelectric, rather than the dielectric effect, there is the potential for an endlessly rotatable polarisation controller [95, 96, 97, 98], which could be used in optical communications.

As presented, this chapter is an introduction to the topic of flexoelectricity and its history, physical properties, some existing measurement and applications. As shown, it is easier to measure the sum $(e_1 + e_3)$ and difference $(e_1 - e_3)$ of the flexoelectric coefficients. However, most experiments are indirect measurements of the sum $(e_1 + e_3)$ and difference $(e_1 - e_3)$, and a theoretical model is required to fit the data and extract the results for either the sum $(e_1 + e_3)$ or the difference $(e_1 - e_3)$. Therefore, the next chapter presents the theory of modelling liquid crystal structures, which is then later used in our own experiments to fit the data and extract the results.

Chapter 3

Theory

3.1 Introduction

In general, it is better to measure the flexoelectric coefficients e_1 and e_3 indirectly. The experimental data has to be fitted with a theoretical model to extract the parameters. This can be done using the Eriksen-Leslie-Parodi Theory [25, 21, 99], which specifies the liquid crystals in terms of macroscopic averages, which can be assumed to be continuous. Therefore it is possible to define a gradient of these averages. One such macroscopic average is the director $\vec{n}$ (Fig. 1.2, Chapter 1.1.2), which is the unit vector in the average direction of the liquid crystal molecules within a certain volume. The first numerical calculation was done by van Doorn [100] and Berreman [101] in 1975. There has been relatively little simulation work on flexoelectricity from a microscopic point of view. In the 1970s, a statistical-mechanical approach was used by Derzhanski and Petrov [51, 52] to examine the relationship between the dielectric and flexoelectric properties of nematics. A similar approach has been used more recently by Zakharov and Dong, showing some information on the temperature dependence of the coefficients [102]. Early molecular dynamical mod-

elling by Stelzer et al. [103] investigated flexoelectricity in pear-shaped molecules, showing a non-zero splay coefficient e_1. Further work [104, 105] has extended the investigation of pear shaped molecules, and has developed the approach. Barmes and Cleaver [106] have shown that it is now possible to model enough pear shaped molecules to mimic the effect of a simple real device: their work used the example of the bistable HAN structure introduced originally by Davidson and Mottram [107]. Recently atomistic level calculations have been undertaken to calculate splay and bend coefficients, producing very interesting results [108]. In addition Ferrarini has undertaken elegant mean field modelling to relate molecular properties to flexoelectric coefficients [37]. Molecular simulations have also been undertaken by Allen and Masters [109], relating this to a statistical mechanical approach.

Our one-dimensional models are based on the coordinate system shown in Figure 3.1. They calculate numerically the director $\vec{n}$ in a defined volume in a layer perpendicular to the z direction. A typical number of layers is in the order of 100 and can go up to 1000. A higher number of layers gives a more accurate results but increases the computation time dramatically. Our C program calculates 100 layers, which is accurate enough to fit the data. The one-dimensional model contains the elastic, electrostatic, and flexoelectric energy. Further it is possible to calculate the surface energy and flow can also be taken into account. The following theory in this

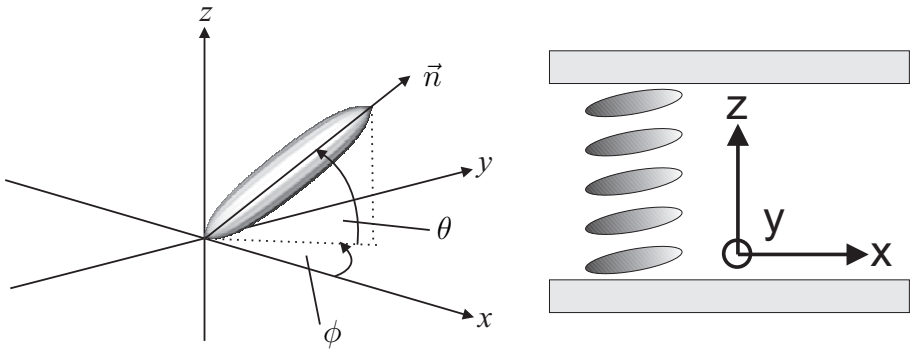


Figure 3.1: Definition of axes and angles

chapter shows the general expressions for a three-dimensional model before being used and modified for a one-dimensional model. To illustrate the calculations of a one-dimensional model, a simple example is used at the end of this chapter.

3.2 Definition

3.2.1 Coordinate System

It is possible to define a cartesian coordinate system as shown in Figure 3.1, with the director $\vec{n}$ along the long axis of the average molecules, defined by

$$\vec{n} = \begin{pmatrix} n_x \\ n_y \\ n_z \end{pmatrix} \tag{3.1}$$

where the length of the director has always to fulfil the criterion of a unit vector, which is

$$n_x^2 + n_y^2 + n_z^2 = 1. \tag{3.2}$$

Alternatively it is possible to define the director $\vec{n}$ in a polar coordinate system with a tilt angle θ and a twist angle ϕ, as shown in Figure 3.1. This coordinate system is limited in certain situations, since ϕ isn't well defined when $\theta = 90°$.
The relation between the cartesian and polar coordinate system is given by

$$\vec{n} = \begin{pmatrix} \cos\theta\cos\phi \\ \cos\theta\sin\phi \\ \sin\phi \end{pmatrix}. \tag{3.3}$$

3.3 Molecular field

The rate of change of free energy L of the system must be equal to the rate of change of dissipated energy $\mathcal{D}$ as given by

$$\frac{\mathrm{d}L}{\mathrm{d}t} = \mathcal{D}. \tag{3.4}$$

Using the chain rule with respect to n_i, gives

$$\frac{\mathrm{d}L}{\mathrm{d}t} = \frac{\mathrm{d}L}{\mathrm{d}n_i}\frac{\mathrm{d}n_i}{\mathrm{d}t} = \mathcal{D} \tag{3.5}$$

where i represents the coordinate system axis x, y, and z.
The value $\frac{\mathrm{d}L}{\mathrm{d}n_i}$ is given by Euler-Lagrange equation with

$$\frac{\mathrm{d}L}{\mathrm{d}n_i} = \frac{\partial}{\partial x}\left(\frac{\partial L}{\partial\left(\frac{\partial n_i}{\partial x}\right)}\right) + \frac{\partial}{\partial y}\left(\frac{\partial L}{\partial\left(\frac{\partial n_i}{\partial y}\right)}\right) + \frac{\partial}{\partial z}\left(\frac{\partial L}{\partial\left(\frac{\partial n_i}{\partial z}\right)}\right) - \frac{\partial L}{\partial n_i}. \tag{3.6}$$

Substituting Equation 3.5 with 3.6, gives

$$\begin{aligned}\frac{\mathrm{d}L}{\mathrm{d}t} = \Bigg\{&\frac{\partial}{\partial x}\left(\frac{\partial L}{\partial\left(\frac{\partial n_i}{\partial x}\right)}\right) + \frac{\partial}{\partial y}\left(\frac{\partial L}{\partial\left(\frac{\partial n_i}{\partial y}\right)}\right)\\ &+\frac{\partial}{\partial z}\left(\frac{\partial L}{\partial\left(\frac{\partial n_i}{\partial z}\right)}\right) - \frac{\partial L}{\partial n_i}\Bigg\}\frac{\mathrm{d}n_i}{\mathrm{d}t} = \mathcal{D}.\end{aligned} \tag{3.7}$$

Differentiating Equation 3.7 with respect to $\frac{\mathrm{d}n_i}{\mathrm{d}t}$, using dots to indicate differentials with respect to time t, gives

$$\frac{\partial}{\partial x}\left(\frac{\partial L}{\partial\left(\frac{\partial n_i}{\partial x}\right)}\right) + \frac{\partial}{\partial y}\left(\frac{\partial L}{\partial\left(\frac{\partial n_i}{\partial y}\right)}\right) + \frac{\partial}{\partial z}\left(\frac{\partial L}{\partial\left(\frac{\partial n_i}{\partial z}\right)}\right) - \frac{\partial L}{\partial n_i} = \frac{\partial \mathcal{D}}{\partial \dot{n}_i} \tag{3.8}$$

or expressed in x, y, and z

$$\begin{aligned}
\frac{\partial \mathcal{D}}{\partial \dot{n_x}} &= \frac{\partial}{\partial x}\left(\frac{\partial L}{\partial\left(\frac{\partial n_x}{\partial x}\right)}\right) + \frac{\partial}{\partial y}\left(\frac{\partial L}{\partial\left(\frac{\partial n_x}{\partial y}\right)}\right) + \frac{\partial}{\partial z}\left(\frac{\partial L}{\partial\left(\frac{\partial n_x}{\partial z}\right)}\right) - \frac{\partial L}{\partial n_x}, \\
\frac{\partial \mathcal{D}}{\partial \dot{n_y}} &= \frac{\partial}{\partial x}\left(\frac{\partial L}{\partial\left(\frac{\partial n_y}{\partial x}\right)}\right) + \frac{\partial}{\partial y}\left(\frac{\partial L}{\partial\left(\frac{\partial n_y}{\partial y}\right)}\right) + \frac{\partial}{\partial z}\left(\frac{\partial L}{\partial\left(\frac{\partial n_y}{\partial z}\right)}\right) - \frac{\partial L}{\partial n_y}, \\
\frac{\partial \mathcal{D}}{\partial \dot{n_z}} &= \frac{\partial}{\partial x}\left(\frac{\partial L}{\partial\left(\frac{\partial n_z}{\partial x}\right)}\right) + \frac{\partial}{\partial y}\left(\frac{\partial L}{\partial\left(\frac{\partial n_z}{\partial y}\right)}\right) + \frac{\partial}{\partial z}\left(\frac{\partial L}{\partial\left(\frac{\partial n_z}{\partial z}\right)}\right) - \frac{\partial L}{\partial n_z}.
\end{aligned} \tag{3.9}$$

The expression $\frac{\partial \mathcal{D}}{\partial \dot{n_i}}$ on the left side is also known as the dissipation function, which defines the time dependence of the system, and the expression on the right side is the Euler-Lagrange equation to minimise the free energy L of the bulk system in space of the three coordinate axis x, y, and z. The final solution of the Euler-Lagrange equation is known as the molecular field $\vec{h}$, with

$$\begin{aligned}
h_x &= \frac{\partial}{\partial x}\left(\frac{\partial L}{\partial\left(\frac{\partial n_x}{\partial x}\right)}\right) + \frac{\partial}{\partial y}\left(\frac{\partial L}{\partial\left(\frac{\partial n_x}{\partial y}\right)}\right) + \frac{\partial}{\partial z}\left(\frac{\partial L}{\partial\left(\frac{\partial n_x}{\partial z}\right)}\right) - \frac{\partial L}{\partial n_x}, \\
h_y &= \frac{\partial}{\partial x}\left(\frac{\partial L}{\partial\left(\frac{\partial n_y}{\partial x}\right)}\right) + \frac{\partial}{\partial y}\left(\frac{\partial L}{\partial\left(\frac{\partial n_y}{\partial y}\right)}\right) + \frac{\partial}{\partial z}\left(\frac{\partial L}{\partial\left(\frac{\partial n_y}{\partial z}\right)}\right) - \frac{\partial L}{\partial n_y}, \\
h_z &= \frac{\partial}{\partial x}\left(\frac{\partial L}{\partial\left(\frac{\partial n_z}{\partial x}\right)}\right) + \frac{\partial}{\partial y}\left(\frac{\partial L}{\partial\left(\frac{\partial n_z}{\partial y}\right)}\right) + \frac{\partial}{\partial z}\left(\frac{\partial L}{\partial\left(\frac{\partial n_z}{\partial z}\right)}\right) - \frac{\partial L}{\partial n_z}.
\end{aligned} \tag{3.10}$$

The molecular field $\vec{h}$ can be seen as a force acting on the director to create a torque $\vec{M}$. The cross product between the director $\vec{n}$ and the molecular field $\vec{h}$ is defined as torque $\vec{M} = \vec{n} \times \vec{h}$.

Substituting Equation 3.9 with 3.10, gives

$$\begin{aligned}
\frac{\partial \mathcal{D}}{\partial \dot{n_x}} &= h_x, \\
\frac{\partial \mathcal{D}}{\partial \dot{n_y}} &= h_y,
\end{aligned}$$

$$\frac{\partial \mathcal{D}}{\partial \dot{n_z}} = h_z, \tag{3.11}$$

which simplifies the relationship between the dissipation function and the molecular field.

3.4 Dissipation function

The general form of the dissipated energy $\mathcal{D}$ for an incompressible anisotropic fluid [110] is given by

$$\begin{aligned}\mathcal{D} = &\left(\frac{\alpha_4}{4}\right)(v_{j,i}v_{j,i} + v_{j,i}v_{i,j}) + \left(\frac{\alpha_5 - \alpha_2}{4}\right)(n_i v_{k,i} - \dot{n_k})(n_j v_{k,j} - \dot{n_k}) \\ &+ \left(\frac{\alpha_2 + 2\alpha_3 + \alpha_5}{4}\right)(n_i v_{i,k} - \dot{n_k})(n_j v_{j,k} - \dot{n_k}) \\ &+ \left(\frac{\alpha_2 + \alpha_5}{4}\right)(n_i v_{k,i} - \dot{n_k})(n_j v_{j,k} - \dot{n_k}) \\ &+ \left(\frac{\alpha_1}{2}\right) n_i n_j n_k n_p v_{j,i} v_{p,k}\end{aligned} \tag{3.12}$$

where $\alpha_1, \alpha_2, \alpha_3, \alpha_4$, and α_5 are the Leslie viscosities coefficients, v is the fluid velocity. The index of i, j, k, p is 1, 2, 3. Further, the index i, j, k, p in Equation 3.12 describe a scalar product, a vector product, a scalar triple product, a gradient of a scalar field, a divergence of a vector and a curl of a vector [111]. Assuming that the changes in x and y direction are negligible, the only non-zero flow terms are $v_{x,z} = v_x^{'}$ and $v_{y,z} = v_y^{'}$ which simplifies Equation 3.12 to

$$\begin{aligned}\mathcal{D} = &\frac{v_x^{'2}}{4}\left[2\alpha_1 n_x^2 n_z^2 + \alpha_2\left(n_x^2 - n_z^2\right) + 2\alpha_3 n_x^2 + \alpha_4 + \alpha_5\left(n_x^2 + n_z^2\right)\right] \\ &+ \frac{v_y^{'2}}{4}\left[2\alpha_1 n_y^2 n_z^2 + \alpha_2\left(n_y^2 - n_z^2\right) + 2\alpha_3 n_y^2 + \alpha_4 + \alpha_5\left(n_y^2 + n_z^2\right)\right] \\ &+ \frac{v_x^{'} v_y^{'}}{2}\left[2\alpha_1 n_z^2 + \alpha_2 + 2\alpha_3 + \alpha_5\right] n_x n_y \\ &+ v_x^{'}\dot{n_x}\alpha_2 n_z + v_x^{'}\dot{n_z}\alpha_3 n_x + v_y^{'}\dot{n_y}\alpha_2 n_z + v_y^{'}\dot{n_z}\alpha_3 n_y\end{aligned}$$

$$\left(\dot{n_x^2} + \dot{n_y^2} + \dot{n_z^2}\right)\left(\frac{\alpha_3 - \alpha_2}{2}\right). \tag{3.13}$$

Differentiating Equation 3.13 with respect to $\dot{n_x}, \dot{n_y}$ and $\dot{n_z}$ gives the dissipation function with

$$\begin{aligned}
\frac{\partial \mathcal{D}}{\partial \dot{n_x}} &= (\alpha_3 - \alpha_2)\,\dot{n_x} + \dot{v_x'}\alpha_2 n_z, \\
\frac{\partial \mathcal{D}}{\partial \dot{n_y}} &= (\alpha_3 - \alpha_2)\,\dot{n_y} + \dot{v_y'}\alpha_2 n_z, \\
\frac{\partial \mathcal{D}}{\partial \dot{n_z}} &= (\alpha_3 - \alpha_2)\,\dot{n_z} + \dot{v_x'}\alpha_3 n_x + \dot{v_y'}\alpha_3 n_y.
\end{aligned} \tag{3.14}$$

3.4.1 Dissipation function with flow

In the case of flow, the fluid velocities gradient can be calculated, using definition of [110], which is

$$\begin{aligned}
\dot{v_x'} &= \frac{C_6\sigma_{zy} - C_7\sigma_{zx}}{E} + \psi_1\dot{n_x} + \psi_2\dot{n_y} + \psi_3\dot{n_z}, \\
\dot{v_y'} &= \frac{C_6\sigma_{zx} - C_5\sigma_{zy}}{E} + \psi_2\dot{n_x} + \psi_4\dot{n_y} + \psi_5\dot{n_z},
\end{aligned}$$

where σ_{zx} and σ_{zy} are the only non-zero terms of the stress tensor [110], defined by

$$\begin{aligned}
\sigma_{zx} &= \frac{\Psi_3 \int_0^d \left(\psi_1\dot{n_x} + \psi_2\dot{n_y} + \psi_3\dot{n_z}\right)\mathrm{d}z + \Psi_1 \int_0^d \left(\psi_2\dot{n_x} + \psi_4\dot{n_y} + \psi_5\dot{n_z}\right)\mathrm{d}z}{\Psi_2\Psi_3 - \Psi_1^2}, \\
\sigma_{zx} &= \frac{\Psi_1 \int_0^d \left(\psi_1\dot{n_x} + \psi_2\dot{n_y} + \psi_3\dot{n_z}\right)\mathrm{d}z + \Psi_2 \int_0^d \left(\psi_2\dot{n_x} + \psi_4\dot{n_y} + \psi_5\dot{n_z}\right)\mathrm{d}z}{\Psi_2\Psi_3 - \Psi_1^2},
\end{aligned}$$

with intermediate variables are being defined, to simplify the calculation, as

$$C_1 = \alpha_3 - \alpha_2,$$

$$C_2 = \alpha_2 n_z,$$

$$C_3 = \alpha_3 n_x,$$

$$C_4 = \alpha_3 n_y,$$

$$C_5 = \frac{1}{2}\left[2\alpha_1 n_x^2 n_z^2 + \alpha_2\left(n_x^2 - n_z^2\right) + 2\alpha_3 n_x^2 + \alpha_4 + \alpha_5\left(n_x^2 + n_z^2\right)\right],$$

$$C_6 = \frac{1}{2}\left[2\alpha_1 n_z^2 + \alpha_2 + 2\alpha_3 + \alpha_5\right] n_x n_y,$$

$$C_7 = \frac{1}{2}\left[2\alpha_1 n_y^2 n_z^2 + \alpha_2\left(n_y^2 - n_z^2\right) + 2\alpha_3 n_y^2 + \alpha_4 + \alpha_5\left(n_y^2 + n_z^2\right)\right],$$

$$E = C_6^2 - C_5 C_7,$$

$$\psi_1 = \frac{C_2 C_7}{E},$$

$$\psi_2 = -\frac{C_2 C_6}{E},$$

$$\psi_3 = \frac{C_3 C_7 - C_4 C_6}{E},$$

$$\psi_4 = \frac{C_2 C_5}{E},$$

$$\psi_5 = \frac{C_4 C_5 - C_3 C_6}{E},$$

$$\Psi_1 = \int_0^d \frac{C_6}{E}\mathrm{d}z,$$

$$\Psi_2 = \int_0^d \frac{C_7}{E}\mathrm{d}z,$$

$$\Psi_3 = \int_0^d \frac{C_5}{E}\mathrm{d}z.$$

3.4.2 Dissipation function without flow

In the case of no flow, the dissipation function (Eq. 3.14) simplifies to

$$\frac{\partial \mathcal{D}}{\partial \dot{n_x}} = (\alpha_3 - \alpha_2)\,\dot{n_x},$$

$$\frac{\partial \mathcal{D}}{\partial \dot{n}_y} = (\alpha_3 - \alpha_2)\, \dot{n}_y,$$
$$\frac{\partial \mathcal{D}}{\partial \dot{n}_z} = (\alpha_3 - \alpha_2)\, \dot{n}_z. \tag{3.15}$$

Substituting $(\alpha_3 - \alpha_2)$ with the rotational viscosity γ_1 leads to

$$\frac{\partial \mathcal{D}}{\partial \dot{n}_x} = \gamma_1 \dot{n}_x,$$
$$\frac{\partial \mathcal{D}}{\partial \dot{n}_y} = \gamma_1 \dot{n}_y,$$
$$\frac{\partial \mathcal{D}}{\partial \dot{n}_z} = \gamma_1 \dot{n}_z. \tag{3.16}$$

Equation 3.16 describes the dynamic behaviour of the director in the bulk and in the absence of flow. Static behaviour is reached when the dissipation function goes to zero, as shown in

$$\frac{\partial \mathcal{D}}{\partial \dot{n}_x} = 0,$$
$$\frac{\partial \mathcal{D}}{\partial \dot{n}_y} = 0,$$
$$\frac{\partial \mathcal{D}}{\partial \dot{n}_z} = 0. \tag{3.17}$$

However, to calculate the static case with a computer program, it is more common to use the dynamic equations because with the dynamic case it is possible to calculate the next time step of the director. This will be done until the director reaches an equilibrium and the change in director goes to zero and therefore the static case is reached.

3.5 Bulk Energy

The bulk energy is the sum of the different energy terms like, elastic, electrostatic and flexoelectric energy.

3.5.1 Elastic Energy

The Frank Elastic energy density w_d [16] is given by

$$\begin{aligned} w_d = & \frac{1}{2}K_{11}\left(\nabla\cdot\vec{n}\right)^2 + \frac{1}{2}K_{22}\left(\vec{n}\cdot\left(\nabla\times\vec{n}\right) - q\right)^2 \\ & + \frac{1}{2}K_{33}\left(\vec{n}\times\left(\nabla\times\vec{n}\right)\right)^2, \end{aligned} \tag{3.18}$$

where K_{11}, K_{22} and K_{33} are the elastic constants for splay, twist, and bend, respectively. The parameter q represents the pitch P of the liquid crystal and the relationship between q and P is $q = \frac{2\pi}{P}$ with P is positive for anti-clockwise rotation in the positive z direction of the system.

The unit of the elastic energy density w_d is $\frac{J}{m^3} = \frac{Nm}{m^3} = \frac{N}{m^2}$, of the elastic constant K_{ii} is N, of *splay* $\vec{S}$ is $\frac{1}{m}$, of *twist* $\vec{T}$ is $\frac{1}{m}$, of *bend* $\vec{B}$ is $\frac{1}{m}$, of $\vec{S}^2$ is $\frac{1}{m^2}$, of $\vec{T}^2$ is $\frac{1}{m^2}$, of $\vec{B}^2$ is $\frac{1}{m^2}$, and these leads to an energy density of $\frac{N}{m^2}$, when K_{ii} is multiplied with e.g. $\vec{S}^2$.

3.5.2 Electrostatic Energy

In general, the electrostatic energy density w_e (or dielectric energy density) is given by

$$w_e = -\frac{1}{2}\vec{D}\cdot\vec{E}, \tag{3.19}$$

where $\vec{E}$ is the electric field and $\vec{D}$ is the displacement field (or electric flux density), where $\vec{D}$ is defined as

$$\vec{D} = \epsilon_0 \overleftrightarrow{\epsilon} \vec{E}, \tag{3.20}$$

and where ϵ_0 is the permittivity of free space and $\overleftrightarrow{\epsilon}$ is the permittivity tensor. This leads to an dielectric energy expression w_e of

$$w_e = -\frac{1}{2}\epsilon_0 \overleftrightarrow{\epsilon} \vec{E}\vec{E}. \tag{3.21}$$

The unit of the electric energy density w_e is $\frac{J}{m^3} = \frac{Nm}{m^3} = \frac{N}{m^2}$, of the electric field $\vec{E}$ is $\frac{V}{m} = \frac{N}{C}$ and of the displacement field $\vec{D}$ is $\frac{C}{m^2}$. ϵ_0 is the permittivity of free space and it is defined as $\epsilon_0 = 8.85 \times 10^{-12}\frac{F}{m} = 8.85^{-12}\frac{C^2}{Nm^2}$.

Permittivity

The permittivity tensor of the molecule $\overleftrightarrow{\epsilon_{mol}}$ is defined as

$$\overleftrightarrow{\epsilon_{mol}} = \begin{pmatrix} \epsilon_{\parallel} & 0 & 0 \\ 0 & \epsilon_{\perp} & 0 \\ 0 & 0 & \epsilon_{\perp} \end{pmatrix},$$

where $\epsilon_{\parallel}$ is the permittivity along the long axis of the molecule, and $\epsilon_{\perp}$ the permittivity perpendicular to the long axis.

To convert the frame of the molecule into the system frame shown in Figure 3.1, we

have to rotate the molecular permittivity tensor about the y axis by θ using

$$\overleftrightarrow{R_y}(\theta) = \begin{pmatrix} \cos\theta & 0 & -\sin\theta \\ 0 & 1 & 0 \\ \sin\theta & 0 & \cos\theta \end{pmatrix}$$

and then rotate about the z axis by ϕ using

$$\overleftrightarrow{R_z}(\phi) = \begin{pmatrix} \cos\phi & -\sin\phi & 0 \\ \sin\phi & \cos\phi & 0 \\ 0 & 0 & 1 \end{pmatrix}$$

to calculate the permittivity tensor.

This is realised by post and pre-multiplication of the molecular permittivity tensor,

$$\begin{aligned} \overleftrightarrow{\epsilon} &= \overleftrightarrow{R_z}(\phi) \cdot \overleftrightarrow{R_y}(\theta) \cdot \overleftrightarrow{\epsilon_{mol}} \cdot \overleftrightarrow{R_y^T}(\phi) \cdot \overleftrightarrow{R_z^T}(\theta) \\ &= \begin{pmatrix} \Delta\epsilon\cos^2\theta\cos^2\phi + \epsilon_\perp & \Delta\epsilon\cos^2\theta\cos\phi\sin\phi & \Delta\epsilon\sin\theta\cos\theta\cos\phi \\ \Delta\epsilon\cos^2\theta\cos\phi\sin\phi & \Delta\epsilon\cos^2\theta\sin^2\phi + \epsilon_\perp & \Delta\epsilon\sin\theta\cos\theta\sin\phi \\ \Delta\epsilon\sin\theta\cos\theta\cos\phi & \Delta\epsilon\sin\theta\cos\theta\sin\phi & \Delta\epsilon\sin^2\theta + \epsilon_\perp \end{pmatrix} \\ &= \begin{pmatrix} \Delta\epsilon n_x^2 + \epsilon_\perp & \Delta\epsilon n_x n_y & \Delta\epsilon n_z n_x \\ \Delta\epsilon n_x n_y & \Delta\epsilon n_y^2 + \epsilon_\perp & \Delta\epsilon n_z n_y \\ \Delta\epsilon n_z n_x & \Delta\epsilon n_z n_y & \Delta\epsilon n_z^2 + \epsilon_\perp \end{pmatrix} \end{aligned} \tag{3.22}$$

where n_x, n_y, and n_z are calculated using Equation 3.3, and $\Delta\epsilon$ is the dielectric anisotropy calculated by

$$\Delta\epsilon = \epsilon_\parallel - \epsilon_\perp. \tag{3.23}$$

The permittivities in the direction of the system axes are the xx, yy, and zz components of Equation 3.22, which are

$$\begin{aligned}\epsilon_{xx} &= \Delta\epsilon n_x^2 + \epsilon_\perp, \\ \epsilon_{yy} &= \Delta\epsilon n_y^2 + \epsilon_\perp, \\ \epsilon_{zz} &= \Delta\epsilon n_z^2 + \epsilon_\perp. \end{aligned} \tag{3.24}$$

Electric field

The electric field inside the cell can be calculated using Maxwell's Equations. The first equation, also known as Gauss's law, is defined as

$$\nabla \cdot \vec{D} = \rho, \tag{3.25}$$

where $\vec{D}$ is the displacement field and ρ is the electric charge density per unit volume. The second equation, also known as Faraday's law of induction, is defined as

$$\nabla \times \vec{E} = -\frac{\partial \vec{B}}{\partial t}, \tag{3.26}$$

where $\vec{B}$ is the magnetic field.

To calculate the electric field inside a liquid crystal cell, the Gauss law will be used. Most of the liquid crystal materials used in this project are ionic materials. These materials have ions and free charges, which effect the electric field and make it more complicated to calculate the electric field because it is unknown which mobility and concentration these free charges have. To simplify the calculation of the electric field, it is assumed, that there are no free charges in the liquid crystal material. This simplification can give an electric field which is not perfectly correct and a method has to be found to compensate for this assumption during the fitting process of the

experimental results. But, assuming there are no free charges in the calculation of the electric field, simplifies Gauss's law to

$$\nabla \cdot \vec{D} = 0. \tag{3.27}$$

It is possible to calculate the voltage profile using the simplified Gauss's law (Eq. 3.27). The general expression of the displacement field $\vec{D}$ (Eq. 3.20) can be extended with the flexoelectric polarisation (Eq. 2.1) to

$$\vec{D} = \epsilon_0 \overleftrightarrow{\epsilon}\ \vec{E} + \vec{P_f}. \tag{3.28}$$

Substituting Equation 3.28 into the simplified Gauss's law (Eq. 3.27) and using the relationship between $\vec{E}$ and applied voltage V, where $\vec{E} = -\nabla V$, gives

$$\nabla \cdot \left(-\epsilon_0 \overleftrightarrow{\epsilon}\ \nabla V + \vec{P_f}\right) = 0. \tag{3.29}$$

Equation 3.29 is a general expression to determine the voltage profile inside the liquid crystal layer and includes the dielectric and flexoelectric properties. Using the voltage profile, it is possible to calculate the electric field $\vec{E} = -\nabla V$, the gradient of the electric field, and the displacement field $\vec{D} = \epsilon_0 \overleftrightarrow{\epsilon}\ \vec{E}$.

3.5.3 Flexoelectric Energy

The flexoelectric energy density w_f is given by

$$w_f = -\vec{P_f} \cdot \vec{E}, \tag{3.30}$$

where $\vec{E}$ is the electric field and $\vec{P}$ is the flexoelectric polarisation, where $\vec{P}$ is defined by

$$\begin{aligned}\vec{P_f} &= e_1\vec{S} + e_3\vec{B},\\ \vec{P_f} &= e_1\vec{n}\,(\nabla\cdot\vec{n}) + e_3\,(\nabla\times\vec{n})\times\vec{n},\end{aligned} \tag{3.31}$$

and where e_1 and e_3 are the splay and bend flexoelectric coefficients. This leads to a flexoelectric energy expression w_f of

$$w_f = -\left(e_1\vec{n}\,(\nabla\cdot\vec{n}) + e_3\,(\nabla\times\vec{n})\times\vec{n}\right)\cdot\vec{E}. \tag{3.32}$$

The units of the flexoelectric energy density w_f is $\frac{J}{m^3} = \frac{Nm}{m^3} = \frac{N}{m^2}$, of the flexoelectric polarisation $\vec{P_f}$ is $\frac{Cm}{m^3} = \frac{C}{m^2}$, of the electric field $\vec{E}$ is $\frac{N}{C}$, of the flexoelectric coefficients e_{ii} is $\frac{C}{m}$, of *splay* $\vec{S}$ is $\frac{1}{m}$, and of *bend* $\vec{B}$ is $\frac{1}{m}$.

3.5.4 Total Bulk Energy

The total bulk energy L_B is a sum of the elastic energy w_d, flexoelectric energy w_f, and dielectric energy w_e as given by

$$\begin{aligned}L_B &= w_d + w_f + w_e\\ L_B &= \frac{1}{2}K_{11}\,(\nabla\cdot\vec{n})^2 + \frac{1}{2}K_{22}\,(\vec{n}\cdot(\nabla\times\vec{n}) - q)^2 + \frac{1}{2}K_{33}\,(\vec{n}\times(\nabla\times\vec{n}))^2\\ &\quad - \left(e_1\vec{n}\,(\nabla\cdot\vec{n}) + e_3\,(\nabla\times\vec{n})\times\vec{n}\right)\cdot\vec{E} - \frac{1}{2}\epsilon_0\overleftrightarrow{\epsilon}\,\vec{E}\vec{E},\end{aligned} \tag{3.33}$$

where the unit of the total bulk energy density L_B is $\frac{J}{m^3} = \frac{Nm}{m^3} = \frac{N}{m^2}$.

3.6 Surface Energy

The surface energy L_S [112, 113] can be defined as

$$\begin{aligned} L_S &= W_\theta \sin^2(\theta - \theta_P) + W_\phi \sin^2(\phi - \phi_P) \\ &= W_\theta \left(n_z \cos\theta_P - \sqrt{n_x^2 + n_y^2} \sin\theta_P \right)^2 \\ &\quad + W_\phi \left(\frac{n_y}{\sqrt{n_x^2 + n_y^2}} \cos\phi_P - \frac{n_y}{\sqrt{n_x^2 + n_y^2}} \sin\phi_P \right)^2, \end{aligned} \tag{3.34}$$

where W_θ is the zenithal surface anchoring, W_ϕ is the azimuthal surface anchoring, θ_P is the zenithal pretilt, and ϕ_P is the azenithal pretwist. The unit of the surface energy L_S is $\frac{J}{m^3} = \frac{Nm}{m^3} = \frac{N}{m^2}$.

The Euler-Lagrange Equations for the boundary condition are defined as

$$\begin{aligned} \frac{\partial \mathcal{D}}{\partial \dot{n_x}} &= \pm \left(\frac{\partial L_B}{\partial \frac{\partial n_x}{\partial x}} + \frac{\partial L_B}{\partial \frac{\partial n_x}{\partial y}} + \frac{\partial L_B}{\partial \frac{\partial n_x}{\partial z}} \right) - \frac{\partial L_S}{\partial n_x} \\ \frac{\partial \mathcal{D}}{\partial \dot{n_y}} &= \pm \left(\frac{\partial L_B}{\partial \frac{\partial n_y}{\partial x}} + \frac{\partial L_B}{\partial \frac{\partial n_y}{\partial y}} + \frac{\partial L_B}{\partial \frac{\partial n_y}{\partial z}} \right) - \frac{\partial L_S}{\partial n_y} \\ \frac{\partial \mathcal{D}}{\partial \dot{n_z}} &= \pm \left(\frac{\partial L_B}{\partial \frac{\partial n_z}{\partial x}} + \frac{\partial L_B}{\partial \frac{\partial n_z}{\partial y}} + \frac{\partial L_B}{\partial \frac{\partial n_z}{\partial z}} \right) - \frac{\partial L_S}{\partial n_z}, \end{aligned} \tag{3.35}$$

where L_B is the general bulk energy. The $\pm$ indicates the difference of the bottom and top surface. The bottom surface uses a '+' and the top surface uses a '-'. The dissipation function $\frac{\partial \mathcal{D}}{\partial \dot{n_i}}$ for the dynamic case (without flow on the surface but flow can be allowed in the bulk) is

$$\frac{\partial \mathcal{D}}{\partial \dot{n_i}} = \gamma_1 L_S \dot{n_i}, \tag{3.36}$$

where L_S is the surface length to scale the effect of the surface energy into the bulk, and simplifies in the static case to

$$\frac{\partial \mathcal{D}}{\partial \dot{n}_i} = 0. \tag{3.37}$$

3.7 Computation

To implement the theory in a numerical model, first a few numerical rules have to be used. The molecular field $\vec{h}$ contains first and second order differentials of $\vec{n}$ with respect to the three axis. To demonstrate the calculation of these differentials, an example is used. The example describes a one-dimensional model along the z axis. The z axis is divided into 100 layers (LMax) whereby each layer is $h = 100nm$ thick, which leads to a cell thickness of $d = 10\mu m$. The first differential equation for the bulk can be numerically determined by

$$\frac{\partial n_i}{\partial z}(LN) = \frac{n_i(LN+1) - n_i(LN-1)}{2h}, \tag{3.38}$$

where i are the axis (x, y, and z) and LN the actual layer number (from 1 to 99). And the second differential equation for the bulk is defined by

$$\frac{\partial n_i}{\partial z}(LN) = \frac{n_i(LN+1) - 2n_i(LN) + n_i(LN-1)}{h^2}. \tag{3.39}$$

In general the layer number goes from 0 to 100 if the maximum layer number is 100, as in this example used. The first layer, with the number 0, represents the lower boundary, the layers 1 to 99 represents the bulk and the layer 100 the upper boundary. This gives a total number of 101. However, to calculate the first or second differential for the bulk, it is necessary to used the lower and upper boundary. The

first differential equations for the boundaries are

$$\frac{\partial n_i}{\partial z}(0) = \frac{n_i(1) - n_i(0)}{h} \tag{3.40}$$

and

$$\frac{\partial n_i}{\partial z}(LMax) = \frac{n_i(LMax) - n_i(LMax-1)}{h}. \tag{3.41}$$

The second differential equations for the boundaries are not required because they don't appear in the surface expression (Eq. 3.35).

Additionally, it is possible to calculate an integral numerically by

$$\int_0^d = \left(\sum_{LN=1}^{LMax-1} (f(LN)h) \right) + \frac{h}{2} f(0) + \frac{h}{2} f(LMax), \tag{3.42}$$

where the first part of the integral calculates the bulk energy, the second part the lower boundary, and the third part the upper boundary. These numerical rules can help to implement differential and integral calculations. To be able to calculate the dynamics or statics of the system, it is important to determine the next time step of the director. In the static case it is easier to use the dynamic case and calculate the next time step until the change in director goes to zero, which means that the director has reached equilibrium. Therefore setting the dynamic case of the dissipation function (Eq. 3.16) equal to the molecular field $\vec{h}$ (Eq. 3.10) and rearranging the equation with respect to $\dot{n}_i$ gives

$$\dot{n}_i = \frac{\vec{h_i}}{\gamma_1}. \tag{3.43}$$

The next time step can be calculated numerically using

$$\dot{n_i} = \frac{n_i(t + \Delta t) - n_i(t)}{\Delta t}, \tag{3.44}$$

where t is the time, $n_i(t + \Delta t)$ is the director at the next time step, $n_i(t)$ is the director at the actual time step, and Δt the time difference between the next time step and the actual time step, which is in range of 10^{-8} to 10^{-6}. If the time step is too small, the difference between the actual time step and the next time step can be very small and falsely interpreted as zero by the program, which would stop the calculation because the program would assume that and equilibrium is reached but this was not the case. If the time step is too big, the calculated solution for the next time step might be far away from the real solution. The calculations might run into a dead end and the program might crash because of unrealistic values. Substituting Equation 3.43 with Equation 3.44 and rearranging with respect to the next time step $n_i(t + \Delta t)$ gives

$$n_i(t + \Delta t) = n_i(t) + \Delta t \left(\frac{\vec{h_i}}{\gamma_1} \right), \tag{3.45}$$

or expanded to the three coordinated axis x, y, and z,

$$\begin{aligned} n_x(t + \Delta t) &= n_x(t) + \Delta t \left(\frac{\vec{h_x}}{\gamma_1} \right), \\ n_y(t + \Delta t) &= n_y(t) + \Delta t \left(\frac{\vec{h_y}}{\gamma_1} \right), \\ n_z(t + \Delta t) &= n_z(t) + \Delta t \left(\frac{\vec{h_z}}{\gamma_1} \right). \end{aligned} \tag{3.46}$$

Similar to the director, the voltage profile can be calculated using

$$V(t+\Delta t) = V(t) + \Delta t \left(\nabla \cdot \left(-\epsilon_0 \overleftrightarrow{\epsilon} \nabla V(t) + \vec{P_f} \right) \right), \tag{3.47}$$

where $V(t+\Delta t)$ is the voltage profile at the next time step and $V(t)$ is the voltage profile at the actual time step.

To summarise and illustrate the computational approach, Figure 3.2 shows a simple example for one fixed voltage and the static case, whereby first all variables are initiated, then the electric field calculated and updated until it is in an equilibrium state. After calculating the molecular field and next time step, the program checks if the system is in an equilibrium state. If not, the whole routine will be run again. The example just shows the routine for one voltage. If a range of voltages are being calculated, then a bigger loop would be required to change the voltage after the director reached an equilibrium state for the given voltage. The dynamic state is similar to the static state except that the calculation is finished when the end of the simulation time is reached.

3.8 Example: Freedericksz geometry

To demonstrate the implementation of the theory into a numerical computation and to present some results, Freedericksz geometry is used, as shown in Figure 3.3, as a simple example. The cell thickness d is $10\mu m$ and divided into 100 layers. The electric field is applied across the device in the z axis and voltages between $0V$ and $10V$ are being applied. The one-dimensional model calculates the director profile along the z axis. This has the big advantage for the calculation that the ∇ operator simplifies to changes in the z direction only and changes in the x and y direction can be set to zero as $\frac{\partial}{\partial x} = 0$ and $\frac{\partial}{\partial y} = 0$. To indicate that a variable is differentiated with

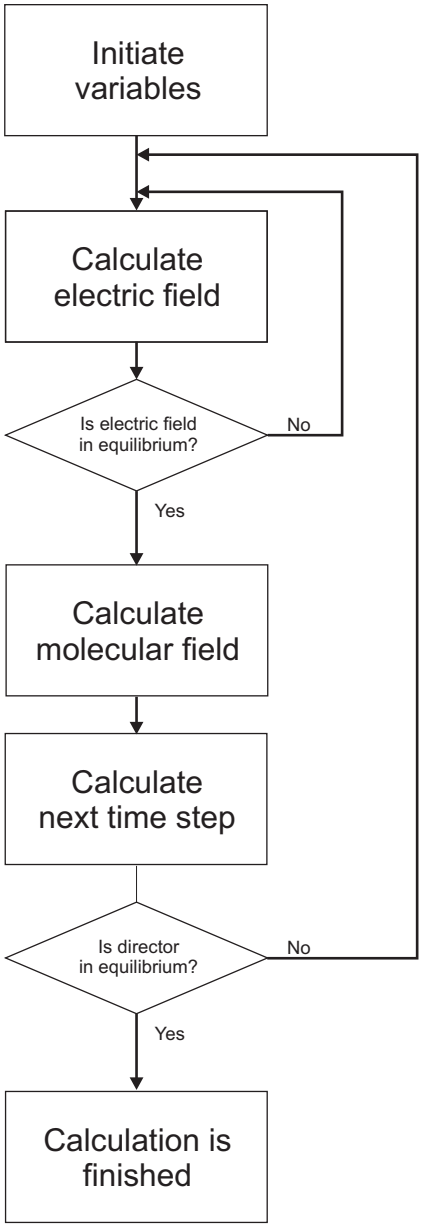


Figure 3.2: Illustration of the computational approach

respect to space and in this case to the z direction, dashes will be used ($n_x^{'} = \frac{\partial n_x}{\partial z}$ and $n_z^{'} = \frac{\partial n_z}{\partial z}$). This should not be confused with dots, which indicate a change with respect to time. Further, it is possible to simplify and reduce the director $\vec{n}$ to the components n_x and n_z, and set the n_y component to zero because the director is only in the $x - z$ plane.

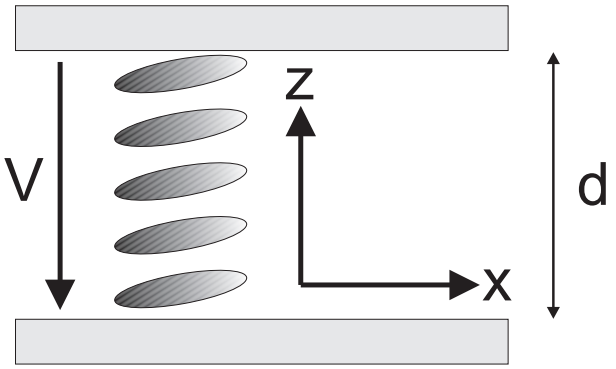


Figure 3.3: Example: Freedericksz geometry

The model includes the bulk energy L_B (Eq. 3.33) with the elastic energy w_d, flexoelectric energy w_f and dielectric energy w_e. The surfaces are being kept fixed at a pretilt of 0.5°, which means that the surface energy is not included. These leads to a bulk energy L_B of

$$\begin{aligned} L_B = & \frac{1}{2}K_{11}n_z^{'2} + \frac{1}{2}K_{33}\left(n_z^2 n_x^{'2} + n_z^2 n_z^{'2}\right) \\ & - (e_1 + e_3)\, n_z n_z^{'} E_z - \frac{1}{2}\epsilon_0\left(\Delta\epsilon n_z^2 + \epsilon_\perp\right) E_z^2, \end{aligned} \tag{3.48}$$

whereby the following calculations are used

$$\nabla = \begin{pmatrix} 0 \\ 0 \\ \frac{\partial}{\partial z} \end{pmatrix}, \vec{n} = \begin{pmatrix} n_x \\ 0 \\ n_z \end{pmatrix}, \vec{E} = \begin{pmatrix} 0 \\ 0 \\ E_z \end{pmatrix},$$

$$\nabla \cdot \vec{n} = \begin{pmatrix} 0 \\ 0 \\ \frac{\partial}{\partial z} \end{pmatrix} \cdot \begin{pmatrix} n_x \\ 0 \\ n_z \end{pmatrix} = \frac{\partial n_z}{\partial z} = n_z^{'},$$

$$\vec{n}\,(\nabla \cdot \vec{n}) = \begin{pmatrix} n_x \\ 0 \\ n_z \end{pmatrix} \cdot n_z^{'} = \begin{pmatrix} n_x n_z^{'} \\ 0 \\ n_z n_z^{'} \end{pmatrix},$$

$$(\nabla \times \vec{n}) \times \vec{n} = \left[\begin{pmatrix} 0 \\ 0 \\ \frac{\partial}{\partial z} \end{pmatrix} \times \begin{pmatrix} n_x \\ 0 \\ n_z \end{pmatrix} \right] \times \begin{pmatrix} n_x \\ 0 \\ n_z \end{pmatrix} = \begin{pmatrix} 0 \\ n_x^{'} \\ 0 \end{pmatrix} \times \begin{pmatrix} n_x \\ 0 \\ n_z \end{pmatrix}$$

$$= \begin{pmatrix} 0 \\ 0 \\ -n_x n_x^{'} \end{pmatrix} = \begin{pmatrix} n_z n_x^{'} \\ 0 \\ n_z n_z^{'} \end{pmatrix},$$

$$(\vec{n} \times (\nabla \times \vec{n}))^2 = \begin{pmatrix} n_z n_x^{'} \\ 0 \\ n_z n_z^{'} \end{pmatrix}^2 = n_z^2 n_x^{'2} + n_z^2 n_z^{'2},$$

$$\vec{n} (\nabla \cdot \vec{n}) \vec{E} = \begin{pmatrix} n_x n_z^{'} \\ 0 \\ n_z n_z^{'} \end{pmatrix} \cdot \begin{pmatrix} 0 \\ 0 \\ E_z \end{pmatrix} = n_z n_z^{'} E_z,$$

$$((\nabla \times \vec{n}) \times \vec{n}) \vec{E} = \begin{pmatrix} n_z n_x^{'} \\ 0 \\ n_z n_z^{'} \end{pmatrix} \cdot \begin{pmatrix} 0 \\ 0 \\ E_z \end{pmatrix} = n_z n_z^{'} E_z,$$

$$\vec{D}\vec{E} = \epsilon_0 \left[\begin{pmatrix} \Delta\epsilon n_x^2 + \epsilon_\perp & 0 & \Delta\epsilon n_z n_x \\ 0 & \Delta\epsilon n_y^2 + \epsilon_\perp & 0 \\ \Delta\epsilon n_z n_x & 0 & \Delta\epsilon n_z^2 + \epsilon_\perp \end{pmatrix} \begin{pmatrix} 0 \\ 0 \\ E_z \end{pmatrix} \right] \begin{pmatrix} 0 \\ 0 \\ E_z \end{pmatrix}$$

$$= \epsilon_0 \begin{pmatrix} \Delta\epsilon n_x n_z E_z \\ 0 \\ (\Delta\epsilon n_z^2 + \epsilon_\perp) E_z \end{pmatrix} \cdot \begin{pmatrix} 0 \\ 0 \\ E_z \end{pmatrix} = \epsilon_0 \left(\Delta\epsilon n_z^2 + \epsilon_\perp \right) E_z^2.$$

The general Euler-Lagrange equation (Eq. 3.10) simplifies for the 1-D model and leads to a molecular field $\vec{h}$ of

$$h_x = \frac{\partial}{\partial z} \left(\frac{\partial L_B}{\partial n_x^{'}} \right) - \frac{\partial L_B}{\partial n_x},$$

$$
\begin{aligned}
h_y &= 0, \\
h_z &= \frac{\partial}{\partial z}\left(\frac{\partial L_B}{\partial n_z^{'}}\right) - \frac{\partial L_B}{\partial n_z},
\end{aligned} \tag{3.49}
$$

and the final solution of the molecular field $\vec{h}$ gives

$$
\begin{aligned}
h_x = &\ K_{33}\left(2n_z n_x^{'} n_z^{'} + n_z^2 n_x^{''}\right), \\
h_y = &\ 0, \\
h_z = &\ K_{11} n_z^{''} + K_{33} n_z \left(n_z n_z^{''} - n_x^{'2} + n_z^{'2}\right) \\
&- \left(e_1 + e_3\right) n_z E_z^{'} + \epsilon_0 \Delta\epsilon n_z E_z^2.
\end{aligned} \tag{3.50}
$$

whereby the following calculations are used

$$
\begin{aligned}
\frac{\partial L_B}{\partial n_x^{'}} &= K_{33} {n_z}^2 {n_x}^{'}, \\
\frac{\partial}{\partial z}\left(\frac{\partial L_B}{\partial n_x^{'}}\right) &= K_{33}\left(2 n_z {n_x}^{'} {n_z}^{'} + {n_z}^2 {n_x}^{''}\right), \\
\frac{\partial L_B}{\partial n_x} &= 0, \\
\frac{\partial L_B}{\partial n_z^{'}} &= K_{11} {n_z}^{'} + K_{33} {n_z}^2 {n_z}^{'} - \left(e_1 + e_3\right) n_z E_z, \\
\frac{\partial}{\partial z}\left(\frac{\partial L_B}{\partial n_z^{'}}\right) &= K_{11} {n_z}^{''} + K_{33}\left({n_z}^2 {n_z}^{''} + 2 n_z {n_z}^{'2}\right) \\
&\quad - \left(e_1 + e_3\right) n_z {E_z}^{'} - \left(e_1 + e_3\right) {n_z}^{'} E_z, \\
\frac{\partial L_B}{\partial n_z} &= K_{33}\left(n_z {n_z}^{'2} + n_z {n_x}^{'2} + n_z {n_y}^{'2}\right) \\
&\quad - \left(e_1 + e_3\right) {n_z}^{'} E_z - \epsilon_0 \Delta\, \epsilon\, n_z {E_z}^2.
\end{aligned}
$$

The voltage profile and, therefore, the electric field is calculated using Equation 3.29, which leads to

$$
\frac{\partial}{\partial z}\left(-\epsilon_0\left(\Delta\epsilon n_z^2 + \epsilon_\perp\right)\frac{\partial V}{\partial z} + \left(e_1 + e_3\right) n_z n_z^{'}\right) = 0, \tag{3.51}
$$

where the solution is

$$-2\epsilon_0\Delta\epsilon n_z n_z^{'}\frac{\partial V}{\partial z}-\epsilon_0\left(\Delta\epsilon n_z^2+\epsilon_\perp\right)\frac{\partial^2 V}{\partial z^2} + (e_1+e_3)\,n_z^{'2}+(e_1+e_3)\,n_z n_z^{''}=0 \tag{3.52}$$

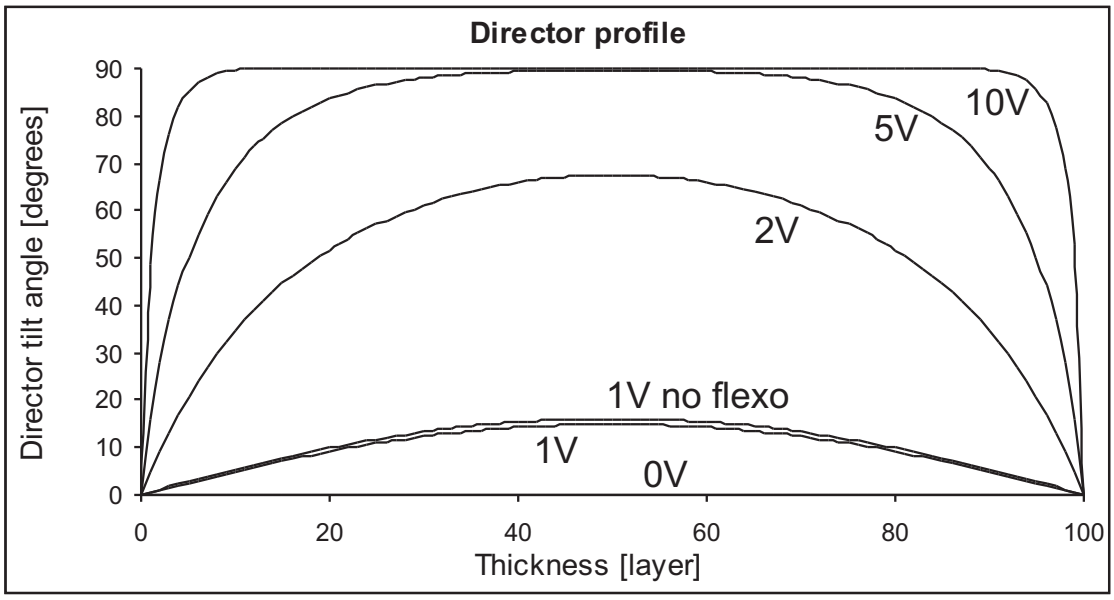
and using Equation 3.47, the next time step for the voltage can be calculated.

The program uses the Equations 3.38 and 3.39 to calculate the first and second differential and Equation 3.46 to calculate the next time step. The following elastic, dielectric, and flexoelectric parameters are used in the model: $K_{11} = 10.7pN$, $K_{33} = 16.2pN$, $\epsilon_\perp = 5.2$, $\epsilon_\parallel = 18.9$, and $(e_1 + e_3) = 10.0pC/m$. The values for the parameters are from the commercial mixture E7, which was used in this project and the parameter were determined using our experiments, as described in Chapter 4.2.7. Figure 3.4 a) shows the director tilt θ (in degree) across the cell thickness (in layers 0 to 100) for different voltages. The director tilt versus cell thickness is also known as *director profile*. The director tilt θ is defined as

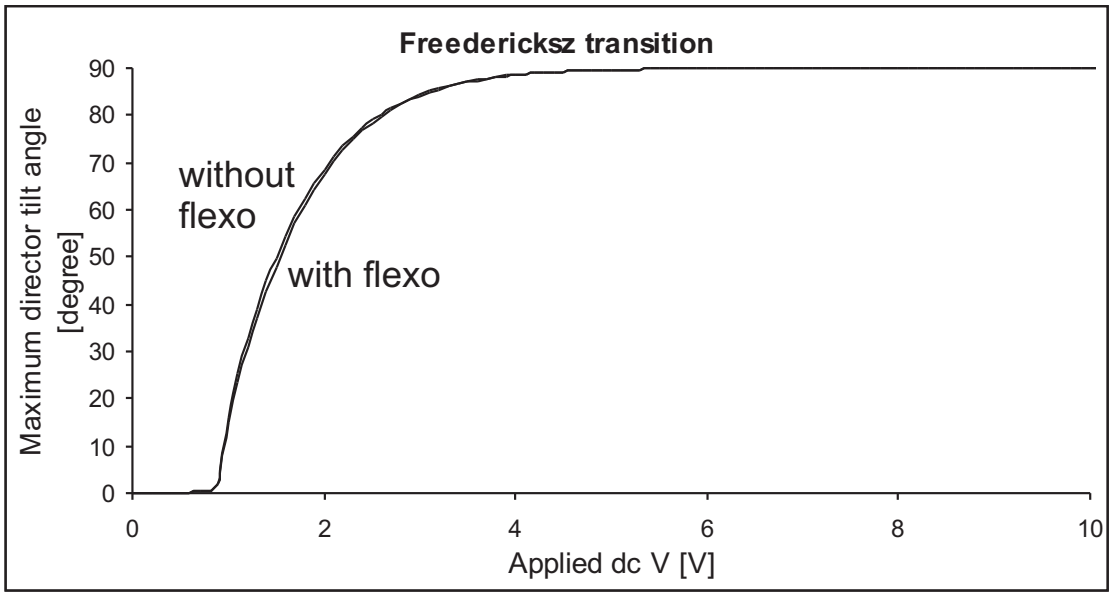
$$\theta = \arctan\frac{n_z}{n_x}. \tag{3.53}$$

Figure 3.4 b) shows the *Freedericksz transition* with the maximal director tilt θ_{max} (from the middle of the cell thickness) versus the applied voltage in the range between $0V$ and $10V$. The results show clearly that the *Freedericksz transition* has the Freedericksz threshold at about $0.9V$. The elastic force dominate below the Freedericksz threshold and the electrostatic forces starts to dominate above the Freedericksz threshold. At high voltages like 10V or higher, the electrostatic forces dominate.

To illustrate the effect of flexoelectricity on the *director profile* (Fig. 3.4 a) and on the *Freedericksz transition* (Fig. 3.4 b), the flexoelectric polarisation (Eq. 3.31) and the flexoelectric energy (Eq. 3.32) was removed from the Equations 3.48 to



a)



b)

Figure 3.4: a) *Director profile* for different voltages of a Freedericksz structure and b) *Freedericksz transition*

3.52. Comparing the results of the *director profile* (Fig. 3.4 a) for the cases of 1V (with flexoelectricity) and of 1V_no_flexo (without flexoelectricity), only a small

difference can be seen. Comparing also the results of the *Freedericksz transition* (Fig. 3.4 b) for the cases with_flexo (with flexoelectricity) and without_flexo (without flexoelectricity), only a small difference can be seen [57]. These comparisons show clearly, that flexoelectricity has only a small effect on the director profile and that it is a subtle effect. In most experiments flexoelectricity can be neglected, which makes it harder to measure flexoelectricity.

3.9 Optics

The example presented above illustrates how theory is implemented in the numerical program. However, most experiments carried out use a laser beam to detect, record and measure the change in director profile. Therefore, it is important to calculate the transmission of a laser beam through the cell. Once the director profile is calculated, the transmission can be calculated [114]. Light is an electromagnetic wave, where the electric wave is perpendicular to the magnetic wave. Using Maxwell's Equations, the magnetic part can be calculated in the electric part, which simplifies the calculation. Using the 2x2 Jones method [115], the magnitude and phase of the electric wave in x and y direction for a wave travelling in z direction can be calculated. Using the settings of the input polariser with the angle ϕ, the change in magnitude and phase of $E_x(in)$ and $E_y(in)$ for the first layer can be calculated by

$$\begin{bmatrix} E_x(in) \\ E_y(in) \end{bmatrix} = \begin{bmatrix} \cos\phi E_0 \\ \sin\phi E_0 \end{bmatrix} \tag{3.54}$$

These results are then used to calculate the next layer with

$$\begin{bmatrix} E_x(out) \\ E_y(out) \end{bmatrix} = \begin{bmatrix} \cos\Gamma - i\sin\Gamma\cos 2\phi & -i\sin\Gamma\sin 2\phi \\ -i\sin\Gamma\sin 2\phi & \cos\Gamma + i\sin\Gamma\cos 2\phi \end{bmatrix} \begin{bmatrix} E_x(in) \\ E_y(in) \end{bmatrix},$$

(3.55)

whereby $E_x(in)$ and $E_y(in)$ are the wave travelling into the layer and $E_x(out)$ and $E_y(out)$ are the wave travelling out of the layer. The calculation includes the retardation Γ, which is defined as

$$\Gamma = \frac{\pi \Delta n_{eff} h}{\lambda} \tag{3.56}$$

with the effective birefringence Δn_{eff}

$$\Delta n_{eff} = n_{\perp} \left(\frac{n_{\parallel}}{\sqrt{n_{\parallel}^2 \sin^2 \theta + n_{\perp}^2 \cos^2 \theta}} - 1 \right). \tag{3.57}$$

The calculation of E_x and E_y is carried out until the last layer, where the setting of the output analyser defines the final magnitude and phase of E_x and E_y. With the final data, it is possible to calculate the transmission.

This approach is used to calculate the transmission for the example of the Freedericksz geometry, which is presented in Figure 3.5. The setting of the input polariser

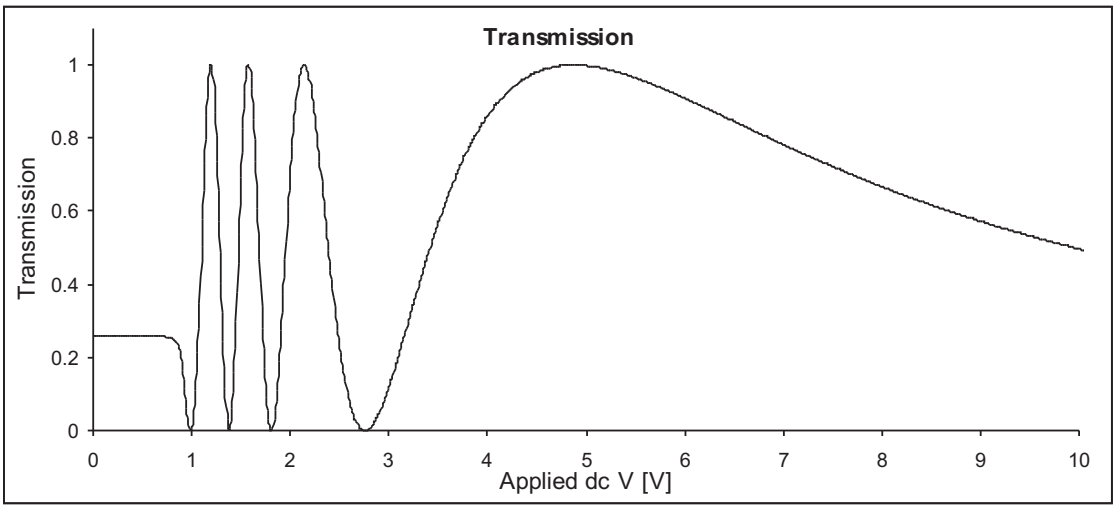


Figure 3.5: Transmission of a Freedericksz structure at crossed polariser

is 45° to the x axis in the $x-y$ plane and the setting of the output analyser is -45° to the x axis in the $x-y$ plane. This gives an angle of 90° between the polariser and analyser, which is also known as crossed polariser setting. The results show the Freedericksz threshold at a voltage of $0.9V$. The transmission is normalized to 100% or 1 and the magnitude of the transmission below the Freedericksz threshold depends on the cell thickness and the optical properties of the liquid crystal material. The behaviour of the transmission above the Freedericksz threshold oscillates between 0% and 100% magnitude. This behaviour is due to the retardation caused by the director profile at different voltages.

The 2x2 Jones method is fast, simple and used in cases where the light travels at normal incidence through the device because reflections are not included in the method. But if the laser beam is applied at oblique incidence, reflections between the layers are very important and have to be taken into account. This can be realised using the extended Jones method or the 4x4 Berreman method, which are basically the same as the 2x2 Jones method but take reflections into account. The mathematical expression of the 4x4 Berreman method is very complex and therefore it will not be explained here in detail.

In this project, external software libraries and functions are used as the 2x2 Jones and the 4x4 Berreman method to calculate the transmission through the device. These libraries and functions were developed by colleagues during their projects. This had the big advantage that the libraries and functions were well known and tested.

The theory presented in this chapter just gives a general overview. The following chapters describe different experimental set-ups and for each experiment the theory is adjusted and explained in detail.

Chapter 4

Overview of Material Properties

4.1 Measurement of elastic, dielectric and refractive properties

Our newly developed experiments to measure flexoelectric are indirect methods, which means that the data has to be fitted using theory and numerical calculations. Therefore, it is important to know the physical properties as the elastic (splay K_{11}, twist K_{22}, bend K_{33}), dielectric ($\epsilon_{\parallel}, \epsilon_{\perp}$, and $\Delta\epsilon = \epsilon_{\parallel} - \epsilon_{\perp}$) and refractive properties ($n_{\parallel}, n_{\perp}$, and $\Delta n = n_{\parallel} - n_{\perp}$). These properties were measured using standard and well known methods.

4.1.1 Measurement of $K_{11}, K_{33}, \epsilon_{\parallel}, \epsilon_{\perp}$

The determination of $K_{11}, K_{33}, \epsilon_{\parallel}$, and $\epsilon_{\perp}$ is realised using a Freedericksz cell, as shown in Figure 4.1, and applying an electric field across the device. If the applied voltage is smaller than the threshold voltage V_C, the elastic force is bigger than the applied electric force and the director does not change significantly (Fig. 4.1

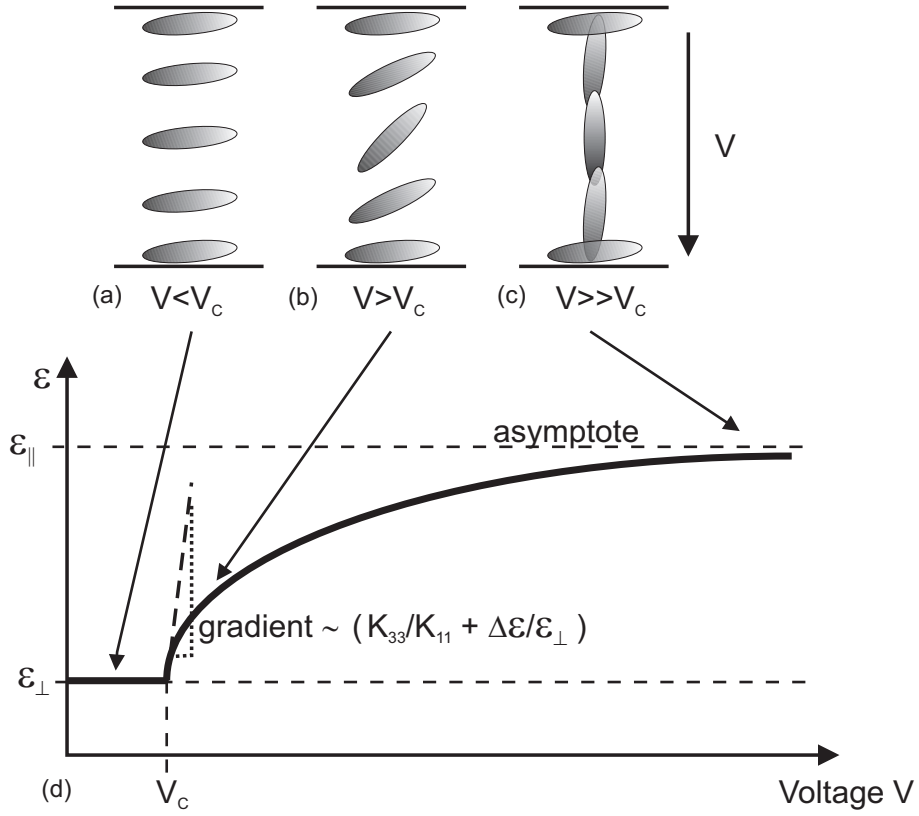


Figure 4.1: Characterisation of Freedericksz transition

a)). Once the voltage is larger than the threshold voltage V_C, the director slowly changes and aligns parallel to the applied field (Fig. 4.1 b)) to minimise the total energy in the system. For very high voltages, the electric force dominates and the director aligns parallel to the field (Fig. 4.1 c)). This behaviour is also known as the *Freedericksz transition* (Fig. 4.1 d)) and is measured using a standard LCR bridge, applying a 1kHz ac voltage and measuring the capacitance C. The relationship between permittivity ϵ and capacitance C is

$$\epsilon = \frac{C}{C_0}, \tag{4.1}$$

where C_0 is the empty cell capacitance, which is measured before filling the device. Using a guardring cell with three connections, as shown in Figure 4.2 b), improves

the accuracy of the capacitance measurement because an error can be avoided due to a fringing electric field (Fig. 4.2 a). Figure 4.2 c) shows an example of a guardring cell with a 3-wire connection. The alignment layer is planar on both glass plates and the rubbing direction anti-parallel which gives a Freedericksz cell.

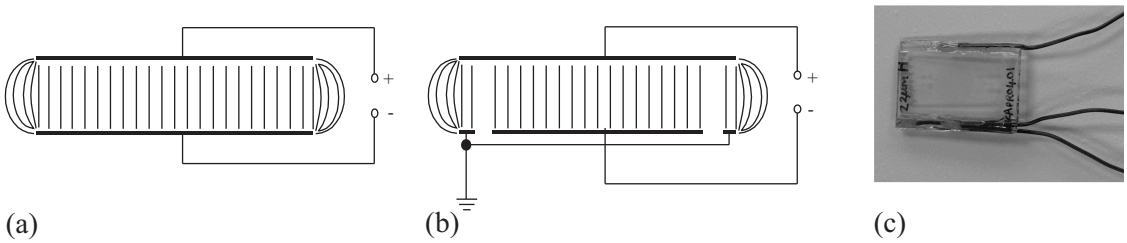


Figure 4.2: a) 2-wired connection with fringing electric field, (b) 3-wired connection without fringing electric field, (c) Example of a guardring cell

The measurement was done using an automated experiment, which was developed during this project. The capacitance was measured by an LCR bridge, which was connected to a PC by GPIB. On the PC, a Labview Program runs the experiment as shown in Figure 4.3. The automation uses, in different voltage ranges, different voltage steps and waiting times. For example, in the voltage range of the threshold voltage V_C, the waiting time must be very long (about 10 minutes per voltage step) because of the weak electric forces compared to the elastic forces (the director change is very slow). At higher voltages, the director change is very fast due to the strong electric forces compared to the elastic forces, and bigger voltage steps with a smaller waiting time are possible. Before the experiment is started, the user has to measure the threshold voltage V_C in a quick run, which takes a few minutes, and then defines the different voltage areas with their waiting times and voltage steps. At each voltage step, the program takes a defined number of measurements and calculates the average. A whole run can take up to 12 hours.

From the measured *Freedericksz transition*, $\epsilon_\perp$ can be directly determined, $\epsilon_\parallel$ can be

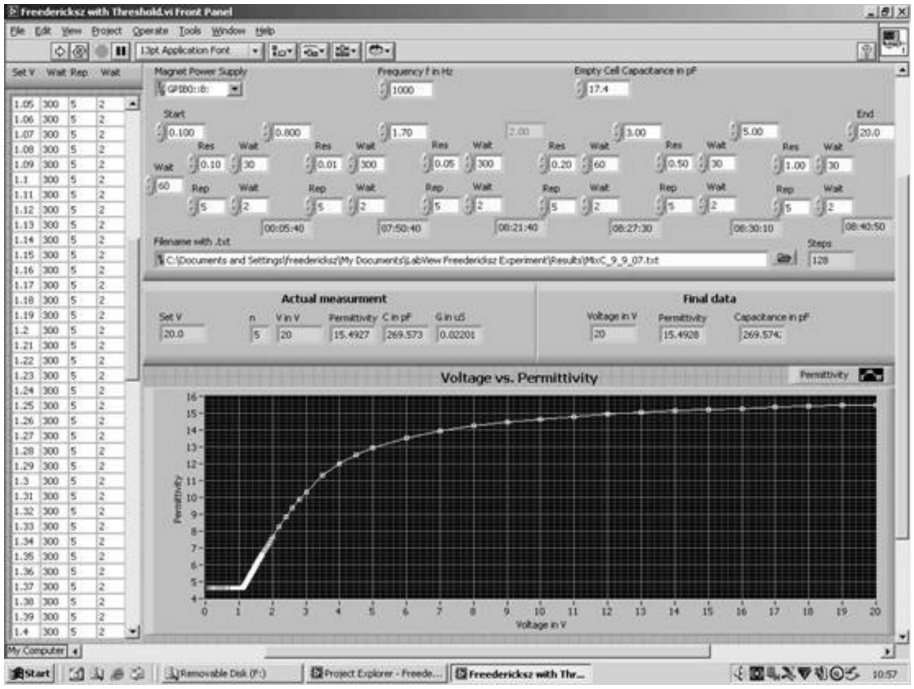


Figure 4.3: Automated experiment to measure the *Freedericksz transition*

estimated by the asymptote (see Fig. 4.1 d)), and K_{11} calculated using

$$K_{11} = \epsilon_0 \Delta\epsilon \left(\frac{V_C}{\pi}\right)^2. \tag{4.2}$$

Knowing K_{11}, K_{33} can be extracted from the gradient of the threshold slope which depends on $\frac{K_{33}}{K_{11}} + \frac{\Delta\epsilon}{\epsilon_\perp}$. Using the gradient to get K_{33} is not very accurate. To decrease the error, not only on K_{33}, but also on the other parameters, it is more common to use theory to fit the whole *Freedericksz transition* to get all four parameters: K_{11}, K_{33}, $\epsilon_\parallel$, and $\epsilon_\perp$. This was done here and a theoretical model was used, as described in the previous chapter. This is more complex and takes more time but using an automated fitting routine gives very good results, as shown in Figure 4.4, and reduces the error. The non-linear minimisation routine e04jbc [Nag] of the commercial package "NAG routines in C" was chosen to perform the automated fit. The error depends on the LCR bridge and the fitting routine. The LCR bridge

has an error of 0.5% for the voltage measurement and also an error of 0.5% for the capacity measurement. The total error after fitting the data is for K_{11} and K_{33} in the range of 4% and for $\epsilon_{\parallel}$ and $\epsilon_{\perp}$ in the range of 1%.

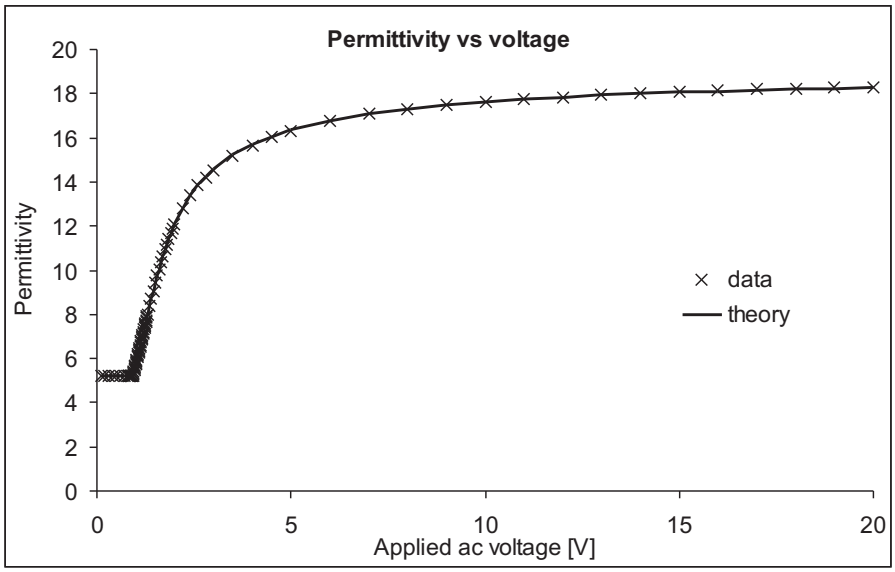


Figure 4.4: Measurement and fit of the Freedericksz Transition

4.1.2 Measurement of K_{22}

To measure the twist elastic constant K_{22} with an electric field, an in-plane applied electric field would be necessary, which is possible, but the exact electric field for a given voltage can only be estimated because of the inhomogeneous electric field and the estimated electrode gap. It is more common to measure K_{22} with magnetic fields. But this requires an electromagnet and a more complex set up. Fortunately for our group, the Department of Physics (University of Oxford) supplied us with an electro-magnet which is able to create magnetic fields up to 1 Tesla. Building and setting up the magnet experiment was part of this project and took about 6 months. Having a magnetic experiment also allows us to think of and develop new experiments in the future, using magnetic fields or combinations between electric

and magnetic fields. But in this project, it was used primarily to measure the twist elastic constant K_{22}.

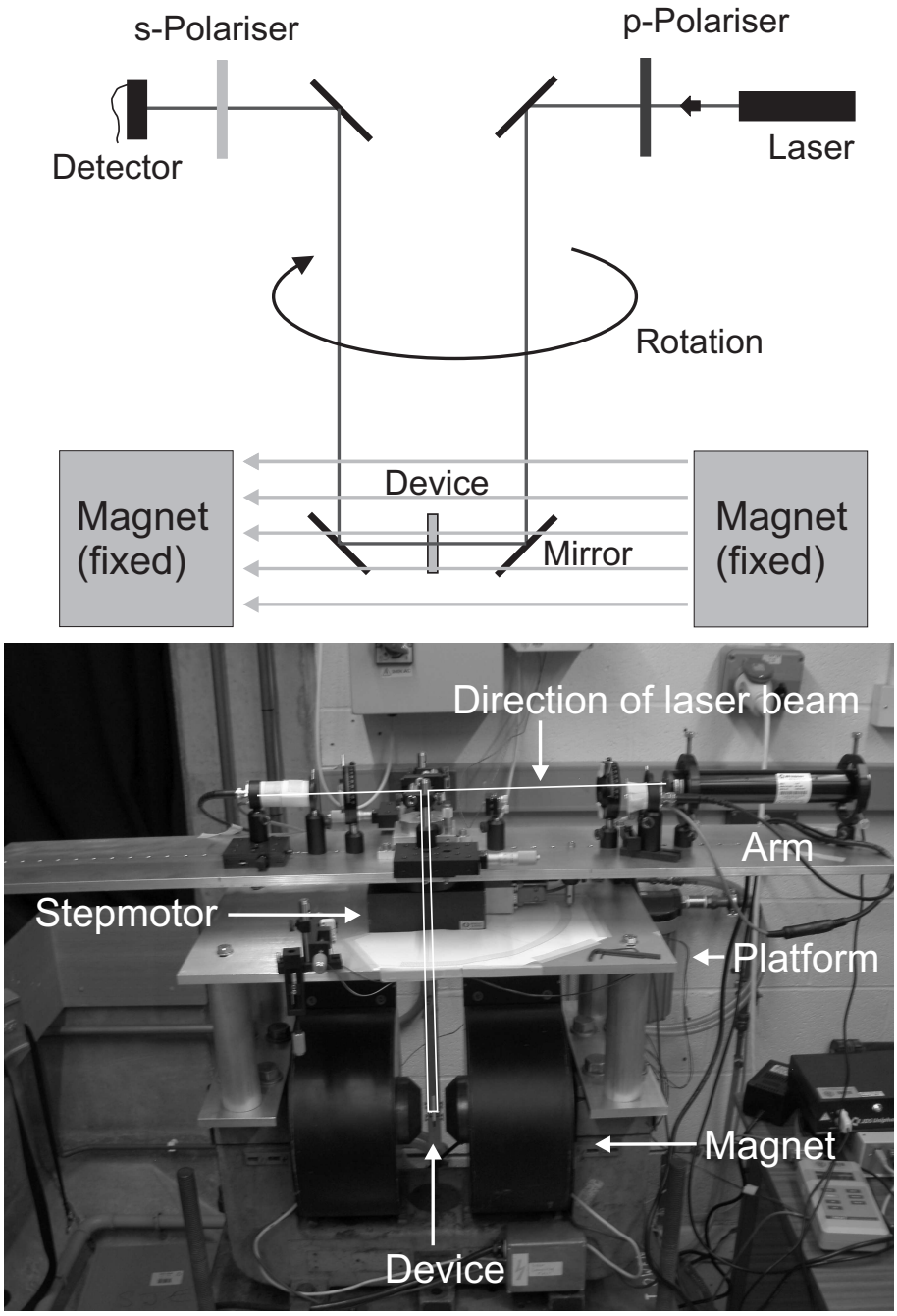


Figure 4.5: Magnet experiment

The device is mounted in a rectangular aluminium tube, which is placed between

the poles of the magnet. Figure 4.5 shows the experimental set up with the magnet and four round tubes holding a platform on top of the magnet. On the platform is mounted a rotational stepper motor, which is able to rotate the arm to any angle. On top of the arm, the optical instruments of the experiment are set up. First the laser, which passes the laser beam horizontally through a polariser onto a 45° mirror. The mirror reflects the laser beam vertically down into the rectangular aluminium tube towards the device. At the bottom of the tube, a second 45° mirror reflects the laser beam horizontally through the liquid crystal device, where the beam always passes perpendicularly through the device. A third 45° mirror reflects the laser beam vertical up towards the arm. A fourth 45° mirror at the arm reflects the beam back to a horizontal direction and through the analyser before the beam hits the detector. This set-up allows us to place a device between the magnetic poles and to apply a magnetic field across the device and in-plane but also at any given angle. The change in director can be observed optically using the laser beam or capacitively using an LCR bridge. Additionally, the magnetic coils are cooled using water, which is necessary if the maximum current of 28 Amperes per coil is applied, giving a maximum magnetic field of 1.0 Tesla. It would be possible to increase the magnetic field further by moving the magnetic poles together but this would require smaller devices or limit the rotational angle of our standard cell. To improve the quality of the data and decrease the labour time, the experiment is fully automated as shown in Figure 4.6, which was very helpful during the measurement and determination of K_{22}. The automation is similar to the program as described in the previous section 4.1.1.

The twist elastic constant K_{22} is measured using the same Freedericksz cell, which was used before in determing K_{11}, K_{33}, $\epsilon_{\parallel}$, and $\epsilon_{\perp}$. This has the big advantage that only one cell is needed for all elastic and dielectric parameters. Applying the magnetic field in-plane and perpendicular to the director, as shown in Figure 4.7 c),

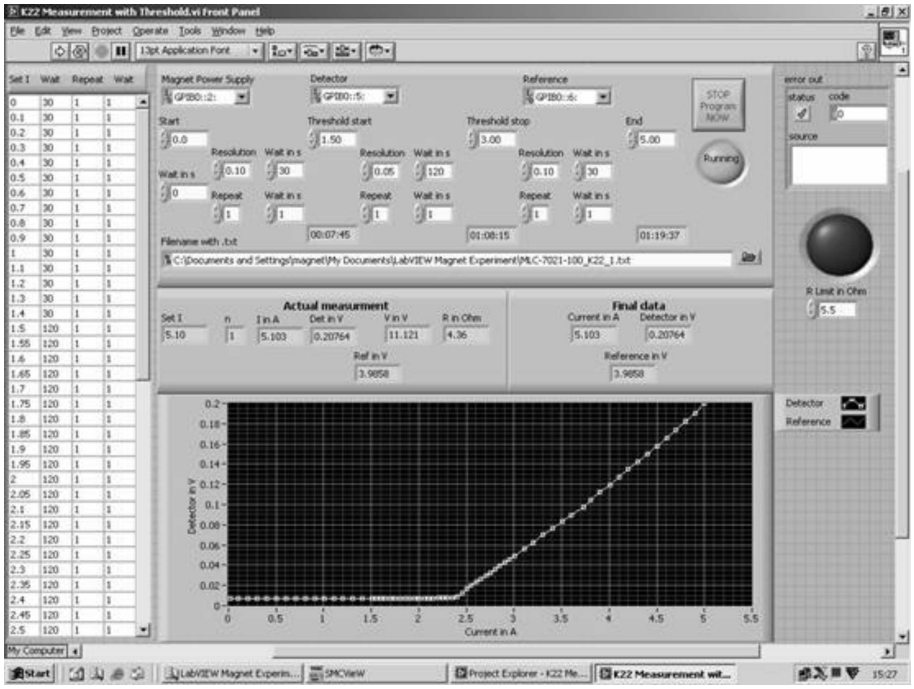


Figure 4.6: Automated magnet experiment to measure K_{22}

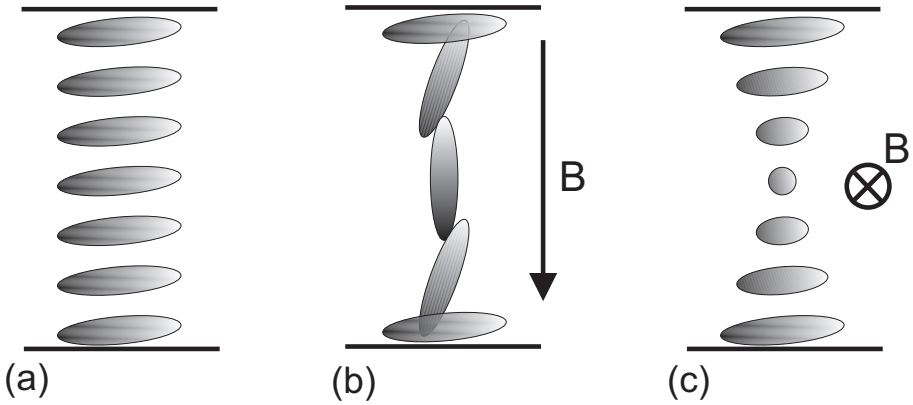


Figure 4.7: a) Freedericksz Cell with b) magnetic field across and c) in-plane the device

the director starts to twist once the magnetic field is larger than the twist magnetic threshold field B_{22}. The elastic constant K_{22} can be calculated by

$$K_{22} = \frac{\Delta\chi}{\mu_0}\left(\frac{B_{22}\cdot d}{\pi}\right)^2, \tag{4.3}$$

where $\Delta\chi$ is the diamagnetic susceptibility anisotropy of the liquid crystal material,

μ_0=1.26 μH/m the permeability constant, and d the thickness of the Freedericksz cell. However $\Delta\chi$ is unknown and has to be measured first. Applying a magnetic field across the device to determine the splay magnetic threshold field B_{11} (Fig. 4.7 b) and knowing K_{11} from the Freedericksz transition, the diamagnetic susceptibility anisotropy $\Delta\chi$ can be calculated by

$$\Delta\chi = K_{11} \cdot \mu_0 \left(\frac{\pi}{B_{11} \cdot d}\right)^2. \tag{4.4}$$

The cell thickness d is unknown but can be measured independently by a capacitive or optical method. This would increase the measurement error of K_{22}. However, substituting Equation 4.4 into 4.3 gives

$$K_{22} = K_{11} \left(\frac{B_{22}}{B_{11}}\right)^2. \tag{4.5}$$

where K_{22} can be calculated more easily by the ratio of the splay and twist threshold fields. The magnetic field B is linear to the applied current I and can be defined as $B = k \cdot I$, where k is the magnetic-current factor. For higher currents above 8 Amperes, the factor k isn't linear any more because the soft iron used in the magnet becomes saturated, as shown in Figure 4.8. However, all of our measurements are done in the linear area below 8 Amperes. The magnetic threshold fields can now be substituted with the threshold currents, which leads to

$$K_{22} = K_{11} \left(\frac{I_{22}}{I_{11}}\right)^2, \tag{4.6}$$

where I_{11} is the splay and I_{22} is the twist threshold current. These threshold currents are measure optically. A laser beam is sent through the device at normal incidence and by increasing the current (and therefore the magnetic field) until the director changes and overcomes the elastic force, the optical signal changes and the threshold

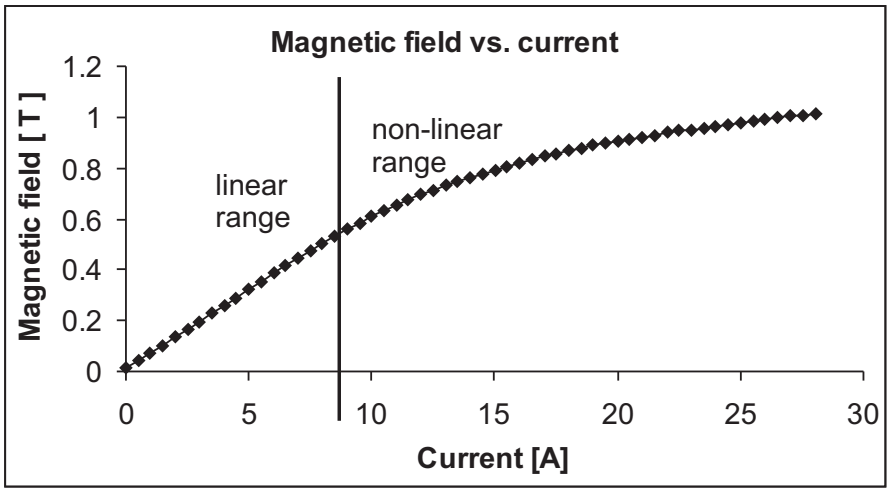


Figure 4.8: Linear and non-linear range of magnetic experiment

current can be detected, as shown in Figure 4.9. The error of the measured value

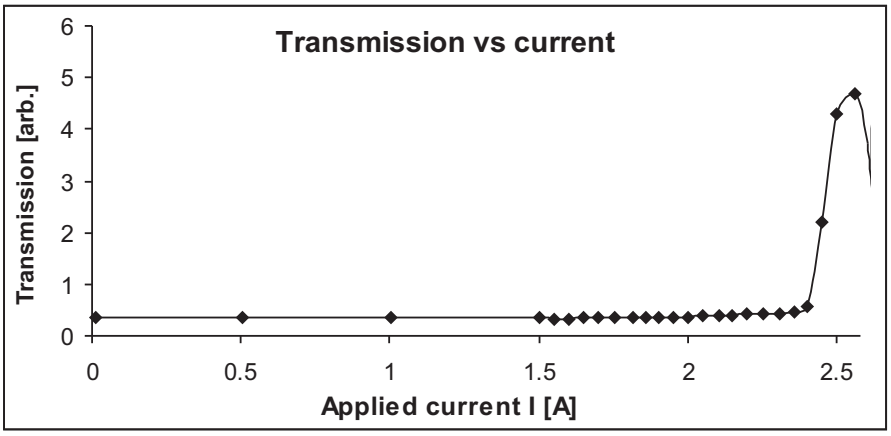


Figure 4.9: Optical measurement of the threshold current

for K_{22} is in the range of 20% because two threshold currents I_{11} and I_{22} have to be measured and K_{11} from the previous experiment is used to determine K_{22}. The threshold current I_{22} has a bigger error due to the guiding problem in twisted structures [6].

4.1.3 Measurement of $n_{\parallel}, n_{\perp}$

The most common method used to measure the refractive index of glass, liquids, and liquid crystals is the Abbé refractometer, first constructed by Ernst Abbé in 1869 [116, 117]. The Abbé refractometer is a standard equipment, very accurate (error within 2% for $n_{\parallel}$ and $n_{\perp}$), easy to use, needs just a few drops of liquid crystal materials, and it just takes 15 minutes to measure one material.

In the Abbé refractometer the liquid crystal sample is homeotropically aligned in a thin layer between two high index prisms, an illuminating prism and a refracting prism, as shown in Figure 4.10. The refracting prism is made of glass with a high re-

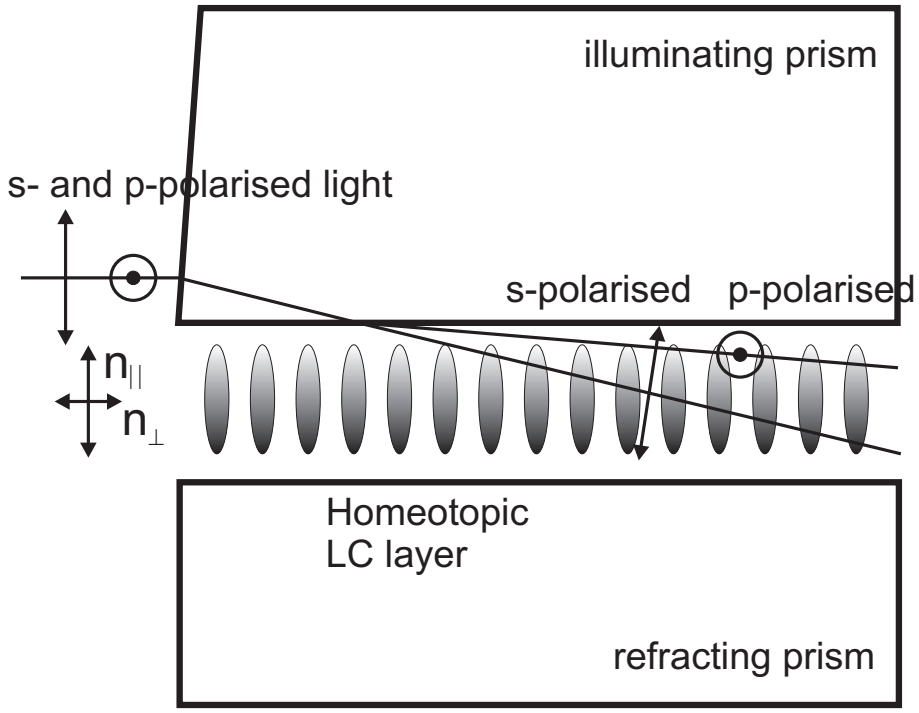


Figure 4.10: Abbe Refractometer

fractive index (e.g. 1.86) and the refractometer is designed to be used with samples having a refractive index smaller than that of the refracting prism. A monochromatic light source (e.g. $\lambda = 633nm$ or $\lambda = 543nm$) is projected through the refracting prism and the liquid crystal material. Light that travels parallel ($n_{\parallel}$) to the liquid

crystals has a different total reflection after leaving the refracting prism compared to light that is perpendicular ($n_\perp$). These total reflections can be observed and measured and the refractive parameter calculated using index tables of the equipment. The Abbé refractometer is temperature controlled and for the measurement of $n_\parallel$ it is very helpful to place a polariser between the light source and the Abbé refractometer to polarise the light parallel and observe the total reflection more clearly. The same is also helpful for the measurement of $n_\perp$, where the polariser is placed perpendicularly.

4.1.4 Measurement of nematic-isotropic transition temperature T_{NI}

All the elastic, dielectric and refractive properties are measured at room temperature (22°C). The measurements of the sum $(e_1 + e_3)$ and difference $(e_1 - e_3)$ of the flexoelectric coefficients e_1 and e_3 are also done at room temperature. But no measurements were carried out in this project to investigate the influence of temperature or order parameter S on flexoelectricity. To do so, it would have been necessary to modify all experiments to be able to change and define the temperature of the experiment. But this would have taken quite a lot of time and it was not a primary goal of this project. However, one simple way to get an easy and fast estimation of the order parameter S is to measure the nematic-isotropic transition temperature T_{NI} where the material is changing from the liquid crystal state into isotropic fluid. The temperature difference $\Delta T = (T_{NI} - T)$ is defined as the difference between the nematic-isotropic temperature T_{NI} and the room temperature (22°C). ΔT is an indirect and easy estimation of the order parameter S. If the temperature difference ΔT is small, which means that nematic-isotropic transition temperature T_{NI} is closer to the room temperature, the order parameter S is also smaller compared

to a material with a big ΔT. This method is not very accurate but it helps us to estimate the correlation between the order parameter S and flexoelectricity.

4.1.5 Error investigation

All our experiments to measure flexoelectricity are indirect methods, which means that the data recorded have to be fitted with a theoretical model. Therefore, it is necessary to supply the simulation with the values of the elastic, dielectric and refractive properties. These values are kept fixed during the fitting process of the data and therefore bring an error to the extracted flexoelectric coefficients. Table 4.1 shows the error for each physical parameter. The influence of the error of the elastic, dielectric and refractive properties are investigated directly in the fitting of the experimental data. This should show, which influence the errors have on fitting parameters like cell thickness, pretilt, cell orientation, and the extracted flexoelectric coefficients like the sum $(e_1 + e_3)$ or the difference $(e_1 - e_3)$.

Parameter	Error [%]
K_{11}	4 %
K_{22}	20 %
K_{33}	4 %
$n_{\parallel}$	2 %
$n_{\perp}$	2 %
$\epsilon_{\parallel}$	1 %
$\epsilon_{\perp}$	1 %

Table 4.1: Overview of experimental error for each physical parameter

4.2 Overview of materials

Being able to measure the elastic, dielectric, and refractive properties, different materials are investigated and the flexoelectric properties measured. The primary

interest was to investigate the correlation between flexoelectricity and the molecular structure, ions, elastic properties, molecular orientation, dielectric anisotropy $\Delta\epsilon$, and order parameter S. The correlation between chirality and flexoelectricity was not investigated in this project because Patrick Salter, who is a colleague from the Oxford liquid crystal group, worked on this topic. His finding showed that there is a negligiable correlation between chirality and flexoelectricity [118].

4.2.1 Molecular structure

It is thought that flexoelectricity is caused by shape anisotropy and therefore it is sensible to investigate the relationship between molecular structure and flexoelectricity. Three materials were used and they are referred to here as CB, PCH, and DE [119, 120, 121]. Each of the materials is a mixture made out of the 3/5/7 ho-

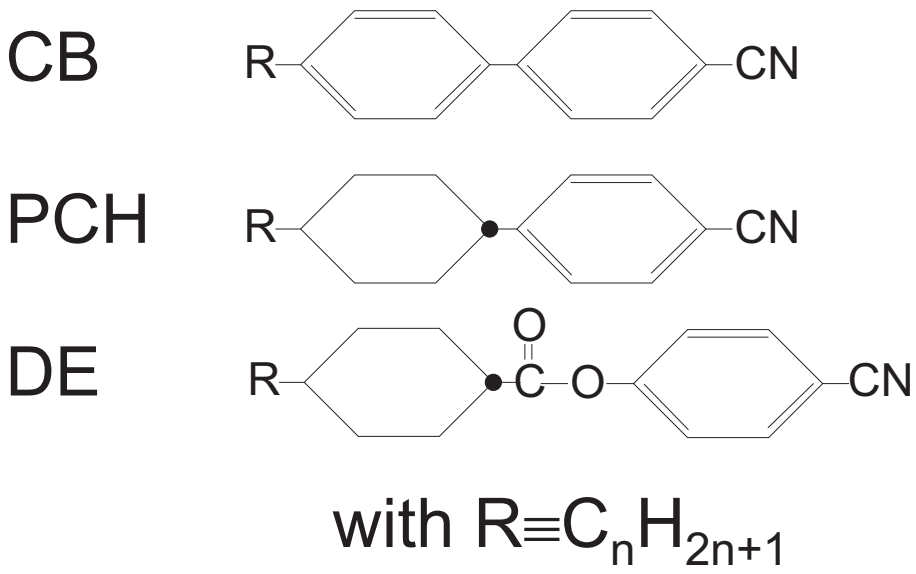


Figure 4.11: The three materials CB, PCH, and DE. Each mixture was made of 3/5/7 homogeneous with a ratio of 30%/40%/30% by weight.

mogeneous with a ratio of 30%/40%/30% by weight. These materials are similar except that one of the ring structures and the link between the two rings varies, as

shown in Figure 4.11. The systematic approach is a first step towards measuring and understanding the influence of molecular structure on flexoelectricity.

4.2.2 Non-Ionic materials

It is also thought that the flexoelectric effect might be partly or completely be influenced by ions [53]. This was investigated using the non-ionic materials TL216, MLC-7021-100, MLC-13900-100, and MLC-15900-100. The materials are TFT mixtures and they were provided by MERCK. The composition is a secret and unknown to us, but we know that the materials are non-ionic and used in commercial display. Our own measurements confirmed that the conductivity is about 1000 times smaller compared to the other materials and they can be classified as non-ionic.

4.2.3 Elastic Properties

To investigate the correlation between elastic properties and flexoelectricity, the two materials MixA and MixC were used. Both materials are mainly made out of 7CB. MixA is made out of 79% 7CB / 12% 80CB / 9% 5CT and has no smectic phase. MixC is made out of 75% 7CB / 16% 80CB / 9% 5CT, also slightly different to MixA, and has a nematic to smectic phase temperature of 7.5°C and a smectic to nematic phase temperature of 20.3°C. The small smectic phase of MixC makes this material very interesting because all measurements are done just above the smectic-nematic temperature and this has the consequence that all physical parameters of MixC are very similar to MixA and E7, except that the bend elastic coefficients K_{33}, which is around $50pN$, is very high. This should give us an insight into the correlation between elastic properties and flexoelectricity.

4.2.4 Molecular orientation

In general, the molecules try to group into couples and orientate anti-parallel to each other so that the positive charged part of one molecule is faced with the negative charged part of the other molecule and vice versa, as shown in Figure 4.12 a). However, this ordering might decrease flexoelectricity because the shape anisotropy

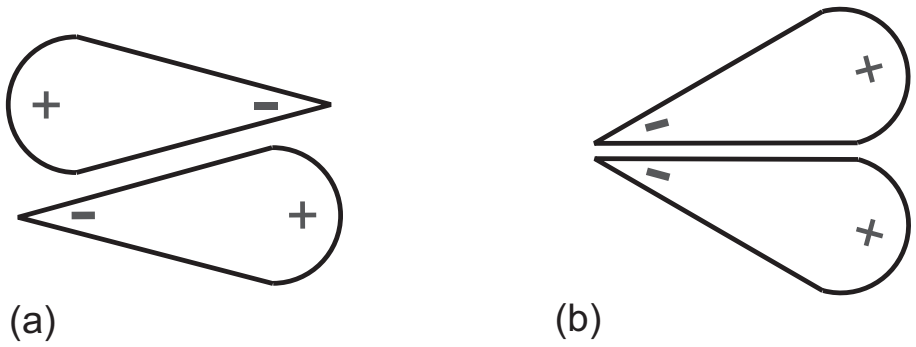


Figure 4.12: a) Anti-parallel orientation of molecules and b) Parallel orientation, which creates an additional splay distortion.

of the molecules are not creating as much distortion as they could if the molecules were orientated parallel to each other. This was investigated by mixing 30% and 50% of Me35 into E7. Me35 is a dialkyl nematic material which reduces the anti-parallel orientation and forces the molecules to orientate parallel to each other, as shown in Figure 4.12 b) [121]. The two mixtures are named here E7+30%Me35 and E7+50%Me35.

4.2.5 Dielectric anisotropy $\Delta\epsilon$

Because flexoelectricity is a coupling between reorientating the molecular dipoles and shape anisotropy, it is thought that the dielectric properties are correlated with flexoelectricity. To investigate this correlation between dielectric anisotropy $\Delta\epsilon$ and flexoelectricity, all measured materials are taken into account but additionally two materials with large dielectric anisotropy $\Delta\epsilon$ between 40 and 50 (MDA-02-2419 and

Materials B [84]) and one material with negative dielectric anisotropy $\Delta\epsilon$ of about -3.5 (MLC-7029) are investigated. These three materials were provided by MERCK and they are commercial materials. The structure of these materials is unknown. Materials B [84]) is used by the company ZBD Displays Ltd in the UK [87] in their zenithally bistable device.

4.2.6 Order Parameter S

It is thought that there is a correlation between flexoelectricity and the order parameter S, whereby the sum $(e_1 + e_3)$ goes approximately with S and the difference $(e_1 - e_3)$ goes approximately with S^2 [122]. To investigate these correlations, the measured temperature difference ΔT is used instead of the order parameter S. ΔT is an indirect and easy estimation of the order parameter S.

4.2.7 Overview of material's properties

The elastic, dielectric, and refractive properties of all investigated materials have been measured at room temperature (22°C) and the results are summarised in Table 4.2. The refractive indexes have been measured for a wavelength λ of $633nm$ (red) and $543nm$ (green) but only the data for the red wavelength is presented in Table 4.2.

Having a list of materials, which are used to investigate flexoelectricity, and being able to measure the physical properties of these materials, we are now in the position to develop and measure flexoelectricity. The knowledge of theory and modelling, which was presented in the previous chapter, and the knowledge of the physical properties of the selected materials, as presented in this chapter, is used in the next chapters, which present our new developed experiments to measure the sum (e_1+e_3) and the difference $(e_1 - e_3)$.

Material	K_{11} [pN]	K_{22} [pN]	K_{33} [pN]	$\epsilon_{\parallel}$	$\epsilon_{\perp}$	$\Delta\epsilon$	$n_{\parallel}$	$n_{\perp}$	Δn	T_{NI} [°C]	ΔT [°C]	Comment
E7	10.7	6.5	16.2	18.9	5.2	13.7	1.738	1.519	0.233	58	36	
E70A	10.0	5.8	10.4	15.8	5.4	10.4	1.682	1.517	0.166	60	38	
CB	6.5	4.1	9.5	19.6	6.4	13.2	1.724	1.522	0.202	35	13	molecular structure
PCH	8.6	5.6	16.9	17.1	4.9	12.2	1.608	1.488	0.120	52	30	molecular structure
DE	9.6	5.0	17.3	14.8	5.8	9.0	1.592	1.479	0.112	72	50	molecular structure
TL216	13.8	8.1	18.6	9.1	4.0	5.1	1.727	1.519	0.207	80	58	non-ionic
MLC-7021-100	10.5	6.1	12.0	14.2	3.7	10.5	1.599	1.487	0.112	81	59	non-ionic
MLC-13900-100	-	-	-	-	-	5.2	-	-	0.108	110	88	non-ionic
MLC-15900-100	-	-	-	-	-	10.1	-	-	0.091	74	52	non-ionic
MixA	12.9	8.5	18.6	16.2	4.6	11.6	1.725	1.515	0.210	66	44	elastic prop.
MixC	12.5	11.7	50.0	16.2	4.7	11.5	1.725	1.513	0.212	70	48	elastic prop.
E7+30%Me35	10.0	6.1	9.5	15.7	5.0	10.7	1.694	1.515	0.179	54	32	molecular orientation
E7+50%Me35	9.9	6.1	7.2	13.1	4.8	8.3	1.558	1.511	0.157	45	23	molecular orientation
MDA-02-2419	8.2	6.1	15.3	46.6	8.1	38.5	1.686	1.506	0.180	97	75	big $\Delta\epsilon$
Material B [84]	8.5	5.0	15.6	49.9	7.8	42.1	1.608	1.490	0.118	95	73	big $\Delta\epsilon$
MLC-7029	16.0	6.7	15.0	3.6	7.3	-3.7	1.611	1.487	0.124	95	73	negative $\Delta\epsilon$

Table 4.2: Overview of elastic, dielectric, and refractive properties measured at room temperature (22°C).

Chapter 5

TN cell to measure difference $(e_1 - e_3)$

5.1 Introduction

The most common structure to measure the difference $(e_1 - e_3)$ is the uniform lying helix (ULH) [43, 67, 68], as shown in Figure 5.1 a) and discussed in Chapter 2. Applying a dc voltage across the device causes the optical axis to rotate in the plane of the device by an angle ϕ (not illustrated in Fig. 5.1 a). This effect is known as the chiral flexoelectro-optic effect and is linear for small electric fields [68]. However the ULH structure is only stable for a few hours and a highly chiral material is necessary. It is difficult to create the ULH structure. Our new method to measure the difference $(e_1 - e_3)$ is based on the idea of the chiral flexoelectro-optic effect but uses a more practical and stable geometry. If we imagine cutting out a 90° rotation out of the lying helix structure as shown in Figure 5.1 a), the structure is twisted as in a TN structure. Using a TN cell with an in-plane applied field (Fig. 5.1 b) aligns the director parallel with the field (for positive $\Delta\epsilon$) to minimise the dielectric energy

and due to flexoelectricity, the director tilts out of plane [94, 123, 124]. The change in tilt is equal to the rotation of the optical axis in the ULH structure but the TN structure is stable and enables us to measure achiral and weakly chiral materials. The in-plane electric field can be realised by creating a gap in the ITO layer. Note that the dimensions shown in Figure 5.1 b) are misleading. The gap is about 500μm width and the thickness of the device about 10μm. Our new method is an indirect method, which means that the data has to be fitted using a theoretical model.

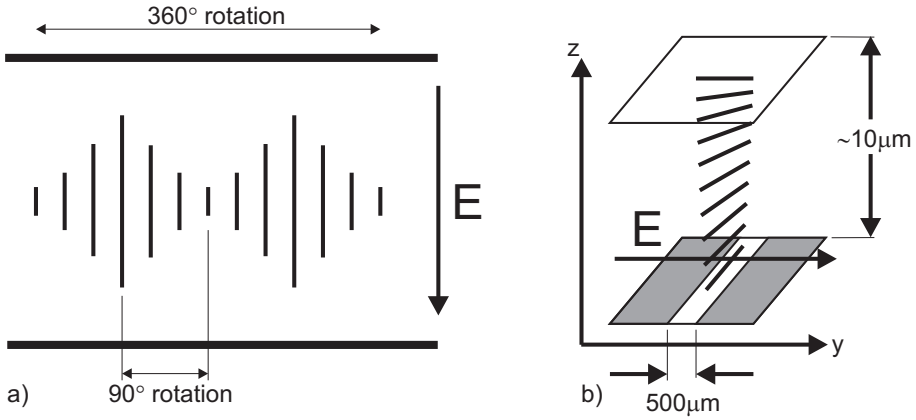


Figure 5.1: (a) 360° lying helix structure. (b) TN cell with in-plane electric field

5.2 Theory

The theoretical model to simulate the behaviour of the TN structure [94] and the in-plane field is based on the coordinate system shown in Figure 5.2, whereby the applied electric field is along the y axis and the director is calculated in a 1-dimensional model along the z axis (in 100 layers). The 1-D model includes the bulk energy L_B and calculates the transmission T through the device using the 4x4 Berreman optics, which enables us to determine the transmission at oblique incidence more accurately than with the 2x2 Jones optics. Flow is not included in the theory because only the static case is investigated. The surface energy is also not included in the model and

therefore the surface pretilt is kept fixed.

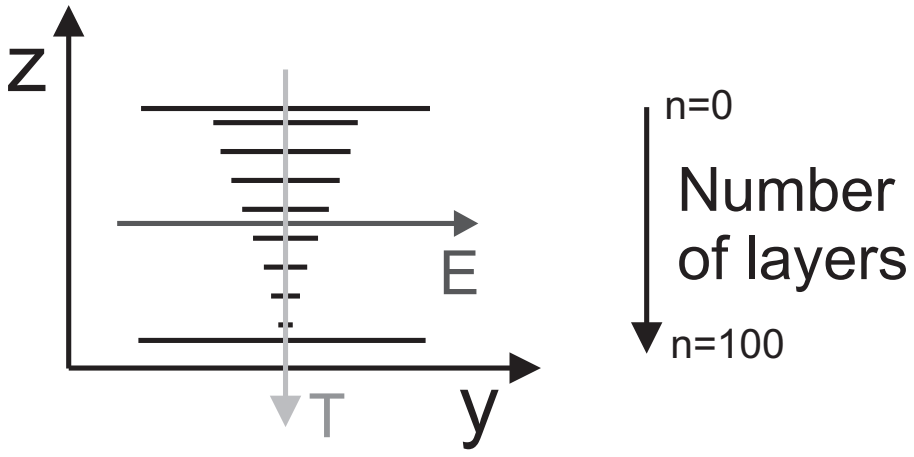


Figure 5.2: Coordinate system for 1-D model

As shown in Chapter 3, the bulk energy L_B (Eq. 3.33) is the sum of the the elastic energy w_d, flexoelectric energy w_f and dielectric energy w_e as

$$\begin{aligned} L_B &= w_d + w_f + w_e \\ L_B &= \frac{1}{2}K_{11}\left(\nabla\cdot\vec{n}\right)^2 + \frac{1}{2}K_{22}\left(\vec{n}\cdot\left(\nabla\times\vec{n}\right) - q\right)^2 + \frac{1}{2}K_{33}\left(\vec{n}\times\left(\nabla\times\vec{n}\right)\right)^2 \\ &\quad - \left(e_1\vec{n}\left(\nabla\cdot\vec{n}\right) + e_3\left(\nabla\times\vec{n}\right)\times\vec{n}\right)\cdot\vec{E} - \frac{1}{2}\vec{D}\cdot\vec{E}. \end{aligned} \tag{5.1}$$

The electric field $\vec{E}$ with its only component along the y direction is assumed to be constant and does not change along the z direction. This leads to a bulk energy L_B of

$$\begin{aligned} L_B = &\frac{1}{2}K_{11}n_z^{'2} + \frac{1}{2}K_{22}\left(n_y n_x^{'} - n_x n_y^{'} - q\right)^2 \\ &+\frac{1}{2}K_{33}\left(n_z^2 n_x^{'2} + n_z^2 n_y^{'2} + n_z^2 n_z^{'2}\right) \\ &-\left(e_1 n_y n_z^{'} + e_3 n_z n_y^{'}\right)E_y \\ &-\frac{1}{2}\epsilon_0\left(\Delta\epsilon n_y^2 + \epsilon_\perp\right)E_y^2, \end{aligned} \tag{5.2}$$

whereby the following calculations are used

$$\nabla = \begin{pmatrix} 0 \\ 0 \\ \frac{\partial}{\partial z} \end{pmatrix}, \vec{n} = \begin{pmatrix} n_x \\ n_y \\ n_z \end{pmatrix}, \vec{E} = \begin{pmatrix} 0 \\ E_y \\ 0 \end{pmatrix},$$

$$\nabla \cdot \vec{n} = \begin{pmatrix} 0 \\ 0 \\ \frac{\partial}{\partial z} \end{pmatrix} \cdot \begin{pmatrix} n_x \\ n_y \\ n_z \end{pmatrix} = \frac{\partial n_z}{\partial z} = n_z^{'},$$

$$\vec{n}\,(\nabla \cdot \vec{n}) = \begin{pmatrix} n_x \\ n_y \\ n_z \end{pmatrix} \cdot n_z^{'} = \begin{pmatrix} n_x n_z^{'} \\ n_y n_z^{'} \\ n_z n_z^{'} \end{pmatrix},$$

$$\vec{n} \cdot (\nabla \times \vec{n}) = \begin{vmatrix} n_x & n_y & n_z \\ 0 & 0 & \frac{\partial}{\partial z} \\ n_x & n_y & n_z \end{vmatrix} = n_y \frac{\partial n_x}{\partial z} - n_x \frac{\partial n_y}{\partial z} = n_y n_x^{'} - n_x n_y^{'},$$

$$(\nabla \times \vec{n}) \times \vec{n} = \left[\begin{pmatrix} 0 \\ 0 \\ \frac{\partial}{\partial z} \end{pmatrix} \times \begin{pmatrix} n_x \\ n_y \\ n_z \end{pmatrix} \right] \times \begin{pmatrix} n_x \\ n_y \\ n_z \end{pmatrix} = \begin{pmatrix} -n_y^{'} \\ n_x^{'} \\ 0 \end{pmatrix} \times \begin{pmatrix} n_x \\ n_y \\ n_z \end{pmatrix}$$

$$= \begin{pmatrix} n_z n_x^{'} \\ n_z n_y^{'} \\ -n_y n_y^{'} - n_x n_x^{'} \end{pmatrix} = \begin{pmatrix} n_z n_x^{'} \\ n_z n_y^{'} \\ n_z n_z^{'} \end{pmatrix},$$

$$(\vec{n} \times (\nabla \times \vec{n}))^2 = \begin{pmatrix} n_z n_x^{'} \\ n_z n_y^{'} \\ n_z n_z^{'} \end{pmatrix}^2 = n_z^2 n_x^{'2} + n_z^2 n_y^{'2} + n_z^2 n_z^{'2},$$

$$\vec{n}\,(\nabla \cdot \vec{n})\,\vec{E} = \begin{pmatrix} n_x n_z^{'} \\ n_y n_z^{'} \\ n_z n_z^{'} \end{pmatrix} \cdot \begin{pmatrix} 0 \\ E_y \\ 0 \end{pmatrix} = n_y n_z^{'} E_y,$$

$$((\nabla \times \vec{n}) \times \vec{n})\,\vec{E} = \begin{pmatrix} n_z n_x^{'} \\ n_z n_y^{'} \\ n_z n_z^{'} \end{pmatrix} \cdot \begin{pmatrix} 0 \\ E_y \\ 0 \end{pmatrix} = n_z n_y^{'} E_y,$$

$$\vec{D}\vec{E} = \epsilon_0 \left[\begin{pmatrix} \Delta\epsilon n_x^2 + \epsilon_\perp & \Delta\epsilon n_x n_y & \Delta\epsilon n_z n_x \\ \Delta\epsilon n_x n_y & \Delta\epsilon n_y^2 + \epsilon_\perp & \Delta\epsilon n_z n_y \\ \Delta\epsilon n_z n_x & \Delta\epsilon n_z n_y & \Delta\epsilon n_z^2 + \epsilon_\perp \end{pmatrix} \begin{pmatrix} 0 \\ E_y \\ 0 \end{pmatrix} \right] \begin{pmatrix} 0 \\ E_y \\ 0 \end{pmatrix}$$

$$= \epsilon_0 \begin{pmatrix} \Delta\epsilon n_x n_y E_y \\ \left(\Delta\epsilon n_y^2 + \epsilon_\perp\right) E_y \\ \Delta\epsilon n_z n_y E_y \end{pmatrix} \cdot \begin{pmatrix} 0 \\ E_y \\ 0 \end{pmatrix} = \epsilon_0 \left(\Delta\epsilon n_y^2 + \epsilon_\perp\right) E_y^2.$$

The general Euler-Lagrange equation (Eq. 3.10) simplifies for the 1-D model and leads to a molecular field $\vec{h}$ of

$$\begin{aligned} h_x &= \frac{\partial}{\partial z}\left(\frac{\partial L_B}{\partial n_x^{'}}\right) - \frac{\partial L_B}{\partial n_x}, \\ h_y &= \frac{\partial}{\partial z}\left(\frac{\partial L_B}{\partial n_y^{'}}\right) - \frac{\partial L_B}{\partial n_y}, \\ h_z &= \frac{\partial}{\partial z}\left(\frac{\partial L_B}{\partial n_z^{'}}\right) - \frac{\partial L_B}{\partial n_z}, \end{aligned} \tag{5.3}$$

and the final solution of the the molecular field $\vec{h}$ is

$$\begin{aligned} h_x = \;& K_{22}\left(n_y^2 n_x^{''} - n_x n_y n_y^{''} + 2 n_y n_x^{'} n_y^{'} - 2 n_x n_y^{'2} - 2 q n_y^{'}\right) \\ & + K_{33}\left(2 n_z n_x^{'} n_z^{'} + n_z^2 n_x^{''}\right), \\ h_y = \;& K_{22}\left(n_x^2 n_y^{''} - n_x n_y n_x^{''} + 2 n_x n_x^{'} n_y^{'} - 2 n_y n_x^{'2} + 2 q n_x^{'}\right) \\ & + K_{33}\left(2 n_z n_y^{'} n_z^{'} + n_z^2 n_y^{''}\right) \\ & + \left(e_1 - e_3\right) n_z^{'} E_y + \epsilon_0 \Delta\epsilon n_y E_y^2 \\ h_z = \;& K_{11} n_z^{''} + K_{33} n_z\left(n_z n_z^{''} - n_x^{'2} - n_y^{'2} + n_z^{'2}\right) \\ & - \left(e_1 - e_3\right) n_y^{'} E_y. \end{aligned} \tag{5.4}$$

whereby the following calculations are used

$$\begin{aligned}
\frac{\partial L_B}{\partial n_x'} &= K_{22}\left({n_y}^2 {n_x}' - n_y {n_y}' n_x - n_y q\right) + K_{33} {n_z}^2 {n_x}', \\
\frac{\partial}{\partial z}\left(\frac{\partial L_B}{\partial n_x'}\right) &= K_{22}\left({n_y}^2 {n_x}'' - {n_y}'^2 n_x - {n_y}' q - n_y {n_y}'' n_x + {n_y}' {n_x}' n_y\right) \\
&\quad + K_{33}\left(2 n_z {n_x}' {n_z}' + {n_z}^2 {n_x}''\right), \\
\frac{\partial L_B}{\partial n_x} &= K_{22}\left(-{n_y}' {n_x}' n_y + {n_y}'^2 n_x + {n_y}' q\right), \\
\frac{\partial L_B}{\partial n_y'} &= K_{22}\left(-n_x {n_x}' n_y + {n_x}^2 {n_y}' + n_x q\right) + K_{33} {n_z}^2 {n_y}' - e_3 n_z E_y, \\
\frac{\partial}{\partial z}\left(\frac{\partial L_B}{\partial n_y'}\right) &= K_{22}\left(-n_x {n_x}'' n_y + {n_x}' {n_y}' n_x + {n_x}' q + {n_x}^2 {n_y}'' - {n_x}'^2 n_y\right) \\
&\quad + K_{33}\left(2 n_z {n_y}' {n_z}' + {n_z}^2 {n_y}''\right) - e_3 {n_z}' E_y, \\
\frac{\partial L_B}{\partial n_y} &= K_{22}\left({n_x}'^2 n_y - {n_x}' {n_y}' n_x - {n_x}' q\right) - e_1 {n_z}' E_y - \epsilon_0 \Delta\epsilon n_y {E_y}^2, \\
\frac{\partial L_B}{\partial n_z'} &= K_{11} {n_z}' + K_{33} {n_z}^2 {n_z}' - e_1 n_y E_y, \\
\frac{\partial}{\partial z}\left(\frac{\partial L_B}{\partial n_z'}\right) &= K_{11} {n_z}'' + K_{33}\left({n_z}^2 {n_z}'' + 2 n_z {n_z}'^2\right) - e_1 {n_y}' E_y, \\
\frac{\partial L_B}{\partial n_z} &= K_{33}\left(n_z {n_z}'^2 + n_z {n_x}'^2 + n_z {n_y}'^2\right) - e_3 {n_y}' E_y.
\end{aligned}$$

As shown in Equation 5.4, the flexoelectric effect term is $(e_1 - e_3)E_y$ and depends on the difference $(e_1 - e_3)$ and on the applied electric field E_y. It should be noted that the sign of the applied electric field is important for the flexoelectric effect. The dielectric effect goes with E_y^2 and doesn't depend on the sign of the applied field.

In conclusion, the theoretical model calculates the director profile in the bulk for the static case with fixed surface conditions. The optics are calculated using 4x4 Berreman method. Now it is possible to simulate and fit the data from the experiment.

5.3 Experiment

5.3.1 Electric field

Our new experiment [94, 123, 124] uses a TN-cell with an in-plane applied electric field. The cell thickness is about 10μm and the electrode-gap for the in-plane field is 500μm. This gives an aspect ratio of 50:1 and a homogeneous electric field can be assumed in the middle of the electrode-gap as shown in Figure 5.3.

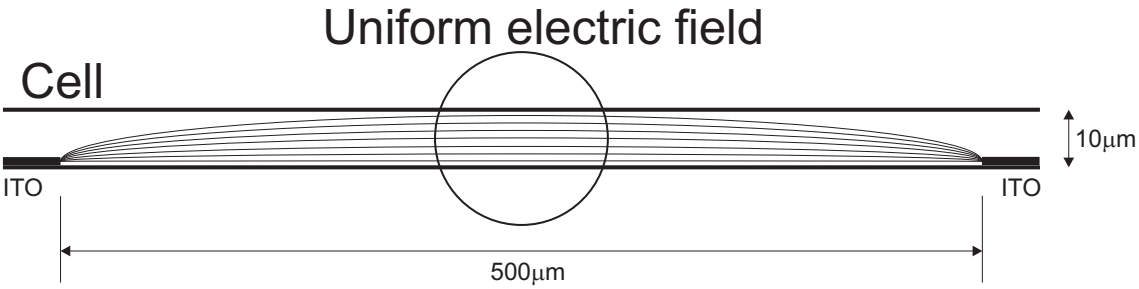


Figure 5.3: Uniform electric field in middle of 500μm electrode gap

Due to the dielectric coupling of the material (positive dielectric anisotropy) with the electric field, the director twists within the plane of the device in order to align with the applied field as shown in Figure 5.4 a). The twist is independent of the sign

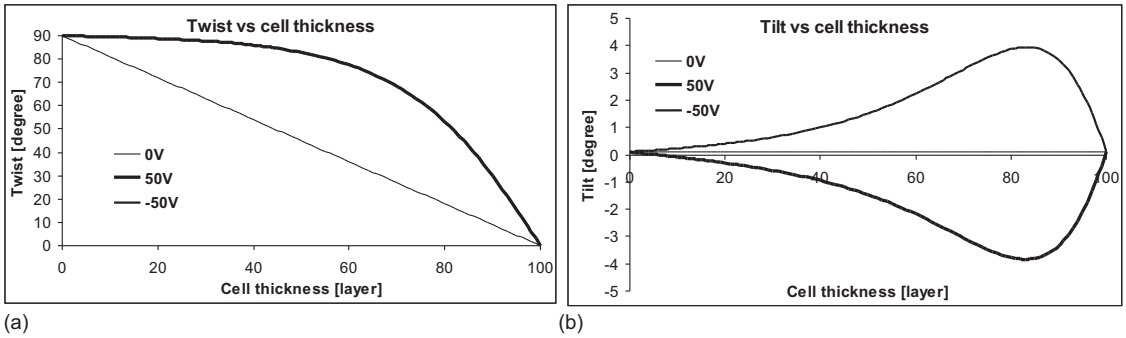


Figure 5.4: (a) Twist director profile and (b) tilt director profile across the cell.

of the applied field. This can also be shown by Equation 5.4, where the dielectric energy goes with E_y^2. However, as a result of the additional flexoelectric coupling,

the director also tilts out of plane. This tilt is in the range of a few degrees, as shown in Figure 5.4 b), and the direction of the tilt depends on the sign of the applied electric field and the sign of the difference $(e_1 - e_3)$. Knowing the sign of the applied field, it is also possible to determine the sign of the difference of the flexoelectric coefficients.

5.3.2 Experimental set-up

The change in director tilt angle is observed optically using a laser beam and by measuring the change of transmission between crossed polarisers within the uniform field region. The laser beam is focused down to a diameter of around 100μm and aligned in the middle of the electrode-gap. Measuring the transmission at normal incidence shows only a small optical response, which is identical for a positive and negative electric field because of the symmetry in the director tilt, as shown in Figure 5.5 a). However, using oblique incidence (e.g. 45°) gives a larger and asymmetric response, because for one sign of the electric field the director tilts toward the direction of incidence, whereas for the other sign the director tilts away from it (Fig. 5.5 b)). The experiment was further improved using two laser beams at oblique incidence, one at 45° and the other one at −45° (Fig. 5.5 c)). Using two laser beams detects any asymmetry in the data due to pretilt in the device and improves the accuracy of the results.

The experiment uses a green laser with a wavelength of λ=532nm. The laser beam is divided by a beam splitter and both components are reflected by mirrors and focused by lenses into a measurement point where the device is mounted, as shown in Figure 5.6. Both laser beams pass through p-polarisers before travelling through the device. The scaling and normalisation of the data is done by using beam splitters, one for each laser beam. The first component passes through an s-analyser (crossed

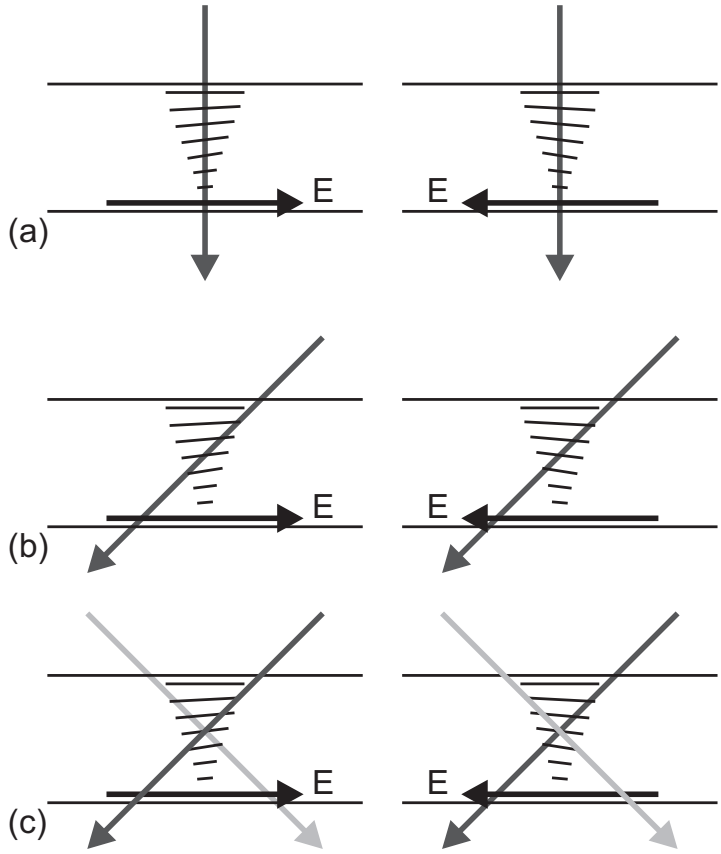


Figure 5.5: a) Laser beam at a) normal incidence, b) at oblique incidence, and c) two laser beams at oblique incidence

polariser) before reaching the detector and the other one through an p-analyser (parallel polariser). Before a measurement is done, the offset of all four detectors and the ratio between the crossed and parallel components for both beam splitters are measured. After taking the raw data, the detector offset is subtracted and the crossed and parallel signals are scaled with the ratio measured. Now the sum of the crossed and parallel voltage signal correspondent to a transmission of 100%. To normalise the data, the crossed and parallel data are now divided by the sum which gives a transmission between 0 and 1. Only the normalised data for the crossed

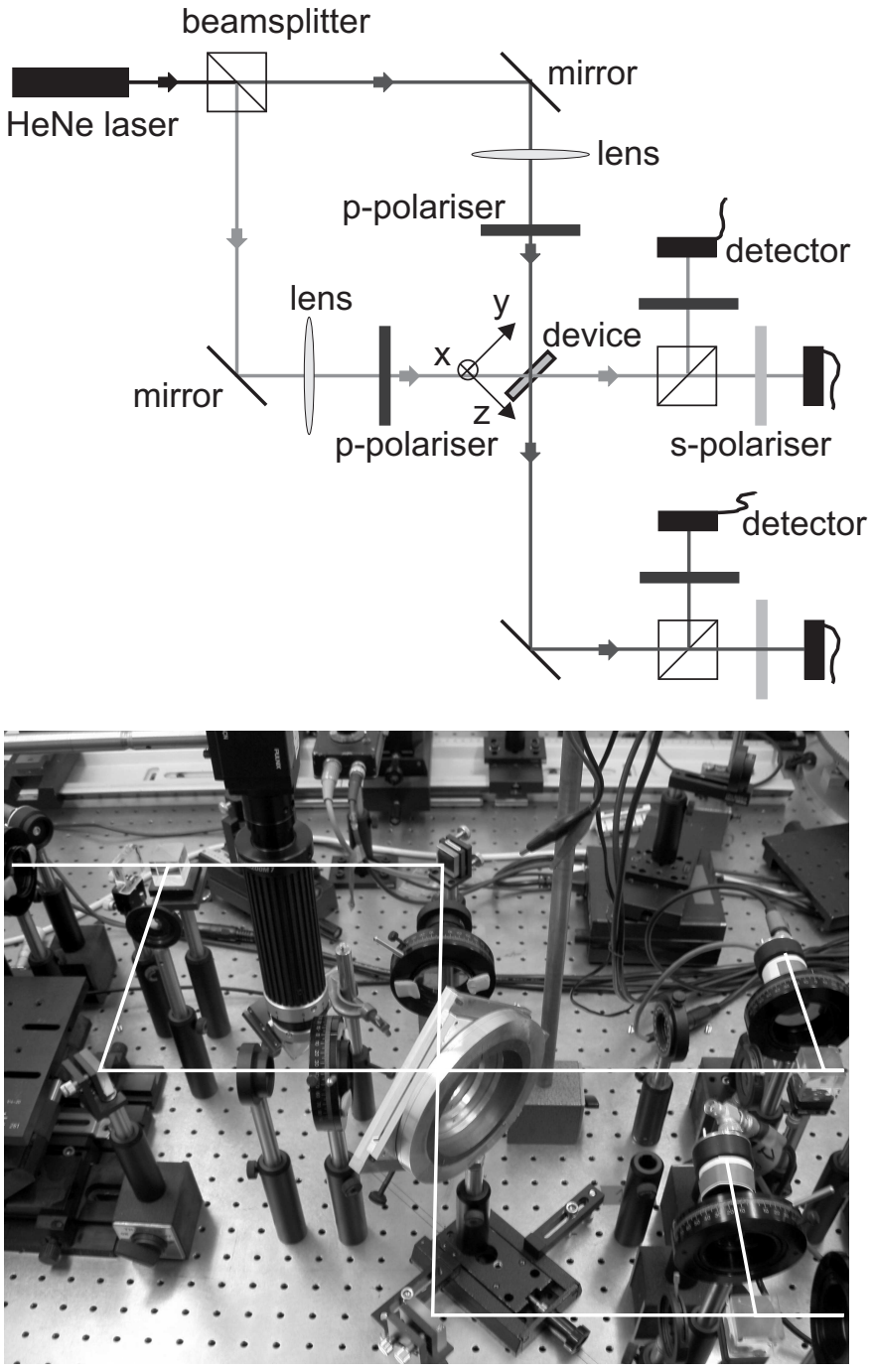


Figure 5.6: Experimental set-up where two laser beams pass through device at oblique incidence

components are used in the fitting process to extract the flexoelectric difference $(e_1 - e_3)$.

In the experiment TN cells were used, as shown in Figure 5.7. The TN cell were made in our own clean room. One glass plate was without a ITO layer. The other glass plate had a ITO layer, in which a electrode gap of 500μm was etched. Both glass plates became a planar alignment layer and they were assembled 90° to each other to realise the TN structure. After the assembly, the cell thickness was measured at different areas of the cell because the glass plates were never perfect parallel to each other and the cell thickness varied along the electrode gap, where the measurement was done. After measuring the cell thickness, the cell was filled with liquid crystal material, wires were soldered to both electrodes and the cell was sealed with glue.

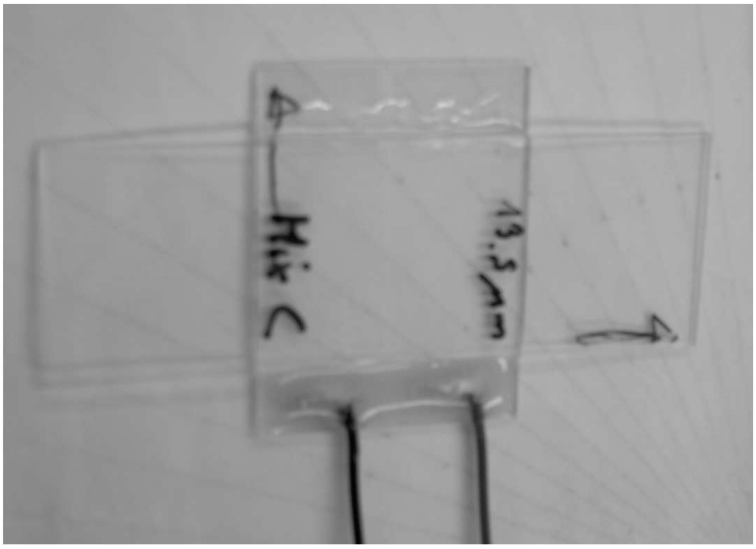
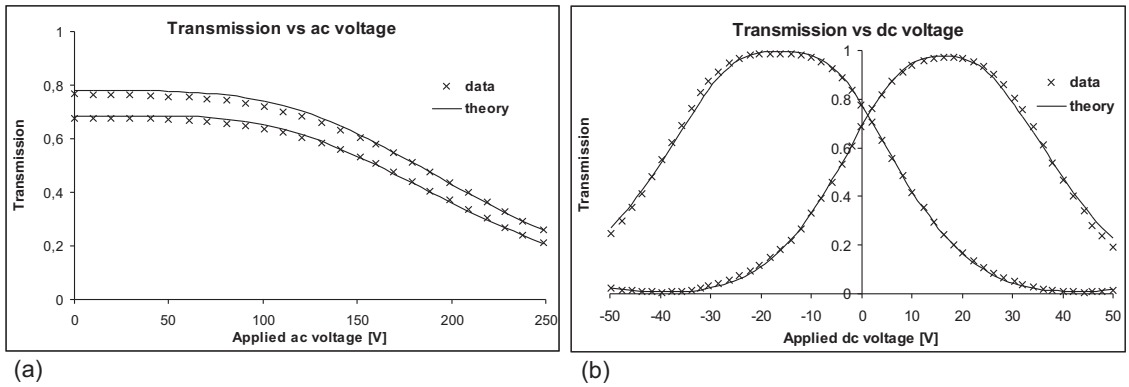


Figure 5.7: Example of a TN cell, which are used in the experiment

5.3.3 Data

Two sets of data are taken during one measurement (at room temperature 22°C), ac voltage data and quasi-dc voltage. First, an ac voltage with a frequency of f=1kHz and an amplitude between 0V and 250V is applied. The transmissions for both laser beams at oblique incidence (45° and −45°) are measured and normalised, as

shown in Figure 5.8 a). The crosses show the experimental data and the solid line



(a) (b)

Figure 5.8: Example of experimental data (crosses) and fitting (solid lines) for E7. (a) ac data and (b) dc data

the fitting. The ac data is used to determine the cell thickness and pretilt, because with the high frequency applied voltage (i.e. the 1kHz signal), flexoelectricity and ions can be neglected (the distortion due to flexoelectricity is only present at lower frequencies, and ions have just a small effect at a high frequency). The thickness and pre-tilt parameters are then kept fixed and used in the fitting of the quasi-dc data to find the difference $(e_1 - e_3)$. The quasi-dc voltage is applied to the device with a voltage amplitude between 0V and 50V (Fig. 5.8 b)). Again, crosses indicate the experimental data and the solid line the fitting. The example shown in Figure 5.8 shows data and fitting for E7, giving an idea of the data taken and the quality of the fit. The agreement between the data and fit is between 95% and 98% and can be seen as very good. This is also the case for the fitted data, which will be presented in the section 5.4.

The quasi-dc voltage is a low frequency square wave signal with a frequency of f=0.2Hz. This leads to a time period of t=5s for a whole square wave and 2.5s for the positive and negative pulses. This long positive and negative pulse can be treated like a dc voltage, but is short enough to minimise the problem with ions. Figure 5.9 shows an applied square wave voltage and the dynamic voltage signal from the two

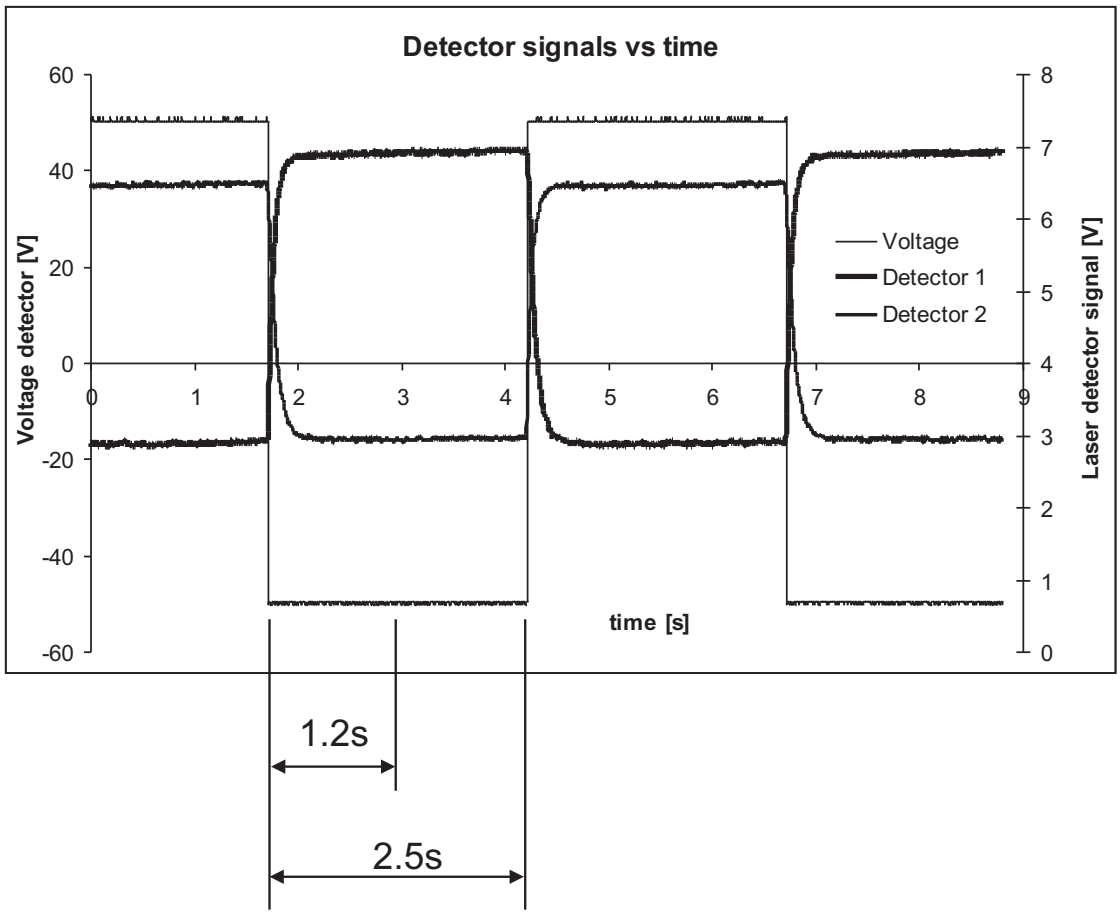


Figure 5.9: Square wave applied voltage with transmission signal from both crossed detectors

crossed detector signals, which represent the transmission for the two oblique laser beams. After the voltage is reversed every 2.5s, the transmission changes strongly. This is expected because the director tilts out of plane due to flexoelectricity and the direction of the tilt depends on the sign of the applied voltage. If there was no flexoelectricity, the signal for a positive and negative pulse would be almost the same. The reorientation of the tilt needs time and it is in the order of about 1s. After about 1.2s, the signal is in an equilibrium state before ions show an effect on the transmission. Without ions, the transmission would be steady (this was observed with the non-ionic materials TL216 and MLC-7021-100). To minimise the effect of ions, the data was always taken at 1.2s after the sign of the applied

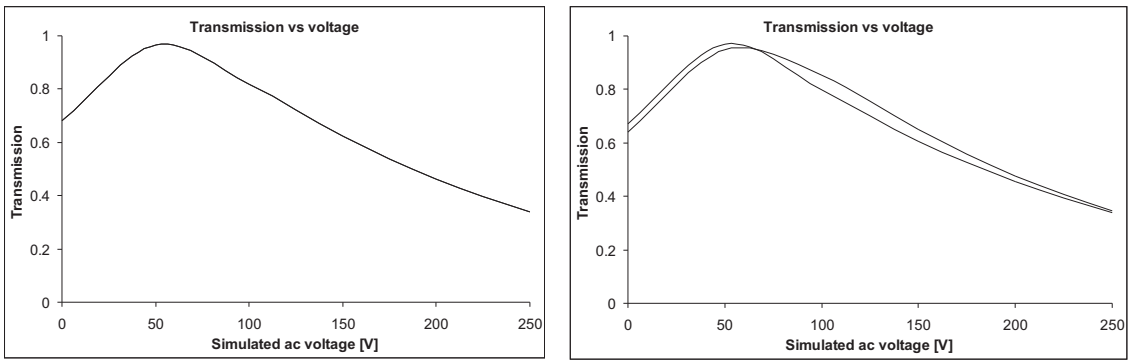
voltage was changed and before ions kicked in. This technique worked very well and it ensured that the data was always taken at the same time for the different applied voltages. Applying voltages up to 50V in the quasi-dc case means that the electric field is roughly E=50V/500μm=0.1V/μm. This electric field is very small compared to devices where electric fields are applied across the device, where they are in the range between 1.0V/μm and 5.0V/μm. The maximal electric field of about 0.1V/μm, which is big enough to show the flexoelectric effect but small enough to avoid problems with ions, worked well.

5.3.4 Automation of experiment

To optimise the measurements and to save time and labour, the whole experiment was fully automated. This enabled us to measure one set of ac and quasi-dc data in 30 minutes. To improve the reliability of the result for $(e_1 - e_3)$, each material was measured at least six times at different positions of the cell, taking about 3 hours and giving a good average value and an idea of the error margin. The automation was realised by connecting the waveform generator to the PC via GPIB. The four detectors are connected to an oscilloscope which is also connected to the PC via GPIB. A C-Program controls and communicates with the waveform generator and oscilloscope. The program sets the voltage of the waveform generator, which is applied to the device, and records the transmission from the oscilloscopes. The automation has the big advantage that in the quasi-dc case, the data is always taken at 1.2s. After taking a set of ac and quasi-dc data, the data is saved in two files. One file contains all raw data. The second file has the scaled and normalised data which can be directly used in the fitting.

5.3.5 Pretilt

Investigating the ac and dc data (Fig. 5.8) more closely, it can be seen that both laser beams at 0V show an asymmetry which occurs due to a pretilt in the device used. This can be checked using the theory and simulating the ac case for no pretilt and 5° pretilt. The simulation shows that if there is no pretilt, as shown in Figure 5.10 a), the optical response of both leaser beams are identically and that there is no asymmetry at 0V. If there is a pretilt of 5°, as shown in Figure 5.10 b), the optical response of both laser beams are different and an asymmetry at 0V can be seen.

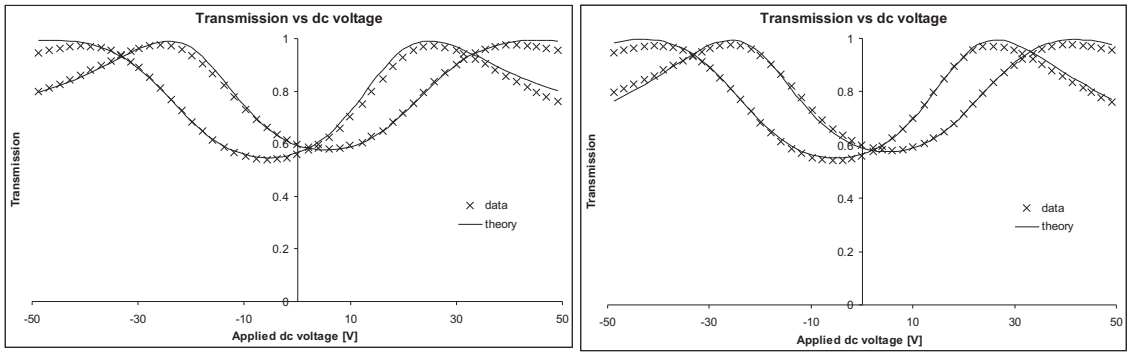


(a) no pretilt (b) 5° pretilt

Figure 5.10: Simulation of ac data for (a) no pretilt and (b) 5° pretilt

5.3.6 Thickness degeneracity

The first measurements were done without taking the ac data. The cell thickness, pretilt and flexoelectric difference $(e_1 - e_3)$ were determined from the quasi-dc data. However, this caused a big problem with thickness degeneracy, whereby the same quasi-dc data could be fitted very well with two different thicknesses, as shown in Figure 5.11. This resulted in different vales for $(e_1 - e_3)$, e.g. in the first case a thickness of d=12.1μm gave a $(e_1 - e_3)$=13.2 pC/m and in the second case a d=13.3μm gave a $(e_1 - e_3)$=9.2 pC/m for E7. The devices used had a thickness



(a) d=12.1μm and (e_1-e_3)=13.2 pC/m (b) d=13.3μm and (e_1-e_3)=9.3 pC/m

Figure 5.11: Quasi-dc data for E7 where two different thickness fit very well the data but give different results for $(e_1 - e_3)$

between 11μm and 14μm, measured before filling, which should help to narrow down the right thickness. However, due to the production process and due to capillary forces during the filling process, the two glass substrates might be pulled together, thus changing the thickness. This uncertainty in thickness led to the wrong value being published in [94] for E7 of $(e_1 - e_3)$=9.2 pC/m.

However, since the ac data was also measured, the problem with thickness degeneracity could be avoided and eliminated. Figure 5.12 shows clearly that for the two cases of d=12.1μm and d=13.3μm, the ac simulation (lines) looks very different and that only the thickness of d=12.1μm fits the data (crosses). The ac data in this case was taken between 0V and 250V in 50V steps. As mentioned before, the ac data are used to determine the cell thickness and pretilt of the device. These two parameters were kept fixed in the fitting process of the quasi-dc data, which decreased the number of parameters in the fitting of the flexoelectric difference $(e_1 - e_3)$. Using the ac and quasi-dc data was a big step forward and improvement, which made the whole method more stable, reliable and accurate. The new and more correct value for E7 will be published in [123] as $(e_1 - e_3)$=(12.2±1.0) pC/m .

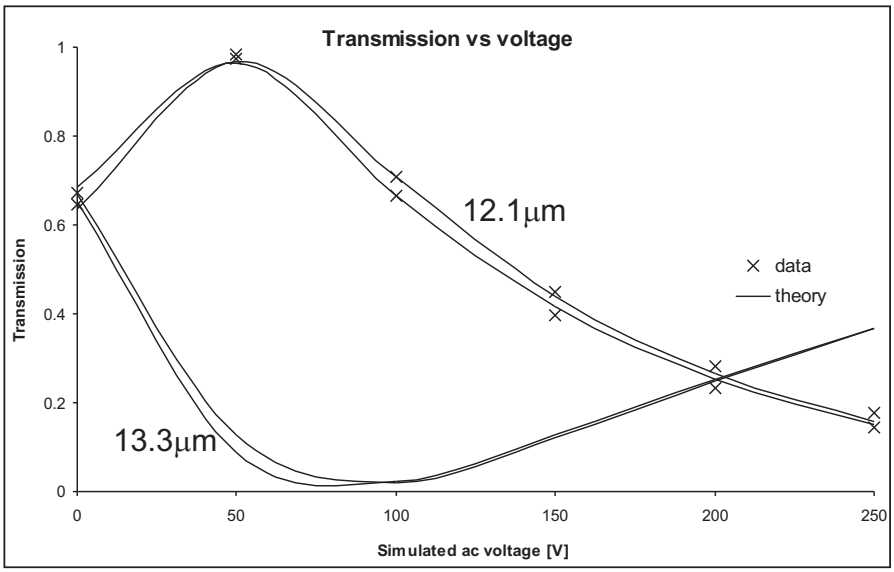


Figure 5.12: Simulation of ac data for d=12.1μm and d=13.3μm

5.3.7 Sign

In determining the value of $(e_1 - e_3)$ using the experiment described here it is important to take great care over the sign. This can be understood if we consider the standard equation for the small angle approximation to tilt in the chiral flexoelectro-optic effect [125]. This can be written as:

$$\phi \approx \frac{(e_1 - e_3)}{(K_{11} + K_{33})q} E, \tag{5.5}$$

where ϕ is the induced tilt, E is the applied electric field, q is the chiral pitch wavenumber, and K_{11} and K_{33} are the splay and bend elastic constants. It can be seen that the sign of q is important in determining whether ϕ is of the same or opposite sign as E. Although our experiment does not directly use chirality, the handedness of the TN structure which forms in the device leads to a similar effect to the sign of q. For an undoped material the TN structure can form with either a positive or a negative quarter-pitch, which dictates the sign of tilt induced by our

in-plane field, which in turn determines the sign of the value of $(e_1 - e_3)$ deduced. Therefore, we need to ensure that the handedness of the TN structure is known. To do this, firstly the devices are checked before being placed in the experiment to ensure that the region under investigation is a mono-domain. Subsequently, during the fitting procedure, it is then clearly established which hand is formed, because only the right sign of the quarter-pitch (domain) gives a fit for the ac and quasi-dc data. This can be illustrated by Figure 5.13, where dc data is fitted with a domain of "1" and "-1". Only the right domain gives a fit. In this example the domain "1" gives a good fit.

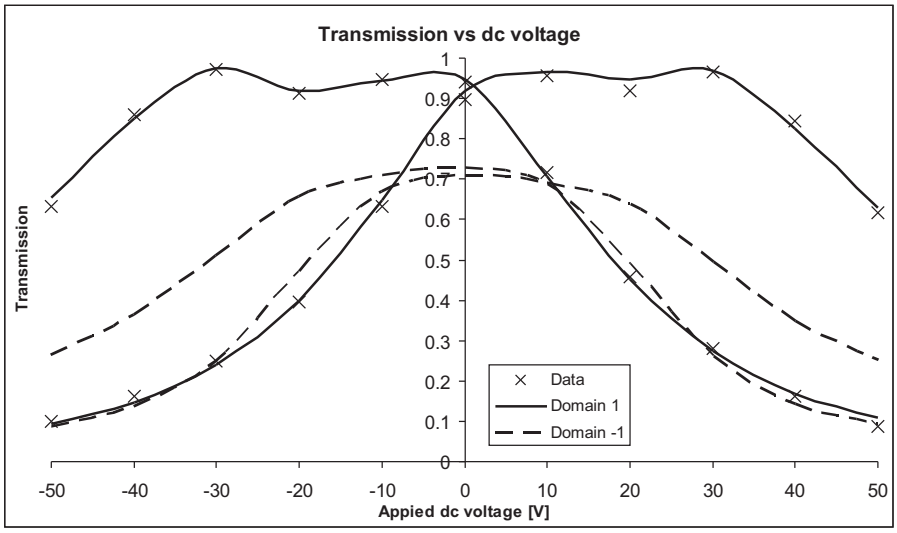


Figure 5.13: Simulation of dc data with a domain of "1" and "-1"

5.3.8 Ions

Although when applying an ac voltage with f=1kHz, the electric field oscillates fast enough for the ions to be neglected, this is not the case for the low frequency square wave used for the quasi-dc measurements, where the ions will have time to drift. There are in fact two possible effects involved, one being drift of ions already

present in the liquid crystal materials and the other being injection of ions from the electrode edges. Combinations of these two effects can lead to field enhancement and/or partial cancellation. Therefore, for a given applied voltage, the electric field at the point of measurement is difficult to determine. To deal with this problem, a variable scaling factor α between the applied voltage and the electric field is introduced in the simulation: $E{=}\alpha V/g$, where g is the electrode gap. Ignoring the permittivity difference between the LC layer compared with the surrounding glass, the scaling factor in theory is $2/\pi{=}0.64$ at the centre of the gap. However, because the permittivity of LCs is generally higher than the glass, this concentrates the electric field and so even without ionic effects, the values can be higher. Fitting the ac data, the scaling factor for the electric field should be slightly bigger than 0.64. When fitting the quasi-dc data, the scaling factor can be significantly different from 0.64 because of the additional electric field effects created by the ions. However, reliable results can still be obtained because the dielectric behaviour is well established. Because the response has components due to both dielectric and flexoelectric effects, the internal field is established by the dielectric coupling. This can perhaps be most clearly understood if we consider the case when there is no flexoelectricity, and only twist distortion is caused by the dielectric interaction. In that case, the general behaviour for the dc data would be similar to that for the ac data but with a different scaling factor due to the influence of ions. This would, therefore, establish the scaling factor for the dc case. However, when flexoelectricity is present, the fact that the coupling to the flexoelectric terms principally induces tilt means that dielectrically induced twist distortion still determines the internal field, and consequently the scaling factor. Therefore, when fitting the data, we can have some confidence that the correct internal fields are established.

During the fitting of the quasi-dc data it was observed that changing the dc-scaling factor, the whole fitting curve is being stretched along the the x-axis, the voltage

axis. Changing the flexoelectric difference ($e_1 - e_3$), changes the whole fitting curve in the y-axis, the transmission axis. It can be clearly seen, that these two parameters have different influences on the fitting curve and even if the dc-scaling factor might be not perfectly correct, this does not influence the parameter for the flexoelectric difference ($e_1 - e_3$).

5.3.9 Automation of fitting

At both the ac and quasi-dc fits, the elastic (K_{11}, K_{22} and K_{33}), dielectric ($\epsilon_\perp$, $\epsilon_\parallel$ and $\Delta\epsilon$) and optical ($n_\perp$, $n_\parallel$ and Δn) parameters were kept fixed with the values described in Chapter 4.2.7. The ac data is fitted with the three parameters of cell thickness, pretilt, and ac-scaling factor. During the fitting of the quasi-dc data, the cell thickness and pretilt from the ac data are used and kept fixed. This leads to a two parameter fit of the quasi-dc data with the dc-scaling factor and flexoelectric difference ($e_1 - e_3$). The theory used in the model contained the bulk torque with fixed surfaces and no flow. The optical response was determined using the 4x4 Berreman matrix method [126, 127]. As shown in the experiment, we automated the set-up which enabled us to take 6 data sets of one material in about 3 hours. To be able to keep up with the fitting of the data, the whole fitting process was also optimised and automated which enabled us to fit one data set in about 24 hours. Using a computer with multicore processors, it was possible to fit all six data sets in parallel on different processors in 24 hours. This means that it takes between 1 and 2 days to measure and fit one material, which is very efficient and allows us to investigate a bigger number of materials. The automated fitting was done using a multi step system and the commercial software NAG [128]. First the transmission at 0V, which is the same for the ac and quasi-dc data, was used to determine possible cell thickness and pretilt combinations. These possible thicknesses were tested with

the ac data with a guessed ac-scaling of 0.70. The best thickness-pretilt combination and an ac-scaling of 0.7 are used as the starting condition in the fit of the ac data. Using NAG, the best cell thickness, pretilt and ac-scaling can be found. The NAG routine works on the principal of calculating the fit for each parameter using a small positive and negative delta of the parameter. Combining all the deltas to a vector, the next calculation point can be found. The new set of parameters is the starting point for the next cycle. The cycles are repeated until the difference between the old and the new minima is smaller than a tolerance set by the user. The best cell thickness parameter and pretilt are than used as fixed parameters in the fitting of the quasi-dc data, where NAG works in the same way as before but now with the two parameters dc-scaling and flexoelectric difference ($e_1 - e_3$). However, in most cases this automated fitting procedure delivers good results but the user must always check them to make sure that the results are sensible and in agreement with the six data sets.

5.3.10 Error investigation

During the automated fitting process the elastic (K_{11}, K_{22} and K_{33}), dielectric ($\epsilon_\perp$ and $\epsilon_\parallel$) and optical ($n_\perp$ and $n_\parallel$) parameters were kept fixed with the values described in Chapter 4.2.7. The errors for each parameter are shown in Table 5.1. To investigate the influence of the errors on the fitting results and therefore on the flexoelectric difference ($e_1 - e_3$), two automated fittings were used. The first fitting used the values of the physical parameter of the original E7 as they were measured and described in Chapter 4. The second fitting used E7 values with the error included in each parameter, where the original E7 values were reduced by the error values. The two parameter sets are presented in Table 5.1.

Comparing the two fitting results, with the original E7 values and the E7 values

Parameter	Error [%]	Original E7 [pN]	E7 with error [pN]	Reduction [%]
K_{11}	4 %	10.7	10.272	-4 %
K_{22}	20 %	6.5	5.2	-20 %
K_{33}	4 %	16.2	15.552	-4 %
$n_{\parallel}$	2 %	18.9	18.711	-2 %
$n_{\perp}$	2 %	5.2	5.148	-2 %
$\epsilon_{\parallel}$	1 %	1.7607	1.725489	-1 %
$\epsilon_{\perp}$	1 %	1.5273	1.496754	-1 %

Table 5.1: Overview of experimental error for each physical parameter; values for original E7 and values for E7 with included errors

with the error included, for the cell thickness, pretilt, ac scaling, dc scaling and flexoelectric difference ($e_1 - e_3$), as shown in Table 5.2, it can be seen, that all fitting parameters are influenced by the errors of the elastic, dielectric and optical parameters. In this example, the cell thickness changed by 2.4%, the pretilt by

Parameter	Original E7	E7 with error	Change [%]
Cell thickness	12.651717	12.952424	2.4 %
Pretilt	1.96037	2.44256	24.6 %
AC scaling	0.746964	0.662758	-11.3 %
DC scaling	1.11686	0.994707	-10.9 %
Difference ($e_1 - e_3$)	11.436999	11.965949	4.6 %

Table 5.2: Overview of fitting results, with the original E7 values and the E7 values with the error included, and the change in the fitting parameter

24.6%, both scaling factors roughly by -11% and the flexoelectric difference ($e_1 - e_3$) by only 4.6%. This shows clearly, that the errors of the physical parameters influence the fitting parameters stronger than the flexoelectric difference ($e_1 - e_3$) and that the error of the physical parameters can be compansated by the fitting process. Therefor it can be assumed, that the fitting error of the flexoelectric difference ($e_1 - e_3$) is approximately 5%.

5.3.11 Surface Energy

During the automated fitting process, the pretilt was kept fixed but the program allowed the pretilt to be changed before a new run. This means that for a single run the pretilt is fixed but overall it can change. However, the surface energy was not taken into account in the automated fitting process. Early investigations showed that with the surface energy included in the fitting, the results are almost the same, as shown in Figure 5.14. For example, using a very weak surface energy

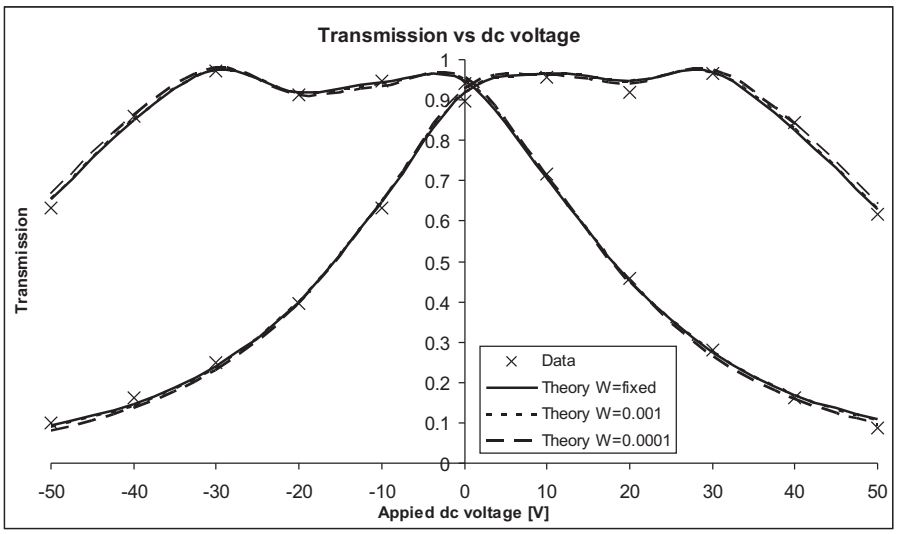


Figure 5.14: Simulation of dc data with a fixed surface, weak surface energy of W=0.001$\frac{J}{m^3}$ and very weak surface energy of W=0.0001$\frac{J}{m^3}$

of W=0.0001$\frac{J}{m^3}$, the result of the flexoelectric difference changed by 5%. However, the value of the surface energy used in the fit was 10 times smaller than a realistic value, which is about W=0.001$\frac{J}{m^3}$. Using a realistic value for the surface energy, the fitting gives the same flexoelectric difference as in the case of fixed surfaces. The very weak effect of the surface energy can be explained by the weak electric field inside the gap (E_{ac}=0.5V/m and E_{dc}=0.1V/m), which is not strong enough to create additional azemuthal distortions on the surface, and the weak tilt of the director due to flexoelectricity, whereby the tilt is in the order of a few degrees and

not strong enough to create additional zimuthal distortion on the surface. These finding, lead to the conclusion that the surface energy is not important and can be ignored in the theory.

5.3.12 Frequency dependence

To show that ions can be neglected in the ac data, which are taken at a frequency of 1kHz, Figure 5.15 shows ac data which are additionally taken at a frequency of 100Hz and 10Hz. The results show clearly that the data at 1kHz, 100Hz and 10Hz looks identically to each other and that ions do not influence the 100Hz and 10Hz data. Therefore, we can neglect ions in the ac data at 1kHz.

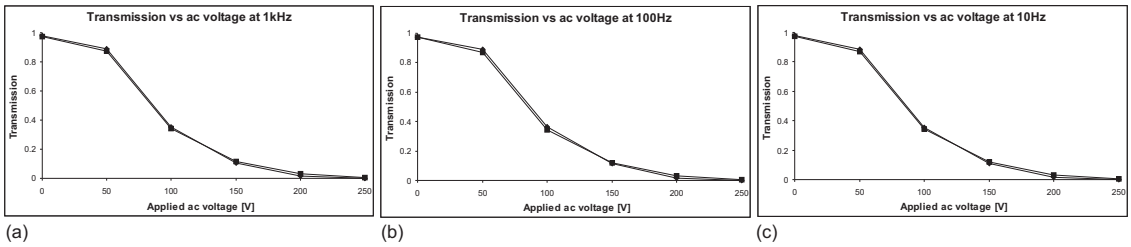


Figure 5.15: Experimental raw data from both detectors for the frequencies a) 1kHZ, b) 100Hz, and c) 10Hz

5.3.13 Limitations of the method

The method has two limitations. The first limitation to our method is materials which have a high viscosity, whereby the optical response to the applied quasi-dc voltage does not reach an equilibrium during the 2.5s pulse. It is possible to decrease the frequency of the quasi-dc voltage and increase the time for the positive and negative pulse but this would also increase the problems with ions. For example, we tried to measure a bi-mesogen material which was very viscous at room temperature.

In general, all our other materials reach equilibrium after 1.0-1.5s but it took the bi-mesogen material more than 500s to reach the equilibrium.

The second limitation is caused by the refractive index Δn. E7 has a Δn of about 0.22 and the results show a strong optical response. However, if Δn is smaller and in the region of 0.1, as in some materials measured, the optical response is also smaller, making it harder to determine the flexoelectric difference accurately. But this problem can be overcome by using a device with a thicker cell gap, e.g. 30-50μm instead of 12μm.

5.4 Results

5.4.1 Materials E7 and E70A

To confirm the reliability of the method, three devices filled with E7 were initially used for the measurement. Each device was used to carry out several measurements, in general about six. Figure 5.16 shows four typical dc results for determining $(e_1 - e_3)$. The values vary between 11.2 pC/m and 13.2 pC/m. The average value of all measurements is 12.2 pC/m, with an error margin of $\pm$2.0 pC/m. The error margin represents the range of fitting results and includes the error from the elastic and dielectric properties. The ac-scaling factor is 0.75 and the dc-scaling factor is 1.09, which gives a dc/ac ratio of 1.45. The scaling factor for ac is, as expected, just a little higher than $2/\pi$=0.64. However, the scaling factor for quasi-dc is rather high, indicating a high concentration of ions, which enhance the electric field when the sign of the quasi-dc is reversed.

A second material E70A, which, although it has a similar name to E7, is different in its composition and physical properties, was used to confirm the robustness and accuracy of the experiment. But this time only one device was produced and several

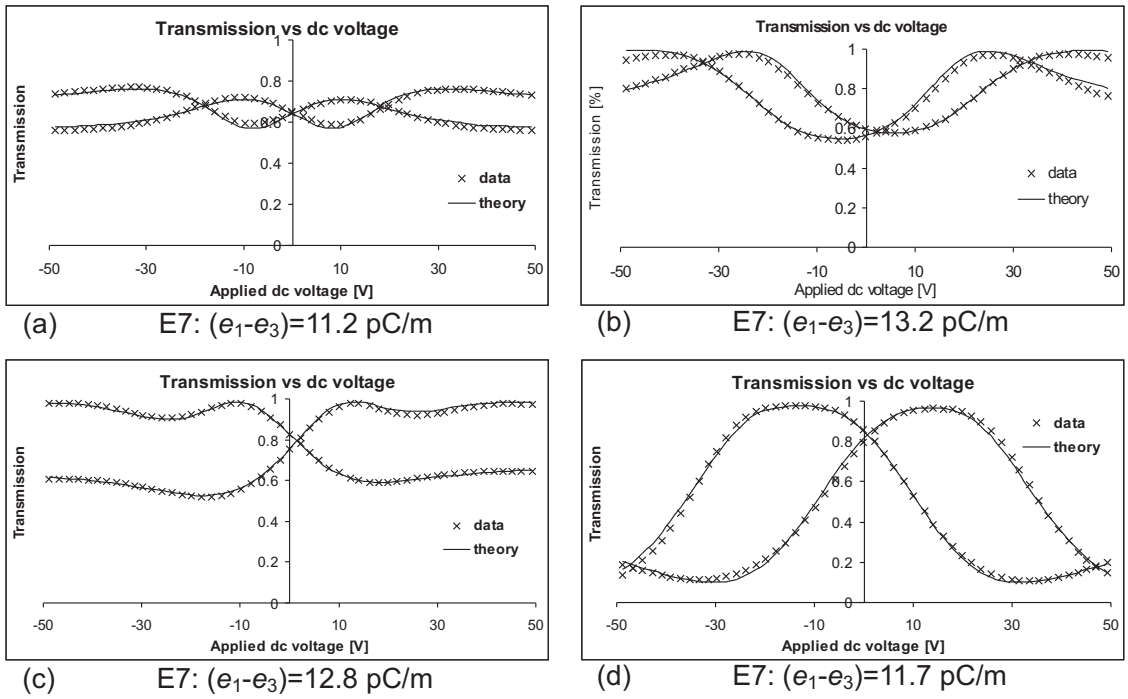


Figure 5.16: E7 result for $(e_1 - e_3)$=(12.2±2.0) pC/m at room temperature (22°C), only 4 measurements are presented

sets of data taken, as shown in Figure 5.17. The average value is (4.2±1.0) pC/m with an ac-scaling of 0.77 and dc-scaling of 1.08. This gives a dc/ac ratio of 1.4. The scaling values and the dc/ac ratio are very similar to E7, which indicates a strong influence of ions in the quasi-dc case. This can be checked using non-ionic materials. Finally, it can be noted that the quality of the quasi-dc data and the dc fitting are very good for E7 and E70A, as shown. But this is also the case for the ac data and the ac fitting which are not presented here.

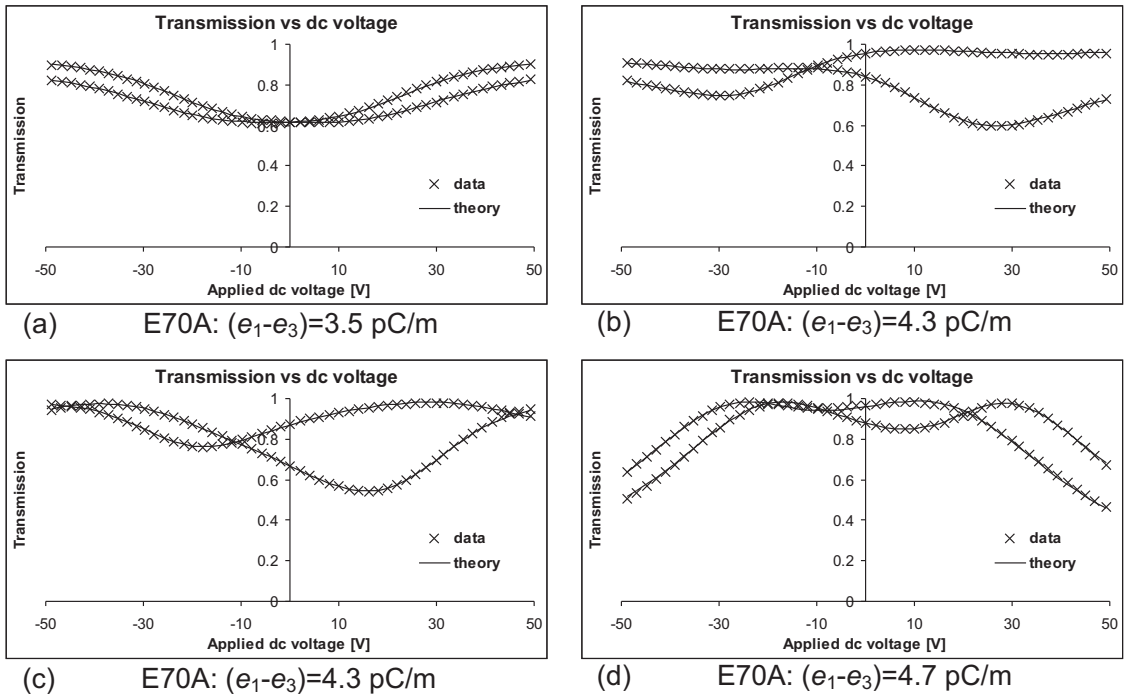
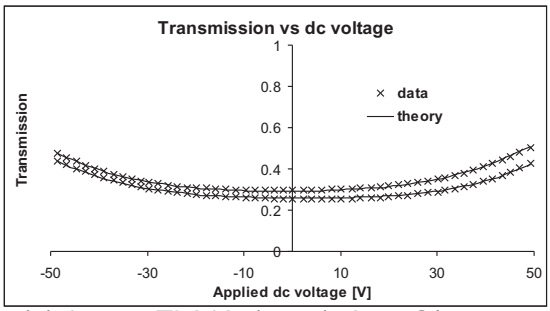


Figure 5.17: E70A result for $(e_1 - e_3)$=(4.2±1.0) pC/m at room temperature (22°C), only 4 measurements are presented

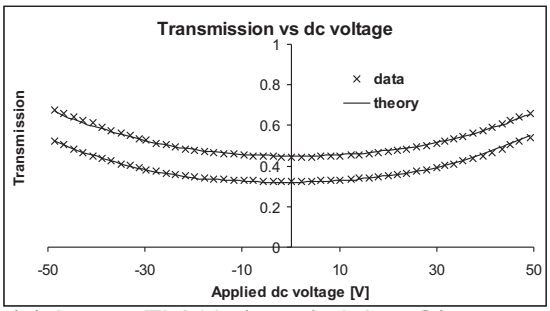
5.4.2 Non-ionic materials

To confirm the influence of the ions, the non-ionic materials TL216 and MLC-7021-100 have been used. TL216 has an ac-scaling factor of 0.71 and a quasi-dc factor of 0.72, which gives a dc/ac ratio of very close to 1.0. The same is true for MLC-7021-100, where the ac-scaling is 0.72 and the dc-scaling is also 0.72, which leads to a dc/ac ratio of 1.0. This is a strong indication that the dc-scaling necessary is due to ionic content and that prior knowledge of the dielectric properties allows the correct internal field to be determined, which is important for correct determination of the flexoelectric coefficients.

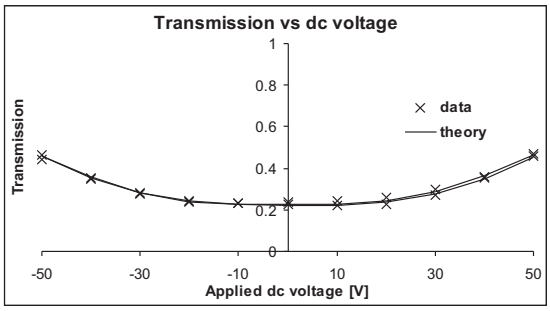
The dc/ac ratios of the ionic materials E7 and E70A, which are about 1.45 compared with the non-ionic materials TL216 and MLC-7021-100, which are 1.0, shows that ions are significantly enhancing the electric field in the quasi-dc measurement. How-



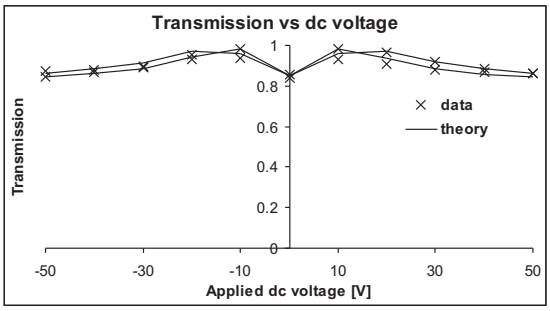
(a) 1. TL216: (e_1-e_3)=0.5 pC/m



(a) 2. TL216: (e_1-e_3)=0.25 pC/m



(b) 1. MLC-7021-100: (e_1-e_3)=0.5 pC/m



(b) 2. MLC-7021-100: (e_1-e_3)=-1.0 pC/m

Figure 5.18: Results at room temperature (22°C) for (a) TL216 with ($e_1 - e_3$)=(0.4±0.5) pC/m, (b) MLC-7021-100 with ($e_1 - e_3$)=(0.0±1.0) pC/m, only 2 measurements per material are presented

ever, as noted above, this issue is taken care of using the scaling factor introduced in the simulation. Example data for TL216 and MLC-7021-100 are shown in Figure 5.18. The difference ($e_1 - e_3$) was determined for TL216 to be (0.4±0.5) pC/m and for MLC-7021-100 to be (0.0±1.0) pC/m.

5.4.3 Molecular structure materials

The difference ($e_1 - e_3$) was measured for 3/5/7 CB as (6.8±1.0) pC/m, for 3/5/7 PCH as (8.2±1.0) pC/m and for 3/5/7 DE as (7.3±1.0) pC/m as shown in Figure 5.19. Each material was filled into one device and six measurements were taken. Figure 5.19 shows only two typical results for each material.

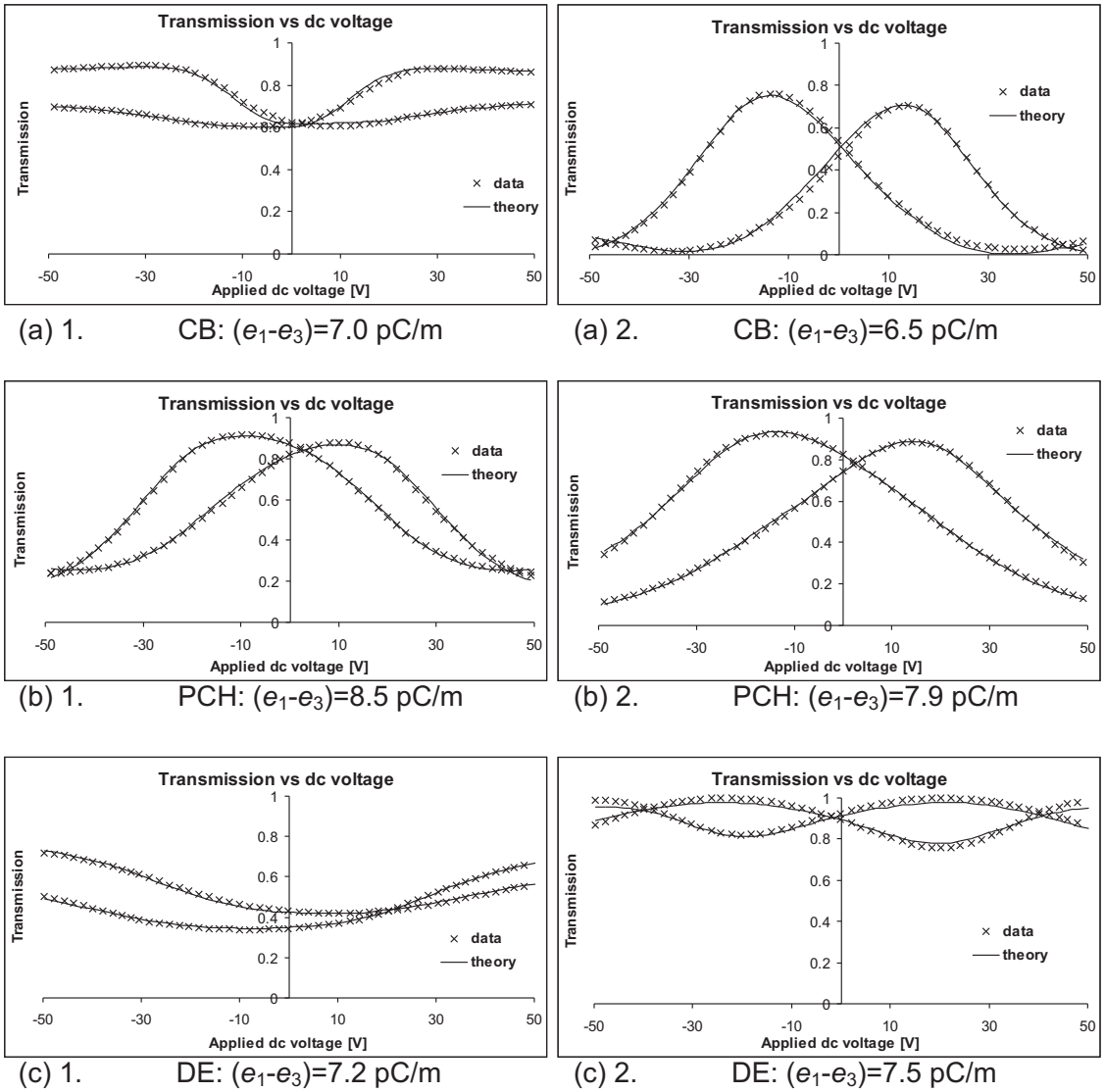


Figure 5.19: Results at room temperature (22°C) for (a) CB with ($e_1 - e_3$)=(6.8±1.0) pC/m, (b) PCH with ($e_1 - e_3$)=(8.2±1.0) pC/m, (c) DE with ($e_1 - e_3$)=(7.3±1.0) pC/m, only 2 measurements per material are presented

5.4.4 Elastic properties materials

For MixA and MixC the difference was measured as (10.5±1.0) pC/m and as (11.5±1.5) pC/m as shown in Figure 5.20. Again, six sets of data were taken of each material and only two typical results are presented in Figure 5.20.

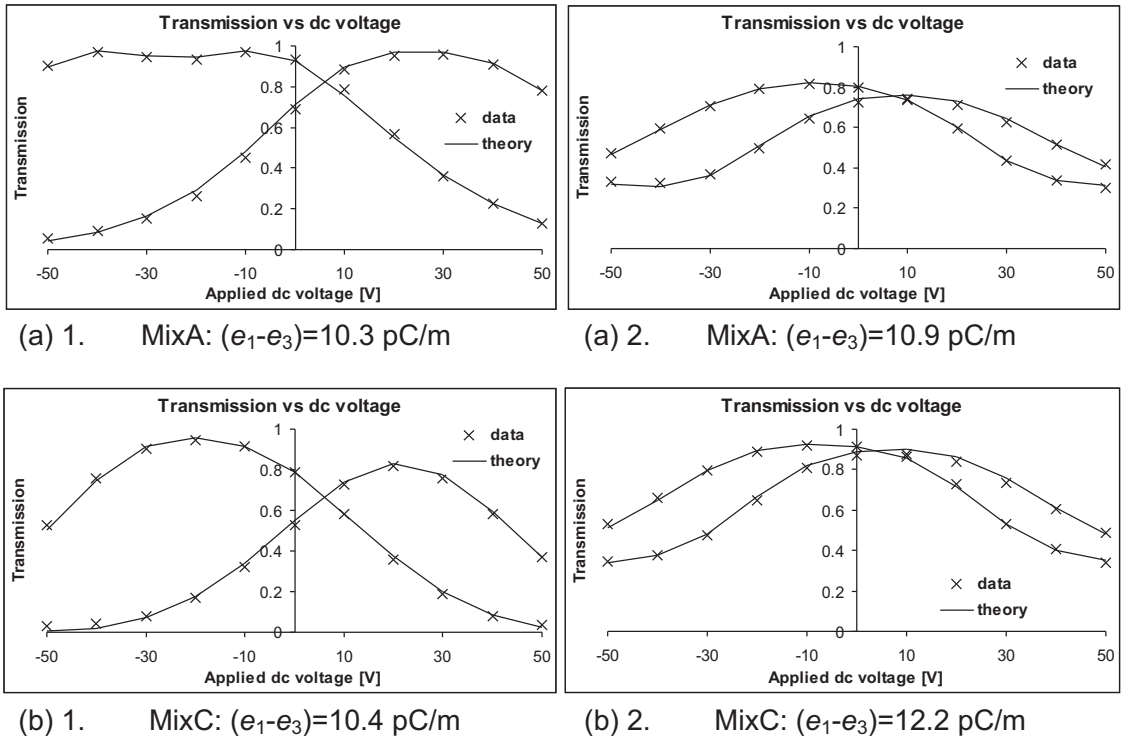
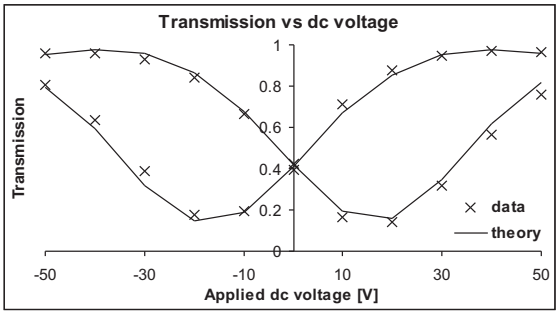


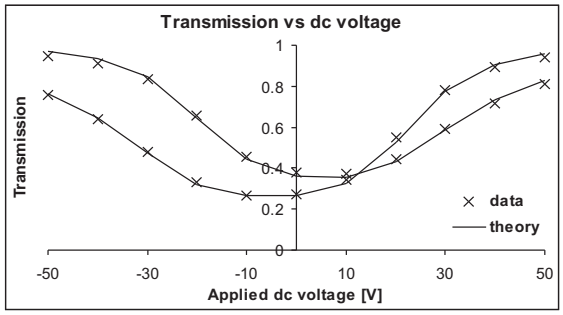
Figure 5.20: Results at room temperature (22°C) for (a) MixA with ($e_1 - e_3$)=(10.5±1.0) pC/m, (b) MixC with ($e_1 - e_3$)=(11.5±1.5) pC/m, only 2 measurements per material are presented

5.4.5 Molecular orientation materials

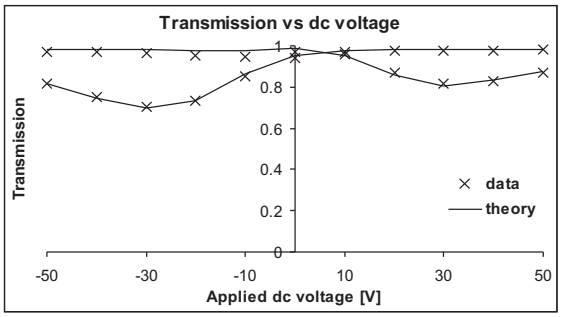
The difference ($e_1 - e_3$) was measured for E7+30%Me35 as (7.0±1.0) pC/m and for E7+50%Me35 as (5.5±1.0) pC/m. Figure 5.21 shows two typical results.



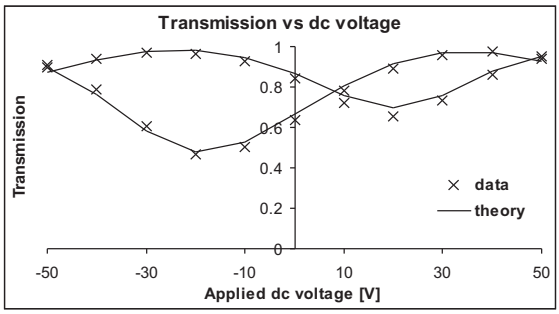
(a) 1. E7+30%Me35: (e_1-e_3)=7.0 pC/m



(a) 2. E7+30%Me35: (e_1-e_3)=7.0 pC/m



(b) 1. E7+50%Me35: (e_1-e_3)=5.1 pC/m



(b) 2. E7+50%Me35: (e_1-e_3)=5.1 pC/m

Figure 5.21: Results at room temperature (22°C) for (a) E7+30%Me35 with ($e_1 - e_3$)=(7.0±1.0) pC/m, (b) E7+50%Me35 with ($e_1 - e_3$)=(5.5±1.0) pC/m, only 2 measurements per material are presented

5.4.6 Dielectric anisotropy $\Delta\epsilon$ materials

Having checked and confirmed the method, the last three materials MDA-02-2419, Material B [84], and MLC-7029 were measured. The difference ($e_1 - e_3$) was mea-

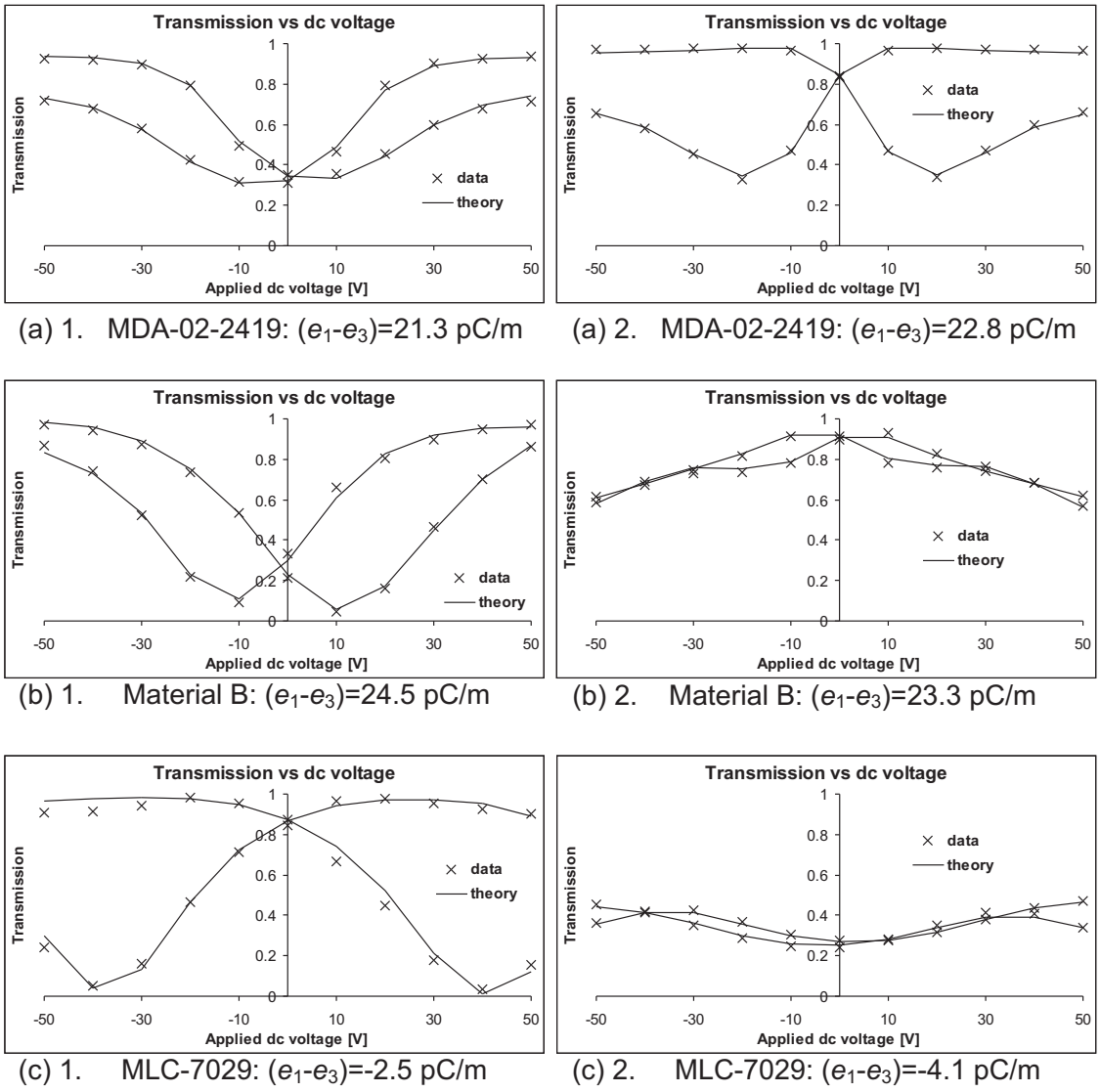


Figure 5.22: Results at room temperature (22°C) for (a) MDA-02-2419 with ($e_1 - e_3$)=(22.0±2.0) pC/m, (b) Material B [84] with ($e_1 - e_3$)=(24.0±2.0) pC/m, (c) MLC-7029 with ($e_1 - e_3$)=(-3.5±1.5) pC/m, only 2 measurements per material are presented

sured for MDA-02-2419 as (22.0±2.0) pC/m, for Material B [84] as (24.0±2.0) pC/m,

and for MLC-7029 as (-3.5±1.5) pC/m. Figure 5.22 shows two typical results for each material out of the six measurements taken for each material.

5.4.7 Overview

First the elastic, dielectric and refractive properties were measured at room temperature (22°C) using well established methods as described in Chapter 4.2.7. These values were used as fixed parameters in the theory to fit the ac and quasi-dc data (at room temperature 22°C) in the main experiment to determine the difference $(e_1 - e_3)$ of the flexoelectric coefficients. Table 5.3 shows the dielectric anisotropy

Material	$\Delta\epsilon$	ΔT [K]	ac-scaling	dc-scaling	dc/ac	$(e_1 - e_3)$ $[pC/m]$
E7	13.7	36	0.75	1.09	1.45	12.2 ±2.0
E70A	10.4	38	0.77	1.08	1.40	4.2 ±1.0
TL216	5.1	58	0.70	0.71	1.0	0.4 ±0.5
MLC-7021-100	10.5	59	0.72	0.72	1.0	0.0 ±1.0
CB	13.2	13	0.75	1.12	1.50	6.8 ±1.0
PCH	12.2	30	0.76	1.06	1.40	8.2 ±1.0
DE	9.0	50	0.71	0.89	1.25	7.3 ±1.0
MixA	11.6	44	0.68	0.92	1.35	10.5 ±1.0
MixC	11.5	48	0.73	1.97	1.34	11.5 ±1.5
E7+30%Me35	10.7	32	0.67	1.05	1.56	7.0 ±1.0
E7+50%Me35	8.3	23	0.68	1.01	1.48	5.5 ±1.0
MDA-02-2419	38.5	75	0.76	0.92	1.22	22.0 ±2.0
Material B [84]	42.1	73	0.74	0.98	1.32	24.0 ±2.0
MLC-7029	-3.7	73	0.74	0.75	1.0	-3.5 ±1.5

Table 5.3: Overview of results for the measured materials at room temperature (22°C).

$\Delta\epsilon$, the temperature difference ΔT, the ac and dc-scaling factors, the ratio between the dc and ac-scaling factors, and the result for the flexoelectric difference $(e_1 - e_3)$.

The "error" given for $(e_1 - e_3)$ is the total error. Each measurement has an error of 5%, which occurs due to the physical parameters like the elastic (K_{11}, K_{22} and

K_{33}), dielectric ($\epsilon_\perp$ and $\epsilon_\parallel$) and optical ($n_\perp$ and $n_\parallel$) parameters. To determine the flexoelectric difference ($e_1 - e_3$), each device was used to carry out at least six measurements. The standard derivation of the six measurements is in the range between 10% and 15%. Including the error due to the physical parameters, which is 5%, increases the error even further to a total error of approximately 20%. Therefore the total error is the addition of the error due to the physical parameters and the standard derivation of the six measurements.

5.5 Conclusion

5.5.1 Experiment

Our newly developed experiment to measure the difference ($e_1 - e_3$) of the flexoelectric coefficients works very well and the results are repeatable and accurate. Even using E7 cells which are more than 1 year old gave the same results because the TN structure is very stable. The quality of the fit is very good, as shown in the graphs above. Automating the experiment and the fitting enabled us to measure one material in a few days, which is very fast and a big advantage in the measurement and understanding of flexoelectricity. However, the production of the TN cells with the electrode pattern for the in-plane electric field is complex and takes time. But this disadvantage can be minimised by producing the cells in bulk for a set of different materials.

The key advantage of the TN-cell experiment using an in-plane electric field compared to the ULH structure is that the TN structure is stable and easier to create. The ULH structure has only the advantage that it is a direct method (but the elastic parameter has to be known to calculate ($e_1 - e_3$)), compared to the TN-cell experiment where the knowledge of elastic, dielectric, and refractive parameters are

necessary to fit the data. However, the flexoelectric effect can be easily observed and measured in the TN-cell experiment. The results are accurate and repeatable.

Further, it is possible to measure achiral and weakly chiral materials, which would enable the investigation of the influence of chirality on flexoelectricity, which was investigated by P. Salter, who is a colleague from the Oxford liquid crystal group. The ULH structure requires a highly chiral material or highly chiral doped material and it was unknown how chirality influences flexoelectricity. His finding showed that there is a negligible correlation between chirality and flexoelectricity [118].

5.5.2 Non-Ionic materials

The influence of ions is taken into account in the method due to the use of the scaling factor. The ac-scaling factors for all materials measured are in the region between 0.7 and 0.75. The theory predicted an ac-scaling factor bigger than $2/\pi$=0.64 due to the concentrated electric field in the middle of the electrode gap. This is shown in our results and confirms the expectations. The dc-scaling factors for the non ionic materials TL216 and MLC-7021-100 are similar to the ac-scaling factors. In the ionic materials, the dc-scaling factors are between 0.9 and 1.1. This is strong evidence that the ions drift while a voltage is applied and enhance the electric field once the sign of the voltage is reversed. However, ions cause big problems in most experiments but we are able to avoid this problem by introducing a scaling factor for the electric field. This technique works very well and using the two non ionic materials TL216 and MLC-7021-100 is strong proof that ions are enhancing the electric field and that the experiment is robust against this problem.

The results for the difference $(e_1 - e_3)$ of the flexoelectric coefficients for the two non-ionic materials TL216 and MLC-7021-100 show a very small $(e_1 - e_3)$, which is almost zero. This is interesting because it is also thought that the flexoelectric effect might

be partly or completely be influenced by ions. Two additional non-ionic materials (MLC-13900-100 and MLC-15900-100) were used to investigate this finding more closely. The quasi-dc data for both materials showed a very small asymmetry which indicated the the flexoelectric difference ($e_1 - e_3$) is also very small. The data was not fitted because the elastic, dielectric and refractive parameters were not known. However, it can be clearly seen from the raw quasi-dc data that the difference is very small and in the range of the other two non-ionic materials. It is very interesting that four non-ionic materials show almost no flexoelectricity. Maybe ions are the cause of flexoelectricity or necessary for flexoelectricity to appear.

5.5.3 Molecular structure

The values of the difference ($e_1 - e_3$) for the three materials CB, PCH, and DE is about $7.5pC/m$ and they are very similar to one another. This indicates that the ring structure appears to have only a small influence on flexoelectricity, despite having a significant influence on the shape and the elastic, dielectric and refractive parameters. This is surprising and not easy to explain, because it is thought that flexoelectricity is due to a shape anisotropy. This was also seen by other scientists [72], who designed the molecular structure in such a way that the shape would look like a pear and hopefully increase the flexoelectric properties. But despite their efforts, the shape did not seem to have a big effect on the flexoelectric properties.

5.5.4 Elastic Properties

MixA and MixC are very interesting materials from the point that MixC has a smectic to nematic transition temperature of 20°C, which is below the measurement temperature. The elastic, dielectric and refractive parameters of these two material are very similar to each other and similar to E7, except that the bend elastic

parameter K_{33} of MixC is about $50pN$, which is very high. But the results for the difference $(e_1 - e_3)$ are about $11pC/m$ for both materials and also similar to E7, which has a flexoelectric difference of $12.2pC/m$. These results show clearly that the elastic properties do not influence the flexoelectric difference $(e_1 - e_3)$ and maybe do not influence flexoelectricity at all.

5.5.5 Molecular orientation

The materials E7+30%Me35 and E7+50%Me35 are mixtures with E7 and the single component Me35. Me35 reduces the anti-parallel orientation, which should increase the splay distortion of the flexoelectric effect. However, the results show that E7+30%Me35 has a difference $(e_1 - e_3)$ of $7.0pC/m$ and E7+50%Me35 of $5.5pC/m$. This is very surprising, because the opposite effect was expected, an increased or at least a similar value to E7. The results do not support the idea that the shape anisotropy causes flexoelectricity. It rather conflicts with the idea of shape anisotropy.

5.5.6 Dielectric anisotropy $\Delta\epsilon$

The results of all 16 measured materials are used to investigate the correlation between dielectric anisotropy $\Delta\epsilon$ and the difference $(e_1 - e_3)$ of the flexoelectric coefficients. This is sensible, because flexoelectricity is caused by molecular dipoles, which align with an external applied field and create an additional distortion due to a shape anisotropy of the molecules. If the molecular dipole is larger, it is more likely that more molecules are orientated in the same direction, which increases the flexoelectric coupling. Results for all materials are shown in Figure 5.23 and they indicate a linear correlation between dielectric anisotropy $\Delta\epsilon$ and the difference

$(e_1 - e_3)$ of the flexoelectric coefficients if the two non ionic materials TL216 and MLC-7021-100 are left out.

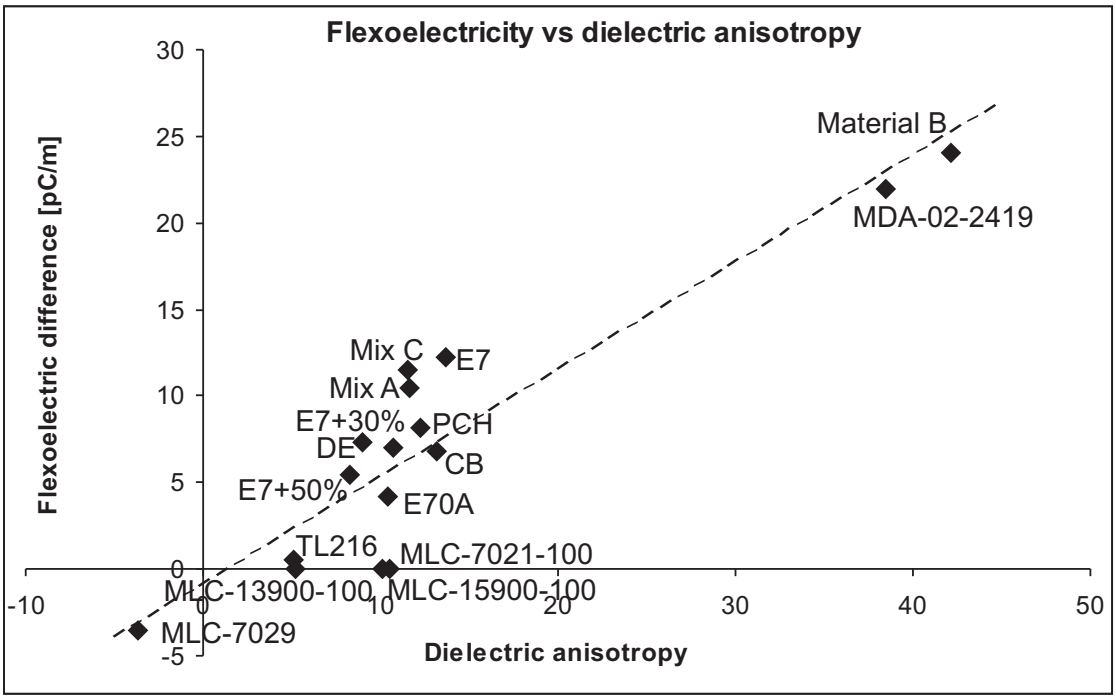


Figure 5.23: Results of all 16 measured materials indicate a rough linear correlation between the difference $(e_1 - e_3)$ and the dielectric anisotropy $\Delta\epsilon$

But the dielectric anisotropy does not explain the complete behaviour. All measurements are done at room temperature (22°C), which means that the temperature difference ΔT for each material depends on the nematic-isotropic transition temperature T_{NI}. Comparing the four materials E7, CB, PCH, and DE, which are in a similar range of $\Delta\epsilon$ with their ΔT values, an interesting behaviour can be observed between dielectric anisotropy $\Delta\epsilon$ and order parameter S, which is represented by the temperature difference ΔT. E7 has the biggest dielectric anisotropy of $\Delta\epsilon$=13.7 of the four presented materials, a temperature difference of ΔT=36K and a flexoelectric difference of $(e_1 - e_3)$=12.2 pC/m. CB has a similar $\Delta\epsilon$ of 13.2 compared to E7 but because of its low nematic to isotropic transition temperature a small ΔT of 13K and it has the smallest $(e_1 - e_3)$ of 6.8 pC/m. DE on the other hand

has the smallest $\Delta\epsilon$ of 9.0 but the largest ΔT of 50K and a $(e_1 - e_3)$ of 6.8 pC/m, which is similar to CB. PCH has slightly smaller $\Delta\epsilon$ and ΔT values compared to E7 and shows the second biggest $(e_1 - e_3)$ of 8.2 pC/m. This indicates a correlation between the dielectric anisotropy $\Delta\epsilon$ and the difference $(e_1 - e_3)$ of the flexoelectric coefficients as presented before and in [123] but also a correlation between the order parameter S and the flexoelectric difference $(e_1 - e_3)$.

In summary, we can conclude that the flexoelectric difference $(e_1 - e_3)$ depends on ions and the dielectric properties. It looks as though it does not depend on the elastic properties. But more importantly, it seems that the flexoelectric difference is not influenced by shape anisotropy as ring structure or molecular orientation.

5.5.7 Future

In the future, we are extremely interested in investigating the influence of ions by mixing different non-ionic materials with ionic materials. One way to check the influence of ions might be to dope ions into MLC-7021-100 or to create mixtures between E7 and MLC-7021-100, which have similar properties to E7. Measuring different concentration of mixtures (90%E7+10%MLC-7021-100, 80%E7+20%MLC-7021-100, 70%E7+30%MLC-7021-100) might help to understand the behaviour, which is crucial for the optimisation of commercial devices relying on flexoelectricity.

Also in the future, we intend to modify our experiment to measure $(e_1 - e_3)$ at different temperatures so that the correlation between order parameter S and flexoelectric difference $(e_1 - e_3)$ can be investigated. It is interesting to note that the leading term in an order parameter expansion for dielectric anisotropy is expected to be $\approx S$, whereas the leading term in an order parameter expansion for flexoelectric difference is expected to be $\approx S^2$ [122]. i.e. $(e_1 - e_3)$ may be expected to behave as $\approx \Delta\epsilon S$, which appears to be consistent with our results. We are inter-

ested in improving our method of measuring $(e_1 - e_3)$ at different temperatures to investigate the influence of the order parameter S, but this is more difficult than it seems. Not only does the TN-cell experiment have to be improved, but also the three experiments to measure the elastic, dielectric and refractive properties must be modified to guarantee that all parameters are determined at the defined temperature and a temperature depends of the elastic, dielectric or refractive properties can be excluded.

The next chapters presents the experiments to measure the sum $(e_1 + e_3)$ of the flexoelectric coefficients.

Chapter 6

Pi cell to measure sum $(e_1 + e_3)$

6.1 Introduction

A hybrid aligned nematic cell (HAN) was first used by Madhusudana [45, 60] to measure the sum $(e_1 + e_3)$ and shows a strong bulk flexoelectric response when an electric field E is applied across the device, because of the asymmetric structure due to the homeotropic alignment on one side and the planar alignment on the other side. Due to flexoelectricity, an applied dc voltage distorts the director differently for positive voltages compared to negative voltages as shown in Figure 6.1. This distortion can be measured and used to determine the sum $(e_1 + e_3)$. However, there is a surface polarisation associated with the homeotropic alignment [62, 63]. This may be caused by the polarity of the surface aligning material, together with the ordering of the liquid crystal molecules at the surface. This surface polarisation acts like an offset voltage and is in the range of a few hundreds millivolts [63]. Another disadvantage of the asymmetrical structure of the HAN cell is the flexoelectric polarisation P_f, which is non zero for asymmetrical structures. This non zero flexoelectric polarisation P_f also acts like an offset voltage and can be in the range of a few tens

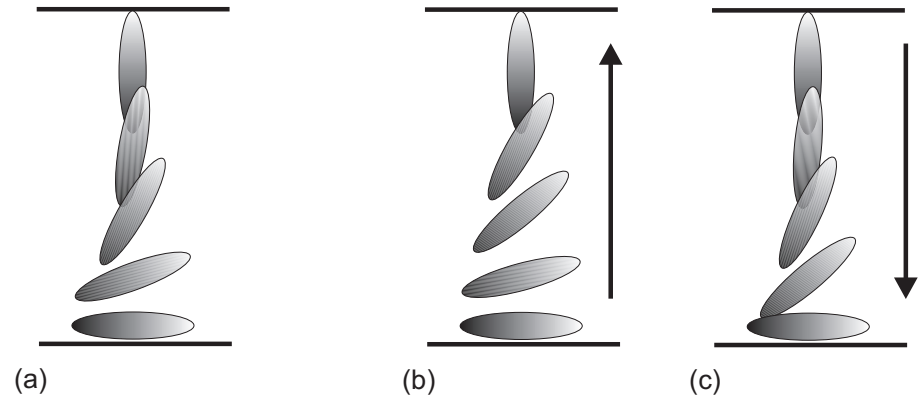


Figure 6.1: a) HAN structure with electric field across the cell for b) positive voltage and c) negative voltage

of millivolts up to a hundred millivolts. Both offset voltages, created by the surface polarisation and by the flexoelectric polarisation, can lead to ionic migration and influence the measurement of the sum $(e_1 + e_3)$ strongly.

Our new method to measure the sum $(e_1 + e_3)$ uses the big advantage of the strong flexoelectric response in the HAN cell but avoids the problems of both offset voltages. This is done using a Pi cell in the V-State, as shown in Figure 6.2. The surface

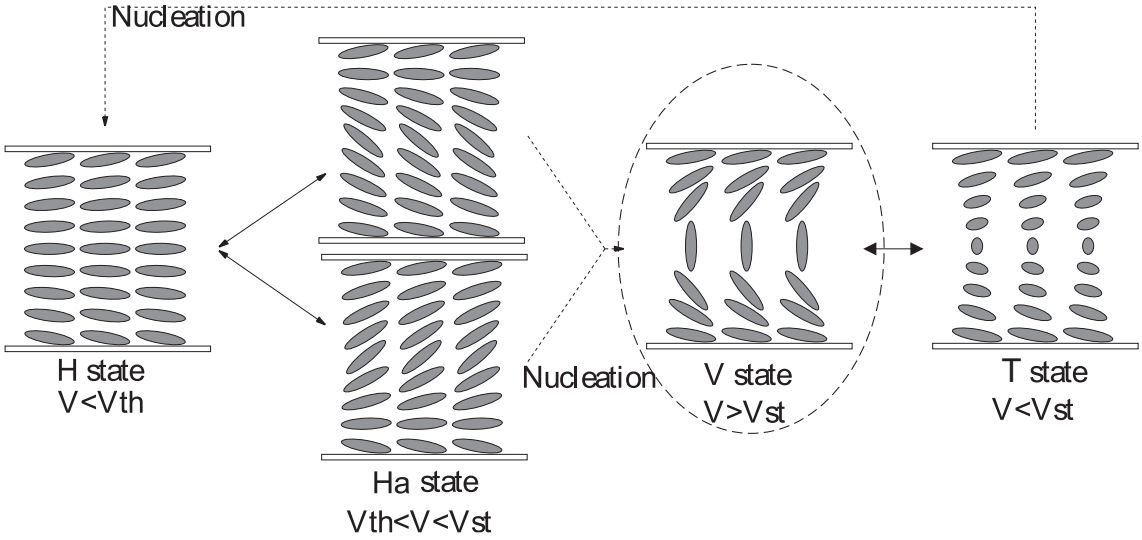


Figure 6.2: Different states of the Pi cell

alignment of the Pi cell shows at both glass plates in the same direction and the

surface alignment is parallel to each other. The parallel surface alignment is realised by the rubbing direction at each glass plate. The Pi cell structure is also called a splayed cell. The cell switches at a voltage V_{th}, which is about $1V$, from the symmetrical horizontal state (H-State) into the asymmetrical horizontal state (Ha-State) and nucleates at V_{st}, which is about $3V$, into the vertical state (V-State), as shown in Figure 6.2. If the voltage is switched off in the V-State, it goes into the twisted state (T-State) and then nucleates back into the H-State [129]. For the measurement of the sum $(e_1 + e_3)$ the V-State is used, which looks like two HAN structures whereby one HAN structure is flipped over and attached to the other one. The big advantage of the V-State is the symmetrical structure, which avoids the problem with the surface polarisation and flexoelectric polarisation.

Our experiment applies an ac voltage and measures the optical response (the transmission and the 1st and 2nd harmonics, which are extracted out from the transmission) to determine the flexoelectric sum $(e_1 + e_3)$ [60]. Therefore, a theoretical model is required to fit the data and extract the results for the sum $(e_1 + e_3)$.

6.2 Theory

The theoretical model to simulate the dynamic behaviour of the Pi structure is based on the coordinate system shown in Figure 6.3, whereby the applied electric field and the director are calculated in a 1-dimensional model along the z axis (in 100 layers). The dynamic 1-D model includes the bulk energy L_B and calculates the transmission through the device using 4x4 Berreman optics which enables us to determine the transmission at oblique incidence more accurately than the 2x2 Jones optics. From the transmission the 1st and 2nd harmonics are calculated. Due to the ac voltage, flow plays an important role and is included in the theory. The surface energy is also implied in the model and therefore the surface pretilt can vary.

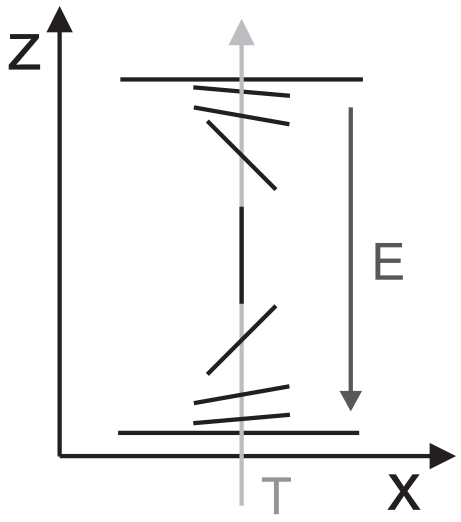


Figure 6.3: Coordinate system for 1-D model

As shown in Chapter 3, the bulk energy L_B (Eq. 3.33) is the sum of the the elastic energy w_d, flexoelectric energy w_f and dielectric energy w_e as

$$\begin{aligned} L_B &= w_d + w_f + w_e \\ L_B &= \frac{1}{2}K_{11}\left(\nabla\cdot\vec{n}\right)^2 + \frac{1}{2}K_{22}\left(\vec{n}\cdot\left(\nabla\times\vec{n}\right) - q\right)^2 + \frac{1}{2}K_{33}\left(\vec{n}\times\left(\nabla\times\vec{n}\right)\right)^2 \\ &\quad - \left(e_1\vec{n}\left(\nabla\cdot\vec{n}\right) + e_3\left(\nabla\times\vec{n}\right)\times\vec{n}\right)\cdot\vec{E} - \frac{1}{2}\vec{D}\cdot\vec{E}. \end{aligned} \tag{6.1}$$

The electric field $\vec{E}$ with its only component along the z direction is not constant and it changes along the z direction. The calculation of E_z will be presented in the next section. This leads to a bulk energy L_B of

$$\begin{aligned} L_B = &\frac{1}{2}K_{11}n_z^{'2} + \frac{1}{2}K_{22}\left(n_y n_x^{'} - n_x n_y^{'} - q\right)^2 \\ &+\frac{1}{2}K_{33}\left(n_z^2 n_x^{'2} + n_z^2 n_y^{'2} + n_z^2 n_z^{'2}\right) \\ &-\left(e_1 + e_3\right)n_z n_z^{'} E_z \\ &-\frac{1}{2}\epsilon_0\left(\Delta\epsilon n_z^2 + \epsilon_\perp\right)E_z^2, \end{aligned} \tag{6.2}$$

whereby the following calculations are used

$$\nabla = \begin{pmatrix} 0 \\ 0 \\ \frac{\partial}{\partial z} \end{pmatrix}, \vec{n} = \begin{pmatrix} n_x \\ n_y \\ n_z \end{pmatrix}, \vec{E} = \begin{pmatrix} 0 \\ 0 \\ E_z \end{pmatrix},$$

$$\nabla \cdot \vec{n} = \begin{pmatrix} 0 \\ 0 \\ \frac{\partial}{\partial z} \end{pmatrix} \cdot \begin{pmatrix} n_x \\ n_y \\ n_z \end{pmatrix} = \frac{\partial n_z}{\partial z} = n_z^{'},$$

$$\vec{n}\,(\nabla \cdot \vec{n}) = \begin{pmatrix} n_x \\ n_y \\ n_z \end{pmatrix} \cdot n_z^{'} = \begin{pmatrix} n_x n_z^{'} \\ n_y n_z^{'} \\ n_z n_z^{'} \end{pmatrix},$$

$$\vec{n} \cdot (\nabla \times \vec{n}) = \begin{vmatrix} n_x & n_y & n_z \\ 0 & 0 & \frac{\partial}{\partial z} \\ n_x & n_y & n_z \end{vmatrix} = n_y \frac{\partial n_x}{\partial z} - n_x \frac{\partial n_y}{\partial z} = n_y n_x^{'} - n_x n_y^{'},$$

$$(\nabla \times \vec{n}) \times \vec{n} = \left[\begin{pmatrix} 0 \\ 0 \\ \frac{\partial}{\partial z} \end{pmatrix} \times \begin{pmatrix} n_x \\ n_y \\ n_z \end{pmatrix} \right] \times \begin{pmatrix} n_x \\ n_y \\ n_z \end{pmatrix} = \begin{pmatrix} -n_y^{'} \\ n_x^{'} \\ 0 \end{pmatrix} \times \begin{pmatrix} n_x \\ n_y \\ n_z \end{pmatrix}$$

$$= \begin{pmatrix} n_z n_x^{'} \\ n_z n_y^{'} \\ -n_y n_y^{'} - n_x n_x^{'} \end{pmatrix} = \begin{pmatrix} n_z n_x^{'} \\ n_z n_y^{'} \\ n_z n_z^{'} \end{pmatrix},$$

$$(\vec{n} \times (\nabla \times \vec{n}))^2 = \begin{pmatrix} n_z n_x^{'} \\ n_z n_y^{'} \\ n_z n_z^{'} \end{pmatrix}^2 = n_z^2 n_x^{'2} + n_z^2 n_y^{'2} + n_z^2 n_z^{'2},$$

$$\vec{n}\,(\nabla \cdot \vec{n})\,\vec{E} = \begin{pmatrix} n_x n_z^{'} \\ n_y n_z^{'} \\ n_z n_z^{'} \end{pmatrix} \cdot \begin{pmatrix} 0 \\ 0 \\ E_z \end{pmatrix} = n_z n_z^{'} E_z,$$

$$((\nabla \times \vec{n}) \times \vec{n})\,\vec{E} = \begin{pmatrix} n_z n_x^{'} \\ n_z n_y^{'} \\ n_z n_z^{'} \end{pmatrix} \cdot \begin{pmatrix} 0 \\ 0 \\ E_z \end{pmatrix} = n_z n_z^{'} E_z,$$

$$\vec{D}\vec{E} = \epsilon_0 \left[\begin{pmatrix} \Delta\epsilon n_x^2 + \epsilon_\perp & \Delta\epsilon n_x n_y & \Delta\epsilon n_z n_x \\ \Delta\epsilon n_x n_y & \Delta\epsilon n_y^2 + \epsilon_\perp & \Delta\epsilon n_z n_y \\ \Delta\epsilon n_z n_x & \Delta\epsilon n_z n_y & \Delta\epsilon n_z^2 + \epsilon_\perp \end{pmatrix} \begin{pmatrix} 0 \\ 0 \\ E_z \end{pmatrix} \right] \begin{pmatrix} 0 \\ 0 \\ E_z \end{pmatrix}$$

$$= \epsilon_0 \begin{pmatrix} \Delta\epsilon n_x n_z E_z \\ \Delta\epsilon n_y n_z E_z \\ \left(\Delta\epsilon n_z^2 + \epsilon_\perp\right) E_z \end{pmatrix} \cdot \begin{pmatrix} 0 \\ 0 \\ E_z \end{pmatrix} = \epsilon_0 \left(\Delta\epsilon n_z^2 + \epsilon_\perp\right) E_z^2.$$

The general Euler-Lagrange equation (Eq. 3.10) simplifies for the 1-D model and leads to a molecular field $\vec{h}$ of

$$\begin{aligned} h_x &= \frac{\partial}{\partial z}\left(\frac{\partial L_B}{\partial n_x^{'}}\right) - \frac{\partial L_B}{\partial n_x}, \\ h_y &= \frac{\partial}{\partial z}\left(\frac{\partial L_B}{\partial n_y^{'}}\right) - \frac{\partial L_B}{\partial n_y}, \\ h_z &= \frac{\partial}{\partial z}\left(\frac{\partial L_B}{\partial n_z^{'}}\right) - \frac{\partial L_B}{\partial n_z}, \end{aligned} \tag{6.3}$$

and the final solution of the Euler-Lagrange equations (Eq. 6.3) gives the molecular field $\vec{h}$ of

$$\begin{aligned} h_x = \;& K_{22}\left(n_y^2 n_x^{''} - n_x n_y n_y^{''} + 2 n_y n_x^{'} n_y^{'} - 2 n_x n_y^{'2} - 2 q n_y^{'}\right) \\ & + K_{33}\left(2 n_z n_x^{'} n_z^{'} + n_z^2 n_x^{''}\right), \\ h_y = \;& K_{22}\left(n_x^2 n_y^{''} - n_x n_y n_x^{''} + 2 n_x n_x^{'} n_y^{'} - 2 n_y n_x^{'2} + 2 q n_x^{'}\right) \\ & + K_{33}\left(2 n_z n_y^{'} n_z^{'} + n_z^2 n_y^{''}\right), \\ h_z = \;& K_{11} n_z^{''} + K_{33} n_z\left(n_z n_z^{''} - n_x^{'2} - n_y^{'2} + n_z^{'2}\right) \\ & - \left(e_1 + e_3\right) n_z E_z^{'} + \epsilon_0 \Delta\epsilon n_z E_z^2. \end{aligned} \tag{6.4}$$

whereby the following calculations are used

$$
\begin{aligned}
\frac{\partial L_B}{\partial n_x'} &= K_{22}\left({n_y}^2 {n_x}' - n_y {n_y}' n_x - n_y q\right) + K_{33} {n_z}^2 {n_x}', \\
\frac{\partial}{\partial z}\left(\frac{\partial L_B}{\partial n_x'}\right) &= K_{22}\left({n_y}^2 {n_x}'' - {n_y}'^2 n_x - {n_y}' q - n_y {n_y}'' n_x + {n_y}' {n_x}' n_y\right) \\
&\quad + K_{33}\left(2 n_z {n_x}' {n_z}' + {n_z}^2 {n_x}''\right), \\
\frac{\partial L_B}{\partial n_x} &= K_{22}\left(-{n_y}' {n_x}' n_y + {n_y}'^2 n_x + {n_y}' q\right), \\
\frac{\partial L_B}{\partial n_y'} &= K_{22}\left(-n_x {n_x}' n_y + {n_x}^2 {n_y}' + n_x q\right) + K_{33} {n_z}^2 {n_y}', \\
\frac{\partial}{\partial z}\left(\frac{\partial L_B}{\partial n_y'}\right) &= K_{22}\left(-n_x {n_x}'' n_y + {n_x}' {n_y}' n_x + {n_x}' q + {n_x}^2 {n_y}'' - {n_x}'^2 n_y\right) \\
&\quad + K_{33}\left(2 n_z {n_y}' {n_z}' + {n_z}^2 {n_y}''\right), \\
\frac{\partial L_B}{\partial n_y} &= K_{22}\left({n_x}'^2 n_y - {n_x}' {n_y}' n_x - {n_x}' q\right), \\
\frac{\partial L_B}{\partial n_z'} &= K_{11} {n_z}' + K_{33} {n_z}^2 {n_z}' - (e_1 + e_3)\, n_z E_z, \\
\frac{\partial}{\partial z}\left(\frac{\partial L_B}{\partial n_z'}\right) &= K_{11} {n_z}'' + K_{33}\left({n_z}^2 {n_z}'' + 2 n_z {n_z}'^2\right) \\
&\quad - (e_1 + e_3)\, n_z {E_z}' - (e_1 + e_3)\, {n_z}' E_z, \\
\frac{\partial L_B}{\partial n_z} &= K_{33}\left(n_z {n_z}'^2 + n_z {n_x}'^2 + n_z {n_y}'^2\right) \\
&\quad - (e_1 + e_3)\, {n_z}' E_z - \epsilon_0 \Delta\, \epsilon\, n_z {E_z}^2.
\end{aligned}
$$

As shown in Equation 6.4, the flexoelectric effect varies with $(e_1+e_3)E_z'$ and depends on the sum (e_1+e_3) and on the gradient of the applied electric field E_z. This makes it clearer why a non uniform electric field is required to measure the sum $(e_1 + e_3)$. Further, it is important to take the sign of the applied electric field into account. The dielectric effect goes with E_z^2 and doesn't depend on the sign of the applied field. An accurate determination of the non uniform electric field E_z is crucial for the theoretical model. This can be done by knowing the applied voltage V and the dielectric properties of the materials, as presented in the next section.

6.2.1 Finding E_z

Because of the non uniform dielectric properties, the electric field E_z is not constant and it changes along the z direction. Using Equation 3.20, the displacement field D is in the z direction

$$D_z = \epsilon_0 \epsilon_{zz} E_z,$$

where ϵ_{zz} is defined by Equation 3.24. Most of the liquid crystal materials used in this project are ionic materials. These materials have ions and free charges, which effect the electric field and make it more complicated to calculate the electric field because it is unknown which mobility and concentration these free charges have. To simplify the calculation of the electric field, it is assumed, that there are no free charges in the liquid crystal material. Therefore, the frequency of the applied ac voltage has to be high enough that ions don't have an effect on the experimental results. Assuming that there are no free charges and negligible changes in x and y direction, this leads to a constant displacement field D_z in z. The flexoelectric polarisation P_{fz}, which is defined by Equation 3.31, contributes to the displacement field with

$$D_z = \epsilon_0 \epsilon_{zz} E_z + P_{fz}.$$

Therefore the electric field E_z is

$$E_z = \frac{D_z - P_{fz}}{\epsilon_0 \epsilon_{zz}}. \tag{6.5}$$

The potential V can be calculated by integrating the electric field across the cell, which gives

$$\begin{aligned} -V &= \int_0^d E_z \mathrm{d}z \\ &= \int_0^d \frac{D_z - P_{fz}}{\epsilon_0 \epsilon_{zz}} \mathrm{d}z \\ &= \frac{1}{\epsilon_0} \left(D_z \int_0^d \frac{1}{\epsilon_{zz}} \mathrm{d}z - \int_0^d \frac{P_{fz}}{\epsilon_{zz}} \mathrm{d}z \right). \end{aligned} \tag{6.6}$$

Therefore Equation 6.6 can be rearranged to find the displacement field D_z with

$$D_z = \frac{-\epsilon_0 V + \int_0^d \frac{P_{fz}}{\epsilon_{zz}} dz}{\int_0^d \frac{1}{\epsilon_{zz}} dz}. \tag{6.7}$$

It is interesting to note that Equation 6.7 explains the effect of the offset voltage caused by an asymmetrical structure. The second term in the denominator is non zero if the integral of P_{fz} is done over an asymmetrical structure. The result of the P_{fz} integral can be seen as an offset voltage, which is about 0.2V for a HAN cell, and is added to the applied voltage V. For a symmetrical structure like a Pi cell, the offset voltage is zero [129]. This offset voltage can lead to ion migration in asymmetrical structures, which leads to a increasing cancellation of the electric field.

Now, inserting D_z into Equation 6.5 gives the electric field E_z with

$$E_z = \frac{\frac{-\epsilon_0 V + \int_0^d \frac{P_{fz}}{\epsilon_{zz}} dz}{\int_0^d \frac{1}{\epsilon_{zz}} dz} - P_{fz}}{\epsilon_0 \epsilon_{zz}}. \tag{6.8}$$

This section shows the calculation of the electric field E_z using an analytical approach. In Chapter 3 a numerical solution was presented, which is valid for the general case of a 3-dimensional model. However, in this special case of a 1-dimensional

model, it is possible to find a solution for E_z analytically, which is an easier and faster approach, whereby the electric field E_z can be directly calculated after determining the director profile. The numerical approach would also give the same results but the computation time is much higher because the calculation of E_z has to be done until an equilibrium is reached.

6.2.2 Surface Energy

The theoretical model includes the surface energy L_S [112, 113], which is defined as shown in Chapter 3 as

$$\begin{aligned} L_S &= W_\theta \sin^2(\theta - \theta_P) + W_\phi \sin^2(\phi - \phi_P) \\ &= W_\theta \left(n_z \cos\theta_P - \sqrt{n_x^2 + n_y^2} \sin\theta_P \right)^2 \\ &\quad + W_\phi \left(\frac{n_y}{\sqrt{n_x^2 + n_y^2}} \cos\phi_P - \frac{n_y}{\sqrt{n_x^2 + n_y^2}} \sin\phi_P \right)^2, \end{aligned} \tag{6.9}$$

where W_θ is the zenithal surface anchoring, W_ϕ is the azimuthal surface anchoring, θ_P is the zenithal pretilt, and ϕ_P is the azimuthal pretwist.

The general Euler-Lagrange equation for the boundary condition (Eq. 3.35) simplifies for the 1-D model and leads to a surface molecular field $\vec{h_s}$ of

$$\begin{aligned} h_{sx} &= \pm \left(\frac{\partial L_B}{\partial n_x'} \right) - \frac{\partial L_S}{\partial n_x} \\ h_{sy} &= \pm \left(\frac{\partial L_B}{\partial n_y'} \right) - \frac{\partial L_S}{\partial n_y} \\ h_{sz} &= \pm \left(\frac{\partial L_B}{\partial n_z'} \right) - \frac{\partial L_S}{\partial n_z}, \end{aligned} \tag{6.10}$$

where L_B is the bulk energy. The $\pm$ indicates the difference of the bottom and top surface. The bottom surface uses a '+' and the top surface uses a '-'. The solution

of the surface molecular field $\vec{h_s}$ leads to

$$
\begin{aligned}
h_{sx} = \pm\Bigg[& K_{22}\left(n_y n_x^{'} - n_x n_y^{'} - q\right) n_y + K_{33} n_z^2 n_x^{'} \\
& + K_{33}\left(n_x n_x^{'} + n_y n_y^{'}\right) n_x + e_3 n_x E_z \Bigg] \\
& + \frac{2W_\theta n_x \sin\theta_P}{\sqrt{n_x^2 + n_y^2}}\left(n_z \cos\theta_P - \sqrt{n_x^2 + n_y^2}\sin\theta_P\right) \\
& + \frac{2W_\phi n_x \left(n_y \cos\phi_P - n_x \sin\phi_P\right)^2}{\left(n_x^2 + n_y^2\right)^2} \\
& + \frac{2W_\phi \sin\phi_P \left(n_y \cos\phi_P - n_x \sin\phi_P\right)}{\left(n_x^2 + n_y^2\right)}, \\
h_{sy} = \pm\Bigg[& - K_{22}\left(n_y n_x^{'} - n_x n_y^{'} - q\right) n_x + K_{33} n_z^2 n_y^{'} \\
& + K_{33}\left(n_x n_x^{'} + n_y n_y^{'}\right) n_y + e_3 n_y E_z \Bigg] \\
& + \frac{2W_\theta n_y \sin\theta_P}{\sqrt{n_x^2 + n_y^2}}\left(n_z \cos\theta_P - \sqrt{n_x^2 + n_y^2}\sin\theta_P\right) \\
& + \frac{2W_\phi n_y \left(n_y \cos\phi_P - n_x \sin\phi_P\right)^2}{\left(n_x^2 + n_y^2\right)^2} \\
& + \frac{2W_\phi \cos\phi_P \left(n_y \cos\phi_P - n_x \sin\phi_P\right)}{\left(n_x^2 + n_y^2\right)}, \\
h_{sz} = \pm\Bigg[& K_{11} n_z^{'} - e_1 n_z E_z \Bigg] \\
& + 2W_\theta \cos\theta_P \left(n_z \cos\theta_P - \sqrt{n_x^2 + n_y^2}\sin\theta_P\right).
\end{aligned}
\tag{6.11}
$$

6.2.3 Dissipation function

The calculation of the dissipation function [110] has already been presented in Chapter 3 but it is also shown here in order to complete this chapter and to give a better understanding of the theory used. The dissipation function uses the Leslie viscosities

coefficients $(\alpha_1, \alpha_2, \alpha_3, \alpha_4, \alpha_5)$ and describes the case of flow in the bulk by

$$\begin{aligned}
\frac{\partial \mathcal{D}}{\partial \dot{n_x}} &= (\alpha_3 - \alpha_2)\, \dot{n_x} + v_x^{'} \alpha_2 n_z, \\
\frac{\partial \mathcal{D}}{\partial \dot{n_y}} &= (\alpha_3 - \alpha_2)\, \dot{n_y} + v_y^{'} \alpha_2 n_z, \\
\frac{\partial \mathcal{D}}{\partial \dot{n_z}} &= (\alpha_3 - \alpha_2)\, \dot{n_z} + v_x^{'} \alpha_3 n_x + v_y^{'} \alpha_3 n_y,
\end{aligned} \tag{6.12}$$

where the fluid velocity gradients [110] can be calculated by

$$\begin{aligned}
v_x^{'} &= \frac{C_6 \sigma_{zy} - C_7 \sigma_{zx}}{E} + \psi_1 \dot{n_x} + \psi_2 \dot{n_y} + \psi_3 \dot{n_z}, \\
v_y^{'} &= \frac{C_6 \sigma_{zx} - C_5 \sigma_{zy}}{E} + \psi_2 \dot{n_x} + \psi_4 \dot{n_y} + \psi_5 \dot{n_z},
\end{aligned}$$

where σ_{zx} and σ_{zy} are the only non-zero terms of the stress tensor [110], defined by

$$\begin{aligned}
\sigma_{zx} &= \frac{\Psi_3 \int_0^d \left(\psi_1 \dot{n_x} + \psi_2 \dot{n_y} + \psi_3 \dot{n_z}\right) \mathrm{d}z + \Psi_1 \int_0^d \left(\psi_2 \dot{n_x} + \psi_4 \dot{n_y} + \psi_5 \dot{n_z}\right) \mathrm{d}z}{\Psi_2 \Psi_3 - \Psi_1^2}, \\
\sigma_{zx} &= \frac{\Psi_1 \int_0^d \left(\psi_1 \dot{n_x} + \psi_2 \dot{n_y} + \psi_3 \dot{n_z}\right) \mathrm{d}z + \Psi_2 \int_0^d \left(\psi_2 \dot{n_x} + \psi_4 \dot{n_y} + \psi_5 \dot{n_z}\right) \mathrm{d}z}{\Psi_2 \Psi_3 - \Psi_1^2},
\end{aligned}$$

with intermediate variables being defined to simplify the calculation as

$$\begin{aligned}
C_1 &= \alpha_3 - \alpha_2, \\
C_2 &= \alpha_2 n_z, \\
C_3 &= \alpha_3 n_x, \\
C_4 &= \alpha_3 n_y, \\
C_5 &= \frac{1}{2}\left[2\alpha_1 n_x^2 n_z^2 + \alpha_2\left(n_x^2 - n_z^2\right) + 2\alpha_3 n_x^2 + \alpha_4 + \alpha_5\left(n_x^2 + n_z^2\right)\right], \\
C_6 &= \frac{1}{2}\left[2\alpha_1 n_z^2 + \alpha_2 + 2\alpha_3 + \alpha_5\right] n_x n_y, \\
C_7 &= \frac{1}{2}\left[2\alpha_1 n_y^2 n_z^2 + \alpha_2\left(n_y^2 - n_z^2\right) + 2\alpha_3 n_y^2 + \alpha_4 + \alpha_5\left(n_y^2 + n_z^2\right)\right],
\end{aligned}$$

$$E = C_6^2 - C_5 C_7,$$

$$\psi_1 = \frac{C_2 C_7}{E},$$
$$\psi_2 = -\frac{C_2 C_6}{E},$$
$$\psi_3 = \frac{C_3 C_7 - C_4 C_6}{E},$$
$$\psi_4 = \frac{C_2 C_5}{E},$$
$$\psi_5 = \frac{C_4 C_5 - C_3 C_6}{E},$$

$$\Psi_1 = \int_0^d \frac{C_6}{E} \mathrm{d}z,$$
$$\Psi_2 = \int_0^d \frac{C_7}{E} \mathrm{d}z,$$
$$\Psi_3 = \int_0^d \frac{C_5}{E} \mathrm{d}z.$$

The dissipation function for the surface (without flow on the surface but flow in the bulk) is defined by

$$\begin{aligned} \frac{\partial \mathcal{D}}{\partial \dot{n}_x} &= (\alpha_3 - \alpha_2) L_S \dot{n}_x, \\ \frac{\partial \mathcal{D}}{\partial \dot{n}_y} &= (\alpha_3 - \alpha_2) L_S \dot{n}_y, \\ \frac{\partial \mathcal{D}}{\partial \dot{n}_z} &= (\alpha_3 - \alpha_2) L_S \dot{n}_z, \end{aligned} \tag{6.13}$$

where L_S is the surface length to scale the effect of the surface energy into the bulk.

6.2.4 Optics

The optical properties are calculated using the 4x4 Berreman method. Further, applying an ac voltage leads to a time dependent transmission with repeating cycles, as shown in Figure 6.4. Each repeating cycle can be analysed in $\sin(t)$ and $\cos(t)$

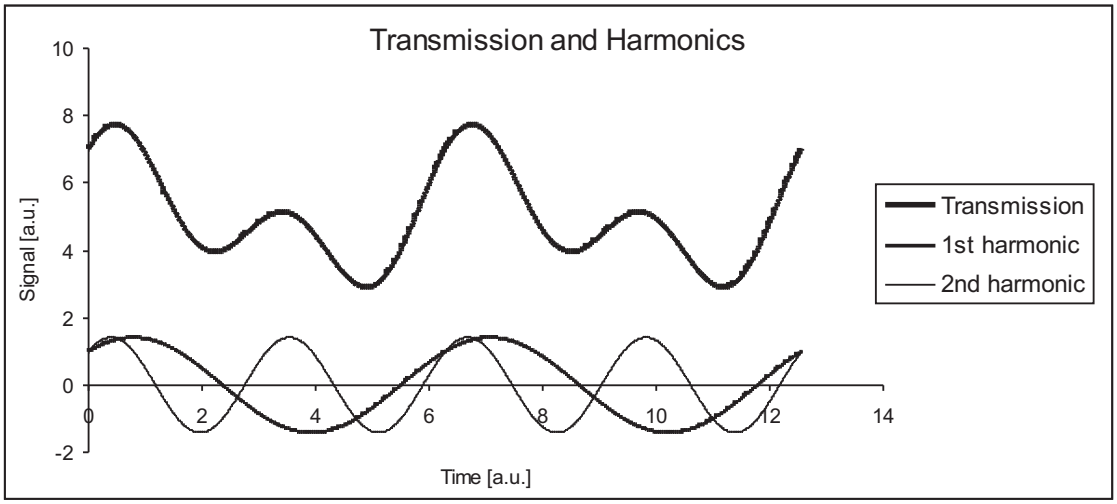


Figure 6.4: Transmission and harmonics

cycles of the frequency $\omega_0 t, 2\omega_0 t, 3\omega_0 t, 4\omega_0 t, ...$ These are called harmonics and can be extracted using the Fourier-Transformation. The general form is given by

$$y(t) = \frac{a_0}{2} + \sum_{n=1}^{\infty} \left[a_n \cos\left(n\omega_0 t\right) + b_n \sin\left(n\omega_0 t\right) \right], \tag{6.14}$$

where $y(t)$ is the time dependent transmission, n is the number of harmonics ($n = 1, 2, 3, 4, ...$), $\omega_0 = 2\pi f$ is the frequency, a_0 is the average of the transmission, a_n the magnitude of the n-th $\cos(t)$, and b_n the magnitude of the n-th $\sin(t)$. The calculation of a_n and b_n is done by

$$a_0 = \frac{2}{T} \int_{(T)} y(t) \mathrm{d}t, \tag{6.15}$$

$$a_n = \frac{2}{T} \int_{(T)} y(t) \cos(n\omega_0 t)\, \mathrm{d}t, \tag{6.16}$$

$$b_n = \frac{2}{T} \int_{(T)} y(t) \sin(n\omega_0 t)\, \mathrm{d}t. \tag{6.17}$$

Therefore the magnitude of the n-th harmonic can be calculated by

$$mag_n = \sqrt{a_n^2 + b_n^2}. \tag{6.18}$$

During the measurement, only the average of the transmission and the magnitude of the 1st and 2nd harmonics are recorded. These three pieces of information are used to determine the fitting parameter and the flexoelectric sum $(e_1 + e_3)$. The first harmonic is the response of the director to E, which corresponds to the flexoelectric part. This can be illustrated by the flexoelectric energy

$$w_f = -\left(e_1 \vec{n} \left(\nabla \cdot \vec{n}\right) + e_3 \left(\nabla \times \vec{n}\right) \times \vec{n}\right) \cdot \vec{E},$$

where

$$\vec{E} = E_0 sin(\omega t). \tag{6.19}$$

The 2nd harmonic response to E^2, which corresponds to the dielectric term. This can be illustrated by the dielectric energy

$$w_e = -\frac{1}{2}\epsilon_0 \Delta\epsilon \left(\vec{n} \cdot \vec{E}\right)^2,$$

where

$$\vec{E}^2 = E_0^2 sin^2(\omega t) = \frac{1}{2}E_0^2 - \frac{1}{2}E_0^2 cos(2\omega t). \tag{6.20}$$

6.2.5 Preinvestigation of cell structure

Using the theory, the director profile can be simulated. Before presenting the simulation for the Pi cell, the theoretical results for the HAN cell are discussed, to illustrated the difference between the HAN and Pi cell. Figure 6.5 shows the the director profile of the HAN cell for different voltages. The cases of 1V, -1V, and

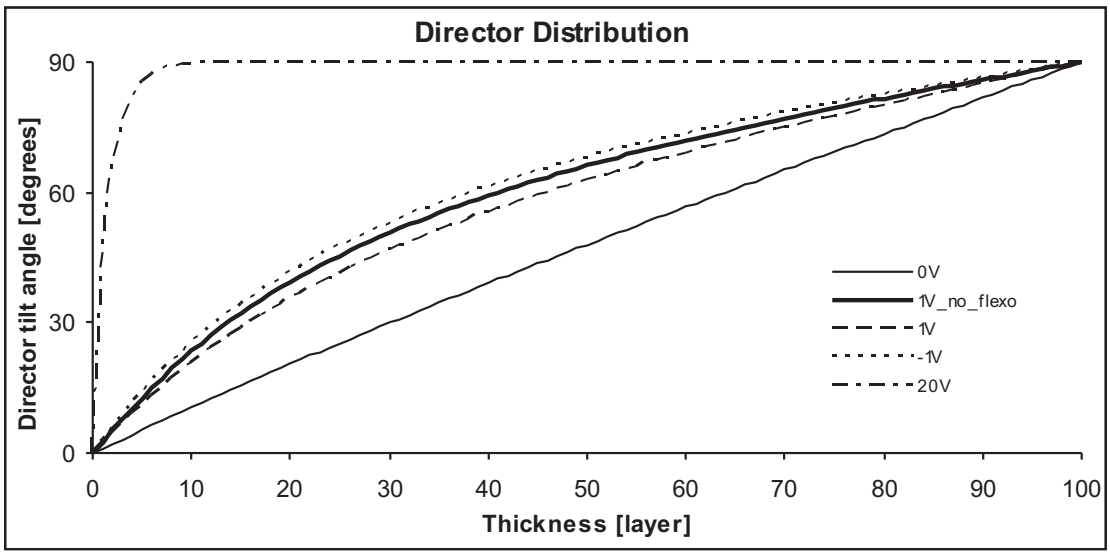


Figure 6.5: Director profile for a HAN structure

1V_no_flexo shows the strong response of the flexoelectric effect. In the HAN cell the flexoelectric effect occurs in the bulk.

The theoretical results for the Pi cell are shown in Figure 6.6. The director profile is simulated for different voltages. But the small bulk flexoelectric response is a big disadvantage. This can be solved using a high pretilt and a weak surface anchoring. A weak surface anchoring means that the molecules at the surface can move. This leads to a stronger flexoelectric response as shown in Figure 6.7. In the Pi cell flexoelectricity is caused mainly by the surface and the area near the surface and is therefore called surface flexoelectricity. The surface anchoring depends on the alignment layer. Simulations showed that if an alignment layer with a low pretilt

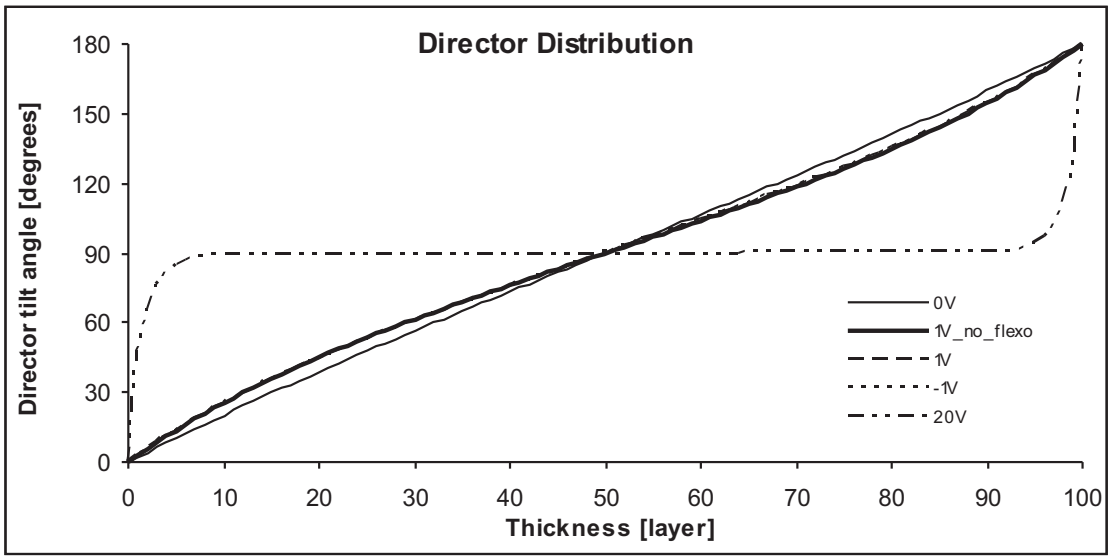


Figure 6.6: Director profile for a Pi cell in the V-state for a pretilt of 0° and strong surface anchoring

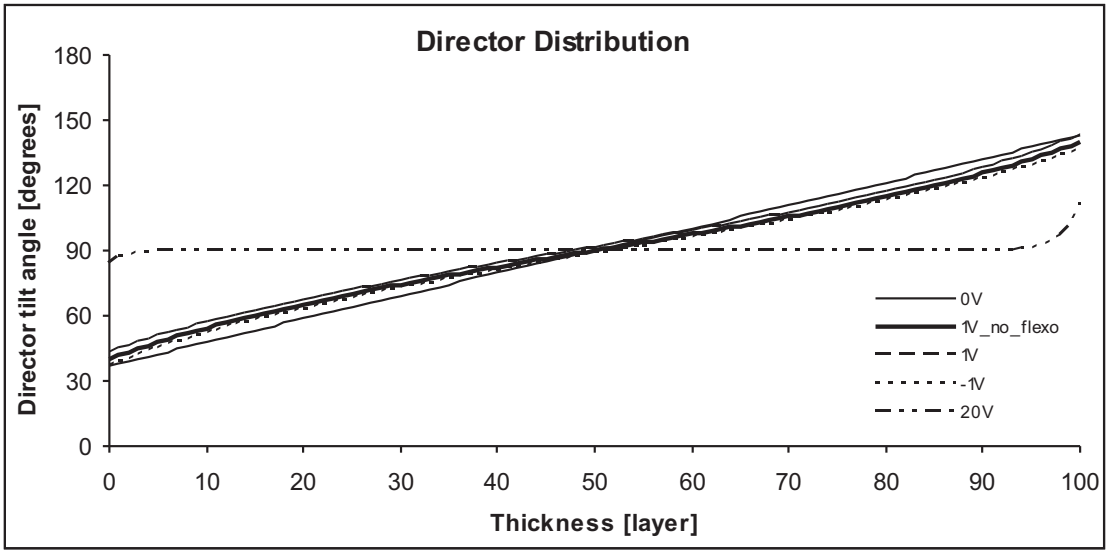


Figure 6.7: Director profile for a Pi cell in the V-state for a pretilt of 30° and weak surface anchoring

is used, i.e. 1°, the surface anchoring must be very weak to allow the surface to be pulled away significantly. But it is difficult to find materials with this property. Therefore it is better to use a high pretilt, i.e. 30°, where the surface anchoring

must still be weak but not as weak as in the low pretilt case. The reason for this is that in a high pretilt structure, the director can be pulled away from the surface and also pushed to the surface. To realise the high pretilt, SiOx is evaporated as described in the next section.

6.3 Experiment

6.3.1 Production of cell with high pretilt

The high pretilt was realised by evaporating SiOx onto the glass plates as shown in Figure 6.8. Evaporating SiOx at an angle of 85° creates a high pretilt [29].

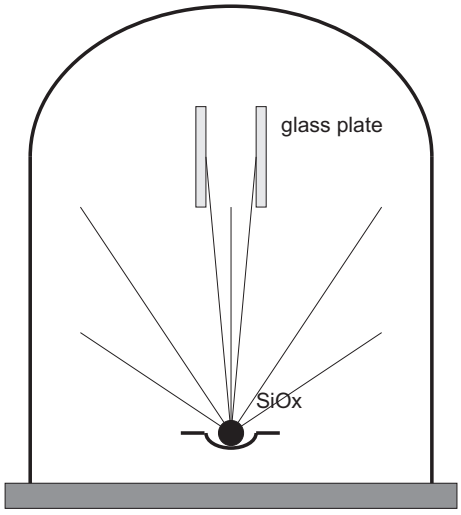


Figure 6.8: Evaporator to create a cell with a high pretilt

The two indium coated glass plates were placed in the evaporation chamber facing each other with a defined distance from the source and to each other, so that the evaporation beam hit the surface at an angle of 85^o. This also ensures that the quality of the alignment layer is the same at both glass plates and therefore has a similar pretilt and surface anchoring. The pretilt depends on the thickness of the SiOx layer (here 4nm) and the liquid crystal material and is about 34° [30]. This

was confirmed, measuring the pretilt at 34°. But the evaporation process is very difficult and the quality of the SiOx layer depends strongly on the vacuum in the chamber, the position of the glass plates relative to the source, the evaporation rate, the thickness of the SiOx layer, the cleanness of the glass plates. The evaporation rate is very critical and depends on the current, which is used to heat up the SiOx. If the temperature is too low, SiO is produced, which condensates quickly as rush. If the temperature is too high, clumps of SiOx are spat out, which could damage the SiOx layer or even attach to the layer. After the evaporation process, the cells were assembled and filled with the liquid crystal material and used for the measurement.

6.3.2 Experimental Set-up

A He-Ne laser with a wavelength of $\lambda = 632nm$ was used for the experiment, as shown in Figure 6.9. Because of the varying quality of the SiOx layer, using a laser

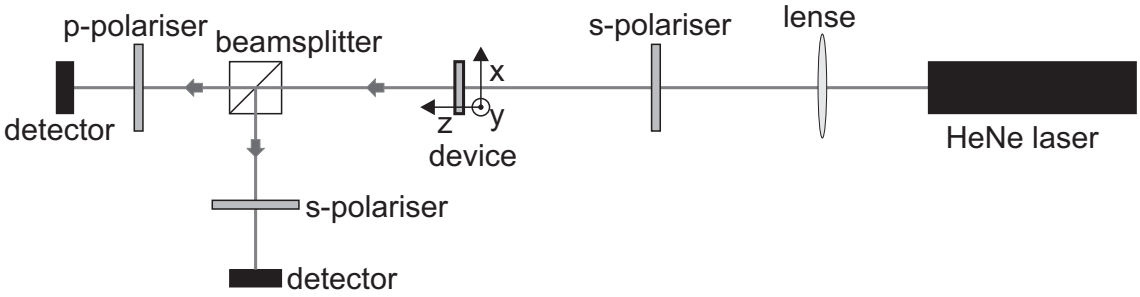


Figure 6.9: Experiment to measure the sum ($e_1 + e_3$)

beam with a diameter of about 2mm catches, in general, a spot where the quality is poor in some parts of the measured area. To decrease this problem a lens with a focal length of 30cm was used. The lens was mounted 30cm in front of the cell, so that the beam was focused into a small spot of about 0.5mm diameter before hitting the cell. This had the big advantage that if a bad area was measured, the whole data looked obviously bad.

The laser beam was polarised with an s-polariser and passed through the cell which was rotated by 45° around the axis of the laser beam (z-axis). A beam splitter divided the laser beam so that one part was passed through a p-analyser (crossed) and the second through an s-analyser (parallel). In this way it was possible to compare and check the results from both detectors. Both detector signals were fed into an oscilloscope to measure the transmission and into a Lock-in amplifier to extract the magnitudes of the first and the second harmonic.

6.3.3 Data

For a transmission at normal incidence as shown in Figure 6.10, there is no difference in director profile for a cycle of positive (+ve) and negative (-ve) voltages (Fig. 6.10 b), because of the symmetrical structure. But for a transmission at oblique incidence, i.e. 45°, the director profile for a cycle of +ve and -ve looks different (Fig. 6.10 c) and therefore a first harmonic can be measured.

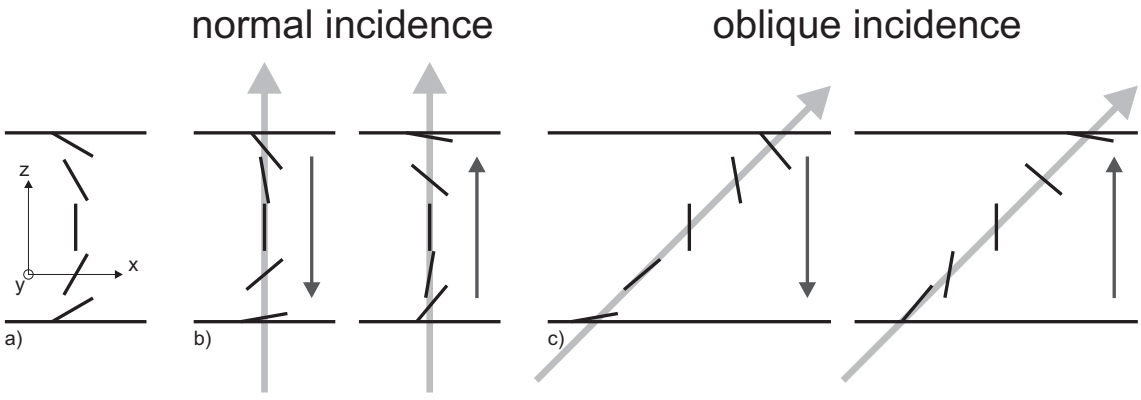
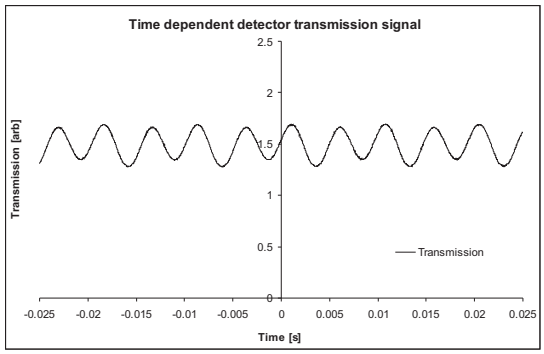
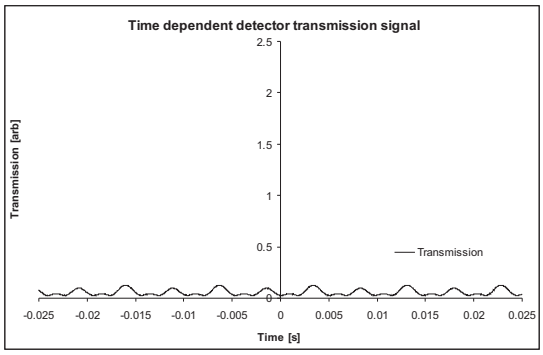


Figure 6.10: Laser beam at normal b) and oblique incidence c) with the director profile, which is seen by the laser beam for positive and negative voltages

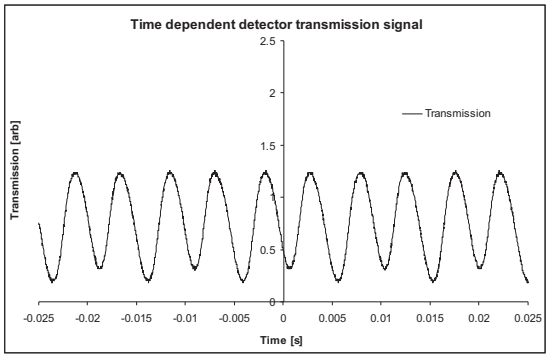
Figure 6.11 shows the transmission signal from an applied ac voltage of 2V, 4V, 8V and 20V. The average of the transmission signal is the magnitude of the transmission. In this case, the transmission at an ac voltage of 4V is almost zero. The first



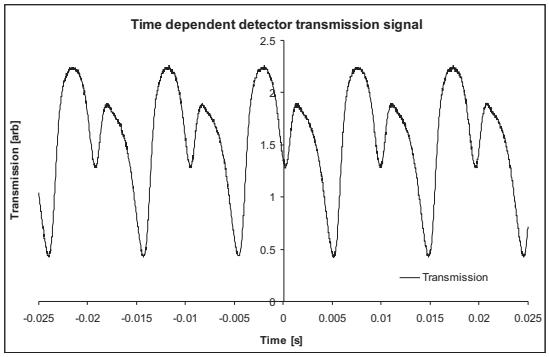
a) Applied voltage: 2V



b) Applied voltage: 4V



c) Applied voltage: 8V



d) Applied voltage: 20V

Figure 6.11: Transmission and Harmonics at oblique incidence (45°)

harmonic is very small at 2V, zero at 4V, bigger at 8V and very big at 20V. On the other hand, the second harmonic is always present at all ac voltage levels because of the dielectric properties.

For the measurement, the ac voltage with a frequency of 100Hz is applied and the transmission and harmonics are measured. Changing the voltage to the next value and measuring the transmission and harmonics leads to a measurement curve where the transmission versus ac voltage and the harmonics versus ac voltage can be drawn. This is done in the first measurement at normal incidence and in the second measurement at oblique incidence, as shown in Figure 6.12. For the measurement at oblique incident, the cell was rotated at 45^o around the y-axis. Figure 6.12 shows the measurement data at normal incident on the left side and the data at oblique incident on the right side. The transmission data is shown in the top graphs, whereby the

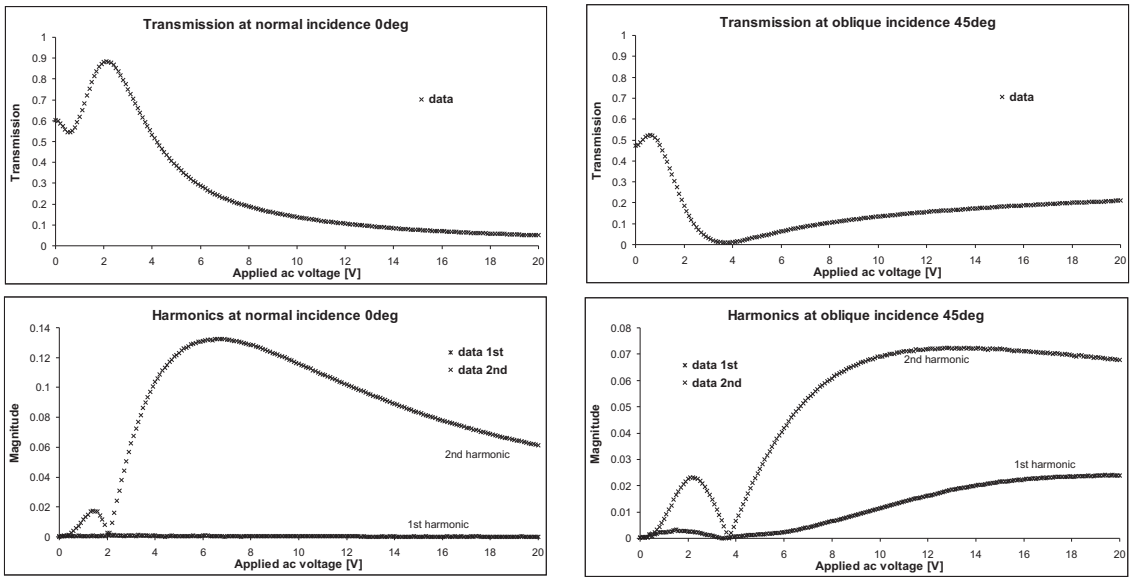


Figure 6.12: Measurement: On the left side is transmission (top) and harmonics (bottom) at normal incident and on the right side the transmission (top) and harmonics (bottom) at oblique incident

transmission versus applied ac voltage is presented. The bottom graphs show the harmonics versus applied ac voltage. In the left bottom graph, where the harmonics at normal incidence are presented, the first harmonic is zero over the whole voltage range. This is due to the symmetrical optical response, as discussed before. The second harmonics shows a big response. In the right bottom graph, where the harmonics at oblique incidence are presented, the first harmonic is present and shows a good response, not as big as the second harmonics, but big enough to measure the flexoelectric response.

Using a cell with a high pretilt has the big advantage that once the cell is switched into the V-State, the director stays in the V-State if the voltage is switched off [130]. In this way it is possible to to start the measurement from 0V and use the whole voltage range. Therefore, the voltage range can be varied between V=0V...20V as shown in Figure 6.12.

6.3.4 Frequency dependence

The measurement, as shown in Figure 6.12, was done at a frequency of 100Hz. A higher frequency, i.e. 5kHz as shown in Figure 6.13, is very good in order to avoid problems with ions but the magnitude of the harmonics is about 10 times smaller compared with a frequency of 100Hz. In particular, the magnitude of the first

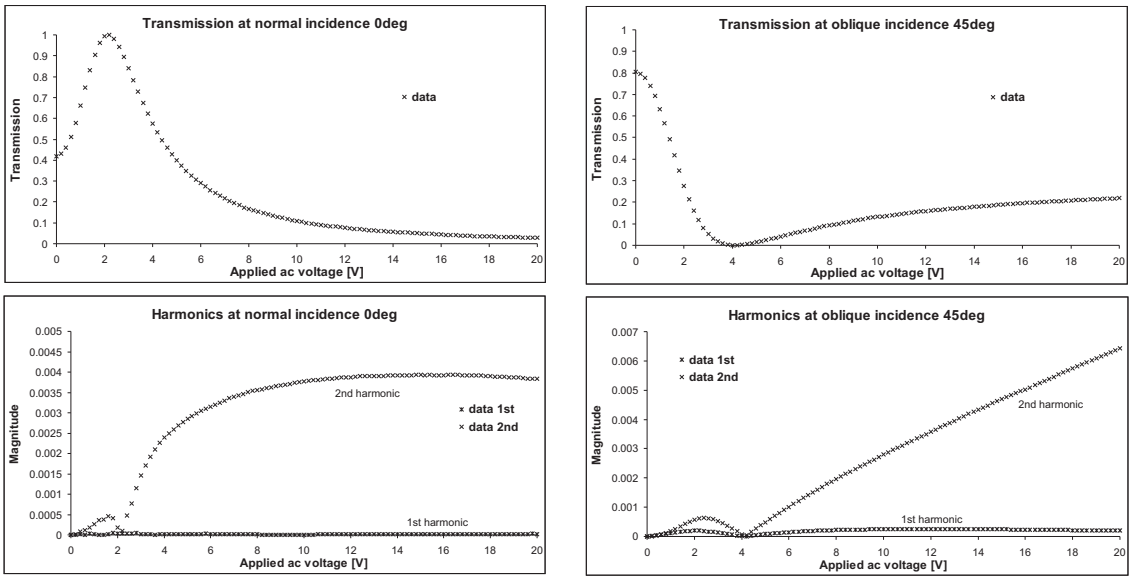


Figure 6.13: Data at a frequency of 5kHz. Very small first harmonics at oblique incidence

harmonic at oblique incidence is so small that a measurement of the flexoelectric coefficients is not possible. On the other hand, a lower frequency such as 10Hz, gives a very strong signal of the harmonics but big problems with ions. Therefore, the best compromise was choosing a frequency of 100Hz, which proved to be sensible and good for the experiment.

6.3.5 Automation

The measurement is done by applying an ac voltage, measuring the transmission and harmonics, from which the average of the transmission and magnitude of the

harmonics is calculated. Increasing the ac voltage and repeating the measurement and calculating the transmission and harmonics leads to a measurement curve. This whole process can be very time consuming if it is done manually. Automating the experiment has the big advantage of running the measurement with small voltage steps of 0.1V in a voltage range between 0V and 20V. This concludes in 200 voltage steps and therefore in 200 single measurements. The automation runs the experiment in a fraction of the time compared with a manual set up. With the automation, time and labour can be saved and the automation program can set the voltage automatically and receive the data from the oscilloscope and Lock-In amplifier. One set of data always contains both data at the normal incidence and the oblique incidence. The automation program first runs with the set up at normal incidence and after finishing the measurement, the user has to change the rotation of the liquid crystal cell by 45^o around the y-axis and start the second measurement. Both measurements give the complete set of data which is used for the fitting of the flexoelectric coefficients. All measurements were carried out at room temperature (22°C).

6.3.6 Fitting

The fitting was done using the data at normal and oblique incidence. This gives more information and increases the quality of the fit and results, because the fitting shows that at least two parameters have the same or opposite influence on one curve. Using the data at normal and oblique incidence, with transmission and two harmonics for each case, gives a total of six curves, which have to be fitted. Even if two parameters have the same influence on one curve, the influence of the other five curves is different. This increases the quality of the fitting but makes it also more complicated and time consuming. For example, one fitting run takes about five minutes, at least.

For the fitting, the following parameters are very important: thickness, pretilt, surface anchoring, incidence angle, flexoelectric coefficients and three flow parameters (η_1, η_2, γ_1). The thickness and pretilt were measured with an empty cell, in order to have a starting condition for the fitting. The incidence angle was set to 45° as close as possible but still small inaccuracies in the setting have a big influence. Only three of the five flow parameter have a significant influence. This means that eight parameter are used for the fitting, which is quite a lot, but necessary.

6.4 Results

6.4.1 Material E7

For the first measurements, the standard commercial mixture E7 was used. The data and fit are in very good agreement, as shown in Figure 6.14. The sum of the

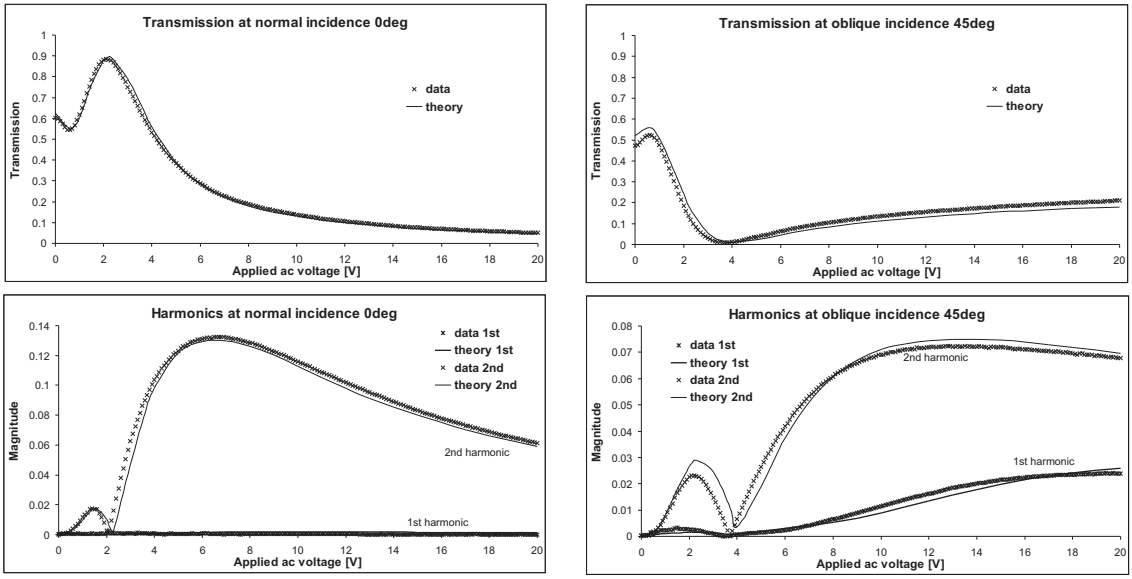


Figure 6.14: First measurement of E7: $(e_1 + e_3)$=(35±5.0) pC/m

flexoelectric coefficients was measured with $e_1 + e_3 = (35.0 \pm 5.0) \cdot 10^{-12} C/m^2$ for

E7. The fitting parameters are: thickness 11.8μm (measured 12.0μm); pretilt 36° (measured 34°); surface anchoring 1.0e-4; incident angle 45° (set 45°); flow parameter η_1=0.25, η_2=0.03, γ_1=0.18.

However, using the same E7 cell as before and taking more data from different areas of the cell, a different picture of the first harmonics can be seen. For example, the second measurement, as shown in Figure 6.15, shows a stronger response of the

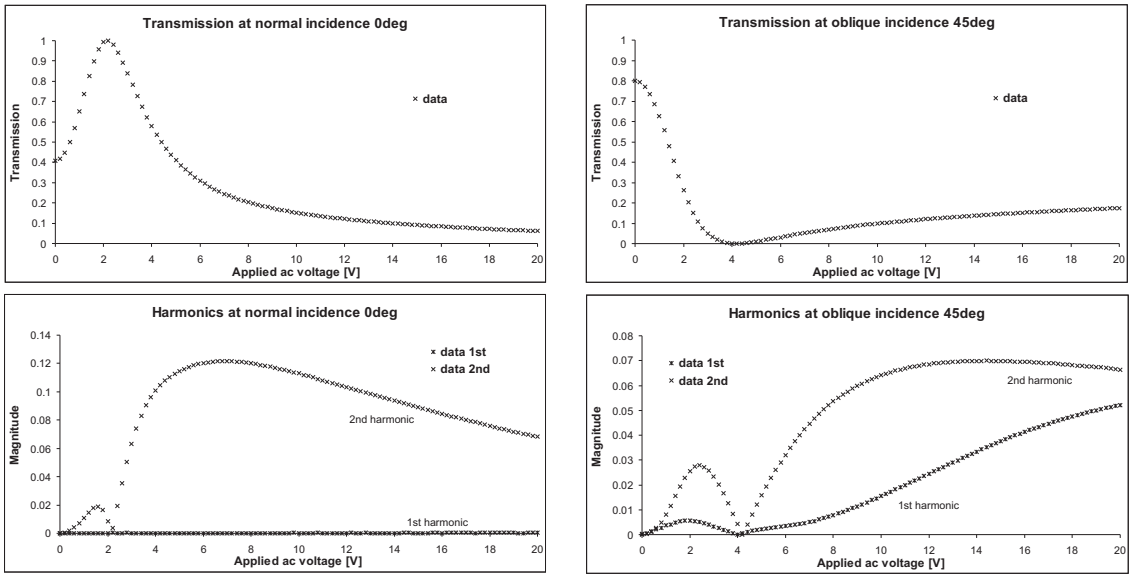


Figure 6.15: Second measurement of E7: $(e_1 + e_3) \approx 70$ pC/m

first harmonics at oblique incidence, which gives a bigger sum of the flexoelectric coefficients of approximately $(e_1 + e_3) \approx 70$ pC/m.

The third measurement, as shown in Figure 6.16, of the same E7 cell revealed an even stronger first harmonic response, which gives a huge sum of the flexoelectric coefficients of approximated $(e_1 + e_3) \approx 120$ pC/m.

The data of the second and third measurements were not fitted. The values of the flexoelectric coefficients $(e_1 + e_3)$ were simulated with the parameters from the first measurement because the transmissions and harmonics looked very similar to the data of the first measurement. These indicated similar parameter of thickness,

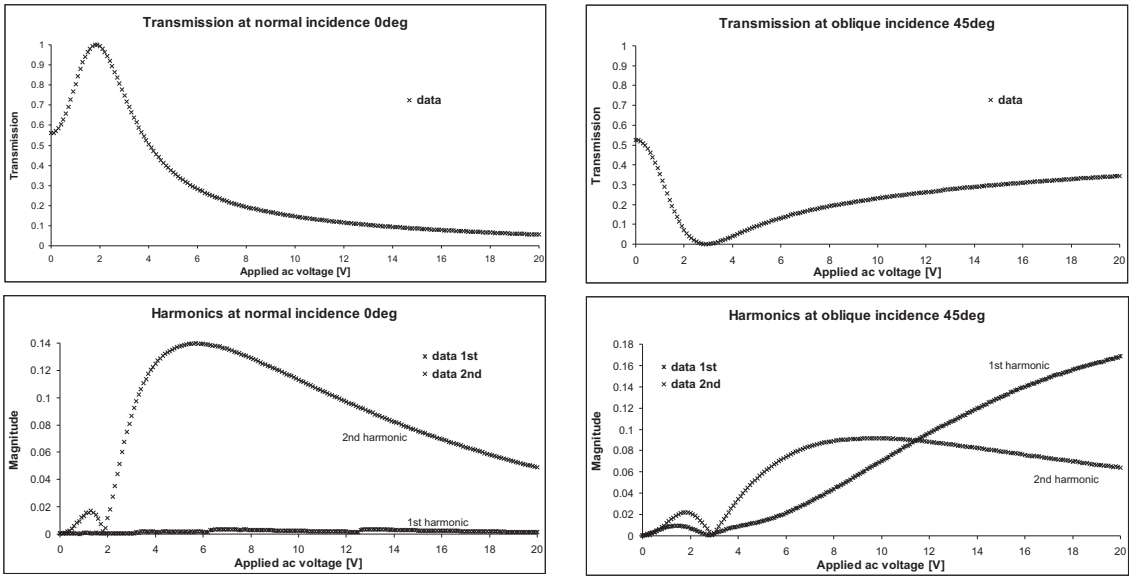


Figure 6.16: Third measurement of E7: $(e_1 + e_3) \approx 120$ pC/m

pretilt, surface anchoring, incidence angle and flow. This is not very surprising because all measurements were done with the same cell. In the simulation, as shown in Figure 6.17, the value of the sum $(e_1 + e_3)$ was varied until the magnitude of

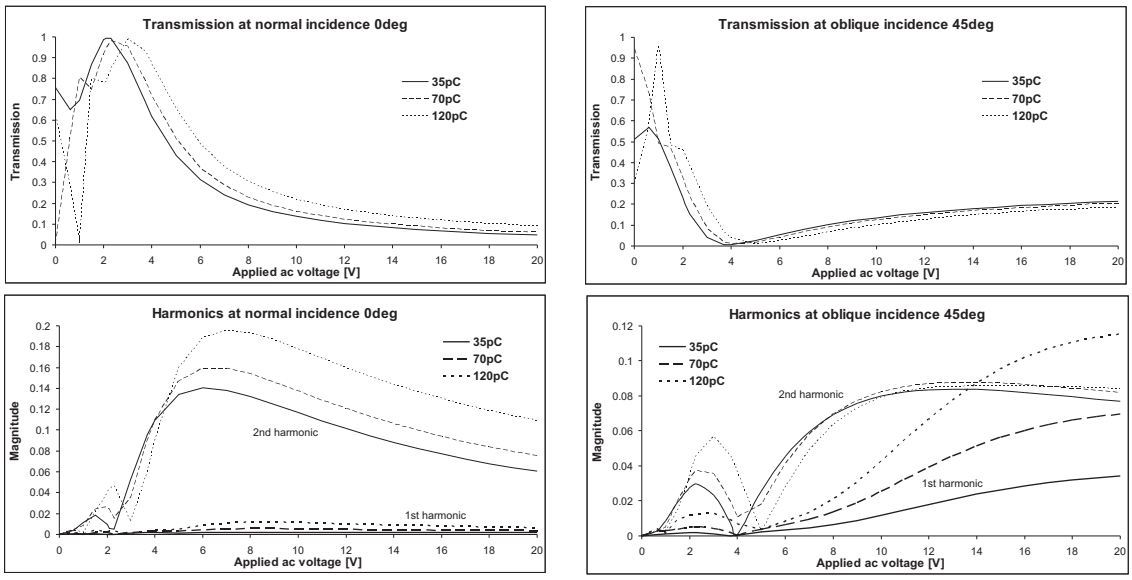


Figure 6.17: Simulation for E7 of the sum $(e_1 + e_3)$ with 35 pC/m, 70 pC/m and 120 pC/m

the first harmonics at oblique incidence was right. The simulation with different flexoelectric values also showed that big values of the sum $(e_1 + e_3)$ have a huge influence on the transmission but this could not be seen in the data. Therefore, a perfect and complete fit of all measurements did not make sense because the results for sum $(e_1 + e_3)$ are very different and are not reliable. To check if this problem occurs only in this this cell or only with the material E7, a second material CB was used in the experiment.

6.4.2 Material CB

The liquid crystal material CB was filled in a second Pi cell and used in the experiment. The first measurement, as shown in Figure 6.18, showed a strong first

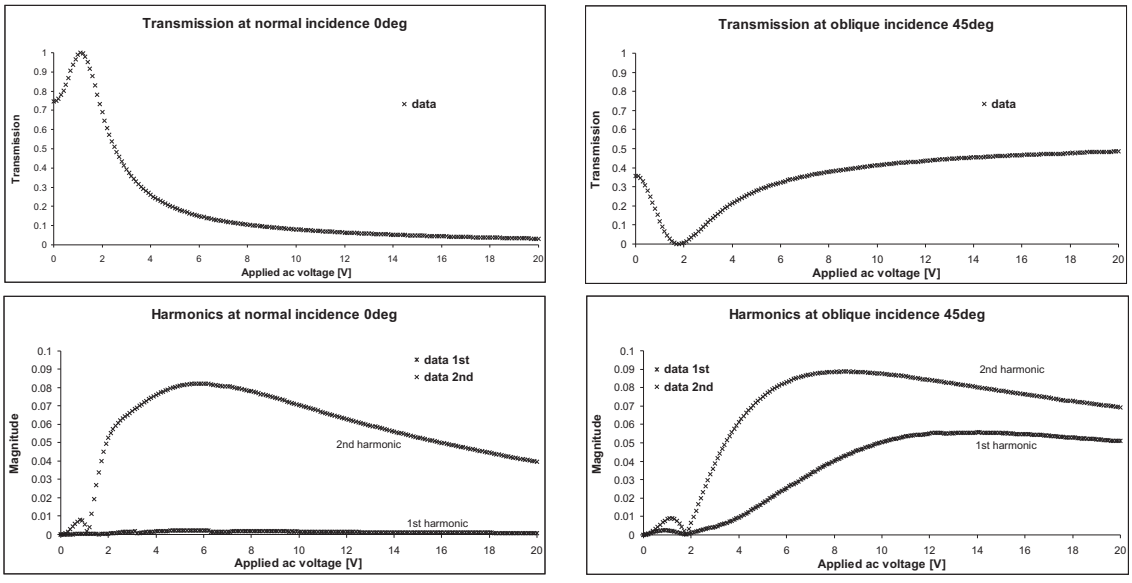


Figure 6.18: First measurement of CB: $(e_1 + e_3) \approx 80$ pC/m

harmonic, which gives a sum of approximated $(e_1 + e_3) \approx 80$ pC/m. The approximation was done, using the simulation with the physical properties of CB but with the cell parameters of the E7 measurement.

The second measurement, as shown in Figure 6.19, gave a sum of approximated

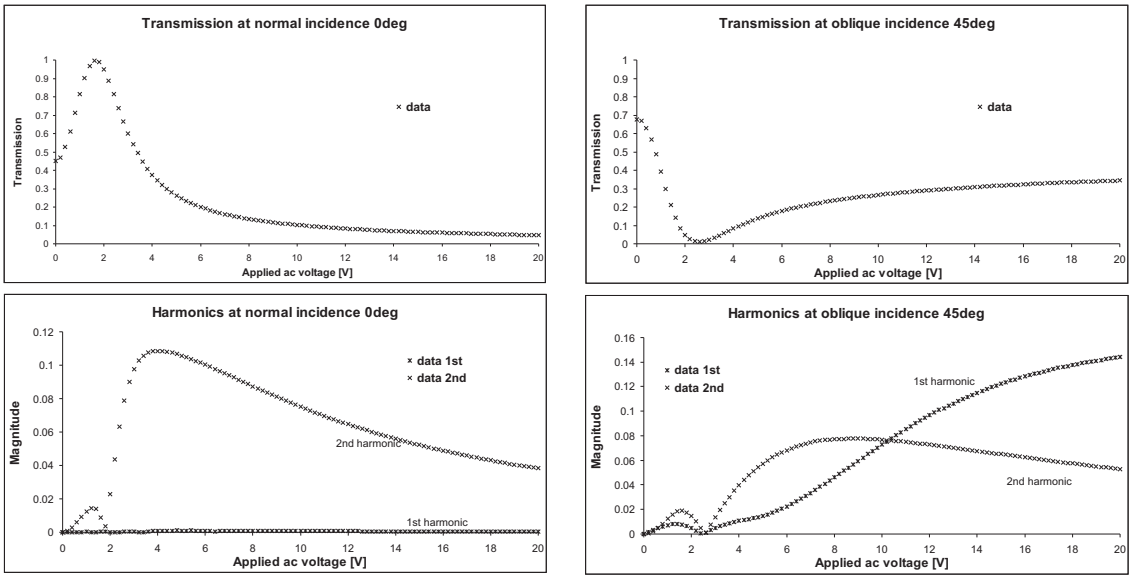


Figure 6.19: Second measurement of CB: $(e_1 + e_3) \approx 170$ pC/m

$(e_1 + e_3) \approx 170$ pC/m. Again, the data shows a strong variety in the first harmonics and proves that the Pi cell method is not reliable for measuring the sum $(e_1 + e_3)$.

6.4.3 Dielectric properties materials

Even though, the Pi cell experiment is not a reliable method to measure the sum $(e_1 + e_3)$, it can be used to investigate the influence of the dielectric properties. Therefore, the Material B [84] with a dielectric anisotropy of $\Delta\epsilon$=42.1 is used for the measurement. The data showed a huge first harmonic, as shown in Figure 6.20, which exceeded all expectations and the sum can only be estimated with $(e_1 + e_3) \approx 1000$ pC/m. We can question, if this value for the sum is realistic. Nevertheless, the magnitude of the first harmonic is outstanding. It is not possible to measure and fit the flexoelectric sum $(e_1 + e_3)$ accurately, but it is possible to say that compared to the materials E7 and CB in a material with a big dielectric anisotropy of $\Delta\epsilon$=42.1, the flexoelectric response is also strong.

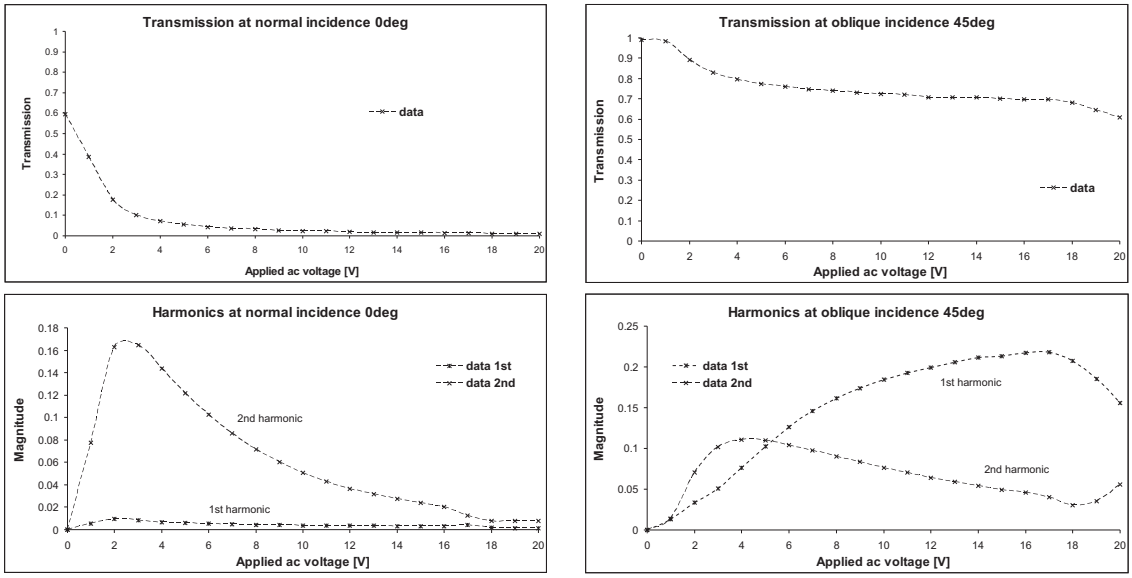


Figure 6.20: Material B [84]: $(e_1 + e_3) \approx 1000$ pC/m

6.4.4 Non-ionic materials

Further, it is possible to use the Pi cell experiment to investigate the influence of ions by using non-ionic materials. The material TL216 was filled in a Pi cell and used in the experiment. The data, as shown in Figure 6.21, shows no first harmonic

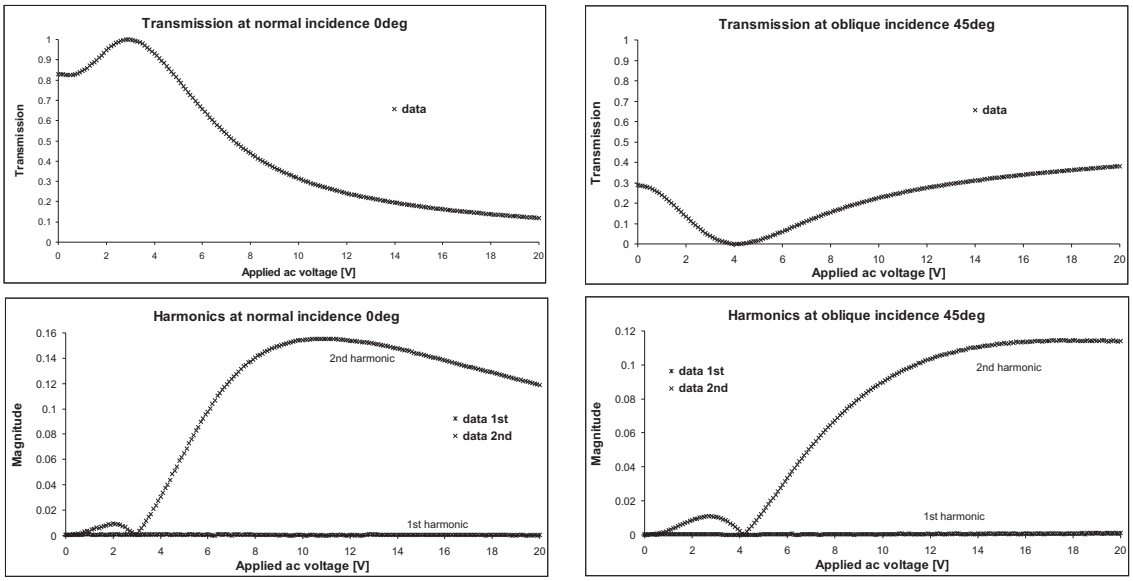


Figure 6.21: TL216: $(e_1 + e_3) \approx 0$ pC/m

at oblique incidence. This shows clearly that TL216 has no flexoelectric properties.

Using the material MLC-7021-100, which is also a non-ionic material, the data also shows no first harmonic at oblique incidence, as shown in Figure 6.22. Also, the

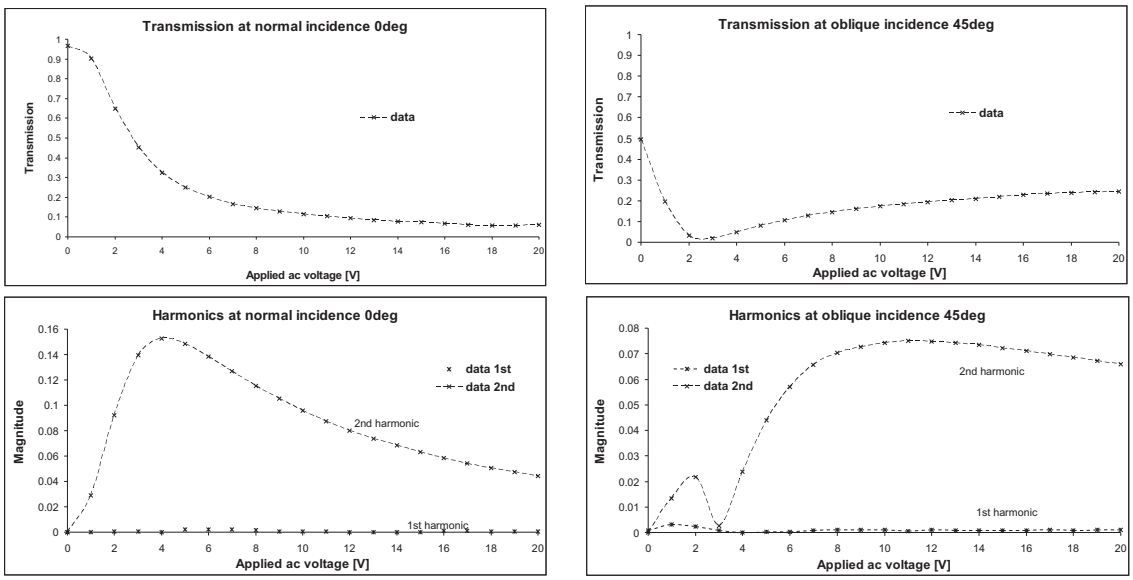


Figure 6.22: MLC-7021-100: $(e_1 + e_3) \approx 0$ pC/m

second non-ionic material has no flexoelectric properties.

The third non-ionic material MLC-13900-100 also shows no first harmonic at oblique incident, as shown in Figure 6.23. All three non-ionic materials show no flexoelectric properties. This is a clear evidence that ions play an important role.

Now, using the non-ionic material TL216 and mixing 10% of the ionic material E7 into TL216 and filling this mixture into a Pi cell shows a very interesting behaviour. The data shows clearly a first harmonic response, as shown in Figure 6.24, whereby the magnitude of the first harmonic is in the range of the magnitude of the first harmonic of the first E7 measurment (Fig. 6.14). This shows clearly that ions are very important for the flexoelectric effect.

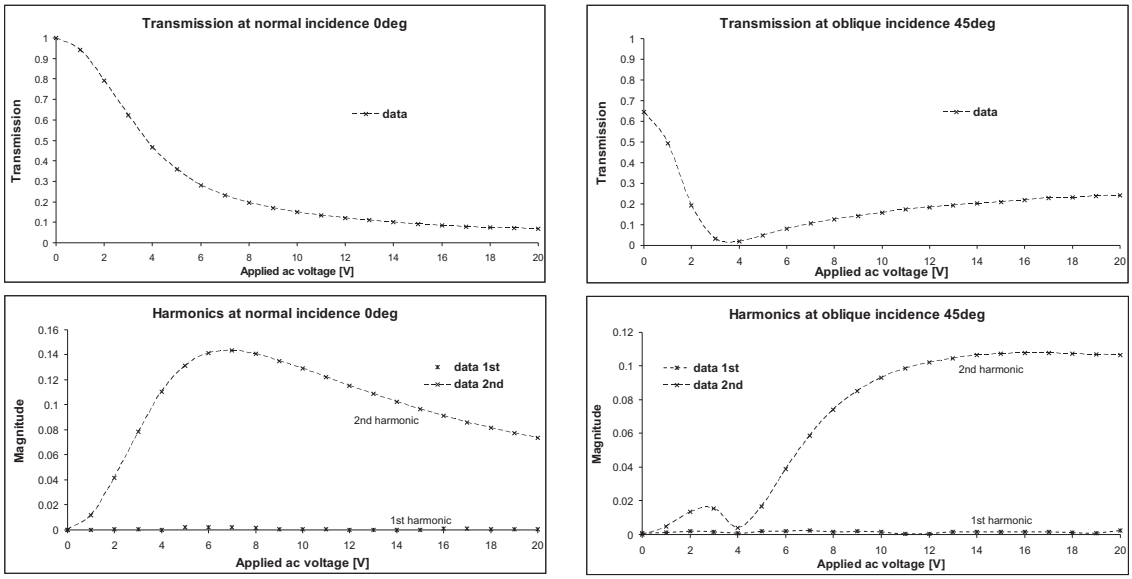


Figure 6.23: MLC-13900-100: $(e_1 + e_3) \approx 0$ pC/m

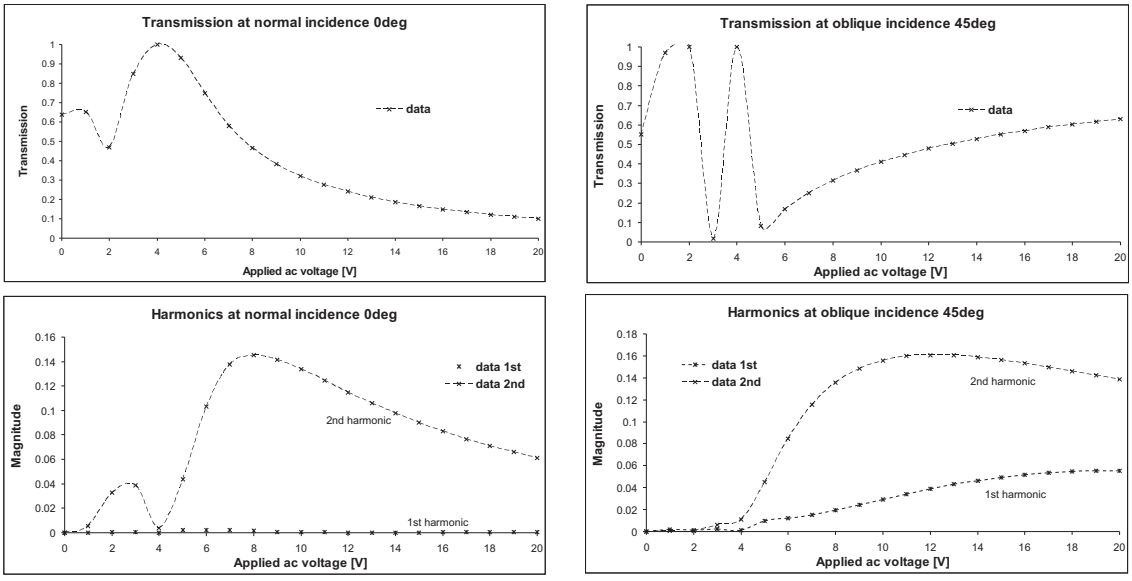


Figure 6.24: TL216 with 10% E7: $(e_1 + e_3) \approx 30$ pC/m

6.5 Conclusion

The Pi cell experiment is not useful for measuring accurately the flexoelectric sum $(e_1 + e_3)$ because there are strong variations in the first harmonic data for different measurements at the same cell. All materials showed an enhanced first harmonic

except the non-ionic materials. Is this enhancement due to flexoelectricity or due to some surface effects? In the Pi cell, the flexoelectric effect is a surface or a near surface effect. It might be that the surface flexoelectric effect occurs in a normal order and an additional surface effect might enhance the first harmonic. Two arguments could back up this idea. First, ions play a very important role and second the strong variation of the first harmonic at different measurements at the same cell. It could be possible, that ions are trapped at the surface and orientate the molecules in the same direction, as shown in Figure 6.25 a), or that the SiOx might orientate the molecules in the same direction, as shown in Figure 6.25 b). The argument that the alignment layer SiOx might influence the effect can be seen in the strong variation of the first harmonic at different measurement areas at the cell. It would be also be possible that due to the inhomogeneous SiOx layer, ions might be trapped in different concentrations at different areas. But this all is just a guess and further investigations are necessary to clearly understand the interesting surface effect in the Pi cell. For this project, the Pi cell showed that it is not possible to measure the flexoelectric coefficients accurately and, therefore, the work on the Pi cell was stopped here. The Pi cell might be interesting for a future project.

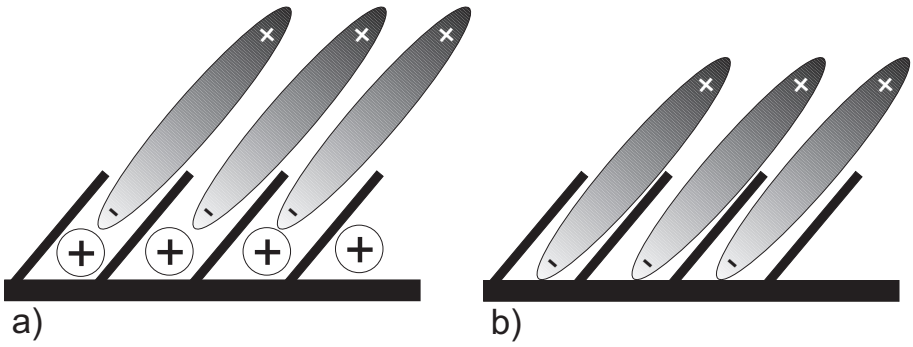


Figure 6.25: Surface effects in Pi cell

However, even if the Pi cell experiment did not give accurate results, the data showed that ordinary materials like E7 or CB had a similar first harmonic response

compared with the Material B [84], which has a big dielectric anisotropy of $\Delta\epsilon$=42.1 and also high first harmonic response. This indicates that the dielectric properties have an influence on the flexoelectric sum (e_1+e_3). Further, it is interesting to notice that all three non-ionic materials TL216, MLC-7021-100 and MLC-13900-100 did not show any first harmonic response. Mixing 10% of the ionic material E7 into the non-ionic material TL216 showed a similar first harmonic response as in the normal E7 material. This indicates that ions are important for the flexoelectric effect. Ions might enhance the first harmonic due to surface effects but without ions there is no first harmonic response at all.

6.5.1 Future

In the future it might be an interesting idea to try a different alignment layer compared to SiOx. The alignment layer should also create a high pretilt and weak surface anchoring. Maybe with a better and more homogeneous alignment layer the results would be more reliable and repeatable.

Originally, the idea for the Pi cell experiment was developed out of the HAN cell. The HAN cell has the big advantage of a strong bulk flexoelectric response, but with the problem of an offset voltage due to a surface polarisation. In the next chapter, a new method is presented which uses the HAN cell but which tries to overcome the disadvantages of the HAN cell.

Chapter 7

Simple pulses to measure sum $(e_1 + e_3)$

7.1 Introduction

In the last chapter the Pi cell experiment was presented. This experiment is based on the advantages of the HAN cell and trying to overcome the disadvantages of the HAN cell. Unfortunately, the Pi cell experiment showed insurmountable problems and was not reliable. This chapter presents a method whereby a HAN cell is used with the goal of minimising the disadvantages of the HAN cell. As explained in the last chapter, the HAN cell shows a strong flexoelectric response when an electric field E is applied across the device, because of the asymmetric structure due to the homeotropic alignment on one side and the planar alignment on the other side. Due to flexoelectricity, an applied dc voltage distorts the director differently for positive voltage compared to negative voltage. This distortion can be measured and used to determine the sum $(e_1 + e_3)$. However, there is a surface polarisation associated with the homeotropic alignment [62, 63]. This may be caused by the polarity of the

surface aligning material together with the ordering of the liquid crystal molecules at the surface. This surface polarisation acts like an offset voltage and is in the range of a few hundred millivolts [63]. To avoid confusion between an external applied offset voltage and the offset voltage created by the surface polarisation, we refer to it here as the "internal bias". This internal bias influences strongly the measurement of the sum $(e_1 + e_3)$ and it is therefore very important to determine the internal bias and include it in the flexoelectric measurement.

The commercial material TL216 is non-ionic and has negligible flexoelectricity; this was investigated in Chapters 5 and 6. Both criteria are important and necessary to determine the internal bias. Negligible flexoelectricity is important because the HAN structure has a strong splay-bend distortion from one substrate to an other substrate, due to the different alignment structures. In a material with flexoelectricity, this strong splay-bend distortion would lead to a net flexoelectric polarisation, which shows electro-optic behaviour similar to that caused by an offset voltage. It would be not possible to differentiate between the apparent offset voltage caused by the flexoelectric polarisation and the internal bias, and it is therefore impossible to measure the internal bias.

Our new method uses short dc pulses and measures the optical response [131]. First a positive pulse with a magnitude of 1V and a pulse length of 2ms is applied and 100ms after the positive pulse, a negative pulse with a magnitude of -1V and a pulse length of also 2ms is applied. The average of the dc pulses is always zero. The dc pulses are long enough to see the flexoelectric effect but short enough to minimise problems with ions. A theoretical model is required to fit the data and extract the results for the sum $(e_1 + e_3)$.

7.2 Theory

The theoretical model to simulate the dynamic behaviour of the HAN cell is based on the coordinate system shown in Figure 7.1, whereby the applied electric field and

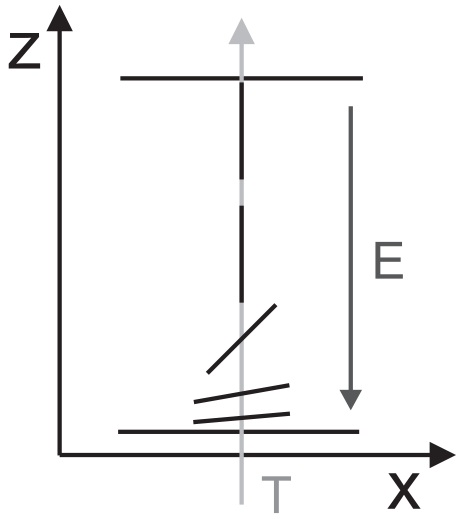


Figure 7.1: Coordinate system for 1-D model

the director is calculated in a 1-dimensional model along the z axis (in 100 layers). The dynamic 1-D model includes the bulk energy L_B and calculates the transmission through the device using the 2x2 Jones optics. The theoretical model of the HAN cell is very similar to the theoretical model used in the Pi cell experiment. The HAN cell model also calculates the dynamic behaviour but in a simpler way, of short dc pulses. The model includes the bulk energy L_B but without flow and with fixed surfaces. The theory presented on the following pages is very similar to the theory of the Pi cell. It would not be necessary to repeat the calculation but to complete this chapter and for a better understanding of the HAN theory compared to the Pi model, the whole theory is presented.

As shown in Chapter 3, the bulk energy L_B (Eq. 3.33) is the sum of the the elastic

energy w_d, flexoelectric energy w_f and dielectric energy w_e as

$$\begin{aligned} L_B &= w_d + w_f + w_e \\ L_B &= \frac{1}{2}K_{11}\left(\nabla\cdot\vec{n}\right)^2 + \frac{1}{2}K_{22}\left(\vec{n}\cdot\left(\nabla\times\vec{n}\right)-q\right)^2 + \frac{1}{2}K_{33}\left(\vec{n}\times\left(\nabla\times\vec{n}\right)\right)^2 \\ &\quad -\left(e_1\vec{n}\left(\nabla\cdot\vec{n}\right)+e_3\left(\nabla\times\vec{n}\right)\times\vec{n}\right)\cdot\vec{E} - \frac{1}{2}\vec{D}\cdot\vec{E}. \end{aligned} \tag{7.1}$$

The electric field $\vec{E}$ with its only component along the z direction is not constant and it changes along the z direction. The calculation of E_z is presented in the next section. But these lead to a bulk energy L_B of

$$\begin{aligned} L_B = &\frac{1}{2}K_{11}n_z^{'2} + \frac{1}{2}K_{22}\left(n_y n_x^{'} - n_x n_y^{'} - q\right)^2 \\ &+\frac{1}{2}K_{33}\left(n_z^2 n_x^{'2} + n_z^2 n_y^{'2} + n_z^2 n_z^{'2}\right) \\ &-\left(e_1+e_3\right)n_z n_z^{'}E_z \\ &-\frac{1}{2}\epsilon_0\left(\Delta\epsilon n_z^2 + \epsilon_\perp\right)E_z^2, \end{aligned} \tag{7.2}$$

whereby the following calculations are used

$$\nabla = \begin{pmatrix} 0 \\ 0 \\ \frac{\partial}{\partial z} \end{pmatrix}, \vec{n} = \begin{pmatrix} n_x \\ n_y \\ n_z \end{pmatrix}, \vec{E} = \begin{pmatrix} 0 \\ 0 \\ E_z \end{pmatrix},$$

$$\nabla\cdot\vec{n} = \begin{pmatrix} 0 \\ 0 \\ \frac{\partial}{\partial z} \end{pmatrix}\cdot\begin{pmatrix} n_x \\ n_y \\ n_z \end{pmatrix} = \frac{\partial n_z}{\partial z} = n_z^{'},$$

$$\vec{n}\left(\nabla\cdot\vec{n}\right) = \begin{pmatrix} n_x \\ n_y \\ n_z \end{pmatrix}\cdot n_z^{'} = \begin{pmatrix} n_x n_z^{'} \\ n_y n_z^{'} \\ n_z n_z^{'} \end{pmatrix},$$

$$\vec{n}\cdot(\nabla\times\vec{n}) = \begin{vmatrix} n_x & n_y & n_z \\ 0 & 0 & \frac{\partial}{\partial z} \\ n_x & n_y & n_z \end{vmatrix} = n_y\frac{\partial n_x}{\partial z} - n_x\frac{\partial n_y}{\partial z} = n_y n_x^{'} - n_x n_y^{'},$$

$$(\nabla\times\vec{n})\times\vec{n} = \left[\begin{pmatrix} 0 \\ 0 \\ \frac{\partial}{\partial z} \end{pmatrix}\times\begin{pmatrix} n_x \\ n_y \\ n_z \end{pmatrix}\right]\times\begin{pmatrix} n_x \\ n_y \\ n_z \end{pmatrix} = \begin{pmatrix} -n_y^{'} \\ n_x^{'} \\ 0 \end{pmatrix}\times\begin{pmatrix} n_x \\ n_y \\ n_z \end{pmatrix}$$

$$= \begin{pmatrix} n_z n_x^{'} \\ n_z n_y^{'} \\ -n_y n_y^{'} - n_x n_x^{'} \end{pmatrix} = \begin{pmatrix} n_z n_x^{'} \\ n_z n_y^{'} \\ n_z n_z^{'} \end{pmatrix},$$

$$(\vec{n}\times(\nabla\times\vec{n}))^2 = \begin{pmatrix} n_z n_x^{'} \\ n_z n_y^{'} \\ n_z n_z^{'} \end{pmatrix}^2 = n_z^2 n_x^{'2} + n_z^2 n_y^{'2} + n_z^2 n_z^{'2},$$

$$\vec{n}\,(\nabla\cdot\vec{n})\,\vec{E} = \begin{pmatrix} n_x n_z^{'} \\ n_y n_z^{'} \\ n_z n_z^{'} \end{pmatrix}\cdot\begin{pmatrix} 0 \\ 0 \\ E_z \end{pmatrix} = n_z n_z^{'} E_z,$$

$$((\nabla\times\vec{n})\times\vec{n})\,\vec{E} = \begin{pmatrix} n_z n_x^{'} \\ n_z n_y^{'} \\ n_z n_z^{'} \end{pmatrix}\cdot\begin{pmatrix} 0 \\ 0 \\ E_z \end{pmatrix} = n_z n_z^{'} E_z,$$

$$\vec{D}\vec{E} = \epsilon_0\left[\begin{pmatrix} \Delta\epsilon n_x^2 + \epsilon_\perp & \Delta\epsilon n_x n_y & \Delta\epsilon n_z n_x \\ \Delta\epsilon n_x n_y & \Delta\epsilon n_y^2 + \epsilon_\perp & \Delta\epsilon n_z n_y \\ \Delta\epsilon n_z n_x & \Delta\epsilon n_z n_y & \Delta\epsilon n_z^2 + \epsilon_\perp \end{pmatrix}\begin{pmatrix} 0 \\ 0 \\ E_z \end{pmatrix}\right]\begin{pmatrix} 0 \\ 0 \\ E_z \end{pmatrix}$$

$$= \epsilon_0\begin{pmatrix} \Delta\epsilon n_x n_z E_z \\ \Delta\epsilon n_y n_z E_z \\ (\Delta\epsilon n_z^2 + \epsilon_\perp)\,E_z \end{pmatrix}\cdot\begin{pmatrix} 0 \\ 0 \\ E_z \end{pmatrix} = \epsilon_0\left(\Delta\epsilon n_z^2 + \epsilon_\perp\right)E_z^2.$$

The general Euler-Lagrange equation (Eq. 3.10) simplifies for the 1-D model and

leads to a molecular field $\vec{h}$ of

$$\begin{aligned} h_x &= \frac{\partial}{\partial z}\left(\frac{\partial L_B}{\partial n_x^{'}}\right) - \frac{\partial L_B}{\partial n_x}, \\ h_y &= \frac{\partial}{\partial z}\left(\frac{\partial L_B}{\partial n_y^{'}}\right) - \frac{\partial L_B}{\partial n_y}, \\ h_z &= \frac{\partial}{\partial z}\left(\frac{\partial L_B}{\partial n_z^{'}}\right) - \frac{\partial L_B}{\partial n_z}, \end{aligned} \tag{7.3}$$

and the final solution of the Euler-Lagrange equations (Eq. 7.3) gives the molecular field $\vec{h}$ of

$$\begin{aligned} h_x = \;& K_{22}\left(n_y^2 n_x^{''} - n_x n_y n_y^{''} + 2n_y n_x^{'} n_y^{'} - 2n_x n_y^{'2} - 2q n_y^{'}\right) \\ & + K_{33}\left(2n_z n_x^{'} n_z^{'} + n_z^2 n_x^{''}\right), \\ h_y = \;& K_{22}\left(n_x^2 n_y^{''} - n_x n_y n_x^{''} + 2n_x n_x^{'} n_y^{'} - 2n_y n_x^{'2} + 2q n_x^{'}\right) \\ & + K_{33}\left(2n_z n_y^{'} n_z^{'} + n_z^2 n_y^{''}\right), \\ h_z = \;& K_{11} n_z^{''} + K_{33} n_z\left(n_z n_z^{''} - n_x^{'2} - n_y^{'2} + n_z^{'2}\right) \\ & - \left(e_1 + e_3\right) n_z E_z^{'} + \epsilon_0 \Delta\epsilon n_z E_z^2. \end{aligned} \tag{7.4}$$

whereby the following calculations are used

$$\begin{aligned} \frac{\partial L_B}{\partial n_x^{'}} &= K_{22}\left({n_y}^2 {n_x}^{'} - n_y {n_y}^{'} n_x - n_y q\right) + K_{33} {n_z}^2 {n_x}^{'}, \\ \frac{\partial}{\partial z}\left(\frac{\partial L_B}{\partial n_x^{'}}\right) &= K_{22}\left({n_y}^2 {n_x}^{''} - {n_y}^{'2} n_x - {n_y}^{'} q - n_y {n_y}^{''} n_x + {n_y}^{'} {n_x}^{'} n_y\right) \\ &\quad + K_{33}\left(2n_z {n_x}^{'} {n_z}^{'} + {n_z}^2 {n_x}^{''}\right), \\ \frac{\partial L_B}{\partial n_x} &= K_{22}\left(-{n_y}^{'} {n_x}^{'} n_y + {n_y}^{'2} n_x + {n_y}^{'} q\right), \\ \frac{\partial L_B}{\partial n_y^{'}} &= K_{22}\left(-n_x {n_x}^{'} n_y + {n_x}^2 {n_y}^{'} + n_x q\right) + K_{33} {n_z}^2 {n_y}^{'}, \\ \frac{\partial}{\partial z}\left(\frac{\partial L_B}{\partial n_y^{'}}\right) &= K_{22}\left(-n_x {n_x}^{''} n_y + {n_x}^{'} {n_y}^{'} n_x + {n_x}^{'} q + {n_x}^2 {n_y}^{''} - {n_x}^{'2} n_y\right) \end{aligned}$$

$$
\begin{aligned}
&+K_{33}\left(2n_z{n_y}'{n_z}' + {n_z}^2{n_y}''\right), \\
\frac{\partial L_B}{\partial n_y} &= K_{22}\left({n_x}'^2 n_y - {n_x}'{n_y}'n_x - {n_x}'q\right), \\
\frac{\partial L_B}{\partial n_z'} &= K_{11}{n_z}' + K_{33}{n_z}^2{n_z}' - (e_1+e_3)\,n_z E_z, \\
\frac{\partial}{\partial z}\left(\frac{\partial L_B}{\partial n_z'}\right) &= K_{11}{n_z}'' + K_{33}\left({n_z}^2{n_z}'' + 2n_z{n_z}'^2\right) \\
&\quad -(e_1+e_3)\,n_z{E_z}' - (e_1+e_3)\,{n_z}'E_z, \\
\frac{\partial L_B}{\partial n_z} &= K_{33}\left(n_z{n_z}'^2 + n_z{n_x}'^2 + n_z{n_y}'^2\right) \\
&\quad -(e_1+e_3)\,{n_z}'E_z - \epsilon_0\Delta\,\epsilon\,n_z{E_z}^2.
\end{aligned}
$$

As shown in Equation 7.4, the accurate determination of the non uniform electric field E_z is crucial for the theoretical model. This can be done by knowing the applied voltage V and the dielectric properties of the materials. As presented in the previous chapter, the electric field E_z can be calculated by Equation 6.8, which gives

$$
E_z = \frac{\frac{-\epsilon_0 V + \int_0^d \frac{P_{fz}}{\epsilon_{zz}}dz}{\int_0^d \frac{1}{\epsilon_{zz}}dz} - P_{fz}}{\epsilon_0\epsilon_{zz}}. \tag{7.5}
$$

7.3 Experiment

In the experiment, 2ms dc pulses, which are 100ms apart and have a magnitude of 1V and -1V, are applied to the HAN cell. The dynamical optical response is measured at normal incidence using a red laser (632.8nm), crossed polarisers, detector and oscilloscope, as shown Figure 7.2.

Using the theory, the optical response (Fig. 7.3 thick line) of the experiment can be simulated, as shown in Figure 7.3 (thick line). Additionally, Figure 7.3 shows the 2ms pulses (thin line) which are 100ms apart, whereby first a positive pulse of +1V is applied and 100ms later a negative pulse of -1V. To investigate the effect

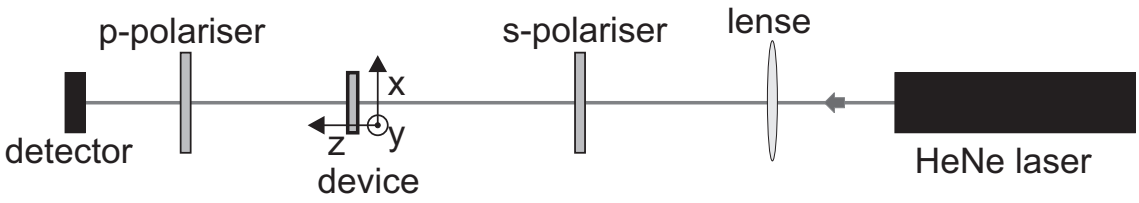


Figure 7.2: HAN experiment to measure the sum ($e_1 + e_3$)

of flexoelectricity, different scenarios of the optical response are simulated with and without flexoelectricity. The effect of the offset is investigated by changing the magnitude of the negative pulse. In one case the magnitude is higher by +100mV, also -0.9V and in the other case smaller by -100mV, also -1.1V. The simulations

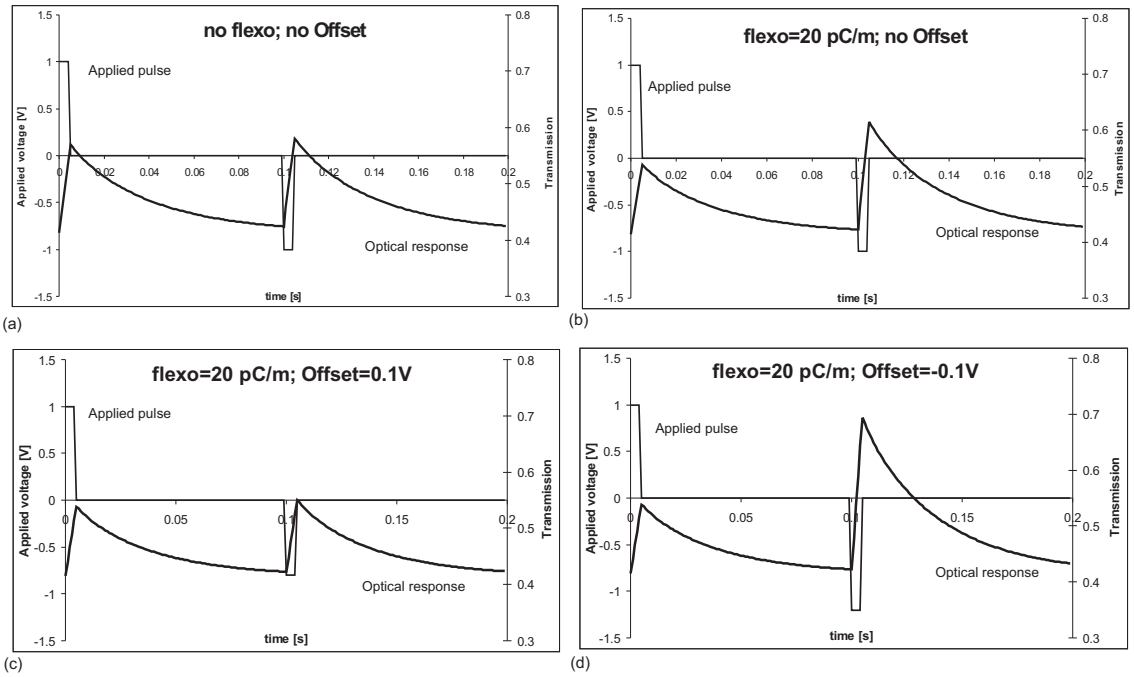


Figure 7.3: Simulation for the flexoelectric sum ($e_1 + e_3$) and offset: a) No flexo and no offset, b) flexo=20 pC/m and offset=0V, c) flexo=20 pC/m and offset=0.1V, d) flexo=20 pC/m and offset=-0.1V

show (Fig. 7.3a) that without flexoelectricity and symmetric pulses (e.g. no offset in negative pulse), the magnitude of the optical response (thick line) is the same for positive and negative pulses. This is not the case if flexoelectricity with 20 pC/m is included in the theory (Fig. 7.3b). The magnitude of the optical response is different

for a positive and negative pulse. Increasing only the negative pulse by +100mV (Fig. 7.3c) decreases the asymmetry in the optical response and decreasing only the negative pulse by -100mV (Fig. 7.3d) increases the asymmetry. With an increase (offset) of +100mV in the negative pulses only, the influence of flexoelectricity can be cancelled out (Fig. 7.3c). Further, it is possible to calculate the flexo-offset correlation for a material using the simulation e.g. for E7 the sum ($e_1 + e_3$) of 20pC/m corresponds to 106mV offset. This correlation allows us to calculate the flexoelectricity once the offset is measured in the experiment. Further, the flexo-offset correlation depends on the elastic, dielectric and refractive properties and has to be calculated for each material. These results are presented in Table 7.1 and will be used for the experimental evaluation.

Material	Simulated flexo-offset correlation
E7	0.106 V per 20pC/m
CB	0.096 V per 20pC/m
PCH	0.116 V per 20pC/m
DE	0.117 V per 20pC/m
E70A	0.117 V per 20pC/m
MDA-02-2419	0.051 V per 20pC/m
Material B [84]	0.049 V per 20pC/m
MLC-7029	0.217 V per 20pC/m

Table 7.1: Simulated flexo-offset correlation

The experimental data with symmetric pulses (no offset in one of the pulses), show an asymmetrical pulse response (Fig. 7.4a), as expected and predicted by the theory. The asymmetrical pulse response is caused by a combination of flexoelectricity and internal bias. Changing the magnitude of the negative pulse only until the asymmetric optical response disappears (Fig. 7.4b) allows us to measure the offset voltage necessary to cancel out the combination of the flexoelectric effect and internal bias. The experimental results shown are for E7 at room temperature (22°C) and an offset of +105mV is measured, which means that the magnitude of the neg-

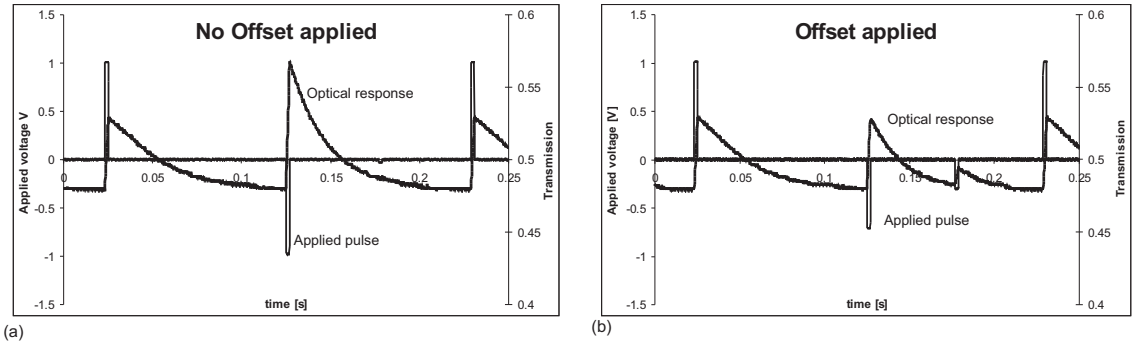


Figure 7.4: Experimental data for E7 at room temperature (22°C): a) Pulses are symmetric (no offset) and optical response asymmetric, b) Offset of -105mV is applied to negative pulse which gives a pulse magnitude of -0.895V and a symmetrical optical response

ative pulse was changed from -1V to -0.895V while keeping the magnitude of the positive pulse at 1V. The same result can be obtained varying the positive pulse and keeping the negative pulse constant. To determine the internal bias, TL216 is used which is non-ionic and has negligible flexoelectricity, and a value of -135mV was measured. Assuming that the measured internal bias of -135mV just depends on the homeotropic alignment and not on the liquid crystal material or ions, and that it is constant and the same in the batch of HAN cells used, it can be treated like a constant offset and taken into account in the flexoelectric measurement of the other materials. For E7, it is now possible to calculate the offset corresponding to flexoelectricity by 105mV-(-135mV)=240mV. Using the simulated flexo-offset correlation for E7 where 20pC/m corresponded to 106mV, the sum $(e_1 + e_3)$ can be calculated by 20pC/m$\cdot\frac{240}{106}$=45pC/m. To avoid problems with ions the pulse length is 2ms, which should be short enough so that ions are not able to move to the edge of the device and cancel out the electric field. However, applying asymmetric pulses e.g. 1V and -0.895V, leads to a net dc voltage which causes ionic drift. This problem is avoided in the experiment by applying a third pulse which is also 2ms long and appears 50ms after the negative pulse. The magnitude of this third pulse is equal to the offset but the sign is opposite to compensate for the offset e.g. -105mV.

7.4 Results

Using our new method, the eight materials E7, CB, PCH, DE, E70A, MDA-02-2419, Material B [84], and MLC-7029 were measured at room temperature (22°C) and investigated, as shown in Table 7.2. As mentioned before, TL216 is non-ionic

Material	Offset measured [V]	Flexoelectric offset [V]	Flexoelectric sum ($e_1 + e_3$)
TL216	-0.135 V	-	-
E7	0.105 V	0.240 V	45 pC/m ± 50%
CB	0.080 V	0.215 V	45 pC/m ± 50%
PCH	0.145 V	0.280 V	48 pC/m ± 50%
DE	0.135 V	0.270 V	46 pC/m ± 50%
E70A	0.065 V	0.200 V	34 pC/m ± 50%
MDA-02-2419	0.125 V	0.260 V	102 pC/m ± 50%
Material B [84]	0.145 V	0.280 V	114 pC/m ± 50%
MLC-7029	-0.210 V	-0.075 V	-7 pC/m ± 50%

Table 7.2: Overview of measured offset at room temperature (22°C) and flexoelectric offset. Results are shown for the sum ($e_1 + e_3$) of the flexoelectric coefficients.

and has negligible flexoelectricity. It was used to determine the internal bias of -0.135V for the batch of HAN cells. The "Offset measured" in the table presents the change in magnitude required in the negative pulses, to cancel out flexoelectricity and internal bias. Subtracting from this "Offset measured" the internal bias of -0.135V gives the "Flexoelectric offset" which correlates to flexoelectricity. Using the calculated "flexo-offset correlation factor" from Table 7.1, which depends on the material and has to be simulated for each material, the sum ($e_1 + e_3$) can be calculated. The materials E7, CB, PCH, DE and E70A show a medium flexoelectric value compared to MDA-02-2419 and Material B [84], which show a high value, and MLC-7029 a negative and low value. The errors (50%) are somewhat arbitrary estimates and are very high because of the assumptions made about the internal bias.

Comparing now the dielectric permittivity $\Delta\epsilon$ values with the sum ($e_1 + e_3$), as

shown in Table 7.3, the two materials MDA-02-2419 and Material B [84] have large

Material	dielectric permittivity $\Delta\epsilon$	Flexo sum $(e_1 + e_3)$
TL216	5.1	≈ 0 pC/m
MLC-7029	-3.7	-7 pC/m $\pm$ 50%
E7	13.7	45 pC/m $\pm$ 50%
CB	13.2	45 pC/m $\pm$ 50%
PCH	12.2	48 pC/m $\pm$ 50%
DE	9	46 pC/m $\pm$ 50%
E70A	10.4	34 pC/m $\pm$ 50%
MDA-02-2419	38.5	102 pC/m $\pm$ 50%
Material B [84]	42.1	114 pC/m $\pm$ 50%

Table 7.3: Comparing dielectric permittivity $\Delta\epsilon$ and the sum $(e_1 + e_3)$, which indicates a correlation. The data was taken at room temperature (22°C).

dielectric permittivity $\Delta\epsilon$ values and also the highest sum $(e_1 + e_3)$ values measured here. The other materials have typical dielectric permittivity $\Delta\epsilon$ values and show

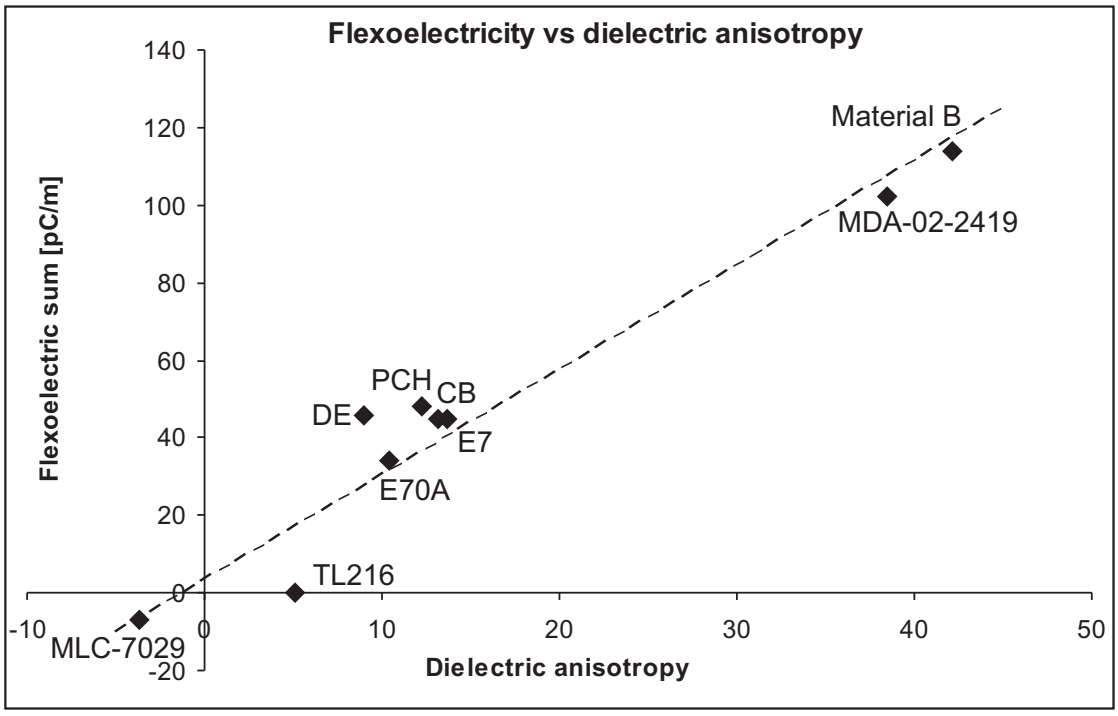


Figure 7.5: Results of 9 measured materials indicate a rough linear correlation between the sum $(e_1 + e_3)$ and the dielectric anisotropy $\Delta\epsilon$

medium sum $(e_1 + e_3)$ values. MLC-7029 has a small negative dielectric permittivity

$\Delta\epsilon$ value with also a small negative sum $(e_1 + e_3)$ value. This indicates a rough linear correlation between dielectric permittivity $\Delta\epsilon$ values and the sum $(e_1 + e_3)$, as shown in Figure 7.5.

7.5 Conclusion

The new experiment, which was described, is a fast, simple and easy approach to measuring the sum $(e_1 + e_3)$ of the flexoelectric coefficients and one material takes less than 10 minutes. Also, the calculation of the flexo-offset correlation is quick as well and has to be done just once for each material. However, the assumption that the internal bias is constant and just depends on the homeotropic alignment material and not on the liquid crystal material or ions, leads to a big error margin. This means that it is not possible yet to measure accurately the sum $(e_1 + e_3)$. The results are only estimations but take the internal bias into account. Our method allows us to measure different materials quickly and to classify the sum $(e_1 + e_3)$ of the flexoelectric coefficients as high, middle, low and negative. We are interested in improving the accuracy of the measurement. If it were possible to determine the internal bias for each material and cell individually, it would improve the accuracy and lead to a fast, simple, and accurate experiment to determine the sum $(e_1 + e_3)$ of the flexoelectric coefficients.

The results show an interesting trend. E7, CB, PCH, DE, and E70A are materials with a dielectric anisotropy $\Delta\epsilon$ between 9 and 14, showing a middle value of the flexoelectric sum. MDA-02-2419 and Material B [84] have a dielectric anisotropy $\Delta\epsilon$ of around 40 and show a high sum. MLC-7029 dielectric anisotropy $\Delta\epsilon$ is -3.5 with a small and negative sum. This indicates a correlation between dielectric anisotropy $\Delta\epsilon$ and the sum $(e_1 + e_3)$, as shown in Table 7.3. A similar correlation has been found between dielectric anisotropy $\Delta\epsilon$ and the difference $(e_1 - e_3)$, as presented in

Chapter 5.

The materials CB, PCH, and DE are mixtures made of the homologues 3/5/7 with a ratio of 30%/40%/30% [124]. These three materials are similar, except that one of the ring structures and the link between the two rings varies. The results indicate that the ring structure and link between the rings has some influence on the elastic, dielectric and refractive properties [124, 119, 120, 121] but only a small or almost no influence on the flexoelectric coefficients. The measured sum ($e_1 + e_3$) for all three materials is in the region of 46 pC/m.

7.5.1 Future

In this experiment it was assumed, that the internal bias only depends on the homeotropic alignment material and not on the liquid crystal material or ions, leads to a big error margin. If it were possible to determine the internal bias for each material and cell individually, it would improve the accuracy and lead to a fast, simple, and accurate experiment to determine the sum ($e_1 + e_3$) of the flexoelectric coefficients. In the future it might be an interesting idea to use the other non-ionic materials to investigate the influence of other materials on the internal bias. It might be also an interesting idea for the future to use different homeotropic alignment layer to investigate the influence of the alignment layer.

In conclusion, the simple pulse experiment presents interesting results. All results from this experiment and also previous experiments like the TN cell and Pi cell method are summarised in the next chapter.

Chapter 8

Summary and Conclusion

8.1 Experiments

In the previous chapters three methods to measure the flexoelectric effect were presented. The TN cell experiment measures the difference $(e_1 - e_3)$ and the Pi cell and Simple Pulses experiment measure the sum $(e_1 + e_3)$.

8.1.1 TN cell to measure difference $(e_1 - e_3)$

Our newly developed TN cell experiment to measure the difference $(e_1 - e_3)$ of the flexoelectric coefficients works very well and the results are repeatable and accurate. Even using E7 cells which are more than 1 year old gave the same results because the TN structure is very stable. The quality of the fits were very good. Automating the experiment and the fitting enabled us to measure one material in a few days, which is very fast and a big advantage in the measurement and understanding of flexoelectricity. However, the production of the TN cells with the electrode pattern for the in-plane electric field is complex and takes time. But this disadvantage can be minimised by producing the cells in bulk for a set of different materials.

The key advantage of the TN-cell experiment using an in-plane electric field compared to the ULH structure is that the TN structure is stable and easier to create. The ULH structure has only the advantage that it is a direct method (but the elastic parameter has to be known to calculate $(e_1 - e_3)$), compared to the TN-cell experiment where the knowledge of elastic, dielectric, and refractive parameters are necessary to fit the data. However, the flexoelectric effect can be easily observed and measured in the TN-cell experiment. The results are accurate and repeatable.

Further, it is possible to measure achiral and weakly chiral materials, which would enable the investigation of the influence of chirality on flexoelectricity, which was investigated by P. Salter, who is a colleague from the Oxford liquid crystal group. The ULH structure requires a highly chiral material or highly chiral doped material and it was unknown how chirality influences flexoelectricity. His finding showed that there is a negligible correlation between chirality and flexoelectricity [118].

The "error" given for $(e_1 - e_3)$ is the margin for the different fitting results and the 5% error which occurs due to the physical parameters like the elastic (K_{11}, K_{22} and K_{33}), dielectric ($\epsilon_\perp$ and $\epsilon_\parallel$) and optical ($n_\perp$ and $n_\parallel$) parameters. The total error of the difference $(e_1 - e_3)$ is roughly 20%.

8.1.2 Pi cell to measure sum $(e_1 + e_3)$

The Pi cell experiment is not useful for measuring accurately the flexoelectric sum $(e_1 + e_3)$ because there are strong variations in the first harmonic data for different measurements at the same cell.

8.1.3 Simple pulses to measure sum ($e_1 + e_3$)

The Simple Pulses experiment is a fast, simple and easy approach to measuring the sum ($e_1 + e_3$) of the flexoelectric coefficients and one material takes less than 10 minutes. Also, the calculation of the flexo-offset correlation is quick as well and has to be done just once for each material. However, the assumption that the internal bias is constant and just depends on the homeotropic alignment material and not on the liquid crystal material or ions, leads to a big error margin. The errors (50%) are somewhat arbitrary estimates and are very high because of the assumptions made about the internal bias. This means that it is not possible yet to measure accurately the sum ($e_1 + e_3$). The results are only estimations but take the internal bias into account. Our method allows us to measure different materials quickly and to classify the sum ($e_1 + e_3$) of the flexoelectric coefficients as high, middle, low and negative.

8.2 Calculation of e_1 and e_3

The goal of this thesis was to develop new experiments for the measurements of the flexoelectric coefficients e_1 and e_3. In practice, it is easier to measure the difference ($e_1 - e_3$) and the sum ($e_1 + e_3$) of the flexoelectric coefficients and then calculate e_1 and e_3. The difference ($e_1 - e_3$) was measured with the TN cell experiment. The measurement of the sum ($e_1 + e_3$) was done by the Pi cell experiment and the simple pulse experiment, which uses a HAN cell. A complete overview of the material properties are shown in Table 8.1 and a complete overview of all flexoelectric results for the difference ($e_1 - e_3$), the sum ($e_1 + e_3$), the calculated e_1 and e_3 are shown in Table 8.2. The flexoelectric parameter e_1 was calculated by

$$e_1 = \frac{sum + difference}{2} \tag{8.1}$$

Material	K_{11} [pN]	K_{22} [pN]	K_{33} [pN]	$\epsilon_\parallel$	$\epsilon_\perp$	$\Delta\epsilon$	$n_\parallel$	$n_\perp$	Δn	T_{NI} [°C]	ΔT [°C]	Comment
E7	10.7	6.5	16.2	18.9	5.2	13.7	1.738	1.519	0.233	58	36	
E70A	10.0	5.8	10.4	15.8	5.4	10.4	1.682	1.517	0.166	60	38	
CB	6.5	4.1	9.5	19.6	6.4	13.2	1.724	1.522	0.202	35	13	molecular structure
PCH	8.6	5.6	16.9	17.1	4.9	12.2	1.608	1.488	0.120	52	30	molecular structure
DE	9.6	5.0	17.3	14.8	5.8	9.0	1.592	1.479	0.112	72	50	molecular structure
TL216	13.8	8.1	18.6	9.1	4.0	5.1	1.727	1.519	0.207	80	58	non-ionic
MLC-7021-100	10.5	6.1	12.0	14.2	3.7	10.5	1.599	1.487	0.112	81	59	non-ionic
MLC-13900-100	-	-	-	-	-	5.2	-	-	0.108	110	88	non-ionic
MLC-15900-100	-	-	-	-	-	10.1	-	-	0.091	74	52	non-ionic
MixA	12.9	8.5	18.6	16.2	4.6	11.6	1.725	1.515	0.210	66	44	elastic prop.
MixC	12.5	11.7	50.0	16.2	4.7	11.5	1.725	1.513	0.212	70	48	elastic prop.
E7+30%Me35	10.0	6.1	9.5	15.7	5.0	10.7	1.694	1.515	0.179	54	32	molecular orientation
E7+50%Me35	9.9	6.1	7.2	13.1	4.8	8.3	1.558	1.511	0.157	45	23	molecular orientation
MDA-02-2419	8.2	6.1	15.3	46.6	8.1	38.5	1.686	1.506	0.180	97	75	big $\Delta\epsilon$
Material B [84]	8.5	5.0	15.6	49.9	7.8	42.1	1.608	1.490	0.118	95	73	big $\Delta\epsilon$
MLC-7029	16.0	6.7	15.0	3.6	7.3	-3.7	1.611	1.487	0.124	95	73	negative $\Delta\epsilon$

Table 8.1: Overview of elastic, dielectric, and refractive properties measured at room temperature (22°C).

Material	$\Delta\epsilon$	TN $(e_1 - e_3)$ $[pC/m]$	Pi $(e_1 + e_3)$ $[pC/m]$	Simple pulses $(e_1 + e_3)$ $[pC/m]$	Calculated e_1 $[pC/m]$	Calculated e_3 $[pC/m]$	Comment
E7	13.7	12.2 ±2.0	≈ 35 to ≈ 120	45 ±50%	28.6 ±70%	16.4 ±70%	
E70A	10.4	4.2 ±1.0	≈ 80 to ≈ 170	34 ±50%	19.1 ±70%	14.9 ±70%	
CB	13.2	6.8 ±1.0	-	45 ±50%	25.9 ±70%	19.1 ±70%	molecular structure
PCH	12.2	8.2 ±1.0	-	48 ±50%	28.1 ±70%	19.9 ±70%	molecular structure
DE	9.0	7.3 ±1.0	-	46 ±50%	26.7 ±70%	19.4 ±70%	molecular structure
TL216	5.1	0.4 ±0.5	≈ 0	≈ 0			non-ionic
MLC-7021-100	10.5	0.0 ±1.0	≈ 0	-			non-ionic
MLC-13900-100	5.2	≈ 0	≈ 0	-			non-ionic
MLC-15900-100	10.1	≈ 0	≈ 0	-			non-ionic
MixA	11.6	10.5 ±1.0	-	-			elastic prop.
MixC	11.5	11.5 ±1.5	-	-			elastic prop.
E7+30%Me35	10.7	7.0 ±1.0	-	-			molecular orientation
E7+50%Me35	8.3	5.5 ±1.0	-	-			molecular orientation
MDA-02-2419	38.5	22.0 ±2.0	-	102 ±50%	62 ±70%	40 ±70%	big $\Delta\epsilon$
Material B [84]	49.9	24.0 ±2.0	≈ 1000	114 ±50%	69 ±70%	45 ±70%	big $\Delta\epsilon$
MLC-7029	-3.7	-3.5 ±1.5	-	-7 ±50%	-5.3 ±70%	-1.8 ±70%	negative $\Delta\epsilon$

Table 8.2: Overview of flexoelectric results

and the flexoelectric parameter e_3 was calculated by

$$e_3 = \frac{sum + difference}{2} - difference. \tag{8.2}$$

The values for the *difference* were taken from the TN cell experiments and the values for the *sum* were taken from the Simple Pulses experiment. The TN cell experiment has an error of roughly 20% and the Simple Pulse experiment of about 50%. The calculation of e_1 and e_3 are addition and subtraction of the *difference* and the *sum*. These leads to an error for e_1 and e_3 which is the addition of the error from the TN cell experiment and the Simple Pulses experiment, which is roughly 70%.

8.3 Results

8.3.1 Non-Ionic materials

In the TN cell experiment the results for the difference $(e_1 - e_3)$ of the flexoelectric coefficients for the two non-ionic materials TL216 and MLC-7021-100 show a very small $(e_1 - e_3)$, which is almost zero. This is interesting because it is also thought that the flexoelectric effect might be partly or completely be influenced by ions [53]. Two additional non-ionic materials (MLC-13900-100 and MLC-15900-100) were used to investigate this finding more closely. The quasi-dc data for both materials showed a very small asymmetry which indicated the the flexoelectric difference $(e_1 - e_3)$ is also very small. The data was not fitted because the elastic, dielectric and refractive parameters were not known. However, it can be clearly seen from the raw quasi-dc data that the difference is very small and in the range of the other two non-ionic materials. It is very interesting that four non-ionic materials show almost no flexoelectricity. Maybe ions are the cause of flexoelectricity or necessary for

flexoelectricity to appear.

Further, it is interesting to notice that in the Simple Pulses experiment all three non-ionic materials TL216, MLC-7021-100 and MLC-13900-100 did not show any first harmonic response. Mixing 10% of the ionic material E7 into the non-ionic material TL216 showed a similar first harmonic response as in the normal E7 material. This indicates that ions are important for the flexoelectric effect. Ions might enhance the first harmonic due to surface effects but without ions there is no first harmonic response at all.

8.3.2 Molecular structure

In the TN cell experiment the values of the difference $(e_1 - e_3)$ for the three materials CB, PCH, and DE is about $7.5 pC/m$ and they are very similar to one another. This indicates that the ring structure appears to have only a small influence on flexoelectricity, despite having a significant influence on the shape and the elastic, dielectric and refractive parameters. This is surprising and not easy to explain, because it is thought that flexoelectricity is due to a shape anisotropy. This was also seen by other scientists [72], who designed the molecular structure in such a way that the shape would look like a pear and hopefully increase the flexoelectric properties. But despite their efforts, the shape did not seem to have a big effect on the flexoelectric properties.

In the Simple Pulses experiment the results also indicate that the ring structure and link between the rings has only a small or almost no influence on the flexoelectric coefficients. The measured sum $(e_1 + e_3)$ for all three materials is in the region of 46 pC/m. This is surprising because flexoelctricity is thought to be caused by shape anisotropy and changing the molecular shape should influence flexoelectricity.

The calculated values of e_1 and e_3 also show, that the three materials CB, PCH, and

DE have almost identically vales for e_1 and e_3. The values for e_1 are in the region of $26pN$ to $28pN$ and the values for e_3 are in the region of $19pN$ to $20pN$. This also shows, that the ring structure in the three materials CB, PCH, and DE did not have any influence on the flexoelectric properties.

8.3.3 Elastic Properties

In the TN cell experiment the two materials MixA and MixC were used to investigate the influence of elastic properties on flexoelectricity. MixA and MixC are very interesting materials from the point that MixC has a smectic to nematic transition temperature of 20°C, which is below the measurement temperature. The elastic, dielectric and refractive parameters of these two material are very similar to each other and similar to E7, except that the bend elastic parameter K_{33} of MixC is about $50pN$, which is very high. But the results for the difference $(e_1 - e_3)$ are about $11pC/m$ for both materials and also similar to E7, which has a flexoelectric difference of $12.2pC/m$. These results show clearly that the elastic properties do not influence the flexoelectric difference $(e_1 - e_3)$ and maybe do not influence flexoelectricity at all.

8.3.4 Molecular orientation

In the TN cell experiment the materials E7+30%Me35 and E7+50%Me35 are mixtures with E7 and the single component Me35. Me35 reduces the anti-parallel orientation, which should increase the splay distortion of the flexoelectric effect. However, the results show that E7+30%Me35 has a difference $(e_1 - e_3)$ of $7.0pC/m$ and E7+50%Me35 of $5.5pC/m$. This is very surprising, because the opposite effect was expected, an increased or at least a similar value to E7. The results do not

support the idea that the shape anisotropy causes flexoelectricity. It rather conflicts with the idea of shape anisotropy.

8.3.5 Dielectric anisotropy $\Delta\epsilon$

The results of all measured materials from the TN cell experiment and the Simple Pulses experiment are used to investigate the correlation between dielectric anisotropy $\Delta\epsilon$ and the flexoelectric coefficients like the difference $(e_1 - e_3)$, the sum $(e_1 + e_3)$, the calculated e_1 and e_3. This is sensible, because flexoelectricity is caused by molecular dipoles, which align with an external applied field and create an additional distortion due to a shape anisotropy of the molecules. If the molecular dipole is larger, it is more likely that more molecules are orientated in the same direction, which increases the flexoelectric coupling. Results for all materials are shown in Figure 8.1 and they indicate a rough linear correlation between dielectric anisotropy $\Delta\epsilon$ and the flexoelectric coefficients like the difference $(e_1 - e_3)$, the sum $(e_1 + e_3)$, the calculated e_1 and e_3. Only the non-ionic materials do not fit into this behaviour.

8.4 Future

8.4.1 Experiments

In the future, it might be interesting to modify the TN cell experiment and the Simple Pulses experiment to measure the difference $(e_1 - e_3)$ and the sum $(e_1 + e_3)$ at different temperatures so that the correlation between order parameter S and flexoelectric coefficients like the difference $(e_1 - e_3)$, the sum $(e_1 + e_3)$, the calculated e_1 and e_3 can be investigated. We are interested in improving our experiments of

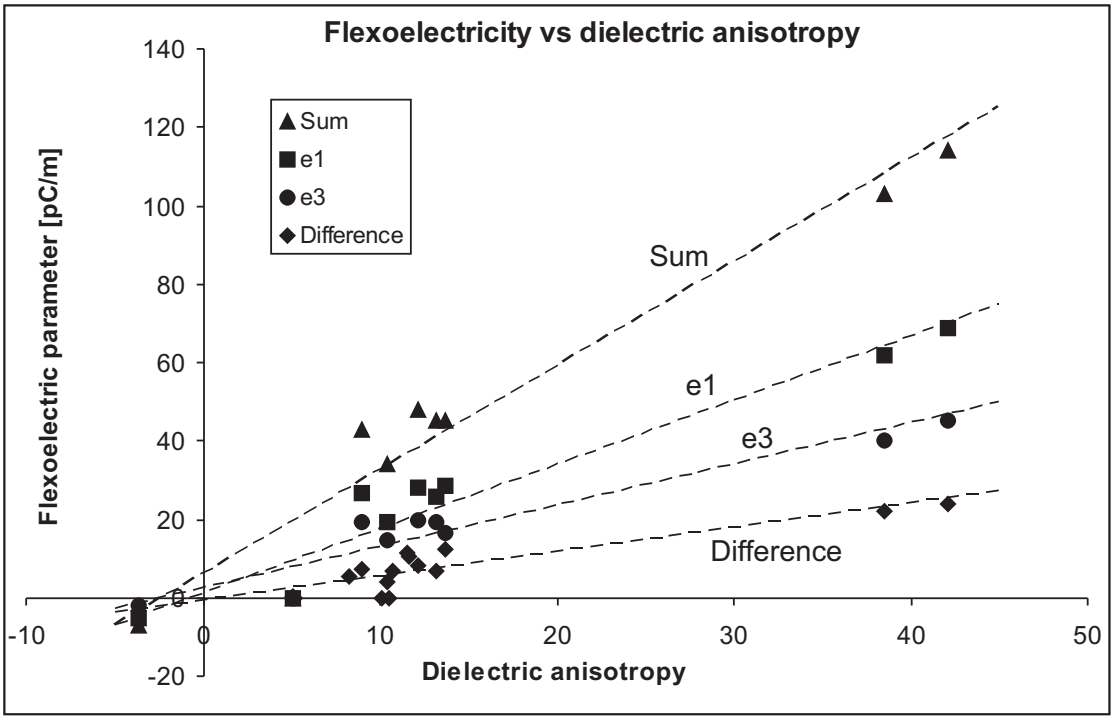


Figure 8.1: Results of all measured materials indicate a rough linear correlation between the dielectric anisotropy $\Delta\epsilon$ and the flexoelectric coefficients like the difference $(e_1 - e_3)$, the sum $(e_1 + e_3)$, the calculated e_1 and e_3

measuring $(e_1 - e_3)$ and $(e_1 + e_3)$ at different temperatures to investigate the influence of the order parameter S, but this is more difficult than it seems. Not only does the TN-cell experiment and the Simple Pulses experiment have to be improved, but also the three experiments to measure the elastic, dielectric and refractive properties must be modified to guarantee that all parameters are determined at the defined temperature and a temperature depends of the elastic, dielectric or refractive properties can be excluded.

In the future it might be an interesting idea to try in the Pi cell experiment a different alignment layer compared to SiOx. The alignment layer should also create a high pretilt and weak surface anchoring. Maybe with a better and more homogeneous alignment layer the results would be more reliable and repeatable.

In the Simple Pulses experiment it was assumed, that the internal bias only depends on the homeotropic alignment material and not on the liquid crystal material or ions, leads to a big error margin. If it were possible to determine the internal bias for each material and cell individually, it would improve the accuracy and lead to a fast, simple, and accurate experiment to determine the sum $(e_1 + e_3)$ of the flexoelectric coefficients. In the future it might be an interesting idea to use the other non-ionic materials to investigate the influence of other materials on the internal bias. It might be also an interesting idea for the future to use different homeotropic alignment layer to investigate the influence of the alignment layer.

8.4.2 Materials

In the future, we are extremely interested in investigating the influence of ions by mixing different non-ionic materials with ionic materials. One way to check the influence of ions might be to dope ions into MLC-7021-100 or to create mixtures between E7 and MLC-7021-100, which have similar properties to E7. Measuring different concentration of mixtures (90%E7+10%MLC-7021-100, 80%E7+20%MLC-7021-100, 70%E7+30%MLC-7021-100) might help to understand the behaviour, which is crucial for the optimisation of commercial devices relying on flexoelectricity.

8.4.3 New theory

In conclusion, it can be said that the results of the experimental work showed, that flexoelectricity is strongly influenced by ions and that a linear behaviour between flexoelectricity and the dielectric anisotropy exists. It also might be possible that ions are the reason for the flexoelectric effect occurring. These two arguments were the motivation to start thinking of a new understanding about flexoelectricity. Is it possible to create a new theory which is based on ions and the dielectric properties?

Bibliography

[1] F. Reinitzer. Beitraege zur kenntnis des cholesterins [contributions to the understanding of cholesterol]. *Monatshefte fuer Chemie*, 9:pp. 421, 1888.

[2] F. Lehmann. Ueber fliessende kristalle [on liquid crystals]. *Zeitschrift fuer Physikalische Chemie*, 4:pp. 462, 1889.

[3] R. Schenck. Ueber die natur der kristallinischen fluessigkeiten und der fluessigen kristalle [on the nature of crystalline liquids and liquid crysatls]. *Zeitschrift fuer Electrochemie*, 11:pp. 951, 1905.

[4] D. Vorlaender. Einfluss der molecularen gestalt auf den kristallinisch-fluessigen zustand [influence of the molecular shape on the crystalline-liquid state]. *Bericht der Deutschen Chemischen Gesellschaft*, 40:pp. 1970, 1907.

[5] G. Friedel. Les etats mesomorphes de la mati'ere [the mesomorphic states of matter]. *Annales de Physique*, 18:pp. 273, 1922.

[6] M. Schadt and W. Helfrich. Voltage-dependent optical activity of a twisted nematic liquid crystal. *Applied Physics Letters*, 18(4):pp. 127, 1971.

[7] G. W. Gray, K. J. Harrison, and J. A. Nash. New family of nematic liquid crystals for displays. *Electronics Letters*, 9(6):pp. 130, 1973.

[8] G. W. Gray, K. J. Harrison, D. S. Hulme, and E. P. Raynes. Liquid crystal compositions. *U.K. Patent*, 1452826, 1974.

[9] A. J. Snell, K. D. Mackenzie, W. E. Spear, P. G. LeComber, and A. J. Hughes. Application of amorphous silicon field effect transistors in addressable liquid crystal display panels. *Applied Physics*, 24(4):pp. 357, 1981.

[10] C. M. Watters, V. Brimmell, and E. P. Raynes. Highly multiplexable dyed liquid crystal displays. *Proc. 3rd Int. Display Res. Conf., Kobe, Japan*, page pp. 396, 1983.

[11] T. J. Sheffer and J. Nehring. Supertwisted nematic (stn) liquid crystal displays. *Journal of Applied Physics*, 58:pp. 3022, 1985.

[12] M. F. Schiekel and K. Fahrenchon. Deformation of nematic liquid crystals with vertical orientation in electrical fields. *Applied Physics Letters*, 19(10):pp. 391, 1971.

[13] R. A. Soref. Field effects in nematic liquid crystals obtained with interdigital electrodes. *Journal of Applied Physics*, 45(12):pp. 5466, 1974.

[14] M. Oh-e and K. Kondo. Electro-optical characteristics and switching behaviour of the in-plane switching mode. *Applied Physics Letters*, 67(26):pp. 3895, 1995.

[15] P. J. Collings and M. Hird. *Taylor and Francis*. Clarendon Press, London, 1997.

[16] F. C. Frank. On the theory of liquid crystals. *Discussions of the Faraday Society*, 25:pp. 19, 1958.

[17] W. H. de Jeu. Liquid crystalline materials: physical properties and intermolecular interactions. *Philosophical Transactions of The Royal Society of London Series A*, 309:pp. 217, 1983.

[18] D. Pauluth and K. Tarumi. Optimization of liquid crystals for television. *Journal of the SID*, 13:pp. 693, 2005.

[19] M. Born and E. Wolf. *Principals of Optics*. Cambridge University Press, Cambridge, 7th edition, 1999.

[20] C. Mauguin. Orientation des cristaux liquides par le champ magnetique [orientation of liquid crystals by a magnetic field]. *Comptes rendus de l'Acadmie des sciences*, 152:pp. 1680, 1911.

[21] O. Parodi. Stress tensor for a nematic liquid crystal. *Journal de Physique*, 31:pp. 581, 1970.

[22] M. Miesowicz. The three coefficients of viscosity of anisotropic liquids. *Nature*, 158:pp. 27, 1946.

[23] W. Helfrich. The torques in sheared nematic liquid crystals: A simple model in terms of the theory of dense fluids. *Journal of Chemical Physics*, 53:pp. 2267, 1970.

[24] S. Hess, J. F. Schwartzl, and D. Baalss. Anisotropy of the viscosity of nematic liquid crystals and oriented ferro-fluids via non-equilibrium molecular dynamics. *Journal of Physics: Condensed Matter*, 2:SA279, 1990.

[25] F. M. Leslie. Some constitutive equations for liquid crystals. *Archive for Rational Mechanics and Analysis*, 28:pp. 265, 1968.

[26] W. A. Crossland, J. H. Morrissy, and B. Needham. Tilt angle measurements of nematic phases of cyano-biphenyls aligned by obilquely evaporated-films. *Journal of Physics D: Applied Physics*, 9:pp. 2001, 1976.

[27] T. J. Scheffer and J. Nehring. Accurate determination of liquid-crystal tilt bias angles. *Journal of Applied Physics*, 48(5):pp. 1783, 1977.

[28] J. S. Gwag, S. H. Lee, K. H. Park, W. S. Park, K. Y. Han, C. G. Jhun, T. H. Yoon, J. C. Kim, D. M. Song, and D. M. Shin. Simple method for measuring the high pretilt angle of nematic liquid crystals. *Journal of Applied Physics*, 93(8):pp. 4936, 2003.

[29] J. L. Janning. Thin-film surface orientation for liquid-crystals. *Applied Physics Letters*, 21(4):pp. 173, 1972.

[30] M. Monkade, P. MartinotLagarde, G. Durand, and C. Granjean. Sio evaporated films topography and nematic liquid crystal orientation. *Journal de Physique II*, 7(11):pp. 1577, 1997.

[31] V. Freedericksz and V. Zolina. On the use of a magnetic field in the measurement of the forces tending to orient an anisotropic liquid in a thin homogeneous layer. *Trans. Americ. Electrochem. Soc.*, 55:pp. 85, 1929.

[32] V. Freedericksz and V. Zolina. Forces causing the orientation of an anisotropic liquid. *Transactions of the Faraday Society*, 29:pp. 919, 1933.

[33] R. B. Meyer. Piezoelectric effects in liquid crystals. *Physical Review Letters*, 22(18):pp. 918, 1969.

[34] P. G. de Gennes. *The Physics of Liquid Crystals*. Clarendon Press, Oxford, 1974.

[35] W. Helfrich. Strength of piezoelectricity in liquid crystals. *Zeitschrift Naturforschung*, 26(5):pp. 833, 1971.

[36] J. P. Marcerou and J. Prost. The different aspects of flexoelectricity in nematics. *Molecular Crystals and Liquid Crystals*, 58(3-4):pp. 259, 1980.

[37] A. Ferrarini. Shape model for the molecular interpretation of the flexoelectric effect. *Physical Review E*, 64(2):021710, 2001.

[38] C. Fan. Comments on piezoelectric effect in liquid crystals. *Molecular Crystals and Liquid Crystals*, 13(1):pp. 9, 1971.

[39] A. Derzhanski, A. G. Petrov, and M. D. Mitov. One-dimensional dielectric-flexoelectric deformations in nematic layers. *Journal de Physique*, 39(3):pp. 273, 1978.

[40] A. G. Petrov. Measurement and interpretation of flexoelectricity. In D. A. Dunmur, A. Fukuda, and G. R. Luckhurst, editors, *Physical Properties of Liquid Crystals: Nematics*, page 251. INSPEC, London, 2001.

[41] J. Prost and P. S. Pershan. Flexoelectricity in nematic and smectic-a liquid-crystals. *Journal of Applied Physics*, 47(6):pp. 2298, 1976.

[42] L. A. Parry-Jones and S. J. Elston. Flexoelectric switching in a zenithally bistable nematic device. *Journal of Applied Physics*, 97(9):093515, 2005.

[43] J. S. Patel and R. B. Meyer. Flexoelectric electrooptics of a cholesteric liquid-crystal. *Physical Review Letters*, 58(15):pp. 1538, 1987.

[44] L. M. Blinov, L. A. Beresnev, S. A. Davidyan, S. G. Kononov, and S. V. Yablonsky. Flexo-electric effects in liquid-crystals. *Ferrolectrics*, 84:pp. 365, 1988.

[45] N. V. Madhusudana and G. Durand. Linear flexo-electro-optic effect in a hybrid aligned nematic liquid-crystal cell. *Journal de Physique, Lettres*, 46(5):pp. L195, 1985.

[46] B. Valenti, C. Bertoni, G. Barbero, P. Tavernavalabrega, and R. Bartolino. Flexoelectricity in the hybrid aligned nematic cell. *Molecular Crystals and Liquid Crystals*, 146:pp. 307, 1987.

[47] I. Dozov, I. Penchev, P. Martinot-Lagarde, and G. Durand. On the sign of flexoelectric coefficients in nematic liquid-crystals. *Ferroelectrics Letters*, 2(4):pp. 135, 1984.

[48] T. Takahashi, S. Hashidate, H. Nishijou, M. Usui, M. Kimura, and T. Akahane. Novel measurement method for flexoelectric coefficients of nematic liquid crystals. *Japanese Journal of Applied Physics*, 37(4A):pp. 1865, 1998.

[49] I. Dozov, P. Martinot-Lagarde, and G. Durand. Flexoelectrically controlled twist of texture in a nematic liquid-crystal. *Journal de Physique, Lettres*, 43(10):pp. L365, 1982.

[50] F. Chungpeng. Comments on piezoelectric effect in liquid crystals. *Molecular Crystals and Liquid Crystals*, 13:pp. 9, 1971.

[51] A. Derzhans and A. G. Petrov. Possible relationship between dielectric permeability and piezoelectric properties of nematic liquid crystals. *Physics Letters*, 34A(7):pp. 427, 1971.

[52] A. Derzhans and A. G. Petrov. Molecular-statistical approach to piezoelectric properties of nematic liquid crystals. *Physics Letters*, 36A(6):pp. 483, 1971.

[53] C. L. Trabi. *PhD Thesis at the Nottingham Trent University with Prof. Carl Brown*, 2009.

[54] J. Prost and J. P.Marcerou. On the microscopic interpretation of flexoelectricity. *Journal de Physique*, 38(3):pp. 315, 1977.

[55] A. L. Alexe-Ionescu, G. Barbero, and A. G. Petrov. Gradient flexoelectric effect and thickness dependence of anchoring energy. *Physical Review E*, 48(3):pp. R1631, 1993.

[56] S. Ponti, P. Ziherl, C. Ferrero, and S. Zumer. Flexoelectro-optic effect in a hybrid nematic liquid crystal cell. *Liquid Crystals*, 26(8):pp. 1171, 1999.

[57] C. V. Brown and N. J. Mottram. Influence of flexoelectricity above the nematic freedericksz transition. *Physical Review E*, 68(3):031702, 2003.

[58] C. V. Brown, J. M. Hind, A. A. Smith, and C. L. Trabi. Transient capacitance study of switching in the nematic freedericksz geometry. *Journal of Applied Physics*, 100(9):094109, 2006.

[59] A. L. Alexe-Ionescu. Flexoelectric polarization and second order elasticity for nematic liquid crystals. *Physics Letters A*, 180(6):pp. 456, 1993.

[60] S. R. Warrier and N. V. Madhusudana. An ac electrooptic technique for measuring the flexoelectric coefficient (e(1)+e(3)) and anchoring energies of nematics. *Journal de Physique II*, 7(12):pp. 1789, 1997.

[61] N. T. Kirkman, T. Stirner, and W. E. Hagston. Continuum modelling of hybrid-aligned nematic liquid crystal cells: optical response and flexoelectricity-induced voltage shift. *Liquid Crystals*, 30(9):pp. 1115, 2003.

[62] A. Mazzulla, F. Ciuchi, and J. R. Sambles. Optical determination of flexoelectric coefficients and surface polarization in a hybrid aligned nematic cell. *Physical Review E*, 64(2):021708, 2001.

[63] S. A. Jewell and J. R. Sambles. Fully leaky guided mode study of the flexoelectric effect and surface polarization in hybrid aligned nematic cells. *Journal of Applied Physics*, 92(1):pp. 19, 2002.

[64] G. Barbero and L. R. Evangelista. Comment on 'optical determination of flexoelectric coefficients and surface polarization in a hybrid aligned nematic cell'. *Physical Review E*, 68(2):023701, 2003.

[65] A. Mazzulla, F. Ciuchi, and J. R. Sambles. Reply on 'optical determination of flexoelectric coefficients and surface polarization in a hybrid aligned nematic cell'. *Physical Review E*, 68(2):023702, 2003.

[66] D. R. Link, M. Nakata, Y. Takanishi, K. Ishikawa, and H. Takezoe. Flexoelectric polarization in hybrid nematic films. *Physical Review E*, 65(1):010701, 2001.

[67] S. D. Lee and J. S. Patel. Surface effect on the field-induced structural change near the isotropic-cholesteric transition. *Physical Review A*, 42(2):pp. 997, 1990.

[68] S. D. Lee, J. S. Patel, and R. B. Meyer. Effect of flexoelectric coupling on helix distortions in cholesteric liquid-crystals. *Journal of Applied Physics*, 67(3):pp. 1293, 1990.

[69] P. Rudquist, M. Buivydas, L. Komitov, and S. T. Lagerwall. Linear electrooptic effect based on flexoelectricity in a cholesteric with sign change of dielectric anisotropy. *Journal of Applied Physics*, 76(12):pp. 7778, 1994.

[70] P. Rudquist, L. Komitov, and S. T. Lagerwall. Linear electro-optic effect in a cholesteric liquid crystal. *Physical Review E*, 50(6):pp. R4735, 1994.

[71] B. Musgrave, P. Lehmann, and H. J. Coles. A new series of chiral nematic bimesogens for the flexoelectro-optic effect. *Liquid Crystals*, 26(8):pp. 1235, 1999.

[72] H. J. Coles, B. Musgrave, M. J. Coles, and J. Willmott. The effect of the molecular structure on flexoelectric coupling in the chiral nematic phase. *Journal of Materials Chemistry*, 11(11):pp. 2709, 2001.

[73] C. Noot, M. J. Coles, B. Musgrave, S. P. Perkins, and H. J. Coles. The flexoelectric behaviour of a hypertwisted chiral nematic liquid crystal. *Molecular Crystals and Liquid Crystals*, 366(1):pp. 725, 2001.

[74] B. Musgrave, M. J. Coles, S. P. Perkins, and H. J. Coles. Enhanced flexoelectric switching behaviour in the chiral nematic phase. *Molecular Crystals and Liquid Crystals*, 366(1):pp. 735, 2001.

[75] A. E. Blatch, M. J. Coles, B. Musgrave, and H. J. Coles. Flexoelectric liquid crystal bimesogens. *Molecular Crystals and Liquid Crystals*, 401(1):pp. 47/[161], 2003.

[76] H. J. Coles, M. J. Clarke, S. M. Morris, B. J. Broughton, and A. E. Blatch. Strong flexoelectric behavior in bimesogenic liquid crystals. *Journal of Applied Physics*, 99(3):034104, 2006.

[77] R. Barberi, M. Giocondo, and G. Durand. Flexoelectrically controlled surface bistable switching in nematic liquid crystals. *Applied Physics Letters*, 60(9):pp. 1085, 19892.

[78] R. Barberi, M. Giocondo, J. Li, R. Bartolino, I. Dozov, and G. Durand. Fast bistable nematic display with grey scale. *Applied Physics Letters*, 71(24):pp. 3495, 1997.

[79] I. Dozov, A. Boissier, and T. Laboureau. *SID 2002*, page pp. 10, 2002.

[80] G. P. Bryan-Brown, E. L. Wood, C. V. Brown, J. C. Jones, I. C. Sage, and P. Brett. Grating aligned bistable nematic devices. *Prodceedings of IDW '97*, PLC2-1:pp. 261, 1997.

[81] G. P. Bryan-Brown, C. V. Brown, J. C. Jones, E. L. Wood, I. C. Sage, P. Brett, and J. Rudin. Grating aligned bistable nematic device. *SID Digest XXVIII*, 5.3:pp. 37, 1997.

[82] G. P. Bryan-Brown, E. L. Wood, and J. C. Jones. Optimisation of the zenithal bistable nematic liquid crystal device (zbd). *Proceedings of IDRC*, 18:pp. 1051, 1998.

[83] J. C. Jones, G. P. Bryan-Brown, E. L. Wood, P. Brett, A. Graham, and J. R. Hughes. Novel bistable liquid crystal displays based on grating alignment. *Proceedings of SPIE*, 3955:pp. 84, 2000.

[84] J. C. Jones, S. M. Beldon, P. Brett, M. Francis, and M. Goulding. Low voltage zenithal bistable devices with wide operating windows. *SID Digest XXXIV*, 26.3(2):pp. 954, 2003.

[85] J. C. Jones, S. M. Beldon, and E.L. BWood. *Journal of SID*, 11(2):pp. 269, 2003.

[86] J. C. Jones, S. M. Beldon, P. Brett, M. Francis, and M. Goulding. Novel geometries of the zenithal bistable device. *SID Digest XXXVII, Book II*, 51.2:pp. 1626, 2006.

[87] www.zbddisplay.com.

[88] S. Kitson and A. Geisow. Controllable alignment of nematic liquid crystals around microscopic posts: Stabilization of multiple states. *Applied Physics Letters*, 80(19):pp. 3635, 2002.

[89] L. Komitov, S. T. Lagerwall, B. Stebler, and A. Strigazzi. Sign reversal of the linear electrooptic effect in the chiral nematic phase. *Journal of Applied Physics*, 76(6):pp. 3762, 1994.

[90] P. Rudquist, L. Komitov, and S. T. Lagerwall. Volume-stabilized ulh structure for the flexoelectro-optic effect and the phase-shift effect in cholesterics. *Liquid Crystals*, 24(3):pp. 329, 1998.

[91] B. J. Broughton, M. J. Clarke, S. M. Morris, A. E. Blatch, and H. J. Coles. Effect of polymer concentration on stabilized large-tilt-angle flexoelectro-optic switching. *Journal of Applied Physics*, 99(2):023511, 2006.

[92] L. Komitov, G. P. Bryan-Brown, E. L. Wood, and A. B. J. Smout. Alignment of cholesteric liquid crystals using periodic anchoring. *Journal of Applied Physics*, 86(7):pp. 3508, 1999.

[93] S. H. Kim, L. C. Chien, and L. Komitov. Short pitch cholesteric electro-optical device stabilized by nonuniform polymer network. *Applied Physics Letters*, 86(16):161118, 2005.

[94] R. A. Ewings, C. Kischka, L. A. Parry-Jones, and S. J. Elston. Measurement of the difference in flexoelectric coefficients of nematic liquid crystals using a twisted nematic geometry. *Physical Review E*, 73(1):011713, 2006.

[95] B. J. Broughton, M. J. Clarke, A. E. Blatch, and H. J. Coles. Optimized flexoelectric response in a chiral liquid-crystal phase device. *Journal of Applied Physics*, 98(3):034109, 2005.

[96] A. J. Davidson, S. J. Elston, and E. P. Raynes. Examination into the maximum rotational frequency for an in-plane switched active waveplate device. *Journal of Physics D: Applied Physics*, 38(9):pp. 1470, 2005.

[97] A. J. Davidson, S. J. Elston, and E. P. Raynes. Optical properties of the cartwheel cell. *Journal of Physics D: Applied Physics*, 38(3):pp. 376, 2005.

[98] A. J. Davidson, S. J. Elston, and E. P. Raynes. Investigation into chiral active waveplates. *Journal of Applied Physics*, 99(9):093109, 2006.

[99] J. L. Eriksen. Conservation laws for liquid crystals. *Trans. Soc. Rheol.*, 5:pp. 23, 1961.

[100] C. Z. van Doorn. Dynamic behavior of twisted nematic liquid-crystal layers in switched fields. *Journal of Applied Physics*, 46(9):pp. 3738, 1975.

[101] D. W. Berreman. Liquid-crystal twist cell dynamics with backflow. *Journal of Applied Physics*, 46(9):pp. 3746, 1975.

[102] A. V. Zakharov and R. Y. Dong. The flexoelectric effect in nematic liquid crystals: A statistical- mechanical approach. *European Physical Journal E*, 6(1):pp. 3, 2001.

[103] R. Berardi J. Stelzer and C. Zannoni. Flexoelectric effects in liquid crystals formed by pear-shaped molecules. a computer simulation study. *Chemical Physics Letters*, 299(1):pp. 9, 1999.

[104] R. Berardi, M. Ricci, and C. Zannoni. Ferroelectric nematic and smectic liquid crystals from tapered molecules. *ChemPhysChem*, 2(7):pp. 443, 2001.

[105] F. Barmes, M. Ricci, C. Zannoni, and D. J. Cleaver. Computer simulations of hard pear-shaped particles. *Physical Review E*, 68(2):021708, 2003.

[106] F. Barmes and D. J. Cleaver. Computer simulation of bistable switching in a nematic device containing pear-shaped particles. *Chemical Physics Letters*, 425(1-3):pp. 44, 2006.

[107] A. J. Davidson and N. J. Mottram. Flexoelectric switching in a bistable nematic device. *Physical Review E*, 65(5):051710, 2002.

[108] D. L. Cheung, S. J. Clark, and M. R. Wilson. Calculation of flexoelectric coefficients for a nematic liquid crystal by atomistic simulation. *Journal of Chemical Physics*, 121(18):pp. 9131, 2004.

[109] M. P. Allen and A. J. Masters. Molecular simulation and theory of liquid crystals: chiral parameters, flexoelectric coefficients, and elastic constants. *Journal of Materials Chemistry*, 11(11):pp. 2678, 2001.

[110] G. Vertogen and W. H. de Jeu. *Thermotropic Liquid Crystals, Fundamentals*. Springer-Verlag, Berlin, 1988.

[111] I. W. Stewart. *The Static and Dynamic Continuum Theory of Liquid Crystals*. Taylor & Francis, London, 2004.

[112] A. Rapini and M. Papoular. Distortion d'une lamelle nematique sous champ magnetique. conditions d'ancrage aux parois [distortion of a planar nematic under application of a magnetic field. conditions of anchoring to the surfaces]. *Journal de Physique*, 33:pp. 237, 1972.

[113] G. E. Durand and E. G. Virga. Hydrodynamic model for surface nematic viscosity. *Physical Review E*, 59:pp. 4137, 1999.

[114] E. Hecht. *Optics*. Addision-Wesley, New York, second edition, 1987.

[115] J. C. Jones. New calculus for the treatment of optical systems. *Journal of the Optical Society of America*, 31:pp. 488, 1941.

[116] E. Abbé. *Neue Apparate zur Bestimmung des Brechungs - und Zerstreuungsvermgens fester und fluessiger Koerper [New Instruments to deremine the refractive index of solid and liquid materials].* Mauke's Verlag, Jena, 1874.

[117] R. E. Pepper and R. J. Samuels. *TVol. 14 of Encyclopedia of Polymer Science and Engineering, 2nd edition.* John Wiley and Sons, New York, 1988.

[118] P. S. Salter, C. Kischka, S. J. Elston, and E. P. Raynes. The influence of chirality on the difference in flexoelectric coefficients investigated in uniform lying helix, grandjean and twisted nematic structures. *Liquid crystals*, 36(12):pp. 1355, 2009.

[119] M. J. Bradshaw, D. G. McDonnell, and E. P. Raynes. Physical properties of nematic materials containing different ring systems. *Molecular Crystals and Liquid Crystals*, 70(1):pp. 289, 1981.

[120] M. J. Bradshaw, J. Constant, D. G. McDonnell, and E. P. Raynes. The physical properties of the cyanophenylcyclohexyl ethanes (pech). *Molecular Crystals and Liquid Crystals*, 97(1):pp. 177, 1983.

[121] M. J. Bradshaw and E. P. Raynes. The elastic constants and electric permittivities of mixtures containing terminally cyano substituted nematogens. *Molecular Crystals and Liquid Crystals*, 91(1-2):pp. 145, 1983.

[122] G. Barbero and L. R. Evangelista. *An Elementary Course on the Continuum Theory for Nematic Liquid Crystals, Theory of Elasticity I: Fundamentals.* World Scientific, London, 2001.

[123] C. Kischka, L. A. Parry-Jones, S. J. Elston, and E. P. Raynes. Investigation of the influence of dielectric anisotropy on the difference $(e_1 - e_3)$ of the flexoelectric coefficients of nematic liquid crystals. *to be submitted.*

[124] C. Kischka, S. J. Elston, and E. P. Raynes. Investigation of the influence of the molecular structure on the difference $(e_1 - e_3)$ of the flexoelectric coefficients of nematic liquid crystals. *to be submitted*.

[125] P. Rudquist, T. Carlsson, L. Komitov, and S. T. Lagerwall. The flexoelectro-optic effect in cholesterics. *Liquid Crystals*, 22(4):pp. 445, 1997.

[126] D. W. Berreman. Optics in stratified and anisotropic media - 4x4-matrix formulation. *Journal of the Optical Society of America*, 62(4):pp. 502, 1972.

[127] D. Y. K Ko and J. R. Sambles. Scattering matrix-method for propagation of radiation in stratified media - attenuated total reflection studies of liquid-crystals. *Journal of the Optical Society of America A-Optics Image Science and Vision*, 5(11):pp. 1863, 1988.

[128] *Numerical Algorithms Group (NAG).* NAG C Library, Mark 6.

[129] P. J. Bos and K. R. Koehler/Beran. The pi-cell - a fast liquid-crystal optical-switching device. *Molecular Crystals and Liquid Crystals*, 113(1-4):pp. 329, 1984.

[130] E. J. Acosta, M. J. Towler, and H. G. Walton. The role of surface tilt in the operation of pi-cell liquid crystal devices. *Liquid Crystals*, 27(7):pp. 977, 2000.

[131] C. Kischka, S. J. Elston, and E. P. Raynes. Measurement of the sum $(e_1 + e_3)$ of the flexoelectric coefficients e_1 and e_3 using a han cell. *Molecular Crystals and Liquid Crystals*, 494:pp. 93, 2008.

[132] W. Zwetkoff (V. N. Tsvetkov). *Zh. Eksp. Teor. Fiz.*, 9:pp. 603, 1935.

[133] M. Miesowicz. *Nature*, 17:pp. 261, 1935.

[134] C. Gahwiller. Viscosity coefficients of a room-temperature liquid crystal (mbba). *Physics Letters A*, 36:pp. 311, 1971.

[135] S. Chandrasekhar. *Liquid Crystals*. Cambridge University Press, Cambridge, second edition, 1992.

[136] J. K. Moscicki. Measurements of viscosities in nematics. In D. A. Dunmur, A. Fukuda, and G. R. Luckhurst, editors, *Physical Properties of Liquid Crystals: Nematics*, page 387. INSPEC, London, 2001.

[137] F. Yang, J. R. Sambles, and G. W. Bradberry. Half-leaky guided wave determination of azimuthal anchoring energy and twist elastic constant of a homogeneously aligned nematic liquid crystal. *Journal of Applied Physics*, 85(2):pp. 728, 1999.

[138] L. A. Parry-Jones and A. G. Morten. Measurement of twist elastic constant in nematic liquid crystals using conoscopic illumination. *Molecular Crystals and Liquid Crystals*, 436:pp. 259, 2005.

[139] P. D. Brimicombe, C. Kischka, S. J. Elston, and E. P. Raynes. Measurement of the twist elastic constant of nematic liquid crystals using pi-cell devices. *Journal of Applied Physics*, 101(4):043108, 2007.

Appendix A

Measurement of the viscosity γ_1

Abstract

A simple experimental method is proposed to measure the rotational viscosity γ_1 in nematic liquid crystals. Using a TN-Cell with an in-plane applied electric field, the distorted structure involves twist (but not splay or bend) and therefore the relaxation speed depends only on the ratio between the twist elastic constant K_{22} and the rotational viscosity γ_1. Knowing the twist elastic constant K_{22}, the rotational viscosity γ_1 can be extracted in a one parameter fit. The TN structure with an in-plane applied electric field is also useful, in that materials with both a positive and negative dielectric anisotropy $\Delta\epsilon$ can be measured. This was done and results will be presented for a few positive $\Delta\epsilon$ materials and one negative $\Delta\epsilon$ material. Where data from MERCK were available, these were compared with our measured values of γ_1.

A.1 Introduction

The rotational viscosity γ_1 is an important parameter for the switch-on and switch-off response in commercial devices. Therefore it is necessary to measure the rotational viscosity γ_1 so that the developed materials can be optimised to be very liquid (small viscosity), thus improving the dynamic response of commercial applications.

The experimental techniques to measure γ_1 can be divided into direct and indirect methods. The direct methods can provide precise and highly accurate data but require substantial amounts of sample. The techniques include the rotational viscosimetry (Tsvetkov [132]), oscillating plate method (Miesowicz [133]), and the shear flow capillary method (Gahwiller [134]). The indirect methods usually require fewer samples but knowledge of other parameters is necessary for the theoretical fitting of the data. Techniques include the dynamic Freedericksz effect and light scattering methods.

In the dynamics Freedericksz effect an electric field (or magnetic field) is applied across the device, which creates a splay and bend distortion. The switch-off dynamics depend on γ_1 and back flow effects, which complicate the fitting of the switch-off response [135, 136, 111]. However, applying an in-plane electric field (or magnetic field) creates only a twist distortion, where the switch-off dynamics only depend on the ratio of the elastic twist constant K_{22} and the rotational viscosity γ_1, as shown by

$$\gamma_1 \frac{\partial \phi}{\partial t} = K_{22} \frac{\partial^2 \phi}{\partial z^2} \quad \Rightarrow \quad \frac{\partial \phi}{\partial t} = \frac{K_{22}}{\gamma_1} \frac{\partial^2 \phi}{\partial z^2}, \tag{A.1}$$

where ϕ is the twist angle. This behaviour is discussed theoretically in detail [135, 136, 111] and used in our experiment to measure the rotational viscosity γ_1.

A.2 Experiment

Our new method uses a TN structure with an in-plane applied electric field with a frequency of f=1kHz [94, 123, 124]. The in-plane electric field just creates a twist deformation (no splay or bend deformation), as shown in Figure A.1 a). Further, the TN structure, compared to an anti-parallel structure, enables us to measure materials with a positive and negative dielectric anisotropy $\Delta\epsilon$ in a single geometry. If $\Delta\epsilon$ is positive, the upper part of the TN structure aligns parallel with the applied field E (Fig. A.1 b) and in the case that $\Delta\epsilon$ is negative, the lower part of the TN structure aligns perpendicular to the applied field E (Fig. A.1 c).

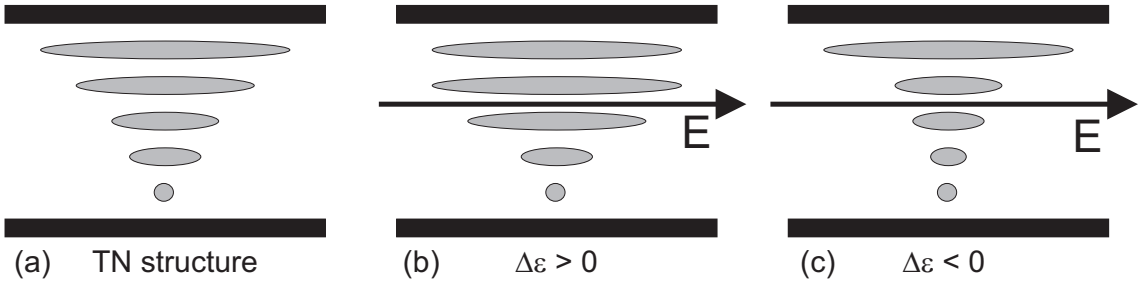


Figure A.1: (a) TN structure with no applied electric field. (b) Applied electric field with distortion for positive dielectric anisotropy material. (c) Applied electric field with distortion for negative dielectric anisotropy material.

The cell structure is created using rubbed PVA on both substrates and assembled perpendicular to each other. The top substrate has no ITO layer, only the bottom substrate. The in-plane electric field is realised etching an electrode gap of 500μm into the ITO layer of the bottom substrate. The ratio of electrode gap (500μm) to cell thickness d (10μm) is 50:1, which creates a homogenous electric field in the middle of the electrode gap. Two laser beams with a diameter of 600μm are focused down to 100μm and aligned in the middle of the electrode gap as shown in Figure A.2. Measuring the transmission at oblique incidence increases the signal and using two laser beams checks if the director tilt is out of plane, thus creating a splay or

bend distortion, which should be avoided.

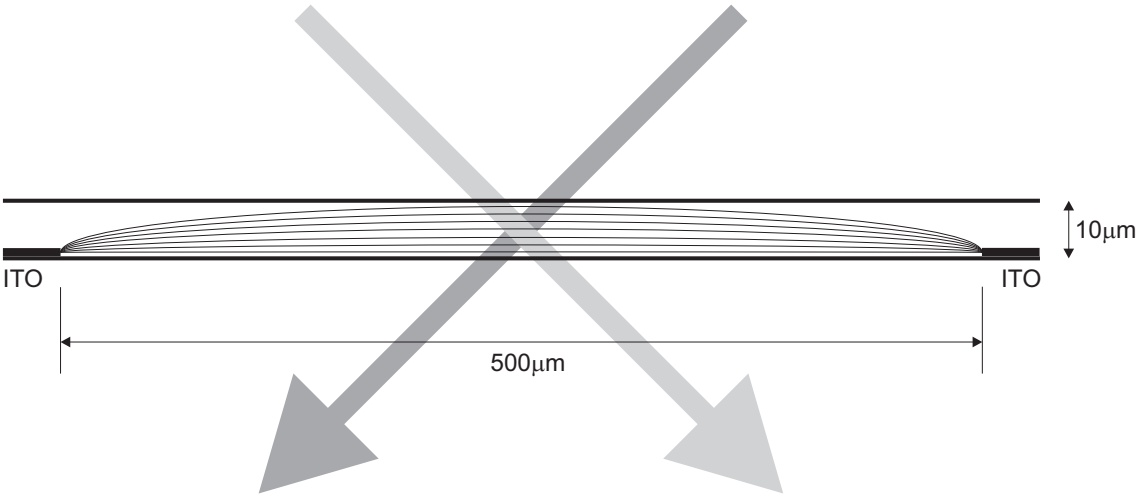


Figure A.2: Two laser beams focused down to 100μm in the middle of the 500μm electrode gap where the applied electric field is homogenous.

Two different sets of data were taken. First an ac voltage (1kHz) was applied between 0V and 250V in 50V steps and the transmission between crossed polariser was measured for both laser beams, as shown in Figure A.3 a). The data were scaled and normalised, measuring the transmission between crossed and parallel polarisers using a beam splitter. A 1D model using liquid crystal continuum theory [16] with 4x4 Berreman optics [126, 127]) is used to fit the ac data to extract the parameters for the cell thickness d, pretilt and internal electric field. These three parameters were kept fixed during the relaxation fitting, whereby the relaxation data were taken by applying an ac voltage (1kHz) of e.g. V_{ac}=250V. After reaching equilibrium, the voltage was switched-off using a triggered signal at t=0.25s and the transmission was recorded over time, whereby the twisted structure relaxed back into the ground state. The relaxation response depends on the ratio of K_{22} over γ_1, as shown in Equation A.1. Knowing the twist elastic constant K_{22}, the rotational viscosity γ_1 can be extracted in a one parameter fit because the parameters of cell thickness, pretilt and internal field were determined using the ac data and were kept fixed

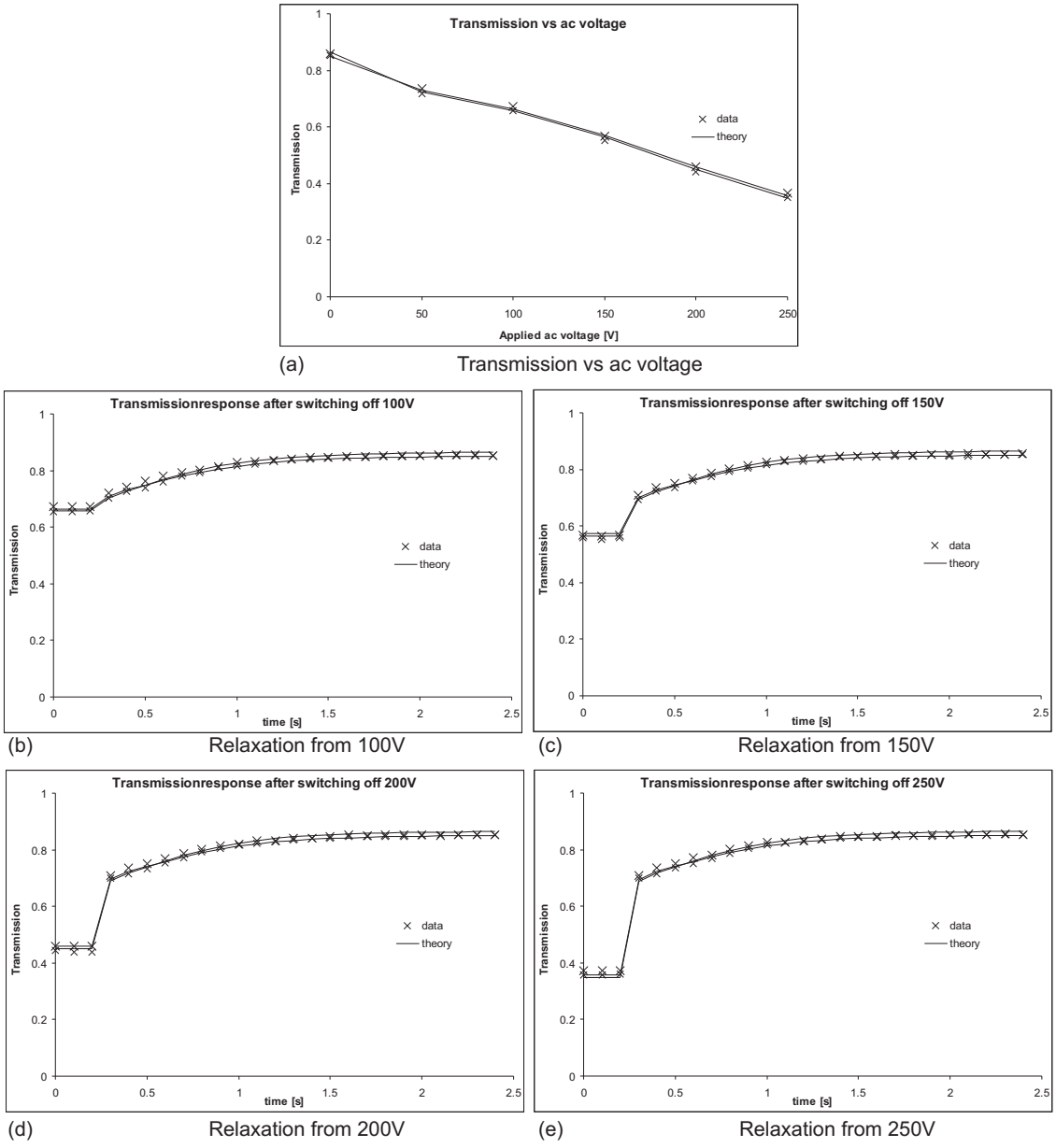


Figure A.3: Dynamics and AC

during the the fitting of the relaxation response. Because the relaxation depends on the ratio, it is also possible to fit and extract K_{22}, if γ_1 is known, but this is not done here. Figure A.3 shows the relaxation response and fitting for the voltages of 100V (Fig. A.3 b), 150V (Fig. A.3 c), 200V (Fig. A.3 d), and 250V (Fig. A.3 e), where crosses indicate data and the solid line the fitting. During the relaxation

measurement, the transmission was taken every 1ms, but for the fitting only values every 100ms were used to improve the fitting time. This works very well and quickly, as the quality of the fit shows. A complete fit for V=250V is shown in Figure A.4 a).

A.3 Results

The optical relaxation response (Fig. A.4 a) shows two different time constants. The first time constant (1) is very fast compared to the second time constant (2). The first, fast time constant between t=0.25s and t=0.3s is due to a higher order distortion in the director profile, which relaxes into a low order distortion after t=0.3s, as shown in Figure A.4 b). After t=0.3s, the director slowly relaxes exponentially into the ground state. The second time constant is also known as the switch-off time constant τ_{off} [135, 136, 111] and is defined as

$$\tau_{off} = \frac{\gamma_1}{K_{22}} \left(\frac{d}{\pi}\right)^2 \quad \Rightarrow \quad \gamma_1 = \tau_{off} K_{22} \left(\frac{\pi}{d}\right)^2 . \tag{A.2}$$

Using equation A.2, γ_1 can be calculated. But this is not as accurate as fitting the whole relaxation response. For example: the fitting result for CB (Fig. A.4 a) gives a γ_1 of 0.10 Pa s, which is in good agreement with the Merck value of 0.09 Pa s. Using equation A.2 with K_{22}=4.1pN [124], d=13.1μm and a measured τ_{off} of 0.5s gives a γ_1, with 0.12 Pa s.

Using our new method to measure γ_1 a set of materials were measured (E7, CB [124, 119, 120, 121], PCH [124, 119, 120, 121], DE [124, 119, 120, 121], MLC-7021-100, MLC-7029, MDA-02-2419, Material B [84] and when data from Merck is available, it is compared with our results. Table A.1 shows our results (at room temperature (22°C)) and data from Merck. The twist elastic constant K_{22} was

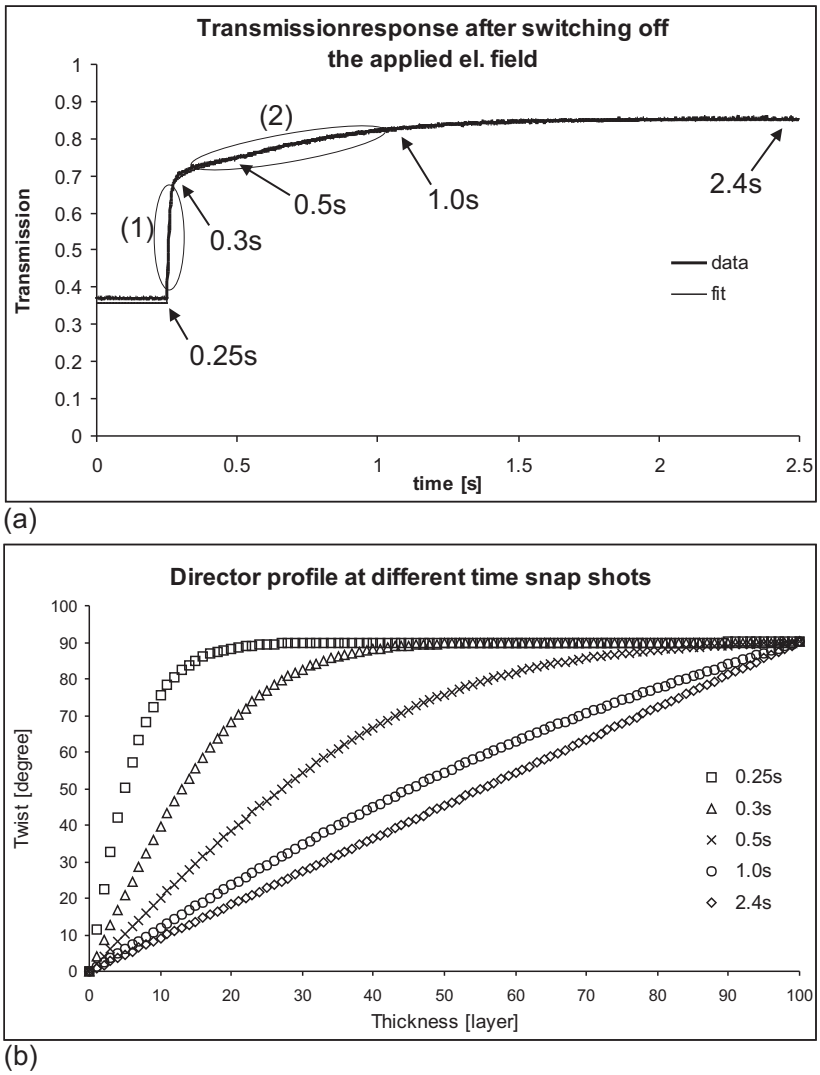


Figure A.4: (a)Triggered signal switched-off applied ac voltage at t=0.25s. Relaxation response was recorded and fitted. The data and fit are almost identical. The relaxation response shows two different time constants. (b) Director profile for snap shots in time of 0.25s, 0.3s, 0.5s, 1.0s, and 2.4s.

determined using a separate experiment, where a magnetic field was applied in-plane in a parallel cell and a twist distortion measured optically. The material MLC-7029 has a negative dielectric anisotropy ($\Delta\epsilon$=-3.7). This is possible because of the TN structure. Our measured γ_1 results are in good agreement with the Merck data.

Material	K_{22} [pN]	Measured γ_1 [Pa s]	Merck γ_1 [Pa s]
E7	6.5	0.18	0.19
CB [124, 119, 120, 121]	4.1	0.10	0.09
PCH [124, 119, 120, 121]	5.6	0.13	0.15
DE [124, 119, 120, 121]	5.0	0.19	-
MLC-7021-100	6.1	0.12	0.13
MLC-7029 ($\Delta\epsilon$=-3.7)	6.7	0.16	0.175
MDA-02-2419 ($\Delta\epsilon$=38.5)	6.1	0.50	-
Material B [84] ($\Delta\epsilon$=42.1)	5.0	0.17	-

Table A.1: Overview of our measured γ_1 results (room temperature (22°C)) and Merck values. The twist elastic constant K_{22} were determined using a separated experiment, where a magnetic field was applied in-plane in a parallel cell and a twist distortion measured optical.

A.4 Conclusion

Our new idea might be more complex than existing experiments but well known theory [135, 136, 111] shows that there are no back flow or kickback effects in this geometry. A TN structure with an in-plane applied electric field was used to record the relaxation response after switch-off an ac voltage. The in-plane applied electric field just creates a twist distortion, which is checked and measured by two laser beams at oblique incidence. Both laser beams show similar responses. The difference between the 2 laser beams can be explained and fitted using a pretilt in the theory. Applying an ac voltage to distort the structure has the advantage that problems with ions can be avoided and the ac data can be used to fit the cell thickness, pretilt and electric field. These three parameters were kept fixed during the fitting of the relaxation response. The fitting gives very good agreement with data and is more accurate than calculating γ_1 using the switch-off time τ_{off}. The TN structure enables us to measure materials with a positive and negative dielectric anisotropy in a single geometry, which is a big advantage. Results compared with Merck data show good agreement and the quality of the fit is very good.

The big advantage of this method is that the relaxation response depends on the ratio between the elastic twist constant K_{22} and the rotational viscosity γ_1. In our case, we had already measured K_{22} and therefore γ_1 could be fitted easily in a one parameter fit. However, it is more common to find γ_1 quoted in data sheet (Merck) of liquid crystal materials rather than K_{22} because it is more common and much easier to measure γ_1. This enables us to use the information given in the data sheets (Merck) of γ_1 to fit and extract K_{22}, which might be an easier and faster method compared to other measurements of K_{22} [137, 138, 139].